Molecular Basis for Heart Growth through Hyperplasia and Hypertrophy

By

Abigail C. Neininger

Dissertation
Submitted to the Faculty of the
Graduate School of Vanderbilt University
in partial fulfillment of the requirements
for the degree of

DOCTOR OF PHILOSOPHY
In
Cell and Developmental Biology
September 30, 2021
Nashville, Tennessee

Approved:
Christopher V.E. Wright, D.Phil.
Vivian Gama, Ph.D.
Edward Levine, Ph.D.
W. David Merryman, Ph.D.

DEDICATION

I dedicate this thesis to my grandparents, Thomas and Judith Ferguson, for imparting curiosity, wisdom, strength, and dependability onto me.

i carry your heart with me (i carry it in
my heart) i am never without it (anywhere
i go you go,my dear; and whatever is done
by only me is your doing, my darling)
-e. e. cummings

ACKNOWLEDGEMENTS

I would first like to thank my mentor, Dylan T. Burnette Ph.D. I came to Vanderbilt with a background in mathematical medicine and knew I wanted to branch out, but where? I rotated in three different departments and was attempting to find a fourth rotation that would suit my needs. Serendipitously, that day Dylan was added to the "Open Lab List". When we had our first meeting, I left and immediately texted my friend that this was it, and I joined one week into my rotation. I would like to thank Dylan for taking a chance on a mathematician with very little cell biology experience but enough enthusiasm to hopefully make up for it. Through the past years, I have been a sponge to every piece of information and advice I can get from Dylan and have emerged a true scientist. I am grateful for the environment he has created in lab which is just as fun as it is studious, and for his unwavering support of his graduate students.

When I joined the lab, it was "me and the boys"-me, Dylan, Nilay Taneja, and Aidan Fenix. I cannot express how thankful I am for these first few months in the lab when I learned everything I know about cell culture, experimental technique, and the minds of true scientists. I learned more about life from Nilay and Aidan than I learned about science-and I learned a *lot* of science from them. Soon after, we welcomed trainees Deeya Patel, Sophie Baillargeon, and Hunter Long, who I would like to personally thank as well. These three students were my first trainees that I mentored, who showed me my passion for teaching as well as being great people and friends. I would also like to thank the current graduate students in the lab and my very close friends, James Hayes and Zach Sanchez, without whom I surely would have lost my mind by now. These two bring me joy every day I work with them and are some of the brightest (very smert) people in my life. I am forever grateful for the fun we have had and the support system we have built.

I would next like to thank Beth Bowman, Ph.D. for introducing me to Vanderbilt and getting me here in the first place. I would not be where I am without Beth, and neither would any of

Vanderbilt's students. She has been the most accessible, friendly, and kind resource and I consider her my true friend for life.

My thesis committee and other mentors in the department have steered me toward my career in science and have helped me a lot along the way. Christopher Wright, Ed Levine, Vivian Gama, and David Merryman have been with me through my qualifying exam and committee meetings (a few of which took place during a global pandemic) and helped to keep me focused and on-track. Chris specifically has been a huge help in writing recommendation letters for me, acting as my co-mentor for grants, and allowing me to talk openly about mental health. Vivian has been an exceptional role model for me as a woman in science and I strive to be half of the professor she is. I would also like to thank the PIs of our collaborating labs, including Vivian Gama, Kathy DelGiorno, Bob Coffey, Matthew Tyska, Marija Zanic, Irina Kaverina, and many more. I would like to thank the Program in Developmental Biology for T32 funding, the Microtubules and Motors Group for assistance on projects, and the Vanderbilt CISR, HTS, and VANTAGE Cores for making new techniques accessible.

Vanderbilt's IGP has introduced me to my lifelong friends. I would like to thank Kelsey Pilewski, Noah Bradley, and Nate Klopfenstein for support, proofreading, memes, and friendship. I would also like to thank Mandy Truelock, my former roommate and forever friend. Our values and personalities mesh as if we were destined to cross paths, and in many ways we were. These friends have permanently intertwined into my soul and have helped make unbearable situations bearable, or at the very least, made me laugh so hard I forgot about any troubles I was having.

Most importantly, I would like to thank my family. My mom Nancy is my most steadfast source of support, laughs, and love, and I appreciate her every day. She has a sixth sense for knowing when I need her and frequently drove to Nashville at the drop of a hat whenever I confirmed that I needed a hug from her. My sister Chelsea and I laugh together, mourn together, and better ourselves together, and I will always be grateful for our lives as forever best friends. My niece Cameron and nephew Carson have given me a new hope for the world, and my sister is raising them to be empathetic and astounding individuals. I cannot wait to see who they become. I would also like to thank my dad, Todd, and the remainder of my amazing family for being supportive of my journey through academia and only asking me when I am going to graduate a few times.

Finally, I would like to thank my fiancé Mac Castro and our dog Bosco. Through everything, I have had a warm home to come to at the end of the day with a sweet dog and a supportive partner. Mac and I have undergone a transformational journey together during our time at Vanderbilt and are leaving the other side ready for anything the world can throw at us. May we find each other in any lifetime, timeline, or dimension.

My life has changed infinitely since I arrived at Vanderbilt, for the better, and every single person mentioned here has changed me into the person I love being. Thank you!

TABLE OF CONTENTS

LIST OF TABLES

LIST OF FIGURES

ABBREVIATIONS

HCM	Hypertrophic cardiomyopathy
iPSC	Induced pluripotent stem cell
ESC	Embryonic stem cell
DNA	Deoxyribonucleic acid
CDK	Cyclin-dependent kinase
ECM	Extracellular matrix
ELC	Essential light chain
RLC	Regulatory light chain
MYBPC	Myosin binding protein C
FRAP	Fluorescence recovery after photobleaching
DCM	Dilated cardiomyopathy
NMII	Nonmuscle myosin II
FAK	Focal adhesion kinase
KO	Knockout
MHC	Myosin heavy chain
MSF	Muscle stress fiber
hiCM	Human induced pluripotent stem cell-derived cardiac myocyte
MADM	Mosaic analysis using double markers
SIM	Structured illumination microscopy
CM	Cardiac myocyte
NMSFLS	Nonmuscle stress fiber-like structures
DSF	Dorsal stress fiber
siRNA	Small interfering ribonucleic acid
GFP	Green fluorescent protein

CHAPTER 1

INTRODUCTION

Mammalian Heart Development and Function

The heart is an essential organ with an emotional connotation. The heart facilitates blood flow throughout the body, transporting oxygenated blood from the lungs to the body and in transporting deoxygenated blood from the body to the lungs. Each beat enables oxygen to fuel metabolism, providing the energy the body requires for functioning. The heart has been considered the source of life force throughout history. It is behind our every step, breath, and movement, beating constantly, made mostly from the same heart cells from birth to death, which can beat every day for over 100 years. Behind each beat is the cardiac sarcomere, a lattice structure containing cytoskeletal filaments and the molecular motors which pull on them[1]. Beating heart muscle cells, or cardiac myocytes, contain this beating machinery and cell-specific instructions on how to assemble them properly. Heart disease is the leading cause of death not only in the United States but globally[2]. Hereditary heart disease, including dilated and hypertrophic cardiomyopathies, can be caused by mutations in sarcomere components, leading them to form aberrantly[3]. Heart attacks, or myocardial infarctions, can also damage the essential cardiac myocytes, which are not regenerative and cannot repair themselves[4,5]. The cardiac myocyte and its sarcomeres are at the center of how the heart forms and functions, and understanding how these cells form sarcomeres and how they divide is essential for disease treatment.

Blood in the developed heart, starting with oxygenated blood from the lungs, travels through the pulmonary veins into the left atrium, then through the mitral valve into the left ventricle, which pumps the blood through the aortic valve to the aorta, where it then travels throughout the body within arteries. Deoxygenated blood then travels through capillaries to veins, through the inferior vena cava (lower body) and superior vena cava (upper body) to the right atrium and through the tricuspid valve to the right ventricle, where it is pumped through the pulmonic valve to the pulmonary artery which transports it to the lungs (Figure 1-1C)[6].

The heart is the first organ formed during mammalian development, developing from mesodermal tissue[7]. The mesoderm is the middle layer of the developing embryo between the endoderm and ectoderm, and differentiates into bone, blood, and muscle[6]. During gastrulation, when cells move toward the interior of the embryo, cardiac progenitors begin to differentiate and the initial heart anatomy begins to form[6]. Cardiac progenitors arise from two distinct regions called “heart fields”, the first heart field and the second heart field. The first heart field are the first cells to differentiate, forming the initial tube-like structure called the “heart tube”. The heart tube forms when cardiac progenitors along the anterior lateral mesoderm are brought together. Some cardiac myocytes begin beating at this stage and blood flow begins through the tube, entering through the sinous venosus and exiting through the aortic sac (Figure 1-1A). The second heart field has delayed differentiation and is added at the start of cardiac looping, which occurs when the cardiac tube loops forward and to the right (from the perspective of the embryo), which develops overall embryonic left-right asymmetry and forms the four chambers of the heart (left and right atria, left and right ventricles)[6] (Figure 1-1B-C). A series of septations and transformations described below then divide the heart into its adult morphology.

The heart tube has five major components, described from the “top down” (superior to inferior, or proximal to distal, Figure 1-1A). The aortic sac develops into the aorta and pulmonary artery and contains the aortic arch. Below the aortic sac is the bulbis cordis, with three divisions. The proximal third of the bulbis cordis develops the muscular right ventricle, the middle third (conus cordis) develops the smooth outflow portions of the ventricles and the proximal aorta, and the distal third (the truncus arteriosis) develops into the pulmonary trunk. Below the bulbis cordis is the primordial ventricle, which forms the left ventricle. The primordial atrium below that forms the right and left auricles and the left atrium. The most distal region of the heart tube is the sinus venosus, which develops the right atrium, vena cava, and coronary sinus[6].

Figure 1-1: Heart Development

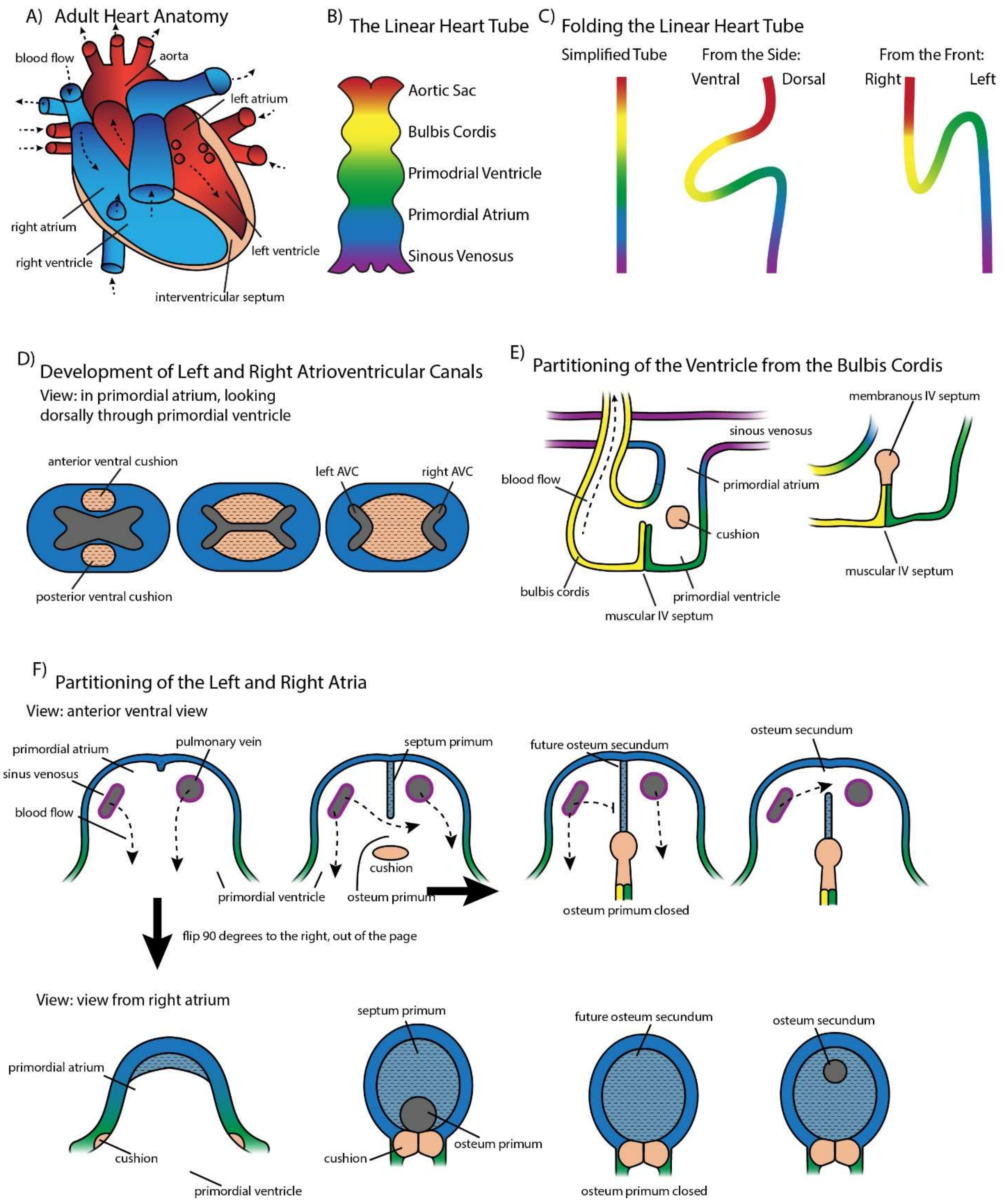

When the heart tube loops, second heart field progenitor cells drive massive cell expansion and growth due to their high proliferative capacity, driven by activation of the Wnt pathway[6]. The heart tube loses its foregut connection and bulges into the coelom as it folds, with the bulbis cordis looping to the anatomical right and primitive ventricle looping to the anatomical left (Figure 1-1B). Next, ventral cushions derived from neural crest cells enlarge to the point where the tube is split into the left and right atrioventricular canals (Figure 1-1D). The bulbis cordis and primordial ventricle then elongate to form the beginning structure of the muscular interventricular septum, while the endocardial cushion forms the membranous portion of the intraventricular septum (Figure 1-1E).

Next, along the primordial atrium wall between the sinus venosus opening and the pulmonary vein opening, a small growing section of membrane forms a “sticking point” in the tissue wall (Figure 1-1F, blue striped tissue), and as the two ventricular walls below the atria begin to move together, the small membrane bulge is compressed and appears to stretch downward to form a wall between the two atria called the “septum primum”, or first wall [6].

Simultaneously, the endocardial cushions push “upward” toward the septum primum, closing the small gap between them called the osteum primum, where blood flows from the right atrium to the left atrium. When the osteum primum closes, blood no longer can flow between the atria, which is incompatible with life. However, a small but growing hole develops in the septum primum through apoptosis. Eventually, the hole, now called the osteum secundum, is large enough to allow blood flow from the right to the left. Finally, the atria expand by pulling in vessels: the sinus venosus on the left, and the single pulmonary vein on the right which then pulls in further vessels. The sinus venosus forms the septum secundum, which is a second wall along the septum primum. Finally, oxygenated blood pushes through the walls to form a small gap called the foramen ovale, which allows oxygenated blood from the placenta to move from the right atrium to the left atrium[6].

The developed heart is comprised of several distinct cell types. Cardiac myocytes are the beating muscle cells that make up 50% of the heart muscle by cell number, with >25% made up of endocardial and endothelial cells which line the inside of the heart chambers and the surface of valves[7,8]. About 15% of the total cell number consists of fibroblasts, which is not a homogenous group but rather a population of cells derived from epicardial, endocardial, circulating, and hematopoietic cells[7]. The remainder of cells in the heart muscle are those derived from hematopoietic cells. Surrounding the heart muscle is a layer of mesothelial tissue named the epicardium[9], then a pericardial cavity and two outer pericardial layers, together comprising the pericardium[10].

During development, cardiac myocytes are highly proliferative, dividing rapidly to form thick heart muscle. This hyperplastic growth ceases perinatally and cardiac myocytes exit the cell cycle. As such, the majority of the growth of the heart muscle postnatally is driven by an increase in the size of individual cardiac myocytes, called hypertrophic growth[11]. This switch between hyperplastic growth to hypertrophic growth results in very few cycling cells, which is thought to protect the heart from tumor growth[12]. However, heart muscle does not grow back (i.e., regenerate) after an infarction or injury [12]. In addition, hypertrophic growth itself can lead to devastating cardiovascular disease, such as hypertrophic cardiomyopathy[13]. As such, several decades of research has concentrated on understanding the mechanisms behind cardiac myocyte cell division and identifying factors that can induce adult cardiac myocyte cell division.

The Cardiac Myocyte Cell Cycle

A reduction in the number of functional cardiac myocytes can result in heart failure (ref). During a myocardial infarction (i.e., a heart attack), an average of one billion cardiac myocytes are permanently lost[14]. The infarct zone is then cleared of dead cardiac myocytes and forms a fibrotic scar which cannot beat[12]. The rate of cardiac myocyte generation and turnover in the postnatal mammalian heart is low to negligible, with the actual rate differing greatly based on methodology[15].

Cell Turnover in the Heart

It is well-defined that cardiac myocytes are much less proliferative postnatally compared to during development, but the degree to which cardiac myocytes turn over in the postnatal mammalian heart depends on time post-partum and the species. Rodent hearts do not lose their proliferative capacity until 1 week post-birth, when cardiac myocytes undergo a final round of division without separating the daughter cells, forming large, non-proliferative binucleated cells[4]. Rodents given a myocardial infarction between birth and 1 week post-birth can almost entirely regenerate their heart, however, this regenerative capacity is lost after this time frame[4,15]. Although these findings are decades-old, it is still debated if there is any period after the first postnatal week in which mammalian cardiac myocytes are proliferative.

The first evidence that human cardiac myocytes undergo any adult turnover was published in 2009. In human history, levels of C12 and C14 isotopes were relatively stable until the 1950s, when nuclear bomb tests elevated global atmospheric C14 levels[16-18]. These levels are reflected in levels found in the human body, providing a creative way to measure turnover of human cells. An individual cell's C14 level in its DNA can mark its "date of birth"[17,18]. In this study, Bergmann et al. measured C14 levels in human left ventricle cells, fit these measurements to a model, and quantified a ~1% annual turnover of cardiac myocytes at 20 years old, and ~0.3% turnover at 70 years old[19].

In order to follow up on these results and determine how much of a contribution cardiac myocyte division makes to the growing postnatal human heart, one lab examined healthy human left ventricle cells for markers of cell division. This study detected an average 3.4X increase in cardiac myocytes in adult humans versus infant humans, and suggested that this increase was due to proliferation of cardiac myocytes. This translates to a 5.8% increase in cardiac myocyte number per year from infancy to age 20, moderately different than the 1% turnover detected in adults previously (own calculations)[19,20].

Binucleation

During the early post-natal period, cardiac myocytes undergo mitosis without cytokinesis which produces two nuclei in the same cell. These cells are binucleated[21]. It is estimated that rodent cardiac myocytes are 80-90% binucleated, whereas human cardiac myocytes are 25-57% binucleated[22-24]. Cardiac myocytes can also have one polyploid nucleus, frequently tetraploid in humans[24]. In this section, “binucleated” refers to two nuclei of any ploidy, whereas “mononucleated polyploid” will refer to cells with single nuclei with an increased ploidy count. Here, I will discuss hypotheses as to why and how binucleated cardiomyocytes form and discuss if binucleated cardiac myocytes are indeed non-proliferative.

While many hypotheses have formed for why binucleation occurs and if it is advantageous for cardiac myocytes, these hypotheses remain speculative. One hypothesis states that having two nuclei could increase a cell’s capacity for RNA synthesis which would be advantageous for very active cells like cardiac myocytes[21,25]. Interestingly, mammalian cardiac myocyte size scales with ploidy, and inducing zebrafish cardiac myocyte polyploidization increased cell size[26]. Another hypothesis suggests that polyploid cells could respond to environmental changes quickly due to gene expression from more than two genomes. Yet another suggests that having fewer, larger cells would reduce the overall number of gap junctions signals need to traverse for each heart contraction[24].

The beating cardiac myocyte is dense with sarcomeres-the filamentous mechanical structure which forms a beat. During cytokinesis, the process of separating two daughter cells, cardiac myocytes disassemble their sarcomeres, which re-form after division is complete[27]. Cytokinesis is driven by the formation and constriction of a ring-shaped structure under the plasma membrane called a contractile ring, which closes like a purse-string to separate two daughter cells[28]. An early hypothesis for the mechanism of binucleation in cardiac myocytes was failed cytokinesis through remnant sarcomeres forming physical barriers[29,30]. Fixed images of rat cardiac myocytes show cytokinetic adult cells with sarcomere bridges in the contractile ring[30]. In this model, a contractile ring closing onto a remnant sarcomere structure would detect failure and cease contraction, forming one binucleated cell.

An alternative, but non-mutually exclusive, hypothesis involves defective contractile ring assembly in postnatal myocytes (rather than incomplete cleavage by a functional contractile ring). While initial studies showed that cardiac myocytes do form a contractile ring during binucleation[31], later studies showed that some proteins are not correctly localized to the formed ring[27]. One example is Anillin, which has been shown to have aberrant localization during cardiac myocyte cytokinesis[27]. Anillin is an actin-binding protein which localizes to the cleavage furrow and binds to recruit septins and myosin II. Interestingly, this study showed that cardiac myocytes fully disassembled myofibrils during binucleation[27]. Further studies from this lab have detected mislocalized RhoA and IQGAP3 during binucleation as well as asymmetric astral microtubules[32,33].

Binucleation and polyploidization correlate temporally with loss of regenerative capacity in cardiac myocytes[4,24]. It is thus hypothesized that binucleation could have arose evolutionarily in order to prevent proliferation, as large-scale cardiac myocyte adult proliferation could affect heart function negatively due to the loss of sarcomeres in dividing cells[24]. However, the role of binucleation in cessation of proliferation is not fully understood[24,34].

Binucleated cells are, on average, larger than mononucleated cells, and the growth in cardiac myocyte size requires formation of new sarcomeres, which is a component of hypertrophy[26]. Hypertrophy is both a physiological and pathological process, a fine balance that when disrupted can cause severe disease [13,35].

Hypertrophy in Development and Disease

Hypertrophy is defined as the growth in size of individual cardiac myocytes[13]. The hypertrophy of cardiac myocytes that occurs during development and in response to stimuli such as exercise is commonly referred to as physiological hypertrophy. However, pathological hypertrophy in which the cardiac myocytes grow too large causes hypertrophic cardiomyopathy (HCM). HCM is defined by otherwise unexplained left ventricular hypertrophy without chamber dilatation (Figure 1-2)[13,36]. HCM can be acquired in response to pressure overload from hypertension or aortic stenosis, or in response to another disease or syndrome like skeletal muscle and metabolic disorders. However, over 50% of HCM cases not related to a syndrome, and are caused by genetic mutations[3].

Hypertrophy occurs when ventricular cardiac myocytes grow larger and produce more sarcomeres to adapt to new demands. These new sarcomeres add laterally to pre-formed sarcomeres, increasing cardiac myocyte width (concentric hypertrophy)[3]. Several mutations which cause HCM are found alter a cardiac myocyte's sarcomeric contractile properties, producing either hypercontractile or hypocontractile cardiac myocytes. Thus, HCM is widely considered a disease of the sarcomere[37]. HCM can also be caused by mutations in adhesion proteins, which connect heart cells together (Table 1-1)[38]. The remainder of this chapter will be in defining the sarcomere and adhesion components that are required for cardiac myocyte functionality and which have been implicated in disease states. Understanding how sarcomeres add laterally to pre-formed sarcomeres as well as understanding how sarcomeres initially develop during development is instrumental in eventually understanding the cellular mechanisms of HCM.

Table 1-1: Mutations in Sarcomere and Adhesion Components Which Cause HCM[38]

Gene	Protein	Component
ACTC1	Alpha actin	Sarcomere, thin filament
ACTN2	Alpha actinin 2	Sarcomere, Z-line
CAV3	Caveolin 3	Sarcomere binding partner
FHL1	Four and a half LIM domains 1	Sarcomere binding partner
MYH6	Alpha cardiac Myosin	Sarcomere, thick filament
MYH7	Beta cardiac Myosin	Sarcomere, thick filament
MYBPC	Myosin binding protein C	Sarcomere, A-band
MYL2	Myosin light chain 2	Sarcomere, myosin regulation
MYL3	Myosin light chain 3	Sarcomere, myosin regulation
MYLK2	Myosin light chain kinase 2	Sarcomere, myosin regulation
MYOM1	Myomesin 1	Sarcomere, M-line
MYPN	Myopalladin	Sarcomere, Z-line and I-band
TCAP	Titin-cap/Telethonin	Sarcomere, Z-line
TNNC1	Troponin C type 1	Sarcomere, thin filament
NNI3	Troponin I type 3	Sarcomere, thin filament
TNNT2	Troponin T type 2	Sarcomere, thin filament
TPM1	Tropomyosin 1	Sarcomere, thin filament
TTN1	Titin	Sarcomere, Z-line to M-line
VCL	Vinculin	Cell-ECM adhesion

Figure 1-2: Cardiac Hypertrophy

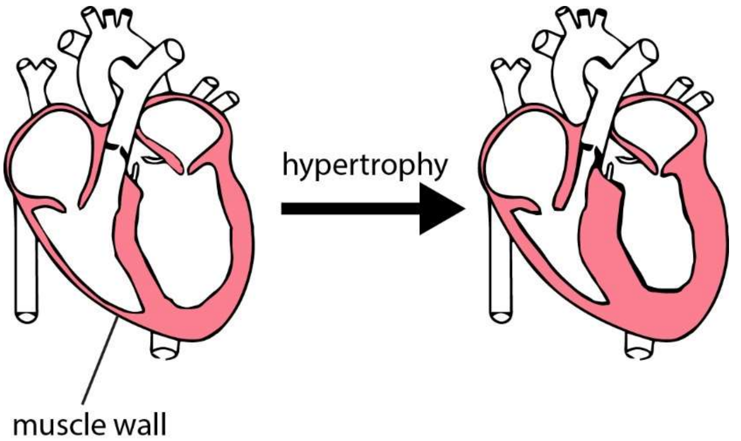

The Cardiac Sarcomere

In order to understand how the heart grows on a cellular level, one has to consider how sarcomeres form initially, and what interactions and environmental components are involved. The sarcomere is a dense and complex paracrystalline structure that produces the force behind a heartbeat[1]. The study of sarcomere formation is multifaceted and depends on how sarcomeres are defined, detected, and quantified in each study. Directly on either side of a Z-line is the I-band ("isotropic"): the region of the actin thin filament that is not interdigitated with muscle myosin. After the I-band is the A-band ("anisotropic), which contains an entire muscle myosin thick filament. Within the A-band is a "bare zone", or H-zone, where there are no thin filaments and only the rod domains of the thick filament. In the H-zone, directly in the middle between the two Z-lines, is the M-line, with elements which crosslink the thick filaments together and retain stability. The protein components and physiology of a sarcomere are described below.

Anatomy and Physiology of a Sarcomere

A sarcomere is made of thick myosin filaments which pull on parallel actin filaments. The biological definition of a sarcomere is the contractile unit of a myofibril between two Z-lines, which are the crosslinking structures that anchor actin filaments into the sarcomere (Figure 1-3). Arrays of sarcomeres align in a myofibril, which is tightly regulated to produce a single, synchronized beat throughout the entire heart. When cardiac myocytes are depolarized, calcium enters the cell through membrane channels as well as is released from the sarcoplasmic reticulum (calcium-induced calcium release). Calcium binds troponin C, one of three troponin isoforms which form a complex that regulates myosin binding sites on the actin thin filament. The troponin complex contains Troponin C, I, and T, the actin binding protein tropomyosin, and the F-actin pointed end binding protein tropomodulin. During rest, muscle contraction Is inhibited by the tropomyosin/troponin complex interaction[1]. Calcium binding induces a conformational change in the troponin complex, displacing inhibitory tropomyosin from actin/myosin binding sites, allowing myosin to bind the thin filament forming cross bridges. Myosin slides along actin filaments (ATP-dependent force) and transmits force (a “beat”). Upon re-binding of ATP, myosin releases actin, the troponin/tropomyosin complex rebinds and re-forms, and calcium is either extruded from the cell or re-enters the sarcoplasmic reticulum[39].

At the Z-line, a-actinin-2 holds the structure of the beating sarcomere, balancing the forces exerted on actin by the thick filament. Actinins are members of the spectrin superfamily of proteins, which also includes spectrin, dystrophin, and utrophin[40]. The spectrin superfamily is defined by spectrin protein domain repeats and the ability to bind actin[41]. There are four mammalian genes of actinin: ACTN1, 2, 3, and 4, producing a-actinin-1/-2/-3/-4, respectively. A-actinin-2 is the muscle-specific isoform which localizes at the Z-disk. Actinin2 also serves as a hub for several other proteins to bind and stabilize the Z-disk[40].

Figure 1-3: The Cardiac Sarcomere

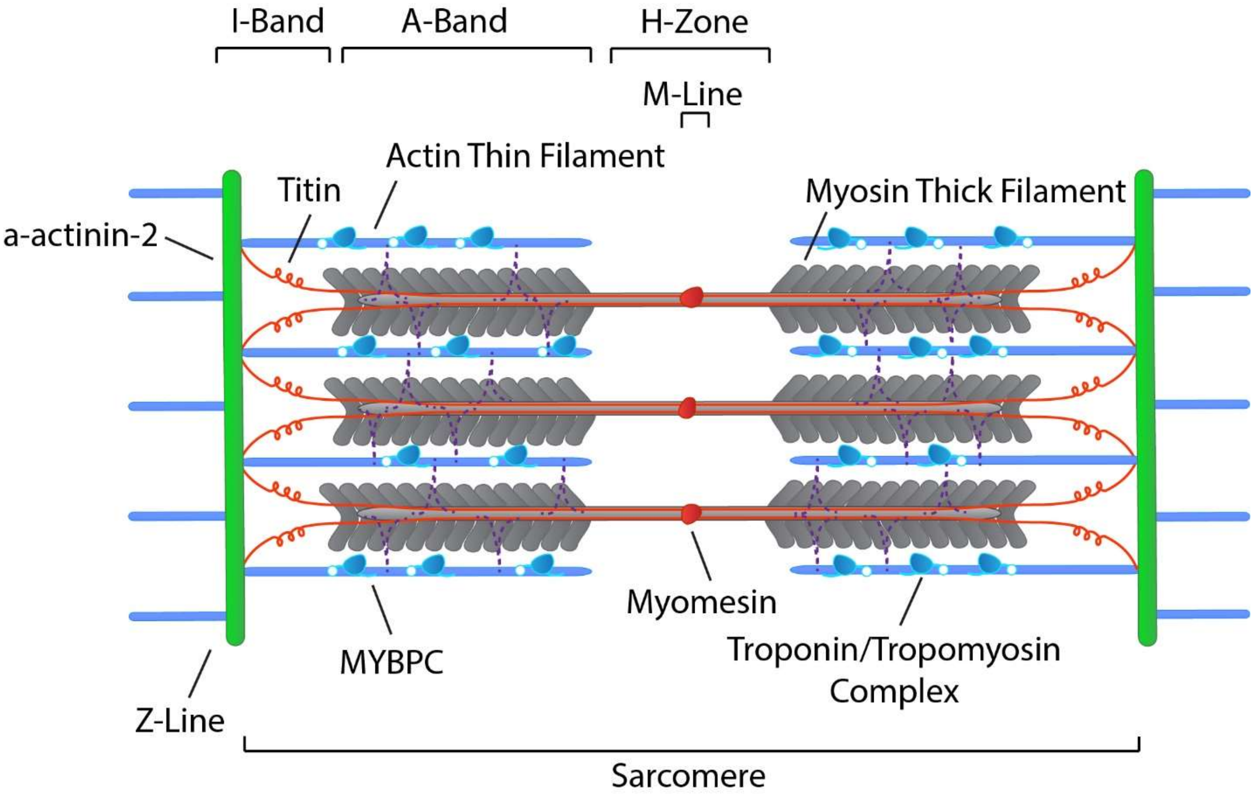

The I-band of the sarcomere contains thin filaments and titin, which regulates sarcomeric tension. In a sarcomere, there are two types of tension: passive and active. Active tension is generated by thick and thin filament force generation[42]. Passive tension and stiffness in the heart is largely defined by titin and the extracellular matrix (ECM, collagen in this case). The ECM provides an elastic force through collagen's high tensile strength, whereas titin provides an entropic force[43]. Titin, also known as connectin, is a massive protein, with a molecular weight of 3.4-3.9 megadaltons. The human titin gene (TTN) has 363 exons[44]. One titin molecule spans half of the sarcomere, that is, from Z-line[1]. The N-terminus of titin localizes at the Z-line and the C-terminus localizes to the M-line[1].

At the Z-line, titin has two immunoglobulin domains which interact with telethonin (also known as "titin-cap") and actinin to anchor titin into the Z-line[43]. I-band titin contains the source of its extensible spring-like segment, responsible for titin's entropic passive tension generation. I-band titin also contains a PEVK domain, essential for titin-based viscosity, arising from interactions between PEVK and actin (Figure 1-4). This interaction slows actin filament sliding via an electrostatic effect between actin (negatively-charged) and the positively-charged PEVK element[43]. In the A-band, titin binds myosin heavy chain and MYBPC, and at the M-line, titin binds several M-line proteins including myomesin[45]. M-line titin also includes the Titin Kinase (TK) domain, which has a dual autoinhibitory mechanism via its regulatory C tail[43].

Parallel to actin thin filaments are muscle myosin thick filaments, which pull on actin through transient interactions which produce force. Myosin heads orient on the thick filament in one direction, which reverses at the M-line at the center of the sarcomere[1].

Myosin has a globular head with four subdomains binding actin, ATP/ADP, the essential light chain (ELC), and the regulatory light chain (RLC) and a C-terminal rod domain[1]. There are two cardiac muscle myosin isoforms: MYH6 (cardiac alpha myosin) and MYH7 (cardiac beta myosin). MYH7 is expressed during development, and nearly immediately after birth, MYH6 takes over as the predominant myosin with a MYH6/7 ratio of 16:1 in rodents persisting through adulthood[46,47].

An interesting recent study used electron cryo-tomography to investigate the protein-level organization within the skeletal muscle sarcomere. Typically, it has been assumed that double-headed myosin binds the same actin filament with each head, but this study found that in ~3% of myosin binding cases, each head bound a different actin filament[48]. Further, this study showed that myosin heads tend to bind actin subunits oriented in the direction of the thick filament it comprises. This provides an interesting dynamic look into myosin binding as a process regulated by physical barriers like actin filament orientation as well as complex signaling pathways[48].

At the center of the thick filament is the M-line (named after the German word for middle: "mittel"). M-line components, including myomesin and skelemin, crosslink the thick filaments into a hexagonal lattice structure. Further stabilizing the sarcomere is MYBPC, or myosin binding protein C, which form the cross-bridges found in the A-band[1].

Several sarcomeres arrange laterally to form a myofibril, which is anchored on each end by cell-ECM adhesions[49].

Figure 1-4: Titin Structure and Binding Partners

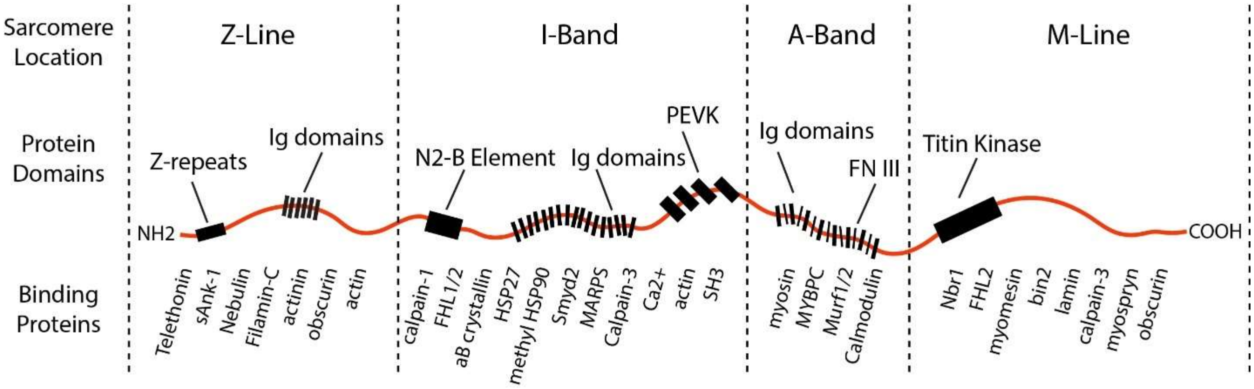

Cell-ECM Adhesions

Cell-ECM adhesions are structures by which cells sense and communicate with their environment and are required for cell migration and spreading. Focal adhesions are cell-ECM adhesions that are mechanosensitive and transmit force. In the cardiac myocyte *in vivo*, focal adhesion-like structures called costameres adhere cardiomyocytes together and to the ECM[49,50]. Costameres act as a physical adhesion to counterbalance the force produced by sarcomere contraction, while also acting as a signaling hub for mechanosensitive pathways and cytoskeleton remodeling. Here, I discuss the function and components of cardiac myocyte focal adhesions and how they regulate actin dynamics.

Cell migration and spreading are complex processes requiring coordinated dynamics of actin retrograde flow, focal adhesion formation and retraction, and contractile force. When actin filaments polymerize and grow at the leading edge, they flow back into the cell body, undergoing retrograde flow. In order for a cell to spread in the opposite direction of actin retrograde flow, adhesions must act as “molecular clutches”, directly linking the actin cytoskeleton to the substrate through focal adhesions and providing a connection for force to transmit through[51]. Spreading is regulated by two distinct zones of actin flow. The lamellipodium is the zone near the cell boundary with fast actin flow. Directly interior to the lamellipodium is the lamella, with slow actin flow[52]. These zones of flow are regulated by adhesion maturation: as a nascent adhesion forms slightly ahead of the lamellipodium/lamella boundary, the local actin flow is slowed, producing a new boundary further toward the cell edge. The width of the recently reduced lamellipodium is then restored as the cell edge advances[52].

Figure 1-5: Focal Adhesion Structure

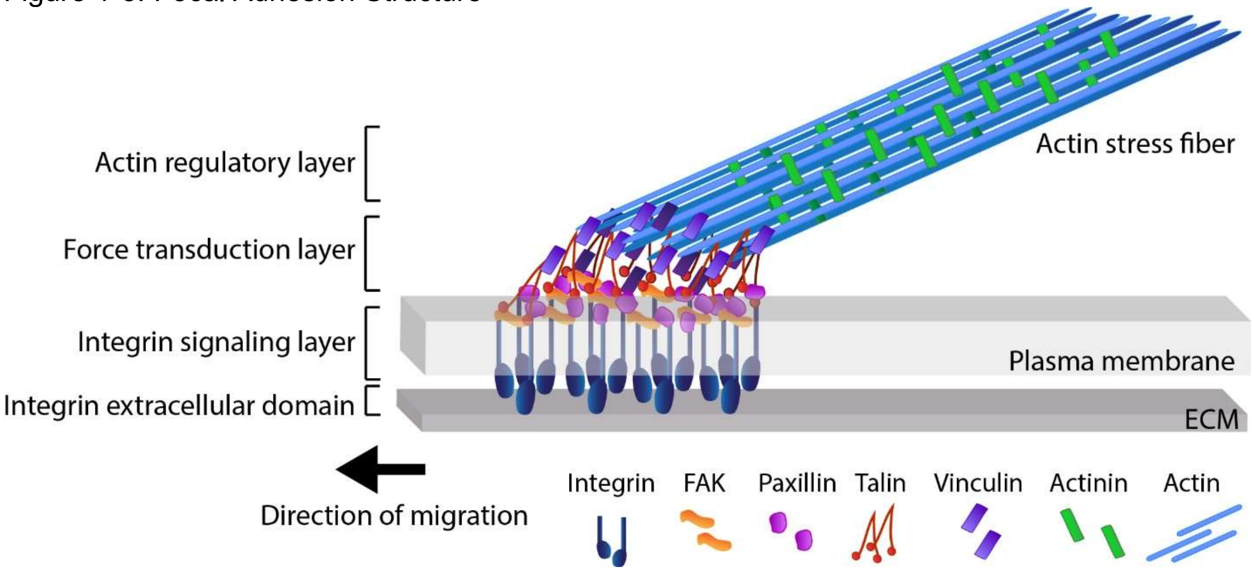

The lamella contains a type of stress fiber called a transverse arc, which is formed by Arp2/3-mediated branched actin polymerization at the lamellipodium/lamella boundary[53]. These arcs can mature into ventral stress fibers, which are long actin-based structures in migrating cells. Arcs form ventral stress fibers by lateral fusion while undergoing centripetal flow (that is, an asymmetrical circular inward flow), which generate tension via connections to focal adhesions on both ends[53,54].

The focal adhesion can be partitioned into five layers, from ventral to dorsal: the extracellular layer, the intracellular integrin signaling layer, the force transduction later, the actin regulatory layer, and the actin stress fiber structure (Figure 1-5). The extracellular layer is composed of integrin receptors which bind to the ECM. Integrins are transmembrane receptors which are comprised of heteromeric combinations of alpha and beta subunits[55]. Extracellular integrin binds different ECM proteins depending on its subunits, while intracellular integrin mediates a large interactome of ~160 proteins[5655]. The intracellular domain of integrin comprises the integrin signaling layer, which also contains focal adhesion kinase (FAK).

FAK is a tyrosine kinase which plays dual roles, acting to increase adhesion formation through its scaffolding function as well as increase adhesion disassembly through its signaling function[49,57]. FAK is activated upon autophosphorylation at its Tyr397 residue, and upon activation, forms a complex with Src to phosphorylate paxillin[57-59]. Paxillin is a protein also in the signaling layer which recruits the components of the mechanosensitive layer: talin and vinculin[60].

Talin is a mechanosensitive protein that plays an essential role in force generation. Talin's head domain localizes to focal adhesions through binding integrins intracellular tail. Talin stretches upon sensing force, which exposes cryptic binding sites which bind to localize and activate vinculin[61]. Vinculin is also mechanosensitive and has an actin-binding head domain and a tail domain, both of which are required for traction force generation. When inactive, vinculin forms a folded conformation in which the head and tail domains interact[62]. When activated, vinculin extends and the head/tail interaction is disrupted[62]. Inactive vinculin localizes lower in the focal adhesion (toward the ECM) in the integrin signaling layer immediately interior to the membrane, binding phospho-paxillin. Once activated, vinculin redistributes higher into the focal adhesion in order to bind actin and engage retrograde flow, acting as the “molecular clutch”[60]. Actin filaments are crosslinked by actinins and are regulated by Zyxin and VASP at the actin regulatory layer. Above the actin regulatory layer is the connected stress fiber.

Cardiac Sarcomere Formation

Models of Sarcomere Formation

The proposed mechanism for sarcomere formation has long been conflicting and competitive in the cardiovascular biology field, beginning with two main models: the template model and the premyofibril model. In 1984, the Sanger lab demonstrated fluorescent alpha-actinin incorporation into Z-lines of living chick cardiac myocytes. They identified small actinin particles at the cell periphery and hypothesized that these aggregates were nascent Z-lines which eventually increase in spacing and form mature Z-lines in myofibrils. Further, they confirmed that mature myofibrils are formed by the annealing of fine actin strands with nascent actinin aggregates laterally into wider bands with organized myofibrils (Figure 1-6A)[63].

Only three months later, the Holtzer lab identified stress fiber-like structures in cardiac myocytes, which appeared to be transient and contained nonmuscle proteins such as nonmuscle myosin and nonmuscle forms of actin. These stress fiber-like structures likely acted as a template for emerging myofibrils with muscle-specific proteins like alpha-actin and muscle myosin, then the stress fibers seem to disappear. This study did not identify a significant role for adhesions in sarcomere formation, only noting that vinculin-positive adhesions linked mature myofibrils to the membrane (Figure 1-6B)[64]. These findings led to the proposal of the Template model.

Figure 1-6: Models of Sarcomere Formation

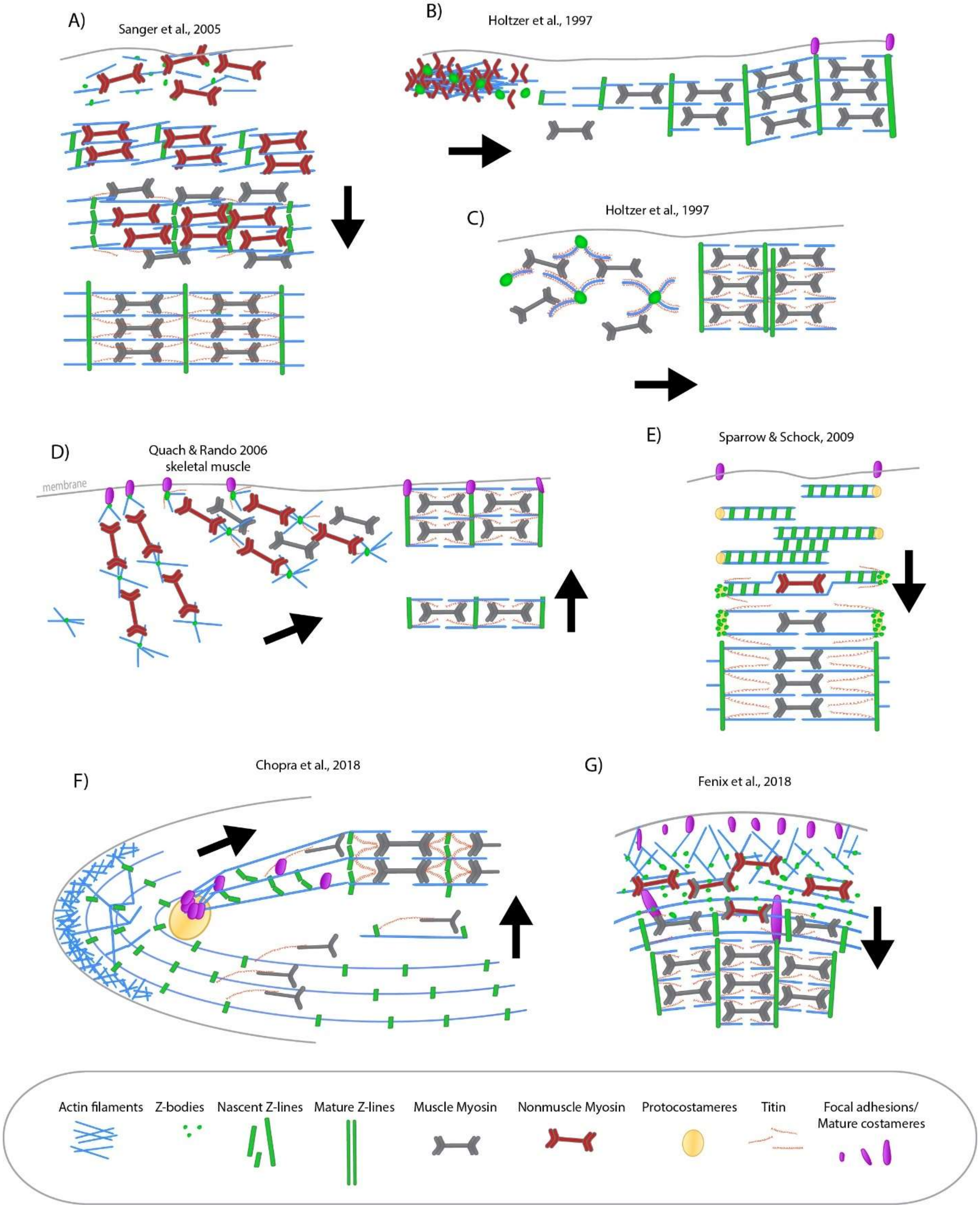

Both models were presented as mutually exclusive with the major difference being the fate and composition of any nascent myofibril/precursor structure. The template model suggests stress fiber-like structures degrade upon myofibril formation, whereas the premyofibrils model suggests that the thin strand-like filaments (analogous to the stress fiber-like structures by eye but labeled separately in each paper) are retained and anneal laterally into wider myofibrils.

Over the next two decades, the template model evolved into a model investigating the existence of I/Z/I bodies and their role in myofibril formation. I-Z-I bodies are small complexes containing actinin2 punctae surrounded by "brushes" of actin decorated with titin[65,66] (Figure 1-6C). The existence of I-Z-I bodies and their relationship with Z-bodies is contested. In 1990, Schultheiss et al. defined which proteins are found in templating structures versus striated myofibrils. Templating structures (or, "nonstriated myofibrils") contained actinin2, actin, troponin I, and titin in complexes, whereas striated myofibrils contained myomesin and MYBPC. Further, small "ectopic patches" were found in some cells which had striated structures which were about half the width of mature myofibrils. These structures have been defined previously as "pseudo-striated myofibrils" with randomly ordered myosin fibrils[65,67]. This study demonstrated that only the Z-Line area of titin localized to I-Z-I bodies, but the I-band region of titin did not. This could be an antibody issue or could reveal different functions of titin domains in myofibril formation. In 1992, the components of stress fiber-like structures in chick cardiac myocytes and the role of adhesions in their formation was investigated in the context of the template model[51]. They determined that the earliest steps of myofibril formation required vinculin, actin, and actinin2, and nascent myofibrils have oppositely oriented adhesion plaques on each end. Further, they identified that nonmuscle myosin does *not* localize to the stress fiber-like templates, directly conflicting with findings from the Sanger lab. One interesting finding from this study is that stress fiber-like structures in cardiac myocytes are not authentic stress fibers, as they do not have nonsarcomeric proteins and have I-Z-I complexes within. However, the sources of catalog numbers of the antibodies targeting nonmuscle proteins in this study were not included, casting doubt on which specific myosins these antibodies were raised against ("nonmuscle actinin" and "non-sarcomeric-MHC" were the definitions given). Interestingly, chick cardiac myocytes do not express NMIIA, so if their antibody was against NMIIA it would not stain anything in a chick cardiac myocyte[51,68].

In 1997, Holtzer's lab further developed the definition of I-Z-I "brushes" as the templates themselves, straying from their previous hypothesis that templates disintegrate once they are used as templates[66]. In their model system of BC3H myoblasts (rhabdomyosarcoma cells), small scattered A-band-like structures form, seemingly independent of any nearby actin filaments or Z-lines. These structures have 1.6 um-long muscle myosin filaments. They did not find evidence of premyofibrils in this cell line, but did define a boundary between nonstriated and striated myofibrils based on protein expression and filament organization. Striated myofibrils contained myomesin at the M-line, organized titin, and arrays of muscle myosin filaments, whereas nonstriated myofibrils contained punctate titin and less-organized muscle myosin filaments. This study also suggests an "end-on" assembly pathway for nonstriated templates to form myofibrils, rather than lateral attachment. While this might seem like a large derivation from the previous template model, it should be noted that these experiments were performed in an engineered cell line which does not properly form myofibrils compared to primary cells[69].

The Pre-myofibril model gained traction in the field as more *in vitro* and *in vivo* evidence was generated. In 1994, Rhee et al. identified premyofibrils, nascent myofibrils, and mature myofibrils in fixed chick cardiac myocytes, and characterized which proteins were found in each myofibril developmental stage[70]. Premyofibrils contained NMIIB, actinin and actin, and exhibited actinin2 spacing between 0.3-1.4 um. Nascent myofibrils contained actinin and actin, both muscle and nonmuscle (NMIIB) myosin, titin, and zeugmatin. Upon maturation, mature myofibrils lose NMIIB and gain MYBPC. Mature myofibrils have actinin2 spacing between 1.8-2.5 um[70]. In 1997, Dabiri et al. showed live evidence of Z-bodies forming at the spreading cell edge and growing to form Z-lines in a live movie of chick cardiac myocyte Z-line formation[71]. The Sanger lab investigated skeletal muscle cells as well as quail and zebrafish cardiac myocytes and found similar evidence in these model systems that there are distinct premyofibril populations which form mature myofibrils[68,72,73]. Interestingly, it appears that in skeletal muscle cells (and potentially in cardiac myocytes), Z-bodies can add on to myofibrils laterally *and* in an end-on fashion. However, a unifying hypothesis between these models (and in *C. elegans* muscle) is that sarcomere formation begins at the membrane, whether through a template structure, actinin2 aggregates, premyofibrils, or some combination of the three[74].

Around this time, a third competing model was proposed by Ehler[75]. This model proposed that thin filaments and thick filaments form separately, then are interdigitated through interactions between titin and myomesin. These studies were performed using fixed sections of embryonic chick cardiac tissue, and proposed that actinin2 aggregates are *not* Z-bodies, but are just smaller striated myofibrils. This hypothesis was derived from the finding that these aggregates had ~2 um spacing, which is the same as Z-line spacing in a mature myofibril. However, observing these images in a present-day context, it appears that more actinin2 puncta are actually present in the image than were detected and/or quantified by the original authors (due, likely, to limitations in microscopy sensitivity and image processing software at the time of study), casting doubt on these conclusions. Of note is that this study also did not identify any evidence of premyofibrils or any stress fibers/stress fiber-like structures[75].

More recently, as evidence surmounts linking mutations in adhesion proteins to cardiomyopathies, the role of adhesions in sarcomere formation has been studied, forming a fourth competing model. This model implicates integrin-mediated adhesions as either precursors to sarcomeres or are the direct areas of sarcomere formation, alongside the possibility of sarcomeres assembling centripetally as cardiac myocytes “turn” on a dish[76]. These studies implicating adhesions in sarcomere formation mostly follow the interdigitating model described above, with a few components of the premyofibril model sprinkled throughout.

In 2006, Quach and Rando studied mouse skeletal muscle sarcomere formation and determined that sarcomeres form first from a focal adhesion, dangling premyofibrils from the membrane like “beads on a string” (Figure 1-6D). These premyofibrils turn to be parallel to the membrane by an unknown mechanism, where they are linked via integrin-based adhesions (costameres). Further elongation of myofibrils occur via lateral addition of premyofibrils to the region of opposite-facing end of the myofibril (directly contrasting to the addition to the membrane-facing region of the myofibril). Myofibril-mediated tension signals to the integrin-based adhesions which cluster underneath the Z-lines of the myofibrils to provide a linkage to the membrane and stability, and FAK signaling is required for this crosstalk[77].

Sparrow and Schock further postulate in 2009 that *protocostameres*, or, nascent focal adhesion-like structures, are not only required for myofibril formation and linkage to the membrane, but actually form Z-bodies and are the site for myofibril formation (Figure 1-6E). In this model, protocostameres polymerize actin filaments in different directions. When two opposing polarity filaments come into contact, they are crosslinked by actinin2 and fuse laterally to form premyofibrils, connected to costameres on each side. These costameres then become Z-bodies when they merge together and with actinin2, which then link with other Z-bodies to form Z-lines. Interestingly, in this model, a nonmuscle myosin filament opens the space between actin filaments to first displace actinin, then is displaced by muscle myosin, providing a role for both myosin isoforms in myofibril formation[76].

The most recent study implicating costameres in myofibrillogenesis was published in 2018, in which the Chen lab determined that protocostameres are the site of myofibril formation, but do not themselves become myofibrils (Figure 1-6F). This publication devises a model different from any previously proposed models, hypothesizing that integrin-mediated protocostameres act as the site for sarcomere assembly, with myofibrils streaming out of adhesions centripetally and gaining titin and muscle myosin along the way. Further, they suggest nonmuscle myosins are not required for sarcomere formation, while muscle myosins are required. Another method of assembly occurs simultaneously, named “transverse assembly”, where pre-formed myofibril "pieces" are removed from the actin network at the cell membrane and transported to the lateral side of a developing myofibril[78].

Two competing models were published in the same year as Chopra's protocostamere model, one implicating both NMII and muscle myosin in sarcomere formation, and one from our lab implicating NMII and formins in sarcomere formation. The former combined pieces of the premyofibril model using evidence from *Drosophila* skeletal muscle to propose that the first premyofibrils simultaneously form, requiring mechanical tension from NMII. In this model, muscle myosin is only required for large-scale organization, not local actin order[79].

Our lab published a study later that year showing myofibril assembly in human iPSC-derived cardiac myocytes, unifying the template and premyofibril models by showing evidence for both during sarcomere assembly (Figure 1-6G)[80]. Our model proposes that the stress fiber-like structures near the cell membrane are muscle stress fibers (MSFs), containing actinin2 Z-bodies. MSFs are similar to, but distinct from nonmuscle stress fibers. MSFs containing Z-bodies undergo slow retrograde flow and have nonmuscle myosin isoforms which are essential to sarcomere formation. These nonmuscle myosins NMIIA and NMIIB form cofilaments with each other, then later in sarcomere formation begin forming cofilaments with muscle myosin. Muscle myosin eventually replaces the nonmuscle myosin in the filaments, growing to form 1.5 um-long filaments which stitch or concatenate together to form the A-band. Simultaneously, Z-bodies stitch together to form Z-lines near the center of the cell, where there is little to no retrograde flow of actin[80].

CHAPTER 2

A HIGH-THROUGHPUT METHOD FOR STUDYING CARDIAC MYOCYTE PROLIFERATION

Neininger, AC., Long, JH., Baillargeon, CM., Burnette, DT. (2019). *Sci. Rep. 9:15917*

Introduction

Cardiac myocytes are the essential muscle cells which drive the beating of the heart. These cells display a balance between hyperplastic growth by cell division and hypertrophic growth by cell enlargement during development. However, after birth, mammalian cardiac myocytes exit the cell cycle and rely solely on hypertrophic growth[81]. As a result, cardiac myocytes lost due to injury cannot be replaced. There has been a concerted effort to find factors that induce cardiac myocytes to reenter the cell cycle and successfully undergo cell division. Identification of these factors would facilitate the ultimate goal of regenerating heart muscle *in vivo*, so the heart can heal from injury. Overexpression of positive cell cycle regulators or transcription factors or deletion of negative cell cycle regulators in rodent models has been shown to induce proliferation (summarized in Figure 2-1). However, there is a limit to the amount of protein that can be overexpressed in a cell due to proteasome-mediated degradation of the excess protein[2]. Excitingly, a recent study has circumvented this by demonstrating a combinatorial approach utilizing both genetic manipulation and small molecule inhibitors which induced cell division in post-mitotic murine cardiac myocytes *in vivo*[82]. This treatment also improved cardiac function after a myocardial infarction, proving to be a promising approach to regenerate cardiac myocytes *in vivo*. Thus, identifying additional small molecules that induce cardiac myocyte proliferation could be beneficial for future combinatorial therapies.

Current technologies lend themselves to high-throughput screening to identify bioactive small molecules. Such a screening platform needs to be robust, sensitive, and large-scale, with a clear readout. There are several *in vitro* model systems that could be considered for such a screen, each with unique advantages and disadvantages. Cardiac myocytes can be isolated from rodents and represent mature, adult cardiac myocytes. However, these primary rodent cardiac myocytes can only beat in culture for a few days, making them unsuitable for long-term screens. Beating can be inhibited, making these cells will last longer; however, they will dedifferentiate to a more immature state[69]. In addition, the isolation protocols can be variable, resulting in cell populations that differ between batches and laboratories. As such, we believe human induced pluripotent stem cells differentiated into cardiac myocytes likely to be a robust model system. These cells can be maintained in culture for weeks to months and beat continuously, facilitating long-term screens. Although these cardiac myocytes are more transcriptionally similar to embryonic cardiac myocytes, this immature state maintains a slight proliferative potential that can be modulated by small molecules[83]. The long-term goal of many such studies are to test compounds in whole animals, such as with a high-throughput zebrafish screen or a more low-throughput treatment in rodents given a myocardial infarction.

A second major consideration in developing a screening platform is accessibility to researchers from a wide range of disciplines. This requires a straight-forward procedure with a simple and quantitative output. The cost of such a screen also needs to be minimized as the initial investment into a project is often a hurdle for laboratories entering a new field of study. Taking these considerations, here we report a strategy for identifying small molecule regulators of cardiac myocyte proliferation. We use human iPSC-derived cardiac myocytes (hiCM) and relatively low-magnification microscopy to monitor the number of nuclei over time. This has allowed us to screen a library of small molecules to identify compounds that both increase and decrease proliferation. This procedure is straight-forward, flexible, and cost-effective.

Results

Identifying hiCMs as a Model System for Cardiac Myocyte Proliferation

It has been noted that hiCMs have a slight proliferative capacity[84, 85]. The vast majority of studies have used methods such as BrdU incorporation into replicating DNA or Ki67 localization in the nucleus to mark cycling cells (Figure 2-1). There are two potential outcomes of DNA synthesis: the nucleus becoming polyploid or mitosis. Following mitosis, the cell can either go through cytokinesis and create two new daughter cells (i.e., hyperplastic growth) or it can become binucleated (i.e., hypertrophic growth)[31, 25]. While studying sarcomere assembly in hiCMs plated at sub-confluent densities[80], we observed both hiCMs that appeared to go through cytokinesis (Figure 2-2B, S1A) and hiCMs which were binucleated (Figure 2-2C). We confirmed these two outcomes by localizing β-catenin to mark the boundaries of cells (Figure 2-2B-C, S1D). We first attempted to use a live-cell membrane marker to identify division events versus binucleation events, but due to the high membrane turnover in cardiac myocytes, live-cell membrane markers immediately become cytoplasmic in localization. While this marker defined boundaries of HeLa cells, the boundaries of hiCMs cannot be defined (Figure 2-S1B-C). For this reason, we turned to fixed-cell imaging with β-catenin. By marking the boundaries of cells, we can identify if a cell has one or two nuclei.

Figure 2-1: Factors Involved in Cardiac Myocyte Proliferation

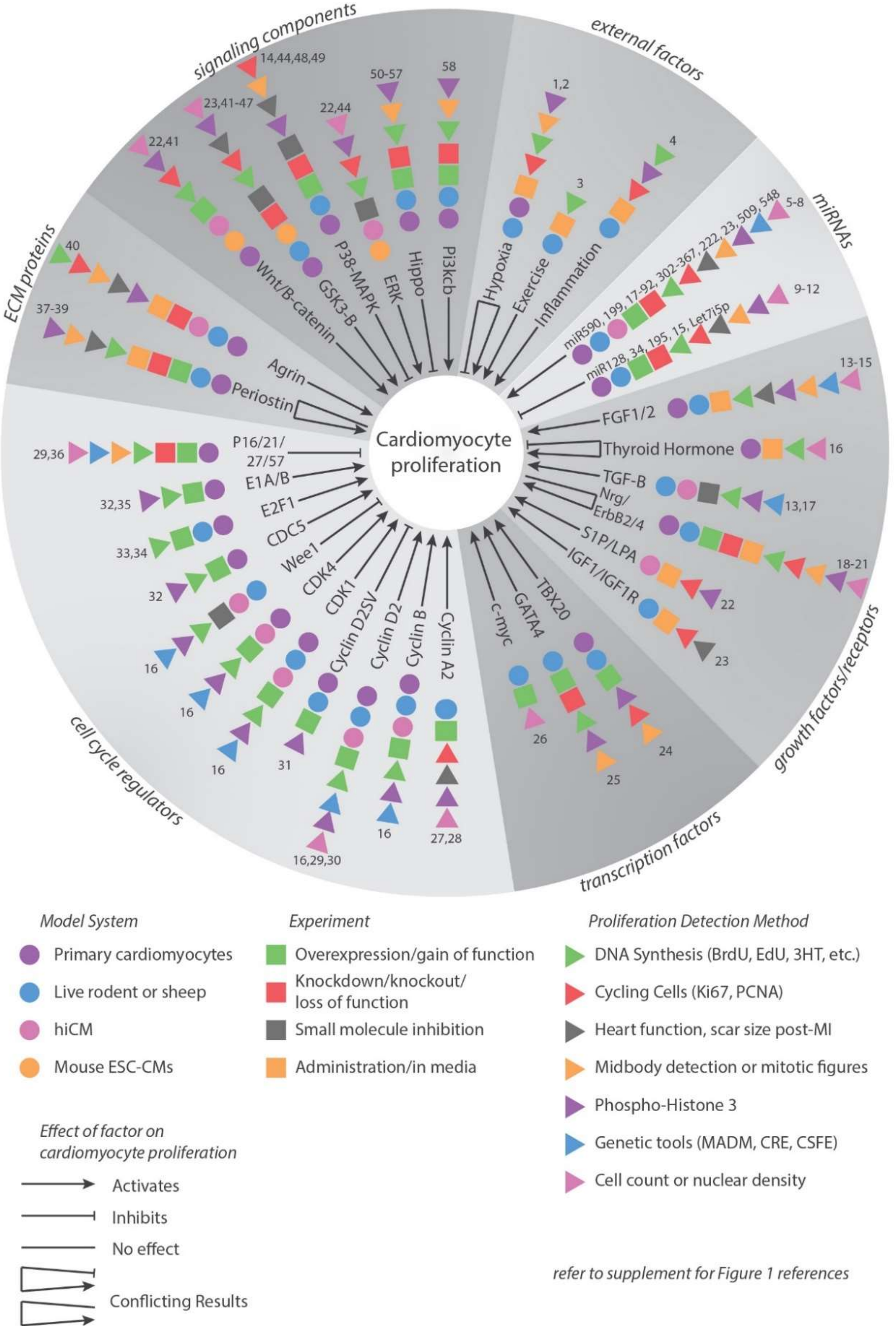

refer to supplement for Figure 1 references

Figure 2-1:

A brief review of factors identified in rodents or using human iPSCs as regulators of cardiac myocyte proliferation. Circles, squares, and triangles show the model system used, experiment, and proliferation detection method, respectively. Arrows show activating factors, blunt arrowheads show inhibitory factors, and lines show factors determined to have no effect. A combination of two types of arrows for the same factor shows conflicting results. Numbers denote the studies for each factor, which can be found in the supplementary references.

Interestingly, we found it was rare to detect mitotic events in hiCM plated at high densities, such as a monolayer. Density-dependent proliferation is well documented in other cell types[86]. Indeed, a previous study has shown that human embryonic stem cell-derived cardiac myocytes incorporate more BrdU when plated at “low” density (~268 cells/mm^2) as opposed to “high” density (~3846 cells/mm^2)[87]. Given our observations and this previous study, we sought to quantify the relationship between plating density and proliferation in hiCM.

We plated hiCMs at various densities to test if there was a relationship between cell density and proliferation (i.e., mitotic events). In order to get a direct measurement of proliferation, we turned to live-cell microscopy. Every nucleus was labeled with a live-cell nuclear marker, and each well was imaged every 12 hours for a week, followed by quantification to determine the proliferative capacity of the cells. Image stitching was used to visualize the entire population of nuclei in each well of a 96-well plate. This resulted in the monitoring of nuclei in approximately 492,188 hiCMs over the course of 5 independent experiments. As expected, we found an inverse relationship between cell density and proliferation from a range of 544 cells/mm^2 to 136 cells/mm^2 (Figure 2-2D). Decreasing the density past 136 cells/mm^2 did not yield corresponding increases in proliferation. 34 cells/mm^2 was the density at which hiCMs were physically isolated from each other.

We next tested whether these observed increases in proliferation were due to binucleation or cytokinesis. Surprisingly, the percentage of binucleated hiCMs was consistent at all densities (Figure 2-2E). Taken together, our data suggested that plating hiCMs at sub-confluent densities increases proliferation but does not influence whether a particular hiCM undergoes binucleation or cytokinesis. Based on these results, we next wanted to explore if hiCMs plated at sub-confluent densities could be used for high-content screening to identify modulators of cardiac myocyte proliferation.

Figure 2-2: Identifying iPSC-Derived Human Cardiac Myocytes as a Model for Cardiac Myocyte Proliferation.

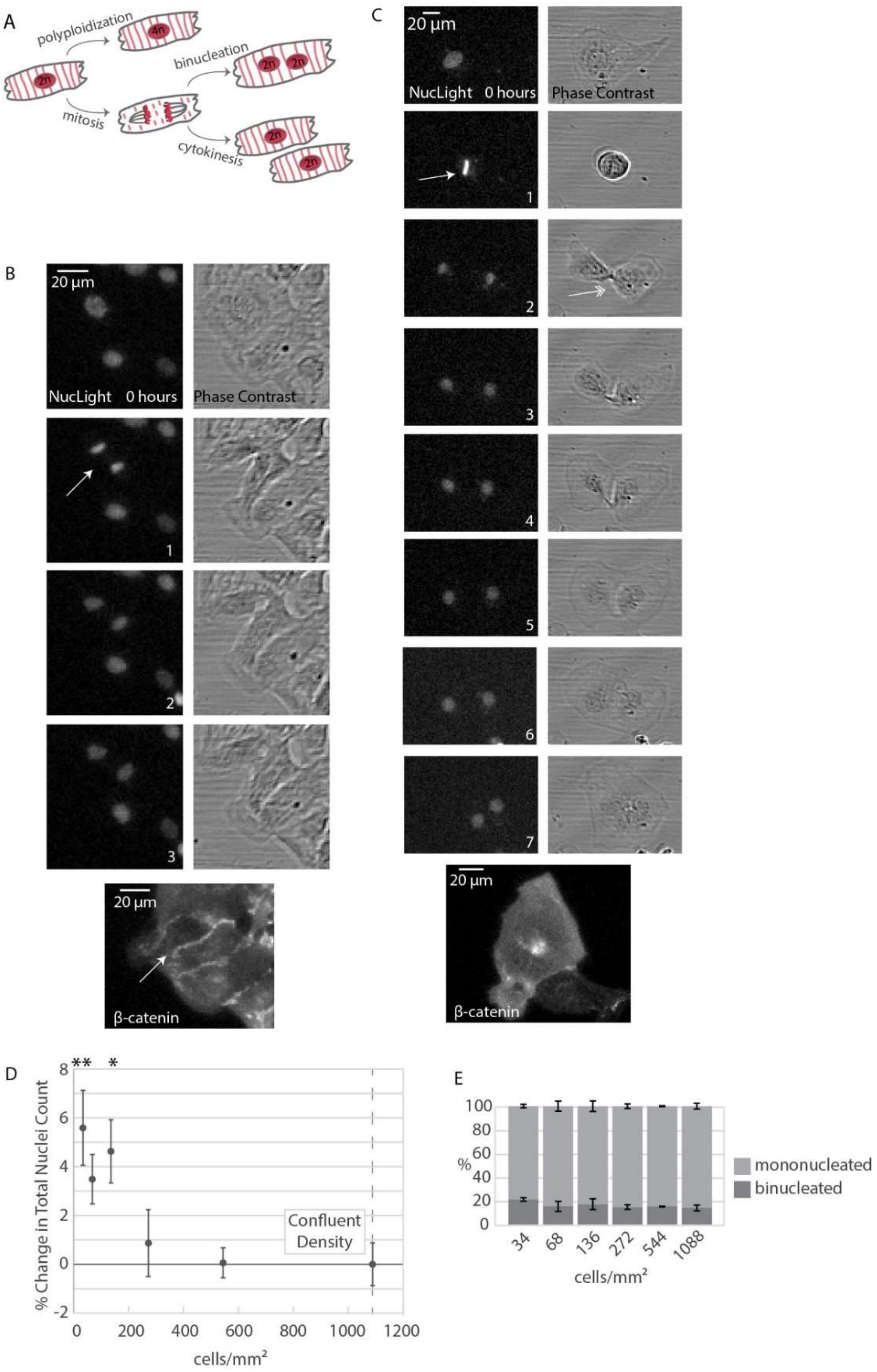

Figure 2-2:

A) Three possibilities resulting from DNA synthesis: proliferation and polyploidization (i.e., endoreduplication), and two possibilities resulting from mitosis: cytokinesis and binucleation. B) Live montage of dividing hiCM using phase contrast and widefield fluorescence microscopy, visualizing nuclei using a live-cell fluorescent nuclear probe. hiCM were then fixed and stained for β-catenin to confirm division. Arrow: cell-cell boundary. C) Live montage of binucleating hiCM using phase contrast and widefield fluorescence microscopy as in Figure 2-2B. Single-headed arrow: metaphase. Double-headed arrow: midbody. D) Proliferative capacity of hiCMs increases with decreasing cell density. Percent change in nuclei count normalized to confluent hiCM so that confluent cells have a 0% change. N=5 experiments per data point, approximately 500,000 hiCM in total; mean +/- SEM over 5 independent experiments. *: $p<0.05$. **: $p<0.01$. E) Binucleation proportion does not change when cells are plated at various densities. Binucleation proportion measured post-fixation stained with β-catenin over three independent experiments. N=4678 total cells; mean +/- SEM. NS by One-Way ANOVA.

Developing a Screen to Identify Modulators of hiCM Proliferation

We next wanted to identify a plating density that would facilitate detection of both positive and negative modulation of hiCM proliferation, lying in the middle of the inverse relationship between density and proliferation (i.e., 544 cells/mm^2 to 136 cells/mm^2). This density would be ~340 cells/mm^2. Due to the nature of making dilutions of cultured hiCMs, we ultimately chose 333 cells/mm^2 as our experimental density. To facilitate a high content screen, we also needed to scale-up the number of samples that could be imaged over time. Our experiments presented in Figure 2-2 were performed in individual wells of a 96-well plate, however, this can limit the number of molecules that can be tested at once. Thus, we moved to culturing hiCMs in 384-well plates (Figure 2-3A). This is cost-effective and allows for the usage of fewer cells per well, and increases the number of possible compounds that can be tested. Of note, cultured hiCMs are fragile and as such are sensitive to physical perturbation during media changes. This rules out less gentle methods of media transfer such as automatic liquid handling, and as such, all media exchanges should be done by hand.

We chose a small molecule library of well-characterized kinase inhibitors from Vanderbilt University's High Throughput Screening Core. This allows for any results of our screen to be immediately informative as to which signaling pathways are controlling hiCM proliferation. Small molecules were plated into a 384-well plate at 10 mM in DMSO using an automatic liquid handling system. To reduce the concentration to 10 μM, cardiac myocyte maintenance media with a nuclear marker was added to each well of the plate. hiCMs were previously plated into a separate 384-well plate, then the hiCM media was replaced with the small molecule-containing media using a multichannel pipette (Figure 2-3B). This allowed for each nucleus in each well to be imaged, masked, and quantified over time (Figure 2-3C). We first tested if the nuclear marker we used had any effect on cardiac myocyte proliferation and found no difference in Ki67-positive nuclei in control or labeled cells (Figure 2-S3C). A detailed protocol is provided in the Methods.

Figure 2-3: Workflow: Identifying Small Molecule Regulators of Cardiac Myocyte Proliferation.

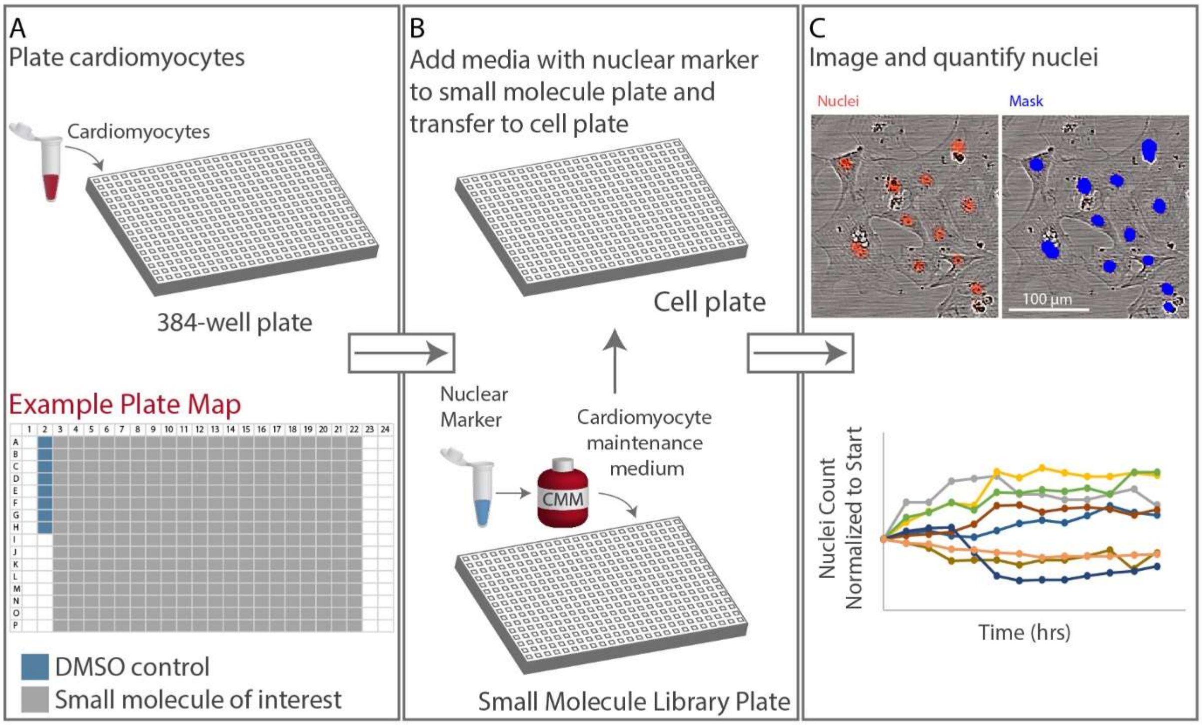

Figure 2-3:

A) Cardiac myocyte plating scheme and example plate map. B) Small molecule addition procedure. C) Nuclei imaging and quantification scheme. For more information, see Methods

Quantifying The Effects of Small Molecules on Cardiac Myocyte Proliferation

Utilizing this protocol, we quantified nuclei count per image over time, taking images every 12 hours for six days. We normalized nuclear increase to control and repeated the screen three more times, resulting in four independent screens using the same small molecules. Interestingly, there was a wide range of changes in hiCM proliferation due to small molecule administration. Some small molecules increased hiCM proliferation, some stopped proliferation altogether, and some caused cell death. The nuclei in each well were quantified as a fold change over time (See equation in the Methods). We averaged the nuclear fold change over four screens (Figure 2-4A).

The top small molecules that had the highest average increase in nuclei over time (Figure 2-4B), the middle small molecules with no effect on nuclei count (Figure 2-4C), and the small molecules that led to death reproducibly in all four screens (Figure 2-4D) were identified. We confirmed by manually observing each well (Figures 4E-G). However, several of these compounds had high standard deviations across screens and did not have a reproducible effect on nuclei count over time, producing false positives. In order to focus on small molecules that reproducibly affected proliferation, we sorted the compounds that had a nuclear fold change greater than 1 by their standard deviation (Figure 2-4H). Interestingly, several of these hits have been identified previously as modulators of the cardiac myocyte cell cycle, including GSK-3β inhibitor BIO[88,89] and a p38-inhibitor SB239063 related to previously identified SB203580[90,91].

Figure 2-4: Effect of Small Molecules on Cardiac Myocyte Proliferation.

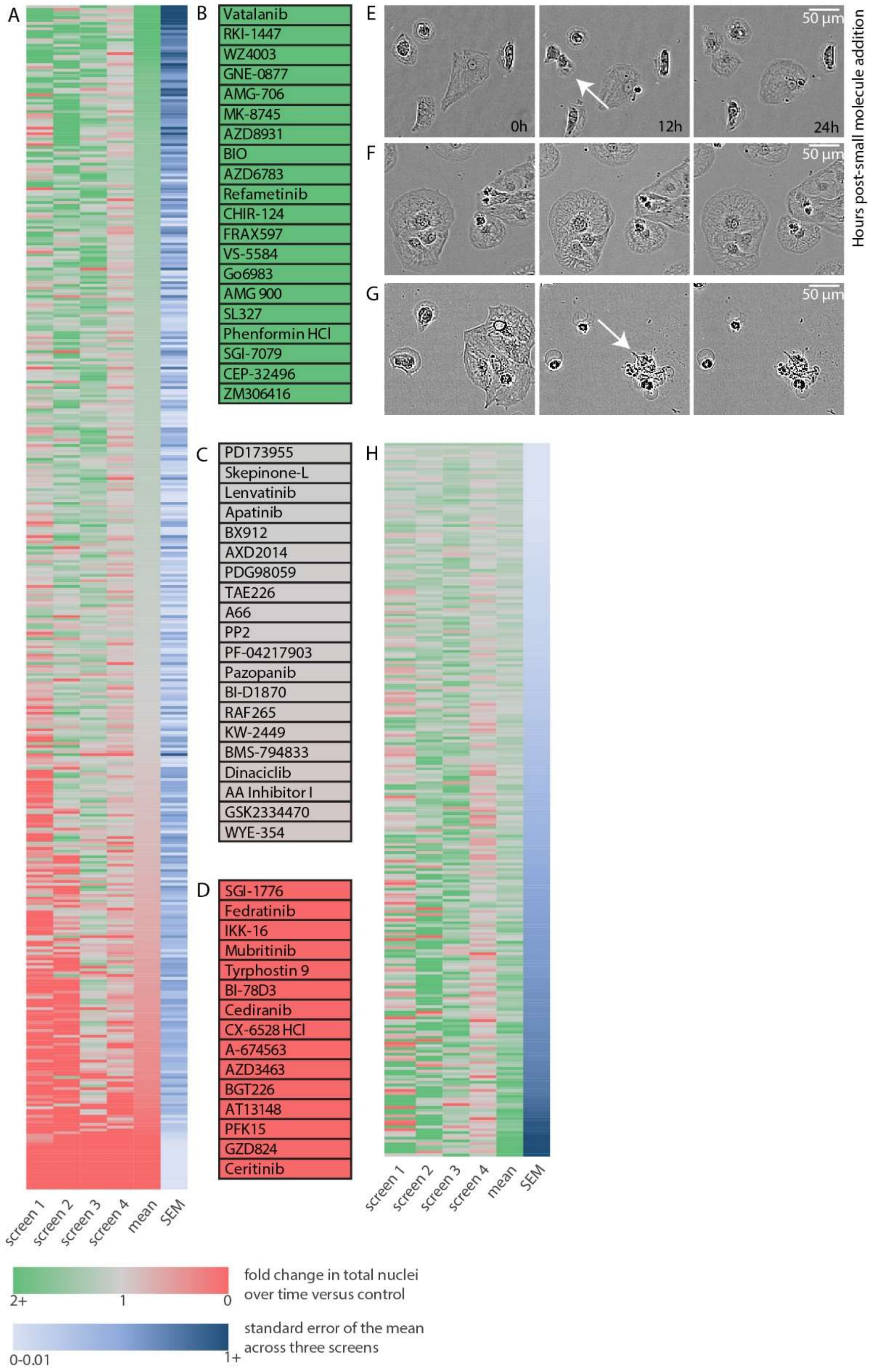

Figure 2-4:

A) Results of small molecule drug screen on nuclei count over a period of 72 hours, normalized to control, averaged over three independent screens. A value of 1 indicates an equivalent rate of nuclei increase to control cells, that is, there is no apparent change in death or proliferation compared to control. A value of 0 indicates cell death, and a value of 2 indicates a doubling of nuclei count over time compared to control. B) Top small molecules that, on average, increased nuclei count. Note that these calculations do not account for variance between screens. C) Middle small molecules that had no observed effect on nuclei count over time. D) Small molecules that led to 100% cell death reproducibly in each screen. E) Example time-lapse of dividing cardiac myocyte over 24h post-small molecule addition. F) Example time-lapse of cardiac myocytes over 24h post-small molecule addition. Note no effect on cardiac myocyte proliferation or death. G) Example time-lapse of cardiac myocytes undergoing cell death after small molecule addition. H) All small molecule compounds with a mean nuclear count increase greater than 1, sorted from top to bottom by smallest to largest standard error of the mean.

Phenotypic Analysis and Small Molecule Compound Follow-Up

After the high-throughput screen, we manually observed each well over 7 days and completed a detailed phenotypic analysis. We noted time of death (quantified post-drug addition) for each well that had total cell death within the 7 day timeframe (Figure 2-5A). Interestingly, several of the small molecules led to eventual cell death, which further supports that many potential therapeutic molecules might be cardiotoxic. We then noted wells in which there were division events, “spindly” cell edges, elongated cells, particularly large cells, and cells which had prominent stress fibers (Figure 2-5B-G).

Once a high-throughput screen is completed specific small molecules need to be identified and further pursued. As an example of such a next step, we chose three small molecules which had high increase in nuclear count over the four screens, but a low variance between screens (Figure 2-4H), and that we found of particular interest based on the literature. These three hits included Acadesine, an AMPK activator, Palomid-529, an mTORC inhibitor, and SB216763, a GSK-3 β inhibitor (Figure 2-5H). Interestingly, activating AMPK in the heart has been shown to be protective against hypertrophy[92]. In addition, a another small molecule inhibition of GSK-3β using BIO and CHIR99021 has been shown to increase hiCM proliferation[93, 88, 89]. On average over the four screens, these compounds led to a 20% increase in nuclei count.

Figure 2-5: Phenotypic Analysis and Small Molecule Compound Follow-Up

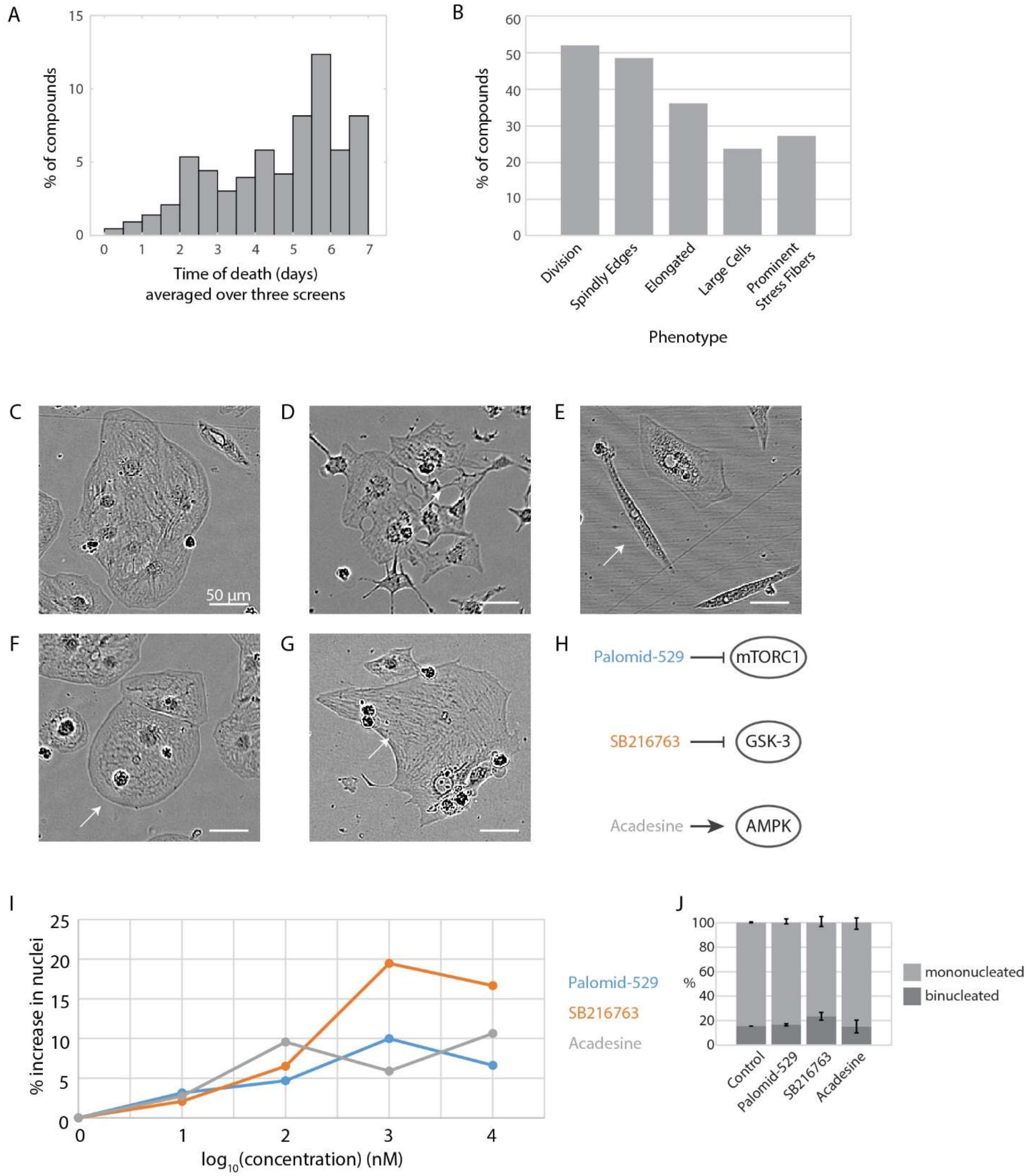

Figure 2-5:

A) Time of death (days) for each well that died within the time frame of the screen, averaged over the three screens. 0 represents that the cells died within the 20 minutes between small molecule addition and initial imaging. 1 represents that cells died before 24 hours post-addition (i.e., between 12 hours and 24 hours). If cells did not die, they are not represented in this graph. Nuclei count was unreliable for cells which died, as there was debris created which fluoresced. Thus, time of death was manually quantified. B) Phenotypic analysis of cardiac myocytes over three screens given 429 small molecules. C) Example of a cluster of approximately 7-8 healthy cardiac myocytes. Small molecule: PD318088. D) Example of a cluster of cardiac myocytes that are especially unhealthy, giving the cells a “spindly” appearance. Small molecule: AT7867. E) Example of an elongated cardiac myocyte (arrow). Note cardiac myocytes directly above the elongated cardiac myocyte that have normal appearances. Small molecule: WAY-600. F) Example of a particularly large cardiac myocyte (arrow). Small molecule: PD318088. G) Example of a cardiac myocyte with stress-fiber like striations on its edge (arrow). Small molecule: APTSTAT3-9R. H) Three small molecules identified by screen as potential regulators of hiCM proliferation. I) Three small molecules from Figure 2-5H tested at 0.01, 0.1, 1, and 10 μM (i.e., 10, 100, 1000, and 10000 nM) over five independent experiments. Shown as mean. J) Binucleation proportion does not change when cells are treated with these small molecules at their most effective concentrations (Palomid-529 5 μM, SB216763 3 μM, and Acadesine 3 μM), measured post-fixation stained with β-catenin. N=6624 total cells over three independent experiments; mean +/- SEM. NS by One-Way ANOVA

As we performed our initial screen using small molecules at 10 μM, we next tested the effectiveness of these compounds at lower concentrations. We found that each compound indeed increased proliferation of hiCM at doses lower than the screening concentration (Figure 2-5I), and that this induction of proliferation does not affect the baseline balance of cytokinesis and binucleation (Figure 2-5J).

Comparing the Number of Division Events to the Overall Number of Cycling Cells

We next wanted to compare our method to a standard method for identifying cycling cells. We chose the localization of Ki67 using immunofluorescence[94]. We treated hiCMs with the identified small molecules and localized Ki67 and α actinin 2 post-fixation (Figure 2-6A). In this way, we can identify cycling cells and simultaneously confirm the cardiac myocyte identity of the hiCMs in control conditions and with the identified small molecules. We also localized Ki67 in hiCMs treated with a previously identified small molecule that has been shown to induce cardiac myocyte proliferation, a p38 inhibitor[90]. Each of the three identified compounds increased the percentage of Ki67-positive nuclei to similar or even higher levels than the previously identified p38 inhibitor (Figure 2-6B). However, the identification of cycling cells using Ki67 accounts for more cells than those which actually subsequently divide[21].

We also wanted to compare the cost of performing a screen using live-cell nuclear localization with the current method of fixed-cell Ki67 localization (Table 1) and found that our method of performing the screen was significantly more cost-effective. We also include a detailed protocol on how to complete both methods of screens, including step-by-step alternative approaches for laboratories with more limited resources with the goal to alleviate the significant financial investment typically required for starting research in the cardiovascular field. In conclusion, fixed-cell localization of cycling markers only allows for imaging one time point and provides an overestimate of cell division, and further, is more costly than live-cell imaging of nuclei.

Figure 2-6: Using Ki67 to Confirm Three Small Molecules Identified in Screen Increase hiCM Proliferation

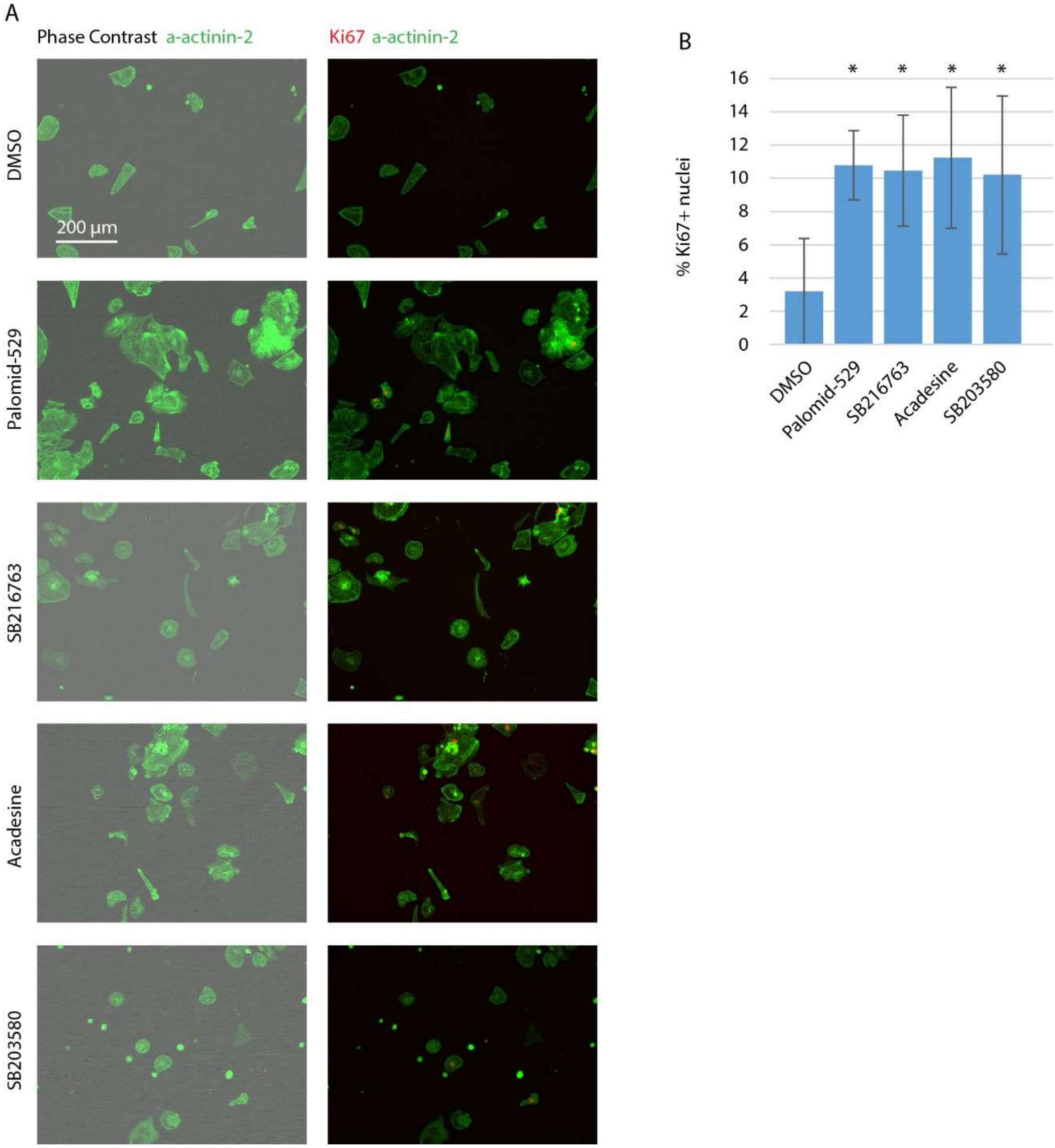

Figure 2-6:

A) Phase contrast, α actinin 2 and Ki67 in control hiCM and hiCMs treated with Palomid-529, SB216763, Acadesine, and SB203580. B) Quantification of Ki67+ hiCMs in control and small molecule-treated hiCMs. *: $p<0.05$

Discussion

The diversity of the scientific community working on a problem is instrumental to the innovation of any field. Previously, the study of cardiac myocytes has been limited to researchers with substantial funding and specialized training to initiate *in vivo* studies or differentiation protocols from iPSCs. Here we present a method that is specifically designed to be straight-forward and accessible to a wide variety of researchers. hiCMs can be purchased, which bypasses the typically rate-limiting and costly step of initiating in-house hiCM-differentiation. Furthermore, the experiments do not require advanced microscopy. Indeed, all the experiments in the main figures were completed using relatively low magnification imaging with a 4x, 10x, or 20x objective, though one objective would be sufficient. Indeed, we have provided a detailed protocol in the supplement that presents how our method can be modified to accommodate any microscope capable of performing fluorescence. Using our method, we present several datasets as a resource for determining small molecules that play an activating or inhibitory role in cardiac myocyte proliferation. Screening a limited compound library revealed many potential regulators of proliferation and cell death.

We chose to use purchased hiCMs because the initial investment is far less than in-house differentiation protocols. In-house hiCM differentiation protocols also do not produce pure populations of myocytes. These protocols can contain ~10% of nonmuscle cells[78]. Because the percentage of dividing hiCMs is so low, a small contamination of highly proliferative non-muscle cells, e.g., fibroblasts, could skew the results. Each batch of purchased cardiac myocytes comes with a certificate of purity, claiming >99%. However, even if 0.99% of the cells were highly proliferative, this would affect results. For this reason, we routinely localize α actinin 2 in our cultures. These cells are positive for α actinin 2. Of note, over the course of this study, we have only found 3 cells present in our cultures that do not express α actinin 2 out of the ~500,000 we have observed. Further, every dividing cell found in cultures stained for α actinin 2 has been α actinin 2-positive (Figure 2-S1A, 2-6A). Taken together, these cultures contain cardiac myocytes which have the capacity to divide.

Another factor to consider when using hiCMs for any experimental purpose is their 'maturity'. It has been well-documented that hiCMs do not resemble *in vivo* adult human cardiac myocytes transcriptionally or morphologically[95]. In addition, adult human cardiac myocytes have a very low potential for division[84,85]. Conversely, hiCMs transcriptionally resemble fetal/neonatal cardiac myocytes[95], and obviously can divide. It is for this reason that we believe hiCMs are an ideal system to explore what regulates the cell cycle and cytokinesis in cardiac myocytes.

There are several reasons we chose to count nuclei as the basis of this screening protocol, rather than previously utilized methods. Proliferative markers such as Ki67 and PCNA give an overestimate of cell proliferation, as they mark any cell that is cycling in general. This can mark cells undergoing endoreduplication (i.e., polyploidization), cytokinesis, and binucleation. DNA synthesis markers such as BrdU/EdU detects these three outcomes as well as DNA damage repair[15]. To circumvent these issues, researchers have turned to midbody markers such as Aurora B kinase to more directly mark cytokinesis. However, groups have recently shown preliminary evidence that binucleating cells can form a midbody[32,96]. Interestingly, we also see examples of binucleating cells that have a clear midbody in a typical position (Figure 2-2C, double-headed arrow). Thus, using midbody markers or even simply identifying mitotic figures does not unequivocally mark cardiac myocytes undergoing cytokinesis. Hesse & Doengi[96] also propose using distance between nuclei after mitosis to differentiate between cytokinesis and binucleation. However, some hiCMs have two nuclei that are well-separated (Figure 2-S2F).

An *in vivo* approach to navigating cardiac myocyte proliferation is to use the MHC promoter to mark only cardiac myocytes and use sophisticated tools such as mosaic analysis using double markers (MADM), etc., to measure CM proliferation[82]. However, the MHC promoter could be active in undifferentiated progenitor cells[15] which could cloud results in mouse models. In fixed tissue, thin sections restrict the identification of binucleated cardiac myocytes. In thicker sections, optical aberrations, limited axial resolution, and imprecise marking of cell boundaries are limitations. Even so, *in vivo* approaches limit the throughput of identifying any compounds or factors that affect cardiac myocyte proliferation.

Given the ambiguity that results from other markers, we propose using live hiCMs for high-throughput screening of regulators of hiCM proliferation by simply counting nuclei. This method allows for a more accurate proliferation approximation. We present this dataset as a resource for other cardiac researchers to follow up on any small molecule or phenomenon of interest. With a nearly endless variety of live-cell markers available and the ease of this protocol, it can be adapted to study several aspects of cardiovascular cell biology. Here we used a small molecule library as a proof-of-concept; however, CRISPR-based screens can be easily incorporated into this platform. Such a simplistic experimental platform can bridge the gap between a limited screen providing preliminary data and a hypothesis-driven follow-up study. hiCMs have been shown to be amenable to genetic and pharmacological perturbations[69,80]. Indeed, we have provided suggestions in the methods as to when genetic or pharmacological experiments can be incorporated.

Supplemental Figures

Figure 2-S1: Dividing cardiac myocytes and screen setup

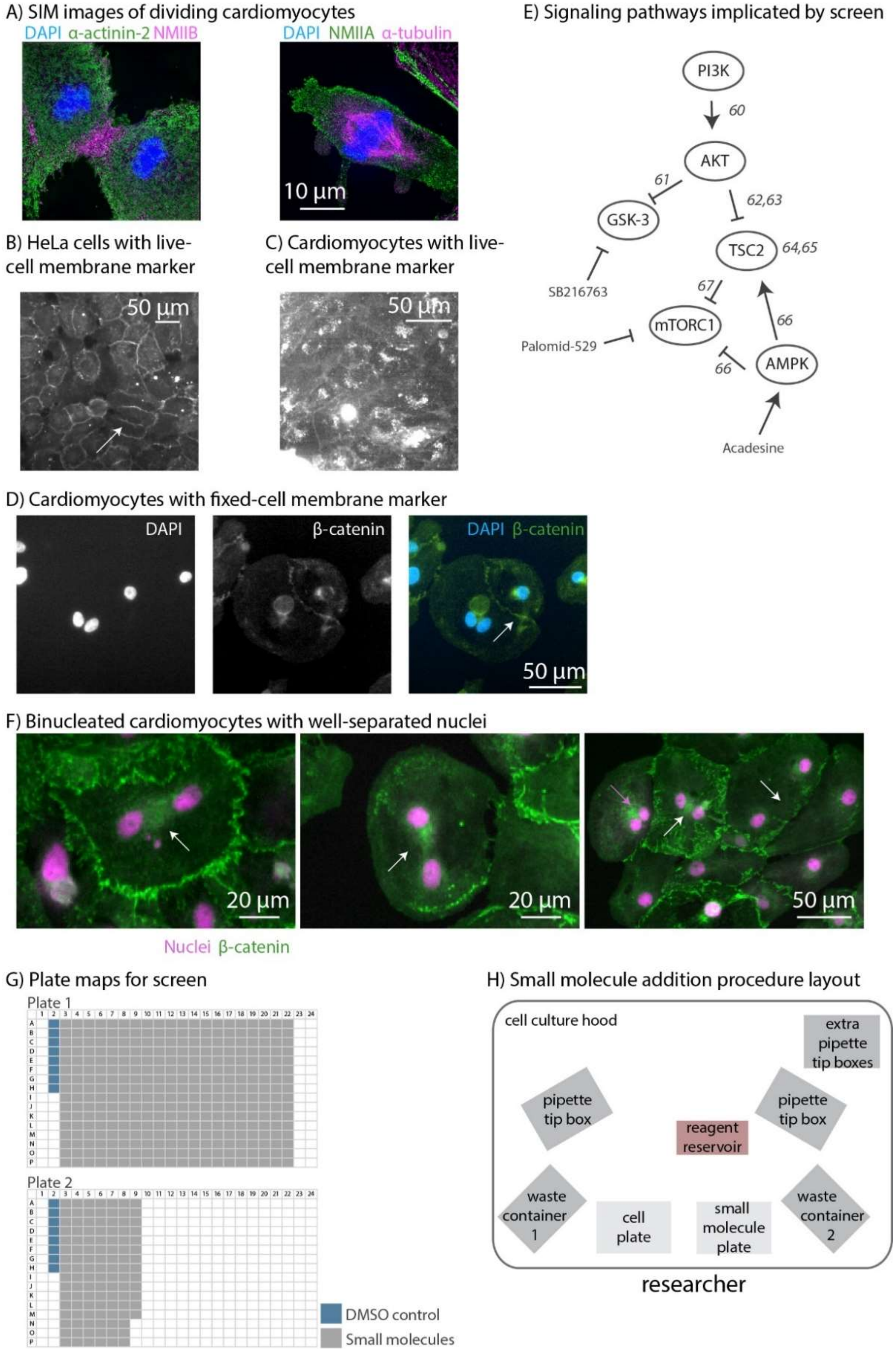

Figure 2-S1:

A) Structured illumination images of dividing cardiac myocytes 1 week post-plating. B) HeLa cells with a live-cell membrane marker. C) Cardiac myocytes with the same live-cell membrane marker as S1B. Poor localization may be attributed to the nature of rapid turnover of the plasma membrane in muscle cells[67] D) Representative widefield image of a binucleated hiCM and a mononucleated hiCM, clearly separated by β-catenin-positive cell-cell adhesions. E) Signaling pathways implicated in screen results. References refer to supplemental references in this chapter F) Representative examples of binucleated cells with well-separated nuclei. White arrows: well-separated nuclei. Magenta arrow: binucleated cell with close nuclei. G) Plate maps used in this manuscript. H) Layout of cell culture hood during small molecule addition

Figure 2-S2: Extended Phenotypic Examples of hiCMs Treated with Small Molecules

A) Flat B) Protrusions C) Vesicular/"Holey" Appearance

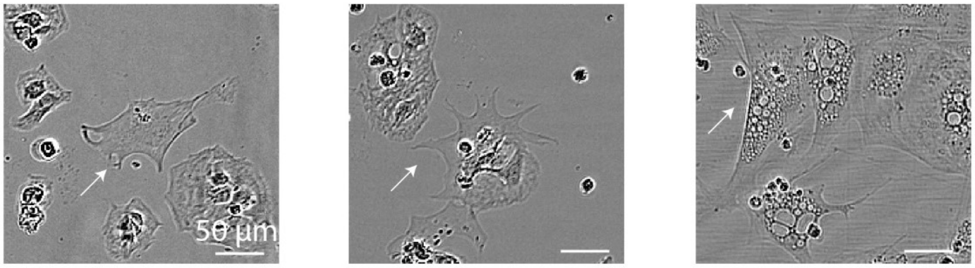

D) Non-motile cardiomyocytes

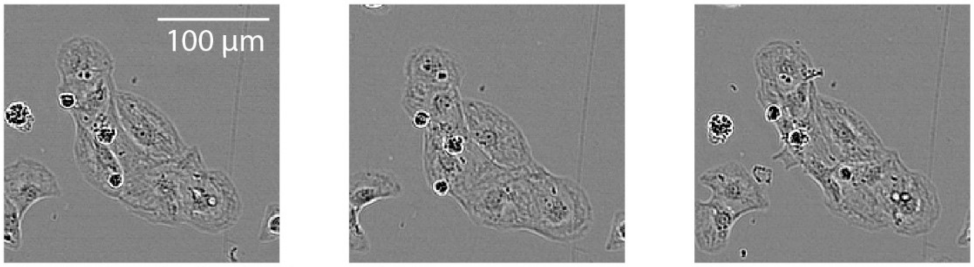

0 hours post-small molecule addition 12 hours 24 hours

E) Motile cardiomyocytes

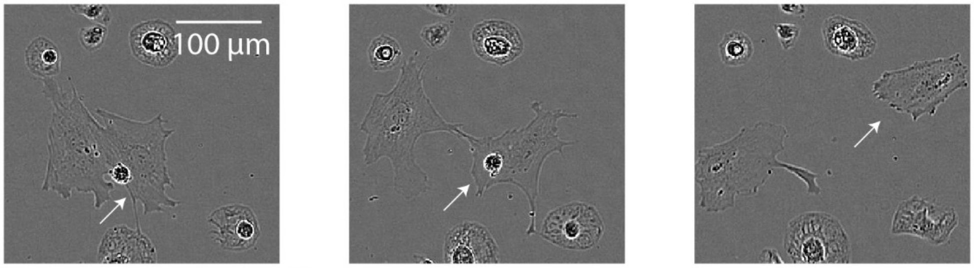

0 hours post-small molecule addition 12 hours 24 hours

Figure 2-S3:

A) Example of a cardiac myocyte which appears more flat (arrow) than a normal cardiac myocyte (below the flat cardiac myocyte). Small molecule: BYL719. B) Example of a cardiac myocyte with protrusions. Small molecule: AZD1480. C) Example of a cluster of cardiac myocytes that appear to have several vesicles throughout the cell, giving the cells a “holey” appearance. Small molecule: LY2603618. D) Montage of a stationary cardiac myocyte. Small molecule: Apatinib. E) Montage of motile cardiac myocytes. Small molecule: AS-252424

Figure 2-S3: Follow Up of Small Molecules Identified in Screen

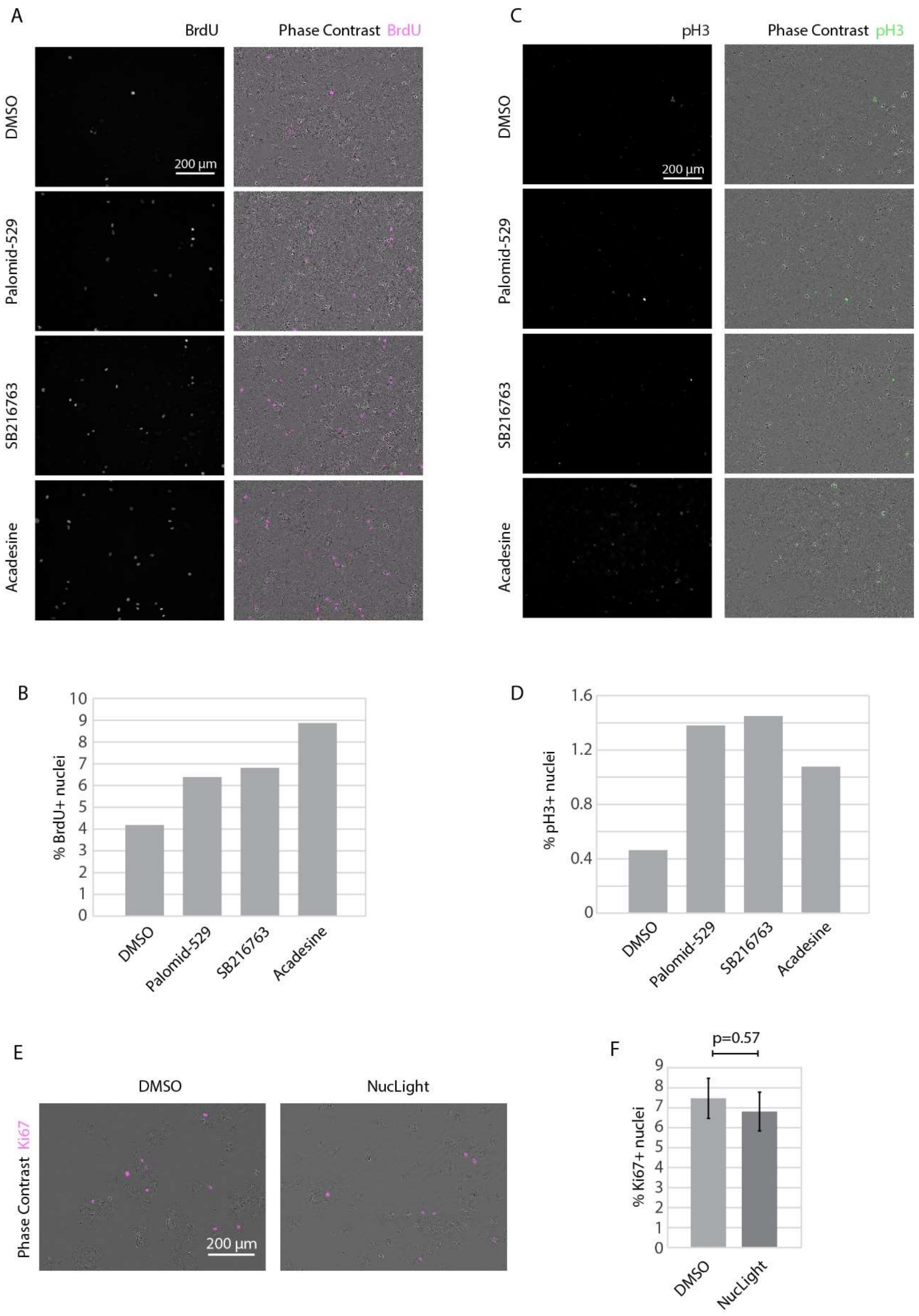

Figure 2-S3:

A) Phase contrast and BrdU localization in hiCMs given 5 μM of each small molecule identified in the screen and BrdU (Palomid-529, SB216763, and Acadesine) or DMSO control. Cells were treated with the small molecule for 48 hours before BrdU and small molecule treatment for 20 hours. B) Quantification of percentage of BrdU-positive nuclei. N = 2443 cells. C) Phase contrast and pH3 localization in hiCMs given 5 μM of each small molecule identified in the screen and BrdU (Palomid-529, SB216763, and Acadesine) or DMSO control. Cells were in the presence of small molecules for three days. D) Quantification of percentage of pH3-positive nuclei. N = 1882 cells. E) Phase contrast and Ki67 localization in control hiCMs and hiCMs treated with nuclight 1:4000 for 48 hours. F) Quantification of percentage of Ki67-positive nuclei. N = 657 cells over 2 independent experiments.

Materials and Methods

Cell Culture and Chemicals

iPSC-derived cardiac myocytes (hiCM, CMC-100-012-000.5, Cellular Dynamics, Madison, WI) were cultured in polystyrene 96-well plates (3599, Corning, Corning, NY) or 384-well plates (781182, Greiner, Kremsmünster, Austria or 164688, ThermoFisher, Waltham, MA) coated with gelatin (ES-006-B, Sigma, St. Louis, MO) in growth medium (M1003, Cellular Dynamics, Madison, WI) as per manufacturer's instructions. Cells were cultured at 37°C and 5% CO_2. For re-plating hiCMs onto glass substrates (Figure 2-S1A-D), cells were washed 2x with 100 μL 1x PBS with no Ca^{2+}/Mg^{2+} (PBS*, 70011-044, Gibco, Grand Island, NY). PBS* was completely removed from hiCMs and 40 μL 0.1% Trypsin-EDTA with no phenol red (15400-054, Gibco, Grand Island, NY) was added to hCMs and placed at 37°C for 2 minutes. Following incubation, the culture well was washed 3x with trypsin inside well, rotated 180 degrees, and washed another 3x. Trypsinization was then quenched by adding 160 μL of culture media and total cell mixture was placed into a 1.5 mL Eppendorf tube. Cells were centrifuged at 1000xg for 3 minutes, and the supernatant was aspirated. Cells were then re-suspended in 200 μL of culture media and plated on 35 mm dishes with 10 mm glass bottom (D35-10-1.5-N; CellVis, Sunnydale, CA) pre-coated with 10 μg/mL fibronectin (#354008, Corning, Corning, NY) for 1 hr at 37°C. Reagent reservoirs were purchased from VWR (89094-682, Radnor, PA).

Mouse anti-β-catenin (1:200, 610153) was purchased from BD Biosciences (San Jose, CA). Mouse anti-α-actinin-2 (1:200, A7811, clone EA-53) and mouse anti-α-tubulin (1:200, B512, Clone DM1α) were purchased from Sigma (St. Louis, MO). Rabbit anti-NMIIA (1:1000, 909801 Clone Poly19098) was purchased from BioLegends (San Diego, CA). Rabbit anti-NMIIB (1:200, 8524S), rabbit anti-Ki67 (1:200, 9129), mouse anti-BrdU (1:200, 5292S), and rabbit anti-pH3 (1:200, 9701S) were purchased from Cell Signaling Technologies (Danvers, MA).

Alexa Fluor 488-goat anti-mouse (A11029), Alexa Fluor 488-goat anti-rabbit (A11034), Alexa Fluor 568-goat-anti-rabbit (A11011), and Alexa Fluor 568-goat anti-mouse (A11004) antibodies were purchased from Life Technologies (Grand Island, NY).

BrdU (ab142567, abcam, Cambridge, UK) was reconstituted to 10 mM in water, then to 10 µM in cardiac myocyte maintenance medium and filtered through a 0.22 µm syringe filter. Cells were incubated with 5 µM of each follow-up compound and BrdU for 20 hours, then fixed and permeabilized as below (see “Fixation and immunostaining”). Then, to hydrolyze DNA, cells were incubated with 1 M HCl for an hour at room temperature, then neutralized with 0.1 M sodium borate buffer (pH 8.5) for 20 minutes at room temperature. Next, cells were washed with PBS and immunostaining continued as usual (see below).

Small Molecule Kinase Inhibitor Library Preparation and Screen

Briefly, a small molecule kinase inhibitor library was acquired from the High Throughput Screening Core at Vanderbilt University, which was originally purchased from Selleck Chemicals (L1200, Houston, TX). 50 nL of each compound was placed in wells of a 384-well plate using an Echo 555 Liquid Handler (Labcyte Inc., San Jose, CA) at 10 mM in DMSO (276855, Sigma, St. Louis), and were subsequently resuspended in 50 µL of cardiac myocyte maintenance media to a final concentration of 10 µM. Four days post-thaw, the cell media was replaced with media containing the compounds of interest and 1:4000 NucLight Rapid Red Reagent (4717, Essen Biosciences, Ann Arbor, MI). This step was repeated again three days later. All control wells contained an equal volume of DMSO: 50 nL. An in-depth protocol can be found below.

Fixation and Immunostaining

Cells were fixed with 4% paraformaldehyde (PFA, 15710, Electron Microscopy Sciences, Hatfield, PA) in PBS (46-013-CM, Corning, Corning, NY) at room temperature for 20 min and then extracted for 5 min with 1% Triton X-100 (BP151100, Fisher Scientific, Suwanee, GA) and 4%

PFA in PBS as previously described[69]. For immunofluorescence experiments, cells were blocked in 5% bovine serum albumin (BSA, 30075-100.0, RPI, Mount Prospect, IL or A3059, Sigma, St. Louis, MO) in PBS, followed by antibody incubations. VectaShield with DAPI (H-1200, Vector Laboratories Inc., Burlingame, CA) was used for mounting.

Structured Illumination Microscopy

SIM imaging and processing (Figure 2-S1A) was performed on a GE Healthcare DeltaVision OMX equipped with a 60x 1.42 NA oil objective and sCMOS camera.

Fluorescence and live-cell microscopy

Some wide-field fluorescence images (Figures S1B-D) were acquired on a Nikon Eclipse Ti equipped with a Nikon 20x 0.4 NA air objective and a Nikon DS-Qi2 CMOS camera. All other images were acquired on an Incucyte (4647, Essen Biosciences, Ann Arbor, MI) at 4x, 10x, or 20x, at 37°C and 5% CO_2.

Data Quantification

For nuclei count over time (Figures 2D, 4A-D, H, 5I), nuclei were counted using the IncuCyte analysis interface. Briefly, nuclei were thresholded using rolling ball background subtraction for each time point. Data were normalized to controls, normalizing control wells to a 1 fold-change or a 0% nuclear count increase. All values shown are mean +/- SEM over three experiments. Binucleation was manually quantified (Figures 2E, 5J, S1F) using an antibody for β-catenin and a nuclear marker (NucLight, 4717, Essen Biosciences, Ann Arbor, MI). Cells on the edge of a field of view that had a portion cut off were not included. Ki67-positive percentage was calculated as percentage of nuclei which were positive for Ki67 localization.

Statistics

P-values were calculated using One-Way ANOVAs with the exception of Figure 2-S3F. In Figure 2-2D, 2E, 5J, repeated measures One-Way ANOVAs were performed. For Figure 2-5J, a one-way ANOVA without repeated measures was performed. A Dunnett's post-hoc test was performed if the ANOVA p-value was less than 0.05. In Figure 2-S3F, a two-tailed paired student's t-test was performed.

Detailed Protocol

We used a relatively small library of 429 small molecules for this proof-of-concept manuscript. In total, we used 445 wells of a 384 well plate (Figure 2-S1G). This included the library with 16 accompanying DMSO controls. As such, we needed 1.5 million human iPSC-derived cardiac myocytes (hiCM) to plate at a density of ~333 hiCM/mm^2, that is, 3333 hiCM/well; accounting for pipette variance. This density was determined by calculating the middle density between the densities at which the hiCMs proliferate the least and the most (Figure 2-1D).

General Notes

Follow manufacturer's instructions and/or a differentiation protocol[68] to obtain 1.5 million cardiac myocytes. We used a variation on Cellular Dynamics plating protocol for a 500 µL tube containing approximately 3 million cells. We thawed the hiCMs into wells of a 384-well plate. This plate was used directly for the experiments as we noticed that re-plating hiCMs caused loss of hiCMs due to cell death. We allowed at least one row of empty wells on the sides of the plate. This minimizes contamination and evaporation, which is an important concern when media is not being changed daily.

There are two main companies that provide quality differentiated hiCMs that we have used. We chose Cellular Dynamics because that is what we had frozen in our liquid nitrogen storage at the start of this project. Cellular Dynamics hiCMs are frozen at 30 days of differentiation.

We have also used hiCMs from Ncardia to study sarcomere assembly and found them to be similar to those from Cellular Dynamics[70]. However, we have not hiCM for cell from Ncardia for proliferation studies as of yet.

It is important to optimize which plate to use based on the type of image information your experiment requires (e.g., fluorescence and/or phase contrast). For example, Greiner 384-well plates (781182) a have larger font size on the plates, allowing for easy addition of small molecules, and work well for fluorescent imaging as they have no detectable auto-fluorescence (Figure 2-2C). However, these plates produce an optical aberration that creates linear patterns, and often have small scratches (Figure 2-2C). On the other hand, some plates (e.g., Thermo Fisher 384-well plates- 164688) do not produce such patterns and have less. However, these plates are labeled with a smaller font that is difficult to read from afar when the plates are in a laminar flow hood behind glass. 96-well plates or even fewer/bigger wells may be used as well. This increases sample size at the expense of cost and overall throughput.

To determine how much plating medium to add, see cell viability calculation of the batch of hiCM purchased. Each 50,000 cells will require a total of 100 µL of medium. For example, a batch with 3 million viable cells will produce 60 x 50,000 cells, so 60 x 100 µL = 6 mL is required in total. After the 1.5 mL (500 µL cells + 1 mL plating medium used to wash cryovial), 4.5 mL remains.

Be careful not to touch the bottom of the wells while changing media, and minimize time the cells are without media. These cells are fragile, so all media changes in this protocol are done by hand rather than with a liquid handling system. A makeshift waste container for large quantities of pipette tips can be made out of a tip box lid. If two multichannel pipettes are not available, add new media immediately after removing old media, row-by-row.

If transducing a stably-expressing nuclear marker (or transducing or transfecting any other construct), it is possible to do so on day 4. For example, if using Cell Light Nucleus (C10602, Invitrogen, Carlsbad, CA).

For our purposes, we obtained two 384-well plates with plate maps as in Figure 2-S1G from the Vanderbilt University High Throughput Screening Core, with 50 nL of each small molecule from the SelleckChem Kinase Inhibitor Library per well at 10 mM. The plates were sealed and stored for ~6 hours in a desiccator until use. In this way, it is simple to add media to each well of the 'small molecule plate', then transfer media from the small molecule plate to the cell plate, 12 wells at a time using a multichannel pipette. We recommend having the small molecules of interest in a separate plate matching the planned map of the cell plate in order to simplify small molecule addition and minimize contamination. See plate maps in Figure 2-S1G or troubleshooting for more information

We used an automatic microscope that can image up to 6 plates at a time. However, any microscope with an automatic stage and multipoint capabilities could be used. This would limit the number of samples imaged at a time as most microscopes can only image one plate at a time. Alternatively, if live-cell imaging is not available, fixed time points at various hours or days post-small molecule addition and imaging of nuclei with a marker such as DAPI will also facilitate nuclei count.

We recognize this uses a large quantity of antibody, which can be costly. To circumvent this issue, we recommend fixing all wells and keeping the plates in a 4°C fridge until the wells are quantified and any hits are identified. Then, only the relevant wells can be stained to conserve antibody. 15 µL is also the minimum requirement for these steps: most 384-well plate wells can hold up to 100 µL of liquid.

If using a 96-well plate, double the calculations, i.e. wash with 50-100 µL PBS or BSA and add at least 30 µL of antibody per well.

Thawing Cardiac Myocytes: Day 1

- Thaw plating medium at room temperature overnight and thaw maintenance medium at 4°C overnight.
- 2 hours before thaw, add 25 µL 0.1% sterile gelatin (ES-006-B, Sigma, St. Louis, MO) to each well of a 384-well plate in a cell culture hood and incubate at 37°C for 2 hours. We use our cell culture incubator for all steps requiring 37°C, unless otherwise noted.
- Immediately before the thaw, aspirate gelatin from all 445 wells in a culture hood and return to 37°C.
- Remove a vial of cells from the vapor phase of liquid nitrogen storage using a large pair of forceps and warm the tube in a 37°C water bath for 3 minutes. Take care to maintain sterility by not submerging the cap of the tube, and hold the tube stationary- NO SWIRLING. The large pair of forceps may be used to hold to tube in the water bath, or a floating tube rack can also be used as long as the cap remains above water.
- Remove the cryovial from the water bath, spray it with 70% ethanol, and place it into the culture hood.
- In the cell culture hood, use a 1 mL pipette to slowly remove cells from the cryovial over two seconds and them to a sterile 50 mL conical centrifuge tube (89039-656, VWR International, Suwanee, GA or 82050-348, Greiner, Kremsmünster, Austria) by slowly expelling them over 4 seconds.
- Gently rinse empty cryovial with 1 mL plating medium to recover remaining cells. To do so, tilt the pipette tip so that the media runs down the inner sides of the tube, rotating the pipette tip to rinse the circumference of the tube. Transfer the 1 mL of plating medium with the recovered cells from the cryovial to the 50 mL conical tube drop-wise over 90 seconds while gently swirling the conical tube. Slow addition of medium in this step is critical to minimizing osmotic shock: add approximately one drop per ~3 seconds.

- Slowly add 4.5 mL of plating medium to the 50 mL conical tube. Add each remaining 1 mL of medium drop-wise over 30 seconds per mL. Gently swirl the tube while adding medium.
- Close the cap on the 50 mL conical tube and invert gently 2 times. Do not shake or vortex the cell suspension.
- Transfer 3 mL of the cell suspension to a new sterile 50 mL conical tube. The remainder of the cell suspension may be used for other purposes such as second screen or other experiments.
- Add 19.5 mL of plating medium to the 3 mL of cell suspension, cap the tube, and invert gently 2 times.
- Pour the entire contents of tube (~22.5 mL) into a sterile reagent reservoir.
- Retrieve the two 384-well plates from incubator and transfer to the culture hood.
- Use the multichannel pipette set to 50 µL to add cells from the reservoir into the wells of the 384-well plates, using the plate map of choice.
- Put the plates into the incubator for at least 5 hours (Note: we have gone up to 7 hours). This allows time for the cells to recover and adhere to the plate so that they are not washed away during the media change.
- During the incubation in Step 15, warm 22.5 mL of maintenance medium to 37°C in a bead bath, water both or incubator.
- 5-7 hours post-thaw, retrieve the plates from incubator and put them in the cell culture hood.
- Pour the warm maintenance medium into new sterile reagent reservoir in the cell culture hood.
- With two multichannel pipettes set to 50 µL each, simultaneously remove 50 µL of plating medium from the wells with one hand and add 50 µL of maintenance media from reservoir to the cells with the other hand.

- Put the cells back in the incubator for 2 days.

Maintaining Cardiac Myocytes: Day 3

- Two days post-plating, change the media as in step 19. Warm 22.5 mL of media. Remove 50 µL from each well and add 50 µL simultaneously from reagent reservoir, being careful not to touch or disrupt cells.

Small Molecule Addition: Day 5

- Warm 22.5 mL of maintenance medium to 37°C in bead bath, water bath or incubator.
- Add the nuclear marker to maintenance medium at desired concentration. We used NucLight Rapid Red at a 1:4000 dilution (i.e., 5.6 µL NucLight to 22.5 mL medium).
- Pour ~1/2 of the contents of the conical tube containing media into a sterile reagent reservoir in hood, then close the conical and return it to the bead bath or equivalent to maintain temperature and sterility. (Small molecule addition can take several minutes depending on the researcher's pipetting speed, and medium that cools down will be dangerous to the cells)
- Remove cell plate 1 from the incubator and remove seal from small molecule plate 1 in the hood.
- Pipette the small molecules in this order (see troubleshooting for addition details on the handling procedure):
    a. Add 50 µL of media to the small molecule plate using a multichannel pipettor and gently mix by pipetting up and down (this dilutes the small molecules to 10 µM).
    b. Remove 50 µL of media from the corresponding wells of the cell plate using a second multichannel pipette.

    c. Transfer 50 μL media from the small molecule plate to the corresponding wells of the cell plate using first multichannel pipette. Discard both sets of pipette tips.

- Repeat Step 26 for plate 2, adding warm media to the reagent reservoir when needed. Take care to avoid cross-contamination by replacing tips at every step. For 445 wells, this protocol will use ~9 pipette tip boxes per drug addition day.
- Place the cell plates on the microscope of choice and start imaging.

Small Molecule Addition (Day 8)

- Warm 22.5 mL of the maintenance medium to 37°C in a bead bath or equivalent.
- Obtain the new plate of small molecules as previously.
- Similarly add media to the small molecule plate, remove media from the cell plate, and transfer media from the small molecule plate to the cell plate as previously (Steps 22-28).
- Place cell plates back on the microscope.

Quantify (Day 11)

- Remove cells from automatic imager 6 days post-small molecule addition 1.
- Quantitative assessment of cardiac myocyte proliferation. We used the Incucyte automatic analysis interface to do so, but thresholding nuclei in FIJI/ImageJ will also provide a mask to quantify nuclei count over time.

Fix and Stain Cells (Optional- Day 11)

- Prepare 4% Paraformaldehyde (PFA) in PBS in a chemical fume hood. Prepare 25 μL per well.

    a. Sample calculation for 445 wells: Prepare 12 mL of 4% PFA by adding 3 mL 16% PFA to 9 mL 1X PBS.

- Gently aspirate media from each well of the cell plate and add 25 µL 4% PFA immediately afterwards. For this step and following steps, minimize amount of time cells are dry.
- Wait 20 minutes.
- Aspirate each well and wash by adding 25 µL PBS.
- Repeat wash step (Step 38) twice more.
- Prepare 4% PFA, 1% Triton X-100 permeabilization solution in a chemical fume hood, 25 µL per well.
    a. Sample calculation for 445 wells: Prepare ~12 mL of permeabilization solution by adding 3 mL 16% PFA and 120 µL Triton X-100 to 9 mL 1X PBS.
- Aspirate PBS from each well of the cell plate and add 25 µL of the permeabilization solution to each well immediately afterwards.
- Wait 5 minutes.
- Wash the wells 3X each with 1X PBS as in Steps 38-39.
- Prepare 5% BSA blocking solution in 1X PBS (25 µL per well).
    a. Sample calculation: Add 2.5 grams BSA powder in a 50 mL conical tube, fill the tube to 50 mL with 1X PBS and vortex until the powder is dissolved.
- Aspirate the PBS from each well of the cell plate and add 25 µL 5% BSA in PBS to each well immediately afterwards.
- Wait 20 minutes.
- Prepare primary antibodies to the desired dilution.
    a. Sample calculation for 445 wells, staining for β-catenin (610153, BD Biosciences, San Jose, CA) and a rabbit antibody of choice, both at 1:200: Add 34 µL antibody to 6.8 mL 5% BSA.

- Aspirate the BSA from each well of the cell plate and add 15 μL of primary antibody to each well.
- Wait 1 hour 45 minutes.
- Prepare the secondary antibodies to the desired dilution.
    a. Sample calculation for 445 wells, using 488-goat-anti-rabbit and 568-goat-anti-mouse at 1:100: Add 68 μL of each secondary antibody to one tube containing 6.8 mL 5% BSA.
- Centrifuge secondary tube at 10,000xg for 2 min to pellet aggregates.
- Meanwhile, wash each well with 5% BSA as in Steps 38-39.
- Aspirate the BSA out of each well and add 15 μL of secondary to each well immediately after.
- Wait 1 hour.
- Wash each well with 1X PBS as in Steps 38-39.
- Keep 25 μL of PBS remaining in each well.
- Put plates on the microscope and image immediately to minimize exposure to 37°C.

Detailed Procedure for Small Molecule Addition

- Add 50 μL of maintenance media from a sterile reagent reservoir to the small molecule plate with right hand, using a multichannel pipette.
- Pipette the media in the small molecule plate up and down gently with the right hand to mix the media with the small molecule. Do not discard the right hand pipette tips yet.
- With left hand, remove 50 μL of media from the corresponding wells of the cell plate. Do not touch the bottom or scrape the cells.
- Discard the left hand pipette tips with the media into waste container 1.
- With right hand, pull up 50 μL of media from the small molecule plate wells from Step 1.

- With right hand, add the 50 µL from the small molecule plate to the wells of the cell plate that had media removed in Step 3.
- Discard the right hand pipette tips into waste container 2.
- Repeat Steps 1-7 for the entire plates

Timing

I. Total with purchased myocytes: 11 days

- Steps 1-20 (Day 1): 1 day (~6 hours)
- Step 21 (Day 3): 1 day (~1 hour)
- Steps 22-28 (Day 5): 1 day (~2 hours)
- Steps 29-32 (Day 8): 1 day (~2 hours)
- Steps 33-34 (Day 11+): 1 day (~2 hours)
- Steps 35-57 (Day 11+): 1 day (~5 hours)

II. Total with in-house differentiated myocytes: 42 days

- Skip steps 1-21
- Maintenance of hiPSCs (Days 1-7): 1 week[68]
- Differentiation of hiPSCs (Days 8-21): 2 weeks[68]
- Re-plating and growing hiCMs for maturation (Days 22-35): 2 weeks[68]
- Steps 22-28 (Day 36): 1 day (~2 hours)
- Steps 29-32 (Day 39): 1 day (~2 hours)
- Steps 33-34 (Day 42+): 1 day (~2 hours)
- Steps 35-57 (Day 42+): 1 day (~5 hours)

Supplemental References

1. Nakada, Y., Canseco, D.C., Thet, S., Abdisalaam, S., Asaithamby, A., Santos, C.X., Shah, A.M., Zhang, H., Faber, J.E., Kinter, M.T., et al. (2017). Hypoxia induces heart regeneration in adult mice. Nature *541*, 222-227.
2. Tong, W., Xiong, F., Li, Y., and Zhang, L. (2013). Hypoxia inhibits cardiomyocyte proliferation in fetal rat hearts via upregulating TIMP-4. Am J Physiol Regul Integr Comp Physiol *304*, R613-620.
3. Vujic, A., Lerchenmuller, C., Wu, T.D., Guillermier, C., Rabolli, C.P., Gonzalez, E., Senyo, S.E., Liu, X., Guerquin-Kern, J.L., Steinhauser, M.L., et al. (2018). Exercise induces new cardiomyocyte generation in the adult mammalian heart. Nat Commun *9*, 1659.
4. Han, C., Nie, Y., Lian, H., Liu, R., He, F., Huang, H., and Hu, S. (2015). Acute inflammation stimulates a regenerative response in the neonatal mouse heart. Cell Res *25*, 1137-1151.
5. Eulalio, A., Mano, M., Dal Ferro, M., Zentilin, L., Sinagra, G., Zacchigna, S., and Giacca, M. (2012). Functional screening identifies miRNAs inducing cardiac regeneration. Nature *492*, 376-381.
6. Tian, Y., Liu, Y., Wang, T., Zhou, N., Kong, J., Chen, L., Snitow, M., Morley, M., Li, D., Petrenko, N., et al. (2015). A microRNA-Hippo pathway that promotes cardiomyocyte proliferation and cardiac regeneration in mice. Sci Transl Med *7*, 279ra238.
7. Diez-Cunado, M., Wei, K., Bushway, P.J., Maurya, M.R., Perera, R., Subramaniam, S., Ruiz-Lozano, P., and Mercola, M. (2018). miRNAs that Induce Human Cardiomyocyte Proliferation Converge on the Hippo Pathway. Cell Rep *23*, 2168-2174.
8. Chen, J., Huang, Z.P., Seok, H.Y., Ding, J., Kataoka, M., Zhang, Z., Hu, X., Wang, G., Lin, Z., Wang, S., et al. (2013). mir-17-92 cluster is required for and sufficient to induce cardiomyocyte proliferation in postnatal and adult hearts. Circ Res *112*, 1557-1566.
9. Huang, W., Feng, Y., Liang, J., Yu, H., Wang, C., Wang, B., Wang, M., Jiang, L., Meng, W., Cai, W., et al. (2018). Loss of microRNA-128 promotes cardiomyocyte proliferation and heart regeneration. Nat Commun *9*, 700.
10. Porrello, E.R., Mahmoud, A.I., Simpson, E., Johnson, B.A., Grinsfelder, D., Canseco, D., Mammen, P.P., Rothermel, B.A., Olson, E.N., and Sadek, H.A. (2013). Regulation of neonatal and adult mammalian heart regeneration by the miR-15 family. Proc Natl Acad Sci U S A *110*, 187-192.
11. Yang, Y., Cheng, H.W., Qiu, Y., Dupee, D., Noonan, M., Lin, Y.D., Fisch, S., Unno, K., Sereti, K.I., and Liao, R. (2015). MicroRNA-34a Plays a Key Role in Cardiac Repair and Regeneration Following Myocardial Infarction. Circ Res *117*, 450-459.
12. Hu, Y., Jin, G., Li, B., Chen, Y., Zhong, L., Chen, G., Chen, X., Zhong, J., Liao, W., Liao, Y., et al. (2019). Suppression of miRNA let-7i-5p promotes cardiomyocyte proliferation and repairs heart function post injury by targetting CCND2 and E2F2. Clin Sci (Lond) *133*, 425-441.

13. Burton, P.B., Raff, M.C., Kerr, P., Yacoub, M.H., and Barton, P.J. (1999). An intrinsic timer that controls cell-cycle withdrawal in cultured cardiac myocytes. Dev Biol *216*, 659-670.
14. Engel, F.B., Hsieh, P.C., Lee, R.T., and Keating, M.T. (2006). FGF1/p38 MAP kinase inhibitor therapy induces cardiomyocyte mitosis, reduces scarring, and rescues function after myocardial infarction. Proc Natl Acad Sci U S A *103*, 15546-15551.
15. Pasumarthi, K.B., Kardami, E., and Cattini, P.A. (1996). High and low molecular weight fibroblast growth factor-2 increase proliferation of neonatal rat cardiac myocytes but have differential effects on binucleation and nuclear morphology. Evidence for both paracrine and intracrine actions of fibroblast growth factor-2. Circ Res *78*, 126-136.
16. Mohamed, T.M.A., Ang, Y.S., Radzinsky, E., Zhou, P., Huang, Y., Elfenbein, A., Foley, A., Magnitsky, S., and Srivastava, D. (2018). Regulation of Cell Cycle to Stimulate Adult Cardiomyocyte Proliferation and Cardiac Regeneration. Cell *173*, 104-116 e112.
17. Naqvi, N., Li, M., Calvert, J.W., Tejada, T., Lambert, J.P., Wu, J., Kesteven, S.H., Holman, S.R., Matsuda, T., Lovelock, J.D., et al. (2014). A proliferative burst during preadolescence establishes the final cardiomyocyte number. Cell *157*, 795-807.
18. Bersell, K., Arab, S., Haring, B., and Kuhn, B. (2009). Neuregulin1/ErbB4 signaling induces cardiomyocyte proliferation and repair of heart injury. Cell *138*, 257-270.
19. Reuter, S., Soonpaa, M.H., Firulli, A.B., Chang, A.N., and Field, L.J. (2014). Recombinant neuregulin 1 does not activate cardiomyocyte DNA synthesis in normal or infarcted adult mice. PLoS One *9*, e115871.
20. Polizzotti, B.D., Ganapathy, B., Walsh, S., Choudhury, S., Ammanamanchi, N., Bennett, D.G., dos Remedios, C.G., Haubner, B.J., Penninger, J.M., and Kuhn, B. (2015). Neuregulin stimulation of cardiomyocyte regeneration in mice and human myocardium reveals a therapeutic window. Sci Transl Med *7*, 281ra245.
21. D'Uva, G., Aharonov, A., Lauriola, M., Kain, D., Yahalom-Ronen, Y., Carvalho, S., Weisinger, K., Bassat, E., Rajchman, D., Yifa, O., et al. (2015). ERBB2 triggers mammalian heart regeneration by promoting cardiomyocyte dedifferentiation and proliferation. Nat Cell Biol *17*, 627-638.
22. Sharma, A., Zhang, Y., Buikema, J.W., Serpooshan, V., Chirikian, O., Kosaric, N., Churko, J.M., Dzilic, E., Shieh, A., Burridge, P.W., et al. (2018). Stage-specific Effects of Bioactive Lipids on Human iPSC Cardiac Differentiation and Cardiomyocyte Proliferation. Sci Rep *8*, 6618.
23. Fang, R., Qiao, S., Liu, Y., Meng, Q., Chen, X., Song, B., Hou, X., and Tian, W. (2015). Sustained co-delivery of BIO and IGF-1 by a novel hybrid hydrogel system to stimulate endogenous cardiac repair in myocardial infarcted rat hearts. Int J Nanomedicine *10*, 4691-4703.
24. Chakraborty, S., Sengupta, A., and Yutzey, K.E. (2013). Tbx20 promotes cardiomyocyte proliferation and persistence of fetal characteristics in adult mouse hearts. J Mol Cell Cardiol *62*, 203-213.
25. Malek Mohammadi, M., Kattih, B., Grund, A., Froese, N., Korf-Klingebiel, M., Gigina, A., Schrameck, U., Rudat, C., Liang, Q., Kispert, A., et al. (2017). The transcription factor GATA4 promotes myocardial regeneration in neonatal mice. EMBO Mol Med *9*, 265-279.

26. Jackson, T., Allard, M.F., Sreenan, C.M., Doss, L.K., Bishop, S.P., and Swain, J.L. (1990). The c-myc proto-oncogene regulates cardiac development in transgenic mice. Mol Cell Biol *10*, 3709-3716.
27. Chaudhry, H.W., Dashoush, N.H., Tang, H., Zhang, L., Wang, X., Wu, E.X., and Wolgemuth, D.J. (2004). Cyclin A2 mediates cardiomyocyte mitosis in the postmitotic myocardium. J Biol Chem *279*, 35858-35866.
28. Zhang, Y., Mignone, J., and MacLellan, W.R. (2015). Cardiac Regeneration and Stem Cells. Physiol Rev *95*, 1189-1204.
29. Busk, P.K., Hinrichsen, R., Bartkova, J., Hansen, A.H., Christoffersen, T.E., Bartek, J., and Haunso, S. (2005). Cyclin D2 induces proliferation of cardiac myocytes and represses hypertrophy. Exp Cell Res *304*, 149-161.
30. Hassink, R.J., Pasumarthi, K.B., Nakajima, H., Rubart, M., Soonpaa, M.H., de la Riviere, A.B., Doevendans, P.A., and Field, L.J. (2008). Cardiomyocyte cell cycle activation improves cardiac function after myocardial infarction. Cardiovasc Res *78*, 18-25.
31. Sun, Q., Zhang, F., Wafa, K., Baptist, T., and Pasumarthi, K.B. (2009). A splice variant of cyclin D2 regulates cardiomyocyte cell cycle through a novel protein aggregation pathway. J Cell Sci *122*, 1563-1573.
32. Williams, S.D., Zhu, H., Zhang, L., and Bernstein, H.S. (2006). Adenoviral delivery of human CDC5 promotes G2/M progression and cell division in neonatal ventricular cardiomyocytes. Gene Ther *13*, 837-843.
33. Agah, R., Kirshenbaum, L.A., Abdellatif, M., Truong, L.D., Chakraborty, S., Michael, L.H., and Schneider, M.D. (1997). Adenoviral delivery of E2F-1 directs cell cycle reentry and p53-independent apoptosis in postmitotic adult myocardium in vivo. J Clin Invest *100*, 2722-2728.
34. Pasumarthi, K.B., and Field, L.J. (2002). Cardiomyocyte cell cycle regulation. Circ Res *90*, 1044-1054.
35. Kirshenbaum, L.A., and Schneider, M.D. (1995). Adenovirus E1A represses cardiac gene transcription and reactivates DNA synthesis in ventricular myocytes, via alternative pocket protein- and p300-binding domains. J Biol Chem *270*, 7791-7794.
36. Di Stefano, V., Giacca, M., Capogrossi, M.C., Crescenzi, M., and Martelli, F. (2011). Knockdown of cyclin-dependent kinase inhibitors induces cardiomyocyte re-entry in the cell cycle. J Biol Chem *286*, 8644-8654.
37. Chen, Z., Xie, J., Hao, H., Lin, H., Wang, L., Zhang, Y., Chen, L., Cao, S., Huang, X., Liao, W., et al. (2017). Ablation of periostin inhibits post-infarction myocardial regeneration in neonatal mice mediated by the phosphatidylinositol 3 kinase/glycogen synthase kinase 3beta/cyclin D1 signalling pathway. Cardiovasc Res *113*, 620-632.
38. Kuhn, B., del Monte, F., Hajjar, R.J., Chang, Y.S., Lebeche, D., Arab, S., and Keating, M.T. (2007). Periostin induces proliferation of differentiated cardiomyocytes and promotes cardiac repair. Nat Med *13*, 962-969.
39. Lorts, A., Schwanekamp, J.A., Elrod, J.W., Sargent, M.A., and Molkentin, J.D. (2009). Genetic manipulation of periostin expression in the heart does not affect myocyte content, cell cycle activity, or cardiac repair. Circ Res *104*, e1-7.

40. Bassat, E., Mutlak, Y.E., Genzelinakh, A., Shadrin, I.Y., Baruch Umansky, K., Yifa, O., Kain, D., Rajchman, D., Leach, J., Riabov Bassat, D., et al. (2017). The extracellular matrix protein agrin promotes heart regeneration in mice. Nature *547*, 179-184.
41. Fan, Y., Ho, B.X., Pang, J.K.S., Pek, N.M.Q., Hor, J.H., Ng, S.Y., and Soh, B.S. (2018). Wnt/beta-catenin-mediated signaling re-activates proliferation of matured cardiomyocytes. Stem Cell Res Ther *9*, 338.
42. Woulfe, K.C., Gao, E., Lal, H., Harris, D., Fan, Q., Vagnozzi, R., DeCaul, M., Shang, X., Patel, S., Woodgett, J.R., et al. (2010). Glycogen synthase kinase-3beta regulates post-myocardial infarction remodeling and stress-induced cardiomyocyte proliferation in vivo. Circ Res *106*, 1635-1645.
43. Zhou, J., Ahmad, F., Parikh, S., Hoffman, N.E., Rajan, S., Verma, V.K., Song, J., Yuan, A., Shanmughapriya, S., Guo, Y., et al. (2016). Loss of Adult Cardiac Myocyte GSK-3 Leads to Mitotic Catastrophe Resulting in Fatal Dilated Cardiomyopathy. Circ Res *118*, 1208-1222.
44. Uosaki, H., Magadum, A., Seo, K., Fukushima, H., Takeuchi, A., Nakagawa, Y., Moyes, K.W., Narazaki, G., Kuwahara, K., Laflamme, M., et al. (2013). Identification of chemicals inducing cardiomyocyte proliferation in developmental stage-specific manner with pluripotent stem cells. Circ Cardiovasc Genet *6*, 624-633.
45. Kim, Y.S., Jeong, H.Y., Kim, A.R., Kim, W.H., Cho, H., Um, J., Seo, Y., Kang, W.S., Jin, S.W., Kim, M.C., et al. (2016). Natural product derivative BIO promotes recovery after myocardial infarction via unique modulation of the cardiac microenvironment. Sci Rep *6*, 30726.
46. Buikema, J.W., Zwetsloot, P.P., Doevendans, P.A., Sluijter, J.P., and Domian, I.J. (2013). Expanding mouse ventricular cardiomyocytes through GSK-3 inhibition. Curr Protoc Cell Biol *61*, 23 29 21-23 29 10.
47. Kerkela, R., Kockeritz, L., Macaulay, K., Zhou, J., Doble, B.W., Beahm, C., Greytak, S., Woulfe, K., Trivedi, C.M., Woodgett, J.R., et al. (2008). Deletion of GSK-3beta in mice leads to hypertrophic cardiomyopathy secondary to cardiomyoblast hyperproliferation. J Clin Invest *118*, 3609-3618.
48. Matsuyama, D., and Kawahara, K. (2011). Oxidative stress-induced formation of a positive-feedback loop for the sustained activation of p38 MAPK leading to the loss of cell division in cardiomyocytes soon after birth. Basic Res Cardiol *106*, 815-828.
49. Engel, F.B., Schebesta, M., Duong, M.T., Lu, G., Ren, S., Madwed, J.B., Jiang, H., Wang, Y., and Keating, M.T. (2005). p38 MAP kinase inhibition enables proliferation of adult mammalian cardiomyocytes. Genes Dev *19*, 1175-1187.
50. Park, S., Choe, M., Yeo, H., Han, H., Kim, J., Chang, W., Yun, S., Lee, H., and Lee, M. (2018). Yes-associated protein mediates human embryonic stem cell-derived cardiomyocyte proliferation: Involvement of epidermal growth factor receptor signaling. J Cell Physiol *233*, 7016-7025.
51. Xin, M., Kim, Y., Sutherland, L.B., Murakami, M., Qi, X., McAnally, J., Porrello, E.R., Mahmoud, A.I., Tan, W., Shelton, J.M., et al. (2013). Hippo pathway effector Yap promotes cardiac regeneration. Proc Natl Acad Sci U S A *110*, 13839-13844.

52. Heallen, T., Zhang, M., Wang, J., Bonilla-Claudio, M., Klysik, E., Johnson, R.L., and Martin, J.F. (2011). Hippo pathway inhibits Wnt signaling to restrain cardiomyocyte proliferation and heart size. Science *332*, 458-461.
53. Xin, M., Kim, Y., Sutherland, L.B., Qi, X., McAnally, J., Schwartz, R.J., Richardson, J.A., Bassel-Duby, R., and Olson, E.N. (2011). Regulation of insulin-like growth factor signaling by Yap governs cardiomyocyte proliferation and embryonic heart size. Sci Signal *4*, ra70.
54. Lin, Z., von Gise, A., Zhou, P., Gu, F., Ma, Q., Jiang, J., Yau, A.L., Buck, J.N., Gouin, K.A., van Gorp, P.R., et al. (2014). Cardiac-specific YAP activation improves cardiac function and survival in an experimental murine MI model. Circ Res *115*, 354-363.
55. Hara, H., Takeda, N., Kondo, M., Kubota, M., Saito, T., Maruyama, J., Fujiwara, T., Maemura, S., Ito, M., Naito, A.T., et al. (2018). Discovery of a Small Molecule to Increase Cardiomyocytes and Protect the Heart After Ischemic Injury. JACC Basic Transl Sci *3*, 639-653.
56. von Gise, A., Lin, Z., Schlegelmilch, K., Honor, L.B., Pan, G.M., Buck, J.N., Ma, Q., Ishiwata, T., Zhou, B., Camargo, F.D., et al. (2012). YAP1, the nuclear target of Hippo signaling, stimulates heart growth through cardiomyocyte proliferation but not hypertrophy. Proc Natl Acad Sci U S A *109*, 2394-2399.
57. Heallen, T., Morikawa, Y., Leach, J., Tao, G., Willerson, J.T., Johnson, R.L., and Martin, J.F. (2013). Hippo signaling impedes adult heart regeneration. Development *140*, 4683-4690.
58. Lin, Z., Zhou, P., von Gise, A., Gu, F., Ma, Q., Chen, J., Guo, H., van Gorp, P.R., Wang, D.Z., and Pu, W.T. (2015). Pi3kcb links Hippo-YAP and PI3K-AKT signaling pathways to promote cardiomyocyte proliferation and survival. Circ Res *116*, 35-45.
59. Liu, T.L., Upadhyayula, S., Milkie, D.E., Singh, V., Wang, K., Swinburne, I.A., Mosaliganti, K.R., Collins, Z.M., Hiscock, T.W., Shea, J., et al. (2018). Observing the cell in its native state: Imaging subcellular dynamics in multicellular organisms. Science *360*.
60. Gingras, A.C., Kennedy, S.G., O'Leary, M.A., Sonenberg, N., and Hay, N. (1998). 4E-BP1, a repressor of mRNA translation, is phosphorylated and inactivated by the Akt(PKB) signaling pathway. Genes Dev *12*, 502-513.
61. Cross, D.A., Alessi, D.R., Cohen, P., Andjelkovich, M., and Hemmings, B.A. (1995). Inhibition of glycogen synthase kinase-3 by insulin mediated by protein kinase B. Nature *378*, 785-789.
62. Inoki, K., Li, Y., Zhu, T., Wu, J., and Guan, K.L. (2002). TSC2 is phosphorylated and inhibited by Akt and suppresses mTOR signalling. Nat Cell Biol *4*, 648-657.
63. Manning, B.D., Tee, A.R., Logsdon, M.N., Blenis, J., and Cantley, L.C. (2002). Identification of the tuberous sclerosis complex-2 tumor suppressor gene product tuberin as a target of the phosphoinositide 3-kinase/akt pathway. Mol Cell *10*, 151-162.
64. Soonpaa, M.H., Kim, K.K., Pajak, L., Franklin, M., and Field, L.J. (1996). Cardiomyocyte DNA synthesis and binucleation during murine development. Am J Physiol *271*, H2183-2189.
65. Pajak, L., Jin, F., Xiao, G.H., Soonpaa, M.H., Field, L.J., and Yeung, R.S. (1997). Sustained cardiomyocyte DNA synthesis in whole embryo cultures lacking the TSC2 gene product. Am J Physiol *273*, H1619-1627.

66. Inoki, K., Zhu, T., and Guan, K.L. (2003). TSC2 mediates cellular energy response to control cell growth and survival. Cell *115*, 577-590.
67. Bhaskar, P.T., and Hay, N. (2007). The two TORCs and Akt. Dev Cell *12*, 487-502.
68. Sharma, A., McKeithan, W.L., Serrano, R., Kitani, T., Burridge, P.W., Del Alamo, J.C., Mercola, M., and Wu, J.C. (2018). Use of human induced pluripotent stem cell-derived cardiomyocytes to assess drug cardiotoxicity. Nat Protoc *13*, 3018-3041.
69. Burnette, D.T., Shao, L., Ott, C., Pasapera, A.M., Fischer, R.S., Baird, M.A., Der Loughian, C., Delanoe-Ayari, H., Paszek, M.J., Davidson, M.W., et al. (2014). A contractile and counterbalancing adhesion system controls the 3D shape of crawling cells. J Cell Biol *205*, 83-96.
70. Fenix, A.M., Neininger, A.C., Taneja, N., Hyde, K., Visetsouk, M.R., Garde, R.J., Liu, B., Nixon, B.R., Manalo, A.E., Becker, J.R., et al. (2018). Muscle-specific stress fibers give rise to sarcomeres in cardiomyocytes. Elife *7*.

CHAPTER 3

THE HIPPO PATHWAY REGULATES DENSITY-DEPENDENT PROLIFERATION IN iPSC-DERIVED CARDIAC MYOCYTES

Neininger, AC., Dai, X., Liu, Q., & Burnette, DT.

Introduction

Cardiac myocytes (CMs) are the cells of the heart that generate contractile force. The mechanisms controlling CM proliferation are critical during both heart development and disease[97,98]. While adult CMs are non-mitotic, CMs in the developing heart proliferate to drive hyperplastic growth[81,99,100]. The Hippo pathway has been shown to regulate proliferation during development[101,102]. The Hippo pathway is a kinase cascade that, when active, negatively regulates the transcriptional coactivators YAP and TAZ. In the absence of inhibition, YAP and TAZ translocate to the nucleus to activate the transcription of pro-proliferative genes[103-105]. In addition, the Hippo pathway regulates contact-dependent cell proliferation in epithelial cells, cancer cells, and pluripotent stem cells[106-109]. In these studies, low density cells with fewer cell-cell contacts have increased YAP nuclear localization, while high density cells have more inactive YAP in the cytosol[110,111]. This evidence supports the notion that cell proliferation is not entirely regulated by paracrine mechanisms (e.g., by growth factors) and that proliferation is in part regulated spatially by density-dependent mechanisms[112]. We asked if the Hippo pathway is involved in non-paracrine mechanisms such as contact inhibition in the heart.

The Hippo pathway is required for cardiac development in mice[113,114]. Cardiac-specific knockout of YAP is lethal in mice and leads to thin ventricular walls and several other structural abnormalities[102]. A YAP mutant that blocks the interaction between YAP and its co-transcription factor TEAD also led to less proliferation in the developing mouse heart[113]. In addition, during the first post-natal week, the mouse heart retains the ability to fully regenerate after an infarction. YAP conditional knockout mice lose the ability to regenerate[102]. Interestingly, constitutively active YAP can induce CM proliferation in the adult mouse heart, as can a mouse with a conditional knockout of Salv1, an upstream Hippo pathway component[101]. Taken together, these studies solidify the Hippo pathway as a key signaling cascade for CM proliferation.

We sought a model system to explore the role of the Hippo pathway in cell density-dependent regulation of CM proliferation. It is difficult to study contact inhibition *in vivo*, where tight control of cell density is not possible. For example, acute mechanical perturbations followed by long-term live cell imaging are currently beyond available technologies. Therefore, we turned to *in vitro* models. It has previously been shown that plating low density human embryonic stem cell-derived CMs induces them to enter the cell cycle[87]. This was shown using flow cytometry to measure the expression of three cell cycle markers: BrdU, YAP, and cyclin D1. Furthermore, our previous work showed that human iPSC-derived CMs (hiCMs) are more proliferative when plated sparsely than when in a monolayer based on cell counting using high-content microscopy[115]. Whether the Hippo pathway regulates the apparent difference in CM-proliferation capacity in dense and sparse populations remains to be elucidated. This led us to probe whether the Hippo pathway is involved in regulating the proliferative capacity of CMs in various densities or if YAP is activated in these sparse populations by another mechanism. We have chosen hiCMs as our model system to study this phenomenon, as they are transcriptionally immature—similar to fetal or neonatal CMs *in vivo*—and have a slight basal proliferative capacity[85,95]. Here, we show that reducing hiCM-density by either a scratch assay or by sparse plating increases nuclear YAP and CM-proliferation, and that this proliferative capacity can be further enhanced by combinatorial pharmacological perturbation of the Hippo pathway.

Results

Reducing hiCM Density in a Scratch Assay Increases Proliferative Capacity

We first investigated whether a reduction in hiCM-density resulted in increased proliferation and/or any changes in Hippo pathway signaling. The hiCMs we used were purchased pre-differentiated and we confirmed the company's claim of a lack of fibroblast contamination (See Materials and Methods, Figure 3-S1B) and slight proliferative capacity (Figure 3-S1D)[115]. The lack of non-muscle cell types is key for interpretation of the data sets measuring proliferation. In addition, hiCMs can be cultured as a dense monolayer in which every cell has the potential to be experiencing contact inhibition.

One well-established method to relieve contact inhibition in culture is to scratch a confluent monolayer of cells[116]. Therefore, we used a micropipette tip to scratch a confluent monolayer of hiCMs (Figure 3-1A-B). We hypothesized that, as in epithelial cells, YAP would translocate to the nucleus of hiCMs near the scratch, as these hiCMs should have reduced contact inhibition compared to those far from the scratch. To test this, we localized YAP using immunofluorescence 48 hours post-scratch. We noticed that hiCMs near the edge of the scratch appeared to have primarily nuclear YAP (Figure 3-1C). A proxy for YAP activity is to measure the nuclear accumulation of YAP[117]. Therefore, we acquired higher magnification images to measure the ratio of nuclear YAP to total YAP. We used β-catenin to mark adherens junctions between myocytes in order to delineate separate cells, and measured nuclear YAP and total YAP using fluorescence localization. We found that hiCMs near the scratch had a higher nuclear YAP to total YAP ratio than either hiCMs farther from the scratch on the same plate or hiCMs in an unscratched monolayer (Figure 3-1C-D). Interestingly, this appeared to be an exponentially decaying relationship, where the nuclear YAP to total YAP ratio decreased rapidly as a function of distance from the scratch.

Figure 3-1: Reducing hiCM density by a scratch assay increases proliferative capacity

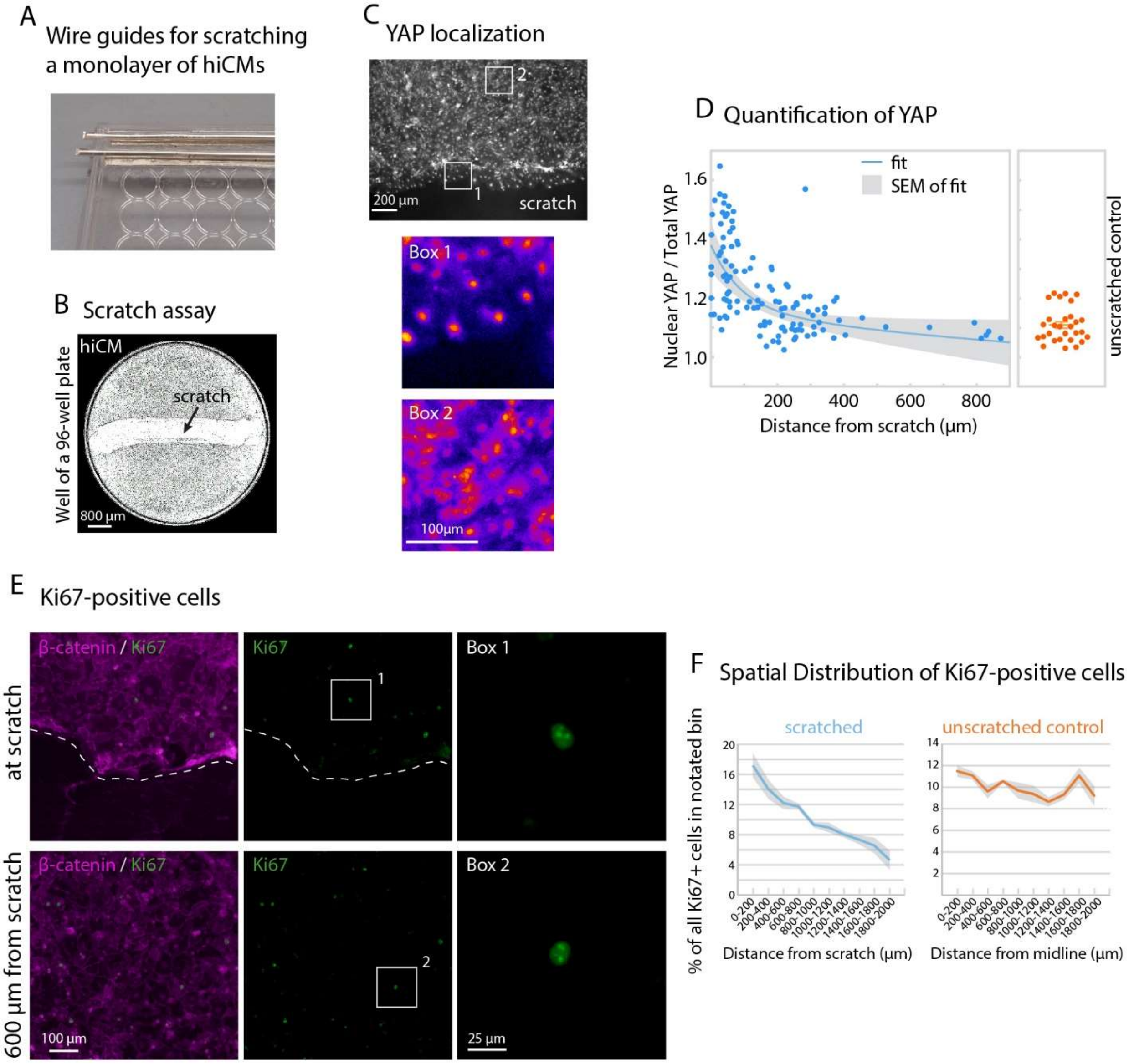

Figure 3-1:

A) Wire guide for scratching a monolayer of hiCMs, using a lid of a 96-well plate and a Dremel tool to drill through the plastic lid. Wire guides are composed of a bottom layer of flattened 21-gauge wire glued to the lid and a top layer of cylindrical wire to guide the pipette tip. B) 4X whole-well phase-contrast image of hiCMs in a well of a 96-well plate, 48 hours post-scratch. C) YAP immunolocalization near the scratch (box 1) and far from the scratched (box 2) using 20X widefield microscopy. D) Quantification of Nuclear YAP divided by total YAP (n= 79 cells from 5 independent experiments). Unscratched control (n= 29 cells from 3 independent experiments). E) Ki67 and β-catenin in a scratched plate 48 hours post-scratch using 20X. F) Spatial distribution of Ki67-positive hiCMs in a scratched well or in an unscratched control well 48 hours post-scratch. ***$p<0.0001$, chi-square = 80.434 with a two by five contingency table comparing distributions of Ki67 in different regions within 2 mm of the scratch or center of the midline of the well. G) Fucci cell cycle probe transduced into a monolayer of hiCMs and scratched or not scratched.

We next wanted to know if the increase in nuclear YAP correlated with an increase in hiCMs entering the cell cycle. One standard way to identify cycling cells is to localize Ki67 using immunofluorescence, as Ki67 is localized in the nuclei of cycling cells[118,119]. We found that in a monolayer of hiCMs, Ki67-positive cells were evenly distributed across the well and were found in actinin2-positive cells (Figure 3-1E-F, Figure 3-S1E). In contrast, for the scratched cells, there was a skewed distribution, in which more Ki67-positive nuclei were near the scratch (Figure 3-1E-F). We further used the Fucci probe as evidence that cells near a scratch are cycling (Figure 3-1G). Taken together, these data indicate that the relief of contact inhibition by a scratch assay increases the amount of YAP in the nuclei of hiCMs and promotes their entry into the cell cycle. However, it is worth noting that a scratch assay is inherently asymmetric as only hiCMs near a scratch respond, limiting measurements of responses on a population level. This further suggests that increase in cell proliferation is not entirely a paracrine mechanism. If a scratch induced cardiac myocyte proliferation in a nonautonomous fashion, all cells would undergo a similar increase in proliferation. While we cannot make the conclusion that in this system, the increase in nuclear YAP/total YAP ratio is directly causative of the increase in Ki67-positive nuclei near the scratch, we can conclude that the increase in proliferative capacity seen in a scratched monolayer of cardiac myocytes is at least in part cell autonomous.

Reducing hiCM Density by Sparse Plating Increases Proliferative Capacity

We next wanted to identify an assay that could model a uniform reduction in contact inhibition across an entire population of hiCMs. A previous study used flow cytometry and Western blotting to show that embryonic stem cell-derived cardiac myocytes begin cycling when they are sparsely plated[87]. Thus, we plated hiCMs as a monolayer or plated them sparsely. Not surprisingly, a monolayer of hiCMs (~1088 hiCMs/mm^2) have a low nuclear YAP/total YAP ratio (Figure 3-2A-B). On the other hand, when cells are plated at an 8-fold dilution (~136 hiCMs/mm^2), the nuclear YAP/total YAP ratio increases almost 2-fold (Figure 3-2A-B).

This increase in nuclear YAP in sparsely-plated hiCMs suggested an increase in proliferative capacity. To test this, we asked if sparse plating caused entry into the cell cycle using Ki67 localization. We localized Ki67 in dense or sparse hiCMs and found an increase in Ki67-positive nuclei, indicating a near doubling in cycling hiCMs (Figure 3-2C-D). We similarly used the Fucci probe system and found that the majority of dense hiCMs were not cycling, whereas sparse hiCMs had increased cycling cells (Figure 3-2E). To directly test if sparse-plating induced proliferation in hiCMs, we counted the number of hiCMs over time. We found that while dense control hiCMs essentially remained the same over 48 hours, there was a ~5% increase in the number of sparsely-plated hiCMs (Figure 3-2F). Taken together, our data indicates that sparse plating induces hiCMs to enter the cell cycle and also divide. This led us to explore the underlying cause of sparsely-plated hiCMs to enter the cell cycle.

It has been postulated that CM division is preceded by dedifferentiation into a more immature phenotype[120,121]. Thus, we employed RNASeq analysis to examine whether the proliferating sparsely-plated hiCMs were as mature as hiCMs in a monolayer. We found CM-maturity genes (Uosaki et al., 2015, Table 1) were modestly downregulated in sparse hiCMs (Figure 3-2G). However, expression of CM-identity genes α-actinin 2 and troponinT did not change (Figure 3-2G, Table 3). Thus, sparsely-plated hiCMs are less mature than densely-plated hiCMs, but they remain CMs.

Table 3-1: YAP Target Genes

Gene	**Sparse (Dense) FC**	**p-value**	**XMU (Dense) FC**	**p-value**	**S1P (Dense) FC**	**p-value**	**XMU (Sparse) FC**	**p-value**	**S1P (Sparse) FC**	**p-value**
CTGF	9.01	2.89E-13	25.81	2.79E-22	17.62	8.25E-24	2.93	0.000134	1.97	0.007319
GADD45G	3.73	0.002072	6.56	0.000193	10.85	0.000115	1.79	0.605755	3.00	0.038005
CYR61	3.66	5.95E-05	10.82	1.04E-13	6.92	6.18E-14	3.01	0.000925	1.91	0.020171
GADD45B	3.26	9.59E-07	5.54	1.41E-08	4.45	0.001261	1.74	0.126936	1.39	0.36164
GLI2	1.53	0.393604	3.82	6.2E-22	2.24	0.185947	2.54	0.004467	1.47	0.316052
CDKN2B	2.54	0.175283	2.99	0.000286	2.57	0.384279	1.22	0.792722	1.01	0.983649
MYC	2.11	0.065524	3.30	9.61E-08	3.98	7.42E-08	1.60	0.275537	1.90	0.012205
VIM	1.85	0.026872	1.39	0.000517	1.68	0.038557	0.77	0.478305	0.92	0.7466
TEAD4	1.87	0.015487	1.63	9.48E-06	1.68	0.023656	0.89	0.778883	0.91	0.679315
GPATCH4	2.18	0.038921	0.78	0.115272	2.01	0.357642	0.37	0.002401	0.93	0.87144
TXN	1.69	0.183088	1.36	0.039324	1.96	0.299241	0.82	0.697661	1.18	0.672179
CAV1	0.63	0.143092	0.33	4.8E-18	0.62	0.135195	0.53	0.004174	1.00	0.99217
CAT	0.81	0.520764	0.84	0.245518	0.73	0.551213	1.06	0.871611	0.90	0.656182
TEAD1	1.08	0.904655	1.70	3.93E-06	1.31	0.694522	1.61	0.246832	1.21	0.571363
AXL	0.71	0.199238	0.62	0.000225	0.70	0.260978	0.88	0.69564	0.99	0.962445
CCND1	1.21	0.480377	0.99	0.95182	1.15	0.630965	0.83	0.467474	0.96	0.791495
ERBB4	0.82	0.630638	0.95	0.814267	1.01	0.995008	1.18	0.703516	1.22	0.533846
WSB2	0.91	0.780978	0.81	0.033037	0.82	0.757739	0.90	0.726643	0.90	0.696159
LMNB2	1.12	0.807049	0.97	0.900838	1.08	0.886014	0.89	0.761298	0.97	0.88176
TNFAIP3	0.74	0.686538	0.35	0.000508	0.50	0.405358	0.48	0.239423	0.68	0.417583
GATA6	0.67	0.057851	0.65	1.49E-07	0.68	0.083787	0.98	0.965776	1.02	0.936819
PLK2	0.72	0.112915	0.41	2.48E-06	0.64	0.002456	0.58	0.142406	0.90	0.570129
YAP	1.00	0.998472	0.83	0.025910	0.97	0.959423	0.84	0.681629	0.97	0.999937
TAZ	1.36	0.720522	0.50	0.002689	0.55	0.126824	0.37	0.111599	0.41	0.999937
MST1	0.86	0.802404	0.95	0.870735	0.68	0.528100	1.12	0.804197	0.80	0.999937
MST2	1.19	0.640836	0.95	0.870735	1.02	0.977948	1.06	0.904359	0.86	0.999937
LATS1	0.74	0.544618	1.17	0.283387	0.95	0.947461	1.62	0.241345	1.29	0.999937
LATS2	1.00	0.999502	1.97	1.01E-12	1.14	0.893674	2.01	0.010439	1.14	0.999937

Table 3-2: Cardiac myocyte maturity genes

Gene	Sparse (Dense) FC	p-value	XMU (Dense) FC	p-value	S1P (Dense) FC	p-value	XMU (Sparse) FC	p-value	S1P (Sparse) FC	p-value
KLF15	0.37	0.001345	0.62	0.015381	0.40	0.081736	1.69	0.216003	1.08	0.852327
PPARA	0.50	0.033375	0.69	0.000397	0.51	0.059213	1.42	0.404501	1.04	0.913521
RB1	0.66	0.377255	1.07	0.637022	0.80	0.801415	1.65	0.23275	1.21	0.62234
RXRA	0.67	0.183603	0.75	0.008464	0.66	0.090851	1.15	0.740298	1.00	0.995685
PPARGC1A	0.69	0.237739	0.46	2.62E-09	0.75	0.403987	0.69	0.305008	1.10	0.703669
NUPR1	0.67	0.718043	0.03	0.00025	1.33	0.902237	0.05	0.065356	2.04	0.421311
PPARD	0.72	0.091847	0.88	0.254178	0.65	0.407204	1.25	0.360958	0.90	0.70345
STAT5B	0.96	0.925941	1.30	0.005076	0.88	0.835451	1.38	0.238056	0.92	0.749992
TP53	1.04	0.919216	0.74	0.007432	1.17	0.620798	0.73	0.178197	1.13	0.501919
SMARCA4	1.38	0.318031	1.07	0.563766	1.37	0.427076	0.79	0.484057	1.01	0.984053
PPARGC1B	0.57	0.118278	0.24	3.94E-19	0.70	0.255304	0.43	0.02966	1.24	0.451305
SIRT1	0.64	0.391808	1.17	0.300566	0.70	0.460866	1.85	0.167862	1.10	0.785253
BRCA1	0.70	0.444602	0.39	5.06E-07	0.68	0.240951	0.57	0.255112	0.97	0.929278
ISL1	0.70	0.72808	0.39	0.047124	1.27	0.832355	0.57	0.575785	1.85	0.226337
EZH2	0.95	0.925928	0.90	0.608155	0.99	0.989079	0.97	0.957506	1.04	0.872184
KLF2	1.07	0.943608	2.03	0.307754	1.36	0.80982	1.93	0.374266	1.31	0.606284
TCF7L2	1.11	0.804331	0.82	0.208738	1.40	0.432616	0.75	0.257579	1.28	0.274109
IRF3	1.22	0.675849	1.29	0.038872	1.26	0.749532	1.08	0.891222	1.05	0.881247
EPAS1	0.33	1.33E-06	0.34	1.38E-16	0.23	0.015726	1.04	0.945471	0.69	0.436981
STAT6	0.55	0.006801	0.19	2.02E-30	0.37	0.000199	0.35	2.87E-05	0.68	0.125648
HMGA1	0.71	0.242416	0.72	0.000562	0.74	0.087149	1.04	0.929241	1.05	0.807651
CREBBP	0.76	0.429739	0.98	0.906761	0.94	0.893223	1.32	0.408709	1.24	0.3625
RORA	0.77	0.632319	1.10	0.719185	0.81	0.681446	1.44	0.432174	1.05	0.881326
TBX5	0.81	0.516316	0.73	0.015109	0.88	0.818683	0.91	0.753349	1.09	0.682947
HIF1A	0.91	0.827102	0.73	0.000624	0.88	0.888031	0.82	0.57784	0.98	0.944643
ESRRA	0.97	0.964559	0.64	0.001142	0.66	0.201523	0.67	0.165544	0.69	0.080643
GATA4	0.97	0.924665	1.54	8.22E-09	1.08	0.894736	1.62	0.002196	1.12	0.607182
MEF2C	1.07	0.85549	1.26	0.043804	1.51	0.008506	1.20	0.525246	1.42	0.054329
MYOCD	1.22	0.587856	0.84	0.148871	1.24	0.38708	0.70	0.236397	1.02	0.931564
SREBF1	0.34	0.00046	0.32	1.42E-11	0.40	0.00197	0.96	0.945008	1.18	0.522472
NR2C2	0.54	0.352976	0.94	0.749191	0.62	0.730363	1.77	0.374012	1.14	0.829856
EP300	0.70	0.467532	1.15	0.234023	0.85	0.847678	1.66	0.220495	1.21	0.612428
FOXO3	0.75	0.349721	0.86	0.130914	0.78	0.216367	1.17	0.641334	1.05	0.805169
CEBPB	0.94	0.922627	0.88	0.386107	1.17	0.797417	0.96	0.952266	1.27	0.462195
AHR	0.93	0.932517	1.35	0.172625	1.00	0.998442	1.46	0.403747	1.07	0.848077
ESRRA	0.97	0.964559	0.64	0.001142	0.66	0.201523	0.67	0.165544	0.69	0.080643
TFAM	0.98	0.972321	0.93	0.638489	1.12	0.815031	0.96	0.925733	1.15	0.524921
TCF3	1.07	0.870547	1.03	0.829302	0.99	0.976384	0.98	0.966962	0.93	0.718576

NR4A3	1.11	0.880451	4.19	0.042536	2.08	0.097711	3.84	0.020697	1.89	0.035762
NFATC2	0.24	8.81E-07	0.31	4.36E-14	0.45	0.01823	1.33	0.590606	1.85	0.066561
TOB1	0.69	0.202871	0.71	0.006508	0.64	0.047766	1.05	0.921464	0.93	0.750685
CTCF	0.77	0.330234	0.91	0.388474	0.73	0.337073	1.20	0.520739	0.95	0.79525
HDAC1	0.93	0.868417	1.14	0.307232	0.80	0.595919	1.25	0.423766	0.86	0.476421
E2F6	0.98	0.964822	1.04	0.850897	0.98	0.95372	1.08	0.834633	1.00	0.980775
GMNN	1.01	0.983859	0.77	0.075827	1.04	0.948911	0.78	0.420264	1.04	0.882408
USF1	1.19	0.652289	1.01	0.9356	1.18	0.807159	0.87	0.699954	1.01	0.985944
STAT5A	1.44	0.745261	0.72	0.622383	0.71	0.869697	0.51	0.548587	0.49	0.406925
ATF3	1.39	0.496897	6.55	0.001271	4.69	3.45E-13	4.80	0.001356	3.44	3.16E-05

Table 3-3: Cardiac Myocyte Identity Genes

Gene	**Sparse (Dense) FC**	**p-value**	**XMU (Dense) FC**	**p-value**	**S1P (Dense) FC**	**p-value**	**XMU (Sparse) FC**	**p-value**	**S1P (Sparse) FC**	**p-value**
ACTN2	0.88	0.59668	0.91	0.278626	0.86	0.683813	1.05	0.874083	0.98	0.913769
TNNT2	1.46	0.250773	1.05	0.770643	1.37	0.735052	0.74	0.400782	0.96	0.915476

Figure 3-2: Reducing hiCM Density by Sparse Plating Increases Proliferative Capacity

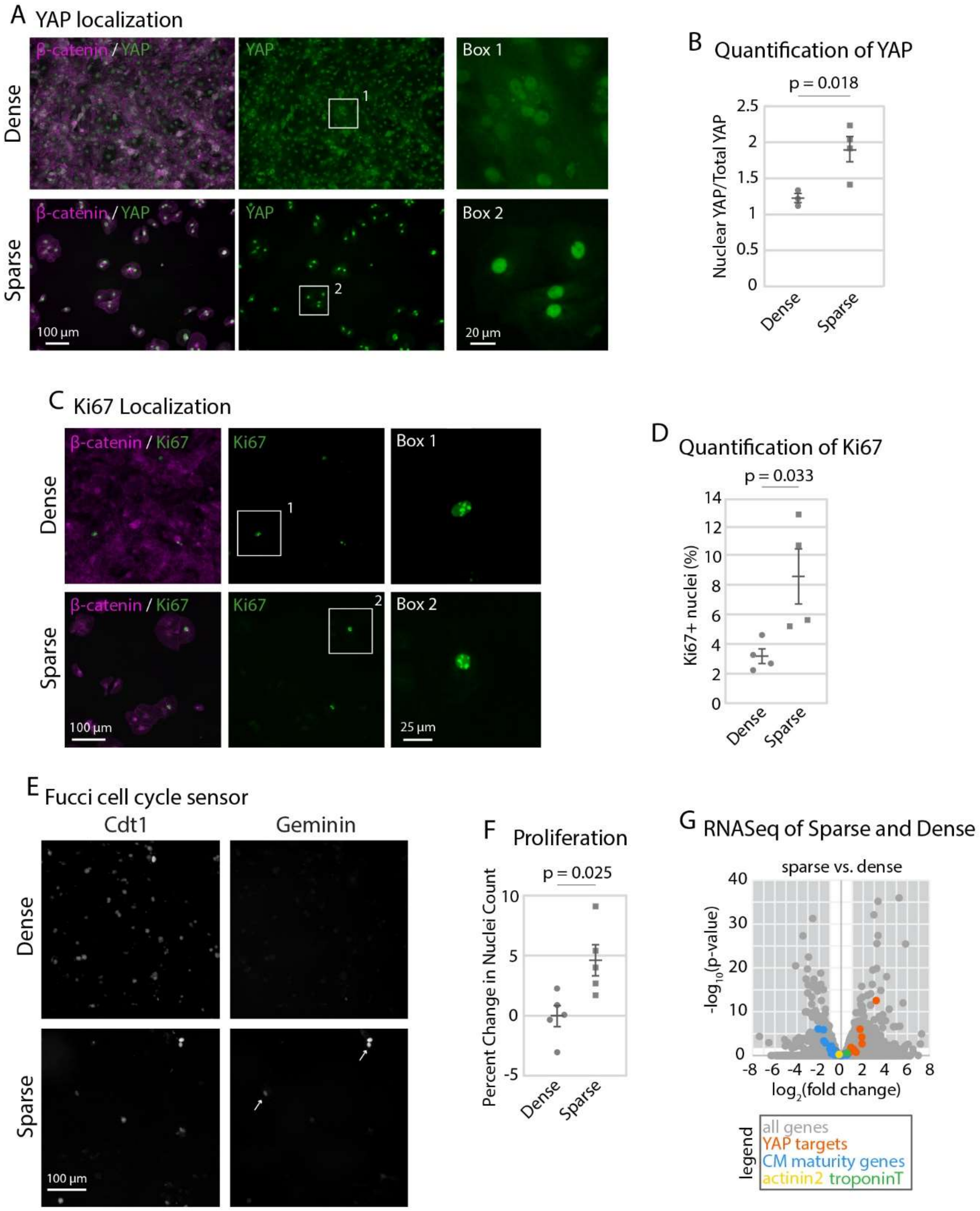

Figure 3-2:

A) YAP and β-catenin in dense and sparse hiCMs using 20X widefield fluorescence microscopy. B) Quantification of nuclear/total YAP ratio. Significance determined by paired two-tailed Student's t test. (N = 23 dense cells and 27 sparse cells from 3 independent experiments) C) Ki67 and β-catenin immunolocalization in dense and sparse hiCMs using 20X widefield fluorescence microscopy. D) Percent of Ki67-positive nuclei in dense (N= 8046 hiCMs from 4 experiments) and sparse (N= 1716 cells from 3 experiments) hiCMs. Significance determined by an unpaired two-tailed Student's t test E) Fucci cell cycle probe transduced into dense or sparse hiCMs. Arrows shows S-M phase. F) Proliferation of dense or sparse hiCMs quantified by counting nuclei fold change over 48 hours (N= 281250 cells from 5 independent experiments). Significance determined by unpaired two-tailed Student's t test. G) RNASeq Volcano plot of genes significantly changed in sparse versus dense hiCMs. (N=300000 hiCMs per treatment from 3 independent experiments). A negative fold change represents a downregulation in sparse hiCMs. A positive fold change represents an upregulation in sparse hiCMs. Gene names of determined YAP target genes (including CTGF and CYR61), cardiac myocyte identity genes (TNNT2 and ACTN2), and cardiac myocyte maturity genes (including GATA4 and FOXOD) can be found in Tables 1-3.

We next wanted to test if the increase in nuclear YAP ratio in sparsely-plated hiCMs was correlated with higher YAP target gene expression. Thus, we curated a list of YAP target genes from the published literature[122-124]. We then compared the expression of these genes between densely-plated and sparsely-plated hiCMs. 32% of YAP target genes had upregulated expression in sparsely-plated hiCMs compared to dense, while 68% did not change, and 0% had decreased expression. In conclusion, plating hiCMs sparsely increases YAP nuclear localization, YAP target gene expression, and ultimately, hiCM proliferation compared to densely-plated hiCMs.

Pharmacological Perturbation of the Hippo Pathway Affects Cardiac Myocyte Proliferation

A loss of contact inhibition not only increased hiCM proliferation but also the nuclear YAP/total YAP ratio, consistent with the hypothesis that the Hippo pathway is involved in density-dependent hiCM proliferation. We next asked if small molecule inhibition of the Hippo pathway would further increase the proliferative potential of hiCMs plated at a low density. We turned to an MST1/2 inhibitor, XMU-MP-1, and a bioactive lipid that activates YAP, sphingosine-1-phosphate (S1P)[85,125,126] (Figure 3-3A). Both of these compounds have been shown to upregulate YAP target genes in human embryonic stem cells, mouse liver cells and human hepatoma cells[122,125]. Furthermore, S1P increases Ki67 in densely plated hiCMs but not cell count when combined with lysophosphatidic acid[85].

We used RNASeq analysis to test if XMU-MP-1 or S1P upregulate YAP/TAZ target genes in hiCMs, and found that YAP/TAZ target genes were indeed significantly upregulated beyond that of sparse-plating alone (Figure 3-3B, Table 1. This increase in YAP target gene expression suggests that the compound-treated hiCMs are less mature than untreated sparsely-plated hiCMs. We found that S1P treatment did not lower the expression of maturity genes compared to untreated hiCMs, whereas 4.2% of maturity genes were expressed lower after XMU-MP-1 treatment (Figure 3-3C, Table 2). We then confirmed that the hiCMs were still expressing CM specific markers (Figure 3-3B, Table 1). Taken together, our data indicates that XMU-MP-1 or

S1P treatment causes an upregulation of YAP/TAZ target genes with minor effects on maturity of hiCMs.

Despite an upregulation in YAP/TAZ target genes, we found that neither XMU-MP-1 nor S1P alone increased proliferation by hiCM count (Figure 3-3D). The result that XMU-MP-1 or S1P failed to induce proliferation was not surprising, as previous studies have postulated that combinations of multiple genetic or pharmacological factors are required to induce cardiac myocyte proliferation both *in vitro* and *in vivo*[82,94]. Therefore, we performed a combinatorial screen to determine if combining XMU-MP-1 and S1P induced proliferation of hiCMs. We started by testing which combination of concentrations was most effective to induce hiCMs to reenter the cell cycle using BrdU incorporation (Figure 3-4A). We found that adding 0.1 μM of each compound to hiCMs significantly increased the percent of BrdU-positive hiCMs when sparsely-plated (Figure 3-4B). We then found that this combination significantly increased hiCM-proliferation by counting nuclei over time (Figure 3-4C). We found that using 0.1 μM of both XMU-MP-1 and S1P also decreased phospho-YAP, which indicated a reduction in the inactivation of YAP (Figure 3-4D-F).

Figure 3-3: Individual Pharmacological Perturbation of the Hippo Pathway Increases YAP Target Genes but Does Not Affect Proliferation

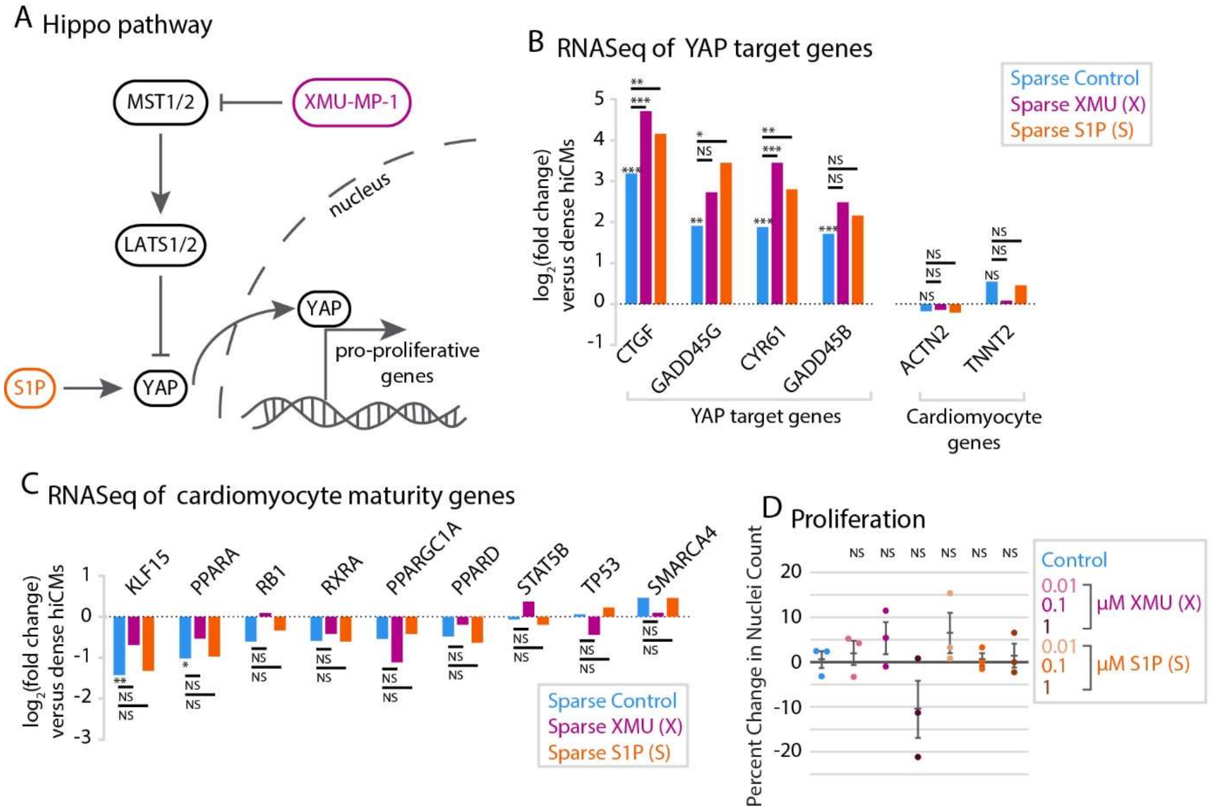

Figure 3-3:

A) Schematic of the Hippo pathway. B) RNASeq data of YAP target genes in sparse cells with treatment of 1 μM XMU-MP-1 or 1 μM S1P. A negative fold change represents a downregulation in treated cells, whereas a positive fold change represents an upregulation in treated cells. N=300000 cells per treatment, over 3 independent experiments and RNA preparations. Right: cardiac myocyte-specific genes do not change upon small molecule treatment. *: $p < 0.05$, **: $p < 0.01$, ***, $p < 0.001$. All p-values and gene names are available in Tables 1-3. Differentially expressed genes were determined using the criteria of fold change >= 2 and FDR <= 0.05. C) RNASeq data of CM-maturity genes as in B. D) Quantification of proliferation of control, XMU-MP-1-, and S1P-treated cells by measuring the percent change in nuclei over 48 hours post-treatment. Significance determined by one-way ANOVA with a Dunnett's post-hoc test corrected for multiple testing.

Figure 3-4: Combination of XMU-MP-1 and S1P Increases Cardiac Myocyte Proliferation

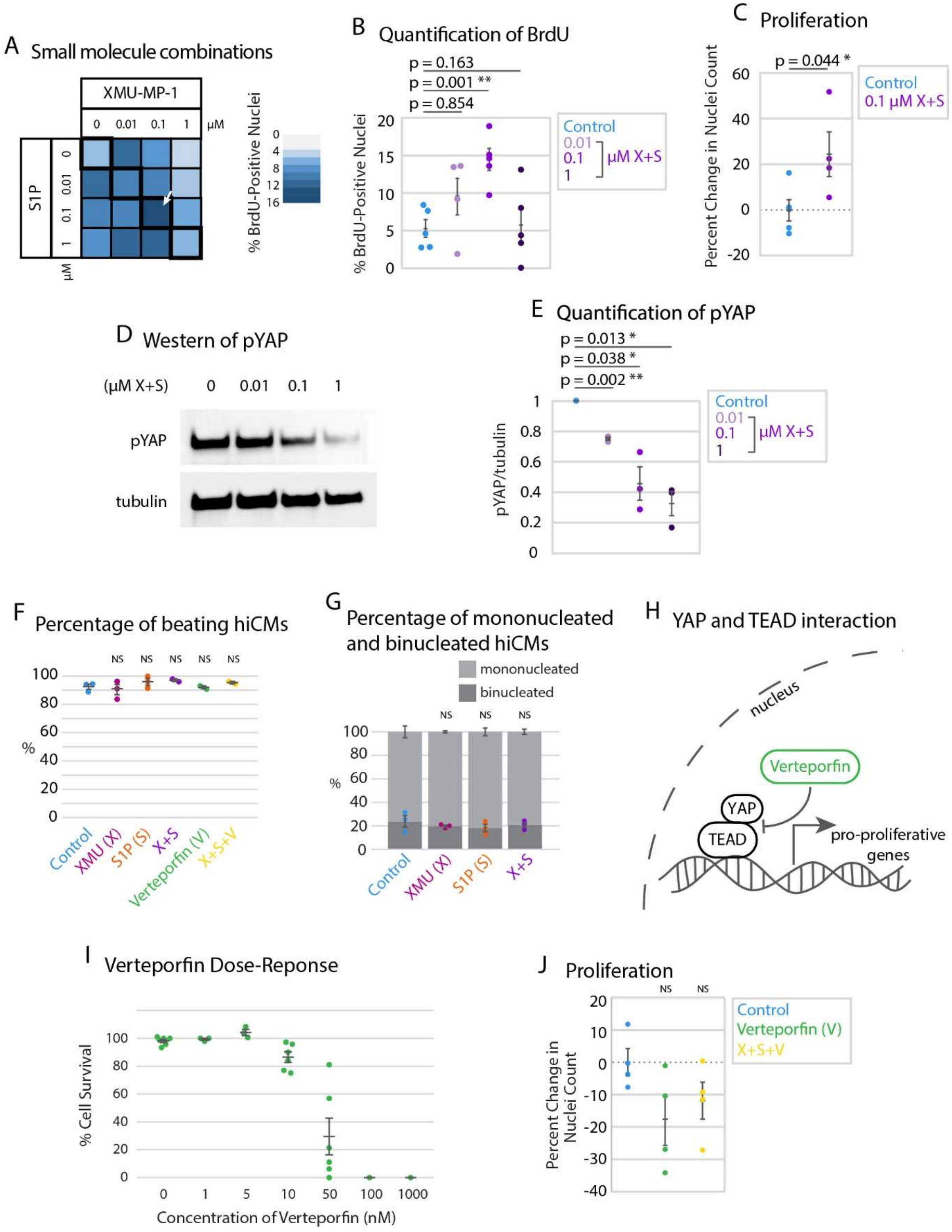

Figure 3-4:

A) Heat map showing percentage of BrdU-positive nuclei in a preliminary screen of combinatorial treatment of hiCMs with XMU-MP-1 and S1P. N = 8393 cells from 5 independent experiments. B) BrdU+ datapoints from black outlined diagonal center boxes from heat map. N = 2229 cells from 5 independent experiments. C) Proliferation of control hiCMs or 0.1 µM XMU-MP-1 and 0.1 µM S1P-treated cells measured by counting nuclei over 48 hours. N = 17318 DMSO-treated cells and 16234 XS-treated cells from 4 independent experiments. Significance determined by two-tailed paired Student's t-test. D) Western blot of hiCMs treated with various concentrations of both XMU-MP-1 and S1P. pYAP: phosphorylated YAP (See Figure S1C-D for the entire blot). E) pYAP amount in hiCMs measured by western blot normalized to tubulin (N= 3 independent experiments). F) The compounds XMU-MP-1, S1P, and Verteporfin do not affect the percentage of beating hiCMs at the doses given (1 µM for XMU-MP-1 and S1P, 0.1 µM for XMU-MP-1 and S1P combined, and 10 nM Verteporfin. In last row, 0.1 µM of XMU-MP-1 and S1P were combined with 10 nM Verteporfin). G) The compounds XMU-MP-1 and S1P do not affect the percentage of binucleated and mononucleated hiCMs at the same doses as Figure 4F. H) Schematic of YAP's downstream transcriptional regulation and interaction with TEAD. I) Verteporfin dose response to detect which concentration of Verteporfin inhibited hiCM proliferation, but did not lead to massive cell death. J) Proliferation of control hiCMs compared to 0.01 µM Verteporfin, or 0.01 µM Verteporfin, 0.1 µM S1P, and 0.1 µM XMU-MP-1-treated hiCMs. N = 1257 cells from 4 independent experiments. K) Proliferation of control hiCMs compared to 0.01 µM Verteporfin, or 0.01 µM Verteporfin and 0.1 µM S1P, and 0.1 µM XMU-MP-1-treated hiCMs. Significance determined by one-way ANOVA with a Dunnett's post-hoc test correcting for multiple testing for panels B, E, F, G, and J.

It is important to confirm that these proliferative hiCMs are functionally beating upon treatment of XMU-MP-1 and S1P. Therefore, we measured the percentage of beating hiCMs upon sparse plating and treatment of XMU-MP-1, S1P, or both, and found no significant difference (Figure 3-4G). Further, it is important to consider that both cytokinetic cell division and binucleation are potential outcomes of increasing overall proliferation of cells. We measured the percentage of binucleated hiCMs upon sparse plating and treatment of XMU-MP-1, S1P, or both, and found no significant difference (Figure 3-4H). In this case, it is presumed that proliferation appears to be induced overall, but the balance between the potential outcomes of cell division and binucleation are not changed, and both outcomes are occurring. These results agree with past research inducing hiCMs to divide, showing both binucleation and cell division as outcomes[115].

Finally, to further confirm that XMU-MP-1 and S1P were acting through the Hippo pathway, we turned to Verteporfin, which inhibits the interaction of YAP with transcription factor TEAD[127] (Figure 3-4I). For this experiment we chose 0.01 μM of Verteporfin, which is the highest concentration that did not result in the death of hiCMs (Figure 3-4J). We found that Verteporfin masked the effect of the combination of XMU-MP-1 and S1P combination on proliferation (Figure 3-4K) without affecting the percentage of beating hiCMs (Figure 3-4G). This result further suggests that the increase in proliferation of hiCMs with XMU-MP-1 combined with S1P is through the Hippo pathway.

Discussion

Taken together, we show that the density at which hiCMs are plated affects proliferative capacity, and that this proliferative capacity is regulated at least in part by the Hippo pathway. Further, we modulate the proliferative capacity by scratching a monolayer of cells to induce cells at the scratch periphery to divide, and induce division of sparsely-plated hiCMs by dual inhibition of the Hippo pathway. These experiments were completed using hiCMs, a model system of developmentally immature cells that both divide and binucleate, providing an ideal model for studying cardiac myocyte division. This is an alternative approach to using isolated primary cardiac myocytes from adult rats or mice, which are unsuitable to the experiments we use here. While primary cardiac myocytes are powerful tools, creating dense monolayer is technically challenging. In addition, primary cardiac myocytes only last a few days in culture and are more representative of modeling cell death[69]. Therefore, it is difficult to do contact inhibition studies and proliferative studies in these cell types. As we show here, hiCMs are well suited for these types of studies[115].

It is not surprising that XMU-MP-1 itself did not increase CM proliferation, as a recent study found that XMU-MP-1 in an intact heart did not increase Ki67 staining[128]. Based on Ki67 staining, recent data has also suggested that inhibiting the Hippo pathway with a single compound in combination with perturbation of another cell cycle pathway (i.e., the Wnt pathway) could be an effective approach to increasing CM proliferation[94]. Here, we show that it is possible to have a combinatorial effect on CM proliferation by only targeting the Hippo pathway. Modulation of the Hippo pathway at two different levels was required to get a proliferative response. This could be part of a new direction for combinatorial therapy, where multiple pathways are each modulated at multiple levels.

There are several other pathways that drive CM proliferation. A recent study suggests the neuregulin receptor, ERBB2, activates YAP in an ERK-dependent manner[129]. The role of ERK signaling in cardiac myocyte proliferation and its crosstalk with the Hippo pathway would constitute an interesting future study. Furthermore, the signaling role that cell-cell adhesions and junctions themselves play in the cardiac regenerative response seems to merge on these pathways. Regenerating cardiac myocytes undergo junction dissolution, and it has been shown that displaced alpha-catenin activates YAP in epidermal cells[110]. Finally, increasing YAP and TAZ activity is likely to have benefits in the heart other than increasing cardiac myocyte proliferation. For example, YAP and TAZ in the epicardium was shown to induce recruitment of T-regulatory cells to the infarcted myocardium. Thus, YAP and TAZ may have the ability to regulate the adaptive immune response and decreasing post-infarct inflammation and myocardial fibrosis[130].

Finally, our work also has implications in the context of a myocardial infarction. In the developed heart, a myocardial infarction results in massive CM death and the remaining CMs do not proliferate[12]. After a myocardial infarct, there is a reduction in cell density at the infarct zone with an increase in cell cycling shown by Ki67 fluorescence[131]. However, it has been shown that the proliferative cells in the infarct region appear to mostly undergo polyploidization and endomitosis, indicating that there is a reduction in contact inhibition but there is also still a barrier to true cytokinetic proliferation in this region. Interestingly, YAP is primarily nuclear in the border zone 21 days post-cardiac apex resection, but only in *Salv* CKO animals[132]. If an ideal treatment for a cardiac infarction existed, it would only induce proliferation at the infarct site where cell-cell contact is reduced. Global induction of proliferation could induce undesired side effects (e.g. tumor formation). As such, targeting pathways which respond preferentially when contact inhibition is lost could be a useful therapeutic direction. Here, we show that targeting the Hippo pathway can increase proliferation in the context of a loss of contact inhibition.

Supplemental Figure

Figure 3-S1: Supplemental Data and Controls

A
Colocalization of BrdU and Ki67 in control hiCMs

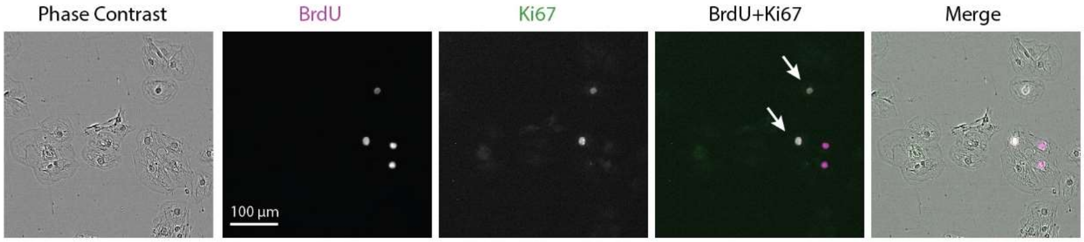

B Actinin2 localization in hiCMs near the edge of a scratch

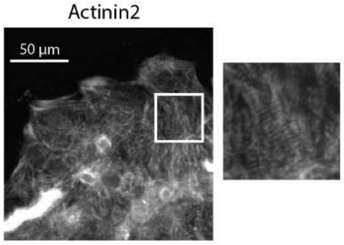

C Actinin2-positive hiCM undergoing cell division

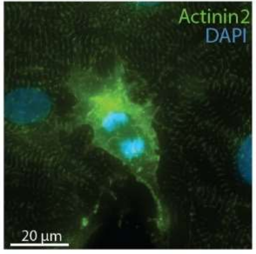

D Actinin2-positive, Ki67-positive hiCM

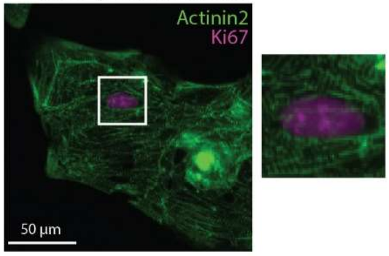

E
Uncropped Western from Fig. 4D, top (pYAP)

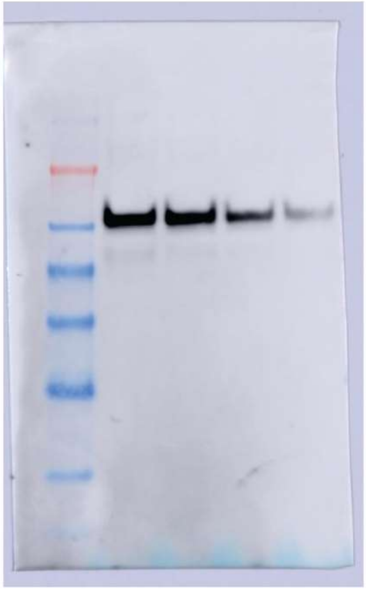

F
Uncropped Western from Fig. 4D, bottom (tubulin)

Figure 3-S1:

A) Colocalization of BrdU and Ki67 in control, sparsely-plated hiCMs. Phase contrast data shows that Ki67 and BrdU localize to nuclei in cardiac myocytes. B) Actinin2 localization in cardiac myocytes at the edge of a scratch, showing that cells at the edge of the scratch have sarcomeres. C) Actinin2 localization in a dividing cardiac myocyte, showing that dividing cells are actinin2-positive. D) Actinin2 and Ki67 localization in control cardiac myocytes, showing that Ki67-positive cells are actinin2-positive. E-F) Uncropped western blots from Figure 4. The ladder on the left of the blot is the SeeBlue Plus 2 standard from Invitrogen (Cat # LC5925).

Materials & Methods

Cardiac Myocyte Culture and Chemicals

iPSC-derived human cardiac myocytes (hiCMs, Cellular Dynamics, Madison, WI) were seeded as per manufacturer's instructions in cardiac myocyte plating medium (M1001, Cellular Dynamics, Madison, WI) in polystyrene 96-well cell culture plates coated in 0.1% sterile gelatin (ES-006-B, Sigma Aldrich, St. Louis, MO). Approximately 50,000 cells were seeded for dense plating and 6,250 cells for sparse plating (1:8), and were subsequently cultured in cardiac myocyte maintenance medium (M1003, Cellular Dynamics, Madison, WI). These cells are verified by Cellular Dynamics (Madison, WI), and each vial of cells is tested at the company for purity by cTNT+ cells using flow cytometry (over 99% pure), identity using SNP genotyping, mycoplasma testing by PCR, sterility testing by 21 CFR 610.12, MEA functionality testing by field potential duration and beating rate, and viability by trypan blue exclusion. We further characterized these cells in Neininger et al., 2019, in which we determined that fewer than 1 in 50,000 cells were actinin2-negative.

Cells were kept at 37°C and 5% CO_2. For re-plating experiments, hiCMs were washed 2x with 100uL 1x PBS with no Ca2+/Mg2+ (PBS*, 70011-044, Gibco, Grand Island, NY). PBS* was completely removed from hiCMs and 40uL 0.1% Trypsin-EDTA with no phenol red (15400-054, Gibco, Grand Island, NY) was added to hiCMs and placed at 37°C for 2 minutes. Following incubation, culture dish was washed 3x with trypsin inside well, rotated 180 degrees, and washed another 3x. Trypsinization was then quenched by adding 120 µL of culture media and total cell mixture was placed into a 1.5mL Eppendorf tube. Cells were spun at 1000gs for 3 minutes, and supernatant was aspirated. Cells were then re-suspended in 200uL of culture media and plated into 2 wells, 100 µL each, on a standard polystyrene 96-well cell culture plate (3599, Corning, Corning, NY) previously coated with 10 ug/mL Fibronectin (#354008, Corning, Mannassas, VA) for 1 hour at 37°C.

XMU-MP-1 (S8334, Selleck Chemicals, Houston, TX) and Verteporfin (SML0534, Sigma Aldrich, St. Louis, MO) were reconstituted to 10 mM in DMSO. S1P (B6707, Apex Bio, Houston, TX) was reconstituted to 10 mM in methanol. When adding drugs to the cells, they were first diluted 1:10 in DMSO then to the appropriate concentration in cardiac myocyte maintenance medium. NucLight Rapid Red Reagent (4717, Essen BioScience, Ann Arbor, MI) was used at a 1:4000 dilution in cell culture media.

Fixation and Immunostaining

Cells were fixed with 4% paraformaldehyde (PFA, 15710, Electron Microscopy Sciences, Hatfield, PA) diluted form 16% in PBS at room temperature for 20 min, then extracted for 5 min with 1% Triton X-100 (BP151100, Fischer Scientific, Suwanee, GA) and 4% PFA in PBS. Cells were washed three times in 1× PBS. After fixation, the following labeling procedures were used: for immunofluorescence experiments, cells were blocked in 10% bovine serum albumin (BSA) in PBS for 20 minutes. Primary antibodies were diluted in 10% BSA. All primary antibodies were used at 1:200 for 1 hour and 45 minutes at room temperature. Secondary antibodies were diluted in 10% BSA at 1:100 and centrifuged at 13,000 rpm for 2 min before use at room temperature for 1 hour.

Mouse anti-β-catenin was purchased from BD Biosciences (610153). Rabbit anti-Ki67 (9129S) and Rabbit anti-YAP (14074T) were purchased from Cellular Signaling Technologies (Danvers, MA). Mouse anti-actinin-2 (a7811) was purchased from Sigma Aldrich (St. Louis, MO). Rabbit anti-phosphoYAP (13008S) was purchased from Cellular Signaling Technologies (Danvers, MA). Mouse anti-BrdU (5292S) was purchased from Cellular Signaling Technologies (Danvers, MA). Alexa Fluor 488-goat anti-mouse (A11029), Alexa Fluor 488-goat anti-rabbit (A11034), Alexa Fluor 568-goat anti-rabbit (A11011), and Alexa Fluor 568-goat anti-mouse (A11004) antibodies were purchased from Life Technologies (Grand Island, NY).

BrdU (ab142567, abcam, Cambridge, UK) was reconstituted to 10 mM in water, then to 10 µM in cardiac myocyte maintenance medium and filtered through a 0.22 µm syringe filter. Cells were incubated with each compound and BrdU for 24 hours, then fixed and permeabilized as above. Then, to hydrolyze DNA, cells were incubated with 1 M HCl for an hour at room temperature, then neutralized with 0.1 M sodium borate (pH 8.5) for 20 minutes at room temperature. Next, cells were washed with PBS and immunostaining continued as usual.

Scratch Assay

Scratches in 10 mm dishes were done by hand with a 10 µL pipette tip. Scratches in 96-well cell culture polystyrene plates were done using a 200 µL pipette tip and a custom plate lid produced by A.C.N. with a slot designed to guide the pipette tip straight across the well. Media was replaced with media containing NucLight Rapid Red Reagent immediately after scratching and every two days afterward until fixation at specified time points.

Western Blotting

Cell lysates were prepared by lysing 50,000 cardiac myocytes with CellLytic (Sigma, St. Louis, MO, #C2978) with 1% protease inhibitor cocktail (P8340, Sigma Aldrich, St. Louis, MO). Gel samples were prepared by mixing cell lysates with LDS sample buffer (Life Technologies, #NP0007) and Sample Reducing Buffer (Life Technologies, #NP00009) and boiled at 95°C for 5 minutes. Samples were resolved on Bolt 4-12% gradient Bis-Tris gels (Life Technologies, #NW04120BOX). Protein bands were blotted onto a nylon membrane (Perkin Elmer, Boston MA, NBA085C001EA) with western blotting filter paper (ThermoFisher Scientific, Rockford, IL, #84783). Blots were blocked using 5% nonfat dairy milk (Research Products International Corp, Mt. Prospect, IL, #M17200) in TBST (TBS: Corning, Mannassas, VA, #46-012-CM. Tween20: Sigma, St. Louis, MO, #P9416). Antibody incubations were also performed in 5% NFDM in TBST. Blots were developed using the Immobilon Chemiluminescence Kit (Millipore, #WBKLS0500).

Statistics and Quantification

Total YAP was measured in FIJI (ImageJ, NIH, Bethesda, MD) by drawing a polygonal ROI around a cell using a 20x IncuCyte image stained for B-catenin to mark cell boundaries, and measuring average fluorescence intensity. Nuclear YAP was measured in FIJI by drawing a Bezier ROI around a nucleus using a 20x IncuCyte image stained for YAP and measuring average fluorescence intensity. Fit of nuclear YAP / total YAP graph in Figure 3-1D was determined using the curve fitting toolbox in MatLab (MathWorks, Natick, MA).

Nuclear fold change was determined by thresholding live-cell whole-well 4x stitches with NucLight Rapid Red Reagent, a live-cell nuclear marker. Thresholding was done using the IncuCyte software (Essen Biosciences, Ann Arbor, MI) and a TopHat Background subtraction using a 20 µM rolling ball. Images were acquired and nuclei counted every hour for specified time points. Nuclei count at the final time point was divided by nuclei count at the first time point and normalized to the average nuclear fold change of cells in control conditions on the same plate.
Statistical significance of Figures 2D and 2F were determined by unpaired two-tailed Student's t-tests performed in Excel. Statistical significance of Figures 2B and 4C were determined by paired two-tailed Student's t-tests performed in Excel. Statistical significance of Figures 3D, 4B, E, F, G, and J were determined by one-way ANOVA with a Dunnett's post-hoc test correcting for multiple testing when applicable performed in GraphPad Prism. Each experiment was performed a minimum of 3 times and the mean of the independent experiments and standard error of the mean (SEM) are displayed.

RNA Sequencing

Cell pellets of 100,000 cells were prepared and RNA was extracted using the RNeasy Mini Kit (Qiagen, #74104). Stranded mRNA (polyA-selected) library preparation was completed by the VANTAGE core at Vanderbilt University. Sequencing was done with an Illumina NovaSeq6000 (S4) PE150. Reads were mapped to reference genome using STAR and differential analyses were performed using DESeq2. Differentially expressed genes were determined using the criteria of fold change >=2 and FDR <= 0.05. YAP target genes and cardiac myocyte maturity genes were determined from literature and are listed below. Datasets will be uploaded to a public database. N=3 for each condition, in that each cell treatment and RNA preparation was done three separate times using three separate purchased vials of cells.

CHAPTER 4

EVIDENCE THAT BINUCLEATED CARDIAC MYOCYTES DIVIDE

Introduction

Cardiac myocytes are the beating muscle cells of the heart. After birth, it is believed that mammalian cardiac myocytes exit the cell cycle and no longer divide, and that further growth of the heart is driven primarily by hypertrophy (i.e., increase in individual cell size) instead of an increase in cell number. Lending credence to this notion is the apparent lack of ability of the mammalian heart regenerate following the death of cardiac myocytes, leading to a concerted effort to identify factors which promote endogenous cardiac myocyte division *in vivo*[5].

With regards to the general notion that cardiac myocytes do not divide after birth, the field may be turning a blind eye to an important subset of cardiac myocytes: those that are binucleated. *In vivo*, the majority cardiac myocytes are believed to be binucleated (as opposed to mononucleated) and yet, the idea that binucleated cardiac myocytes are non-proliferative is so well-accepted within the field that some authors make the claim without even providing citations[25] (and such claims clearly manage to pass peer review). However, it should be noted that this consensus opinion is based solely on correlative, qualitative data[4,15], a major caveat when considering how broadly it could impact the field by either or both i) deterring future studies into binucleated myocyte division and ii) influencing aberrant conclusions based on a potentially false assumption. Importantly, a recent article in *Cell* provided a data set that we believe can be used to implicate binucleated cells as a source for cardiac myocyte renewal *in vivo*[82]. Here we provide a mathematical framework to illustrate how a genetic tool known as Mosaic analysis with double markers (MADM) can be used to explore if and how frequently binucleated cardiac myocytes divide.

Mohamed et al. identified four factors that, through simultaneous co-overexpression within the mouse heart, can induce cardiac myocyte division post-myocardial infarction: CDK2, CDK4, Cyclin B, and Cyclin D1, named the ‘4F’ treatment[82]. They also showed similar results can be achieved using the ‘2F2i’ treatment, in which CDK4 and Cyclin D1 are overexpressed, and TGF-B and Wee1 are inhibited using small molecule inhibitors. They used a variety of detection methods to show that these treatments increased cardiac myocyte proliferation. One of the methods they used was Mosaic analysis with double markers (MADM).

MADM was originally developed to track individual cells in a mouse[133] (Figure 1A) and utilizes Cre-mediated intrachromosomal recombination rather than the typical interchromasomal recombination. The N-terminus of GFP and the C-terminus of RFP (or tdTomato, etc.) are on one chromosome separated by an intron containing a loxP site. On the homologous chromosome in the same site, the N-terminus of RFP and the C-terminus of GFP are similarly included, separated by an intron containing the same loxP site. Without recombination, no fluorescent proteins are made. However, if a cell is in G2 and Cre-mediated recombination occurs between loxP sites, one chromosome will now have both halves of GFP, and another will have both halves of RFP (Figure 1A). Once this G2 cell divides, there are two possible ways that the chromosomes can segregate: X-segregation, in which the two recombinant chromatids segregate into different daughter cells, and Z-segregation, in which the two recombinant chromatids segregate together into the same daughter cell. In the case of X-segregation, one cell will contain a functional GFP-encoding sequence, and the other cell will contain a functional RFP-encoding sequence. Because the intron containing the loxP site is excluded during RNA splicing, GFP and RFP protein can be produced in the respective cells and be detected using fluorescence microscopy. In the case of Z-segregation, one cell will express both GFP and RFP and will thus appear yellow, and the other cell will express neither and will be colorless (Figure 1A). If a cell is in G1 and Cre-mediated recombination occurs, this cell will express both GFP and RFP and will also appear yellow (Figure 1B)[133].

Figure 4-1: MADM Overview

A) MADM setup and recombination in G2

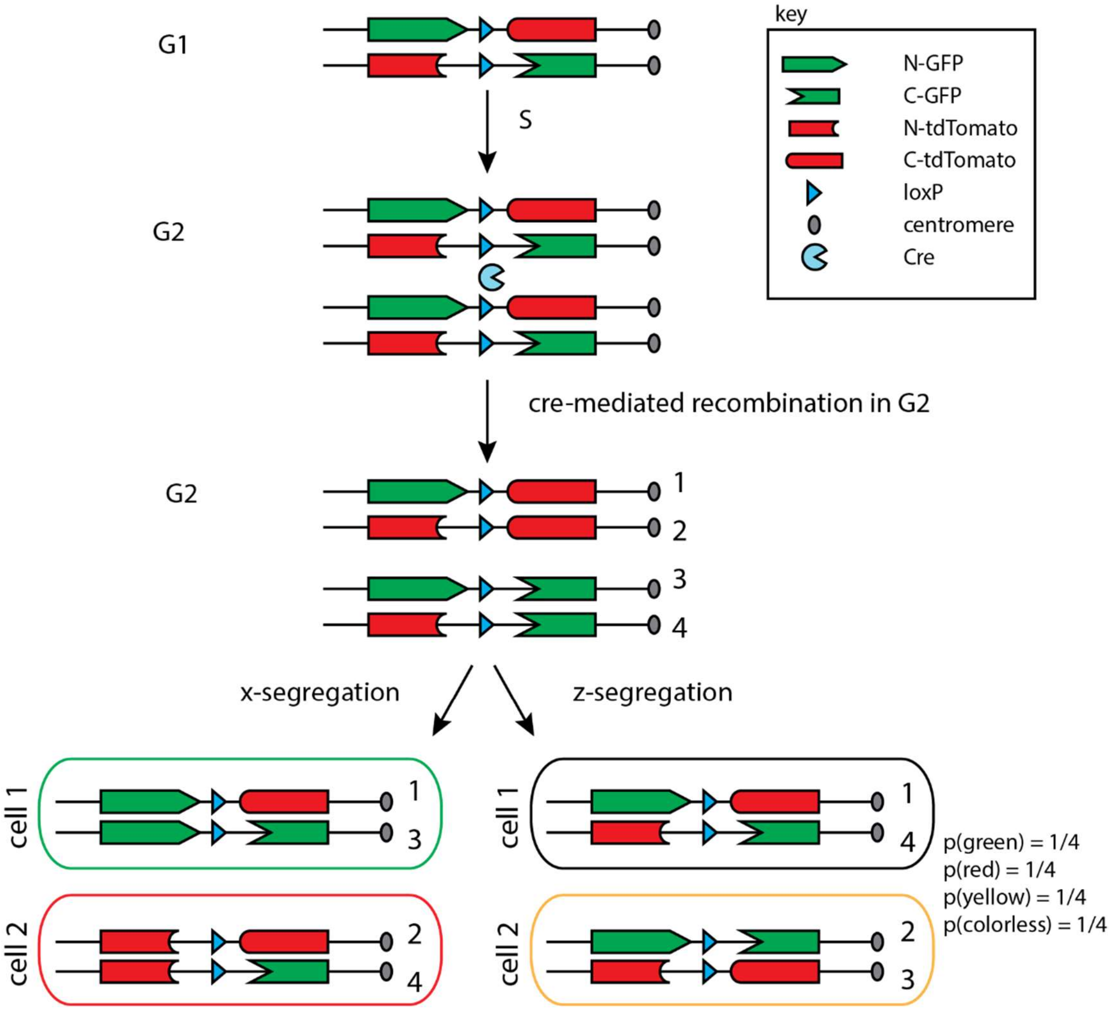

B) Recombination in G1

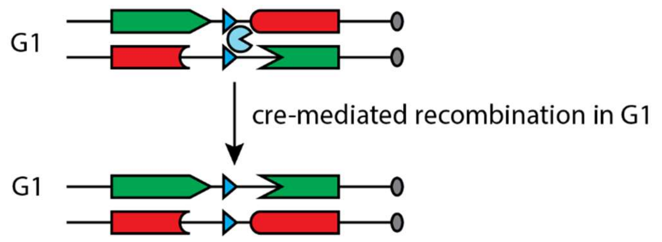

Mohamed et al. creatively used the MADM system as a marker for cytokinesis[82]. Any single-colored cell can be assumed to have undergone cell division at some point in time, as recombined cells that do not undergo cell division remain double-labeled (yellow). In a constitutively-active cTnt-Cre MADM model, control mice post-infarction showed ~14% single-colored cells out of all labeled cells, while mice treated with 4F post-infarction showed almost 50% single-colored cells out of all labeled cells. Interestingly, Mohamed et al. reported in their supplemental data that 7% of single-colored cells were binucleated[82]. Here we show these cells are likely to be the product of the division of binucleated cells and unlikely to be the product of mitosis without cytokinesis, cell fusion or reversible recombination.

Mechanisms for Single-Colored Binucleated Cells to Arise

To determine the origin of these single-colored binucleated cardiac myocytes, one must first consider how a binucleated cell may arise. A universally accepted path is that a mononucleated cell undergoes mitosis without cytokinesis[25]. The main evidence from this literature was a failure to detect cleavage furrows in fixed binucleating cardiac myocytes[32,33]. More recently, live cell microscopy combined with post-fixation immuno-fluorescence has confirmed that little or no cleavage furrow ingression occurs during binucleation. In the case of failed cytokinesis, if a cell is recombined in G2 and undergoes x-segregation without cytokinesis, one nucleus will produce GFP and one will produce RFP, producing a yellow cell. Rather, if a cell undergoes z-segregation, one nucleus will produce both GFP and RFP and one will not produce a color, resulting in a yellow cell. Therefore, a mononucleated cell that undergoes Cre-mediated recombination in G2 and becomes binucleated will always be yellow. If a cell is recombined in G1 and undergoes sequential DNA synthesis and mitosis without cytokinesis, it will similarly produce a yellow binucleated cell.

Another option to consider is that two mononucleated cells fuse to produce a binucleated cell (Figure 2B). The amount of cardiac myocyte fusion that does or does not occur is contentious[134]. If binucleated cells indeed do not divide, then this would be the main option for single-colored binucleated cells to arise, that is, for two single-colored mononucleated cells of the same color to be near enough to each other and fuse to produce a binucleated cell. However, this seems unlikely, given that the labeling frequency of cardiac myocytes using this system is ~2-5%, and that a fusion event of this exact type would happen to approximately 12.3% of single-colored cardiac myocytes, not including any fusion events of different colored cardiac myocytes to produce a yellow binucleated cell. Another option is that a single-colored mononucleated cell could fuse with a colorless cell, producing a single-colored binucleated cell. Of the options presented thus far, this appears to be the most likely. However, the likelihood of cardiac myocyte fusion in a mouse heart is low to none, and the percentage of mononucleated cells in these mouse strains average at around 5.5% (Table 4-1), again rendering the probability of such a fusion very low[135].

Table 4-1: Percentage of mononucleated cells in mouse strains used to produce MADM mice in Mohamed et al.

Mouse	Strain(s) of origin	% Mononucleated
Igs2tm2$^{\text{(ACTB-tdTomato,-EGFP)}}$Luo/J	(129X1/SvJ x 129S1/Sv)F1-Kitl+	5.59%;unknown
Igs2tm1$^{\text{(ACTB-EGFP,-tdTomato)}}$Luo/J	(129X1/SvJ x 129S1/Sv)F1-Kitl+	5.59%;unknown
Tg$^{\text{(Cag-Cre/Esr1*)}}$5AMC	(C57BL/6 x CBA)F1	5.21%;8.29%
B6.FVB(129)-A1cf$^{\text{Tg(Myh6-Cre/Esr1*)}}$IJMKIJ	FVB/N	4.92%
Tg$^{\text{(Tnnt2-Cre)}}$5Blh	(C57BL/6 x DBA/2)F2	5.21%;7.09%

Figure 4-2: Potential Origins of Single-Colored Binucleated Cells

A) Cardiomyocyte proliferation overview

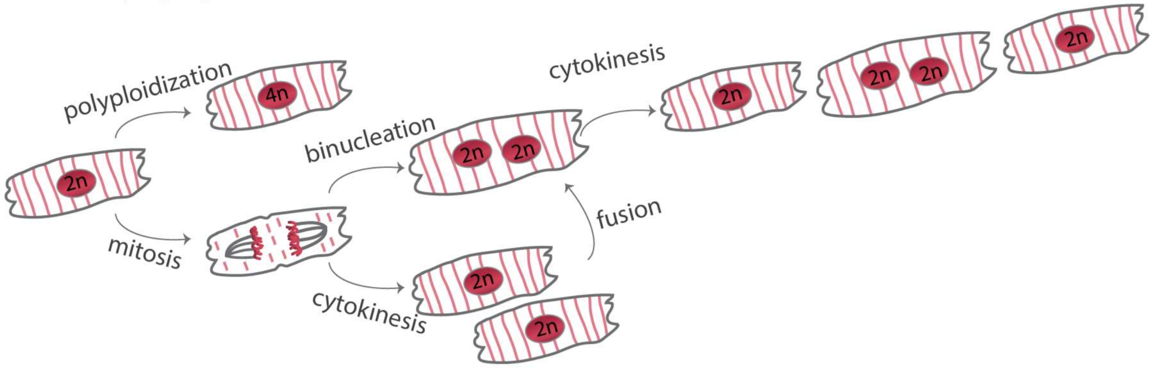

B) Mitosis without cytokinesis

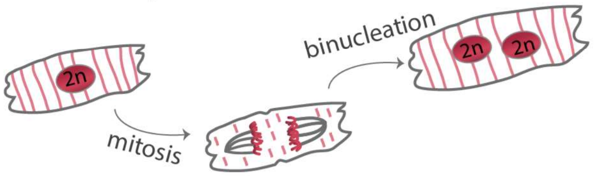

C) Cell fusion

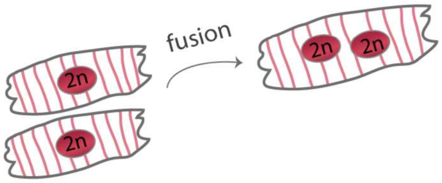

D) Reversible recombination

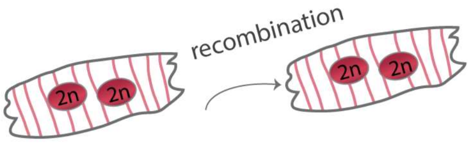

E) Division of binucleated cells

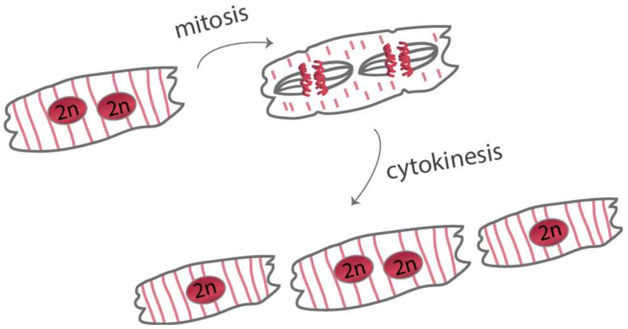

Because Cre-mediated recombination does not eliminate the loxP site in the MADM system, when Cre is constitutively active like in the Tnt-Cre model, it is important to consider the likelihood that a recombined cell recombined again at the same frequency (Figure 2C)[133,136]. For a single-colored, mononucleated cell, reversible recombination will not affect the phenotype. However, a yellow mononucleated cell may become colorless and vice versa. Interestingly, a yellow binucleated cell, perhaps arisen by a mononucleated cell undergoing mitosis without cytokinesis, could become single-colored binucleated cell. This would occur if one nucleus produced only one fluorescent protein, while the other produced both, and the nucleus producing both underwent a second recombination event to become colorless, thus rendering the binucleated cell one color once the second fluorescent protein was degraded. Another point to address is the origin of such a cardiac myocyte that has one single-color producing nucleus and one double-color producing nucleus. If a binucleated cell arises from mitosis without cytokinesis, and one of the nuclei undergoes recombination a second time, the binucleated cell will remain yellow (Figure S1). In order for a binucleated cell to arise that has the capability to undergo another round of recombination in order to produce a single-colored binucleated cell, the cell would have to arise from a cell fusion event (or a binucleated cell division, which we will describe later). One could assume that if the recombination frequency of the Tnt-Cre model is 2-5%, that the frequency of the same loxP sites then undergoing a second round of recombination would also be 2-5%, for a combined probability of 0.04-0.25%. Of this 0.04-0.25% probability, the cell in question would likely have to arise from a fusion event in the first place (Figure S1). This might not fully explain the 7% of single-colored cells that are binucleated.

The last event that could produce a single-colored binucleated cell is binucleated cell division (Figure 2D). While the likelihood of a binucleated cell dividing is not known, it has been purported that binucleated cardiac myocytes divide with two cleavage furrows to form two mononucleated cells and one binucleated cell (Figure 3A)[137]. If a binucleated cell contains two nuclei that are recombined in G2 (Figure 3B), there are 16 outcomes of a cell division of this type

(Figure 3C). These outcomes depend on the segregation type of both nuclei and the left/right direction of the resultant segregation, that is, if the nucleus A chromosomes 1 and 3 segregate from 2 and 4, which chromosomes are included in the mononucleated cell (cell 1, in this scenario) and which chromosomes are included in the 'left' nucleus of the resultant binucleated cell (cell 2, in this scenario) (Figure 3C options I/V and II/V). If this is the case, then out of each of the 16 options, single-colored binucleated cells arise 6/16 times (3 red, 3 green) (Figure 3C options I/VI, I/VII, II/VI, II/VII, IV/V, and IV/VI). Interestingly, in 12/16 of these scenarios, one or two single-colored mononucleated cell(s) also arise (Figure 3D). If so, a proportion of single-colored mononucleated cells do not indeed arise strictly from mononucleated cell division. Binucleated cells could also form one cleavage furrow, forming two binucleated cells, or could undergo cytokinesis alone to produce two mononucleated cells. These outcomes were calculated and considered as well.

"MADM Solver": A Quantification Scheme to Predict Outcomes of MADM Experiments

To determine which of these possible outcomes discussed above are the most likely to happen, I calculated the probability of each outcome given one or two rounds of division during the measuring period, and three different mechanisms for binucleated cell division to occurs (with the fourth mechanism being that it *does not* occur). Each outcome has an equation associated with it (Supplemental Equations), with six variables. "r" denotes the recombination frequency of Cre. "m" denotes the percentage of starting cardiac myocytes that are mononucleated. "n" denotes the total number of starting cells. "d" represents the probability that a cell will undergo mitosis, "c" represents the probability that a mitotic cell will then undergo cytokinesis, and "b" is the probability that a binucleated cell will divide (0 if they do not divide). The software will also allow 1 or 2 rounds of division, selection of any (or all) of the types of proposed binucleated division, and allows for input of the endpoint values calculated in the MADM experiment. As many of these variables are not absolute and difficult to perfectly quantify, the software also will allow for a range of values to be input, and will test each number within the range. The software then solves the equations from the Supplemental equations and outputs which values of each variable are most likely to results in the experimental output. To test the potential origin of binucleated single-cells, I input the values calculated from Mohamed et al., and found that when binucleated cell division was not allowed, even after 1 or 2 rounds of division, the differential equations model could not be solved, showing that there is not a possible way using these calculations for 7% of binucleated cells to be single-colored if binucleated cells are not dividing, even if other possibilities for single-colored binucleated cells to arise exist. Further, binucleated cell division after 1 round does not account for the high percentage of single-colored binucleated cells. I propose that in the 24 hour time-frame of measurement in Mohamed et al., at least 2 rounds of cell division occur, with binucleated cell division accounting for the majority of the single-colored binucleated cells found.

Figure 4-3: Binucleated Cell Division as an Origin for Single-Colored Binucleated Cells

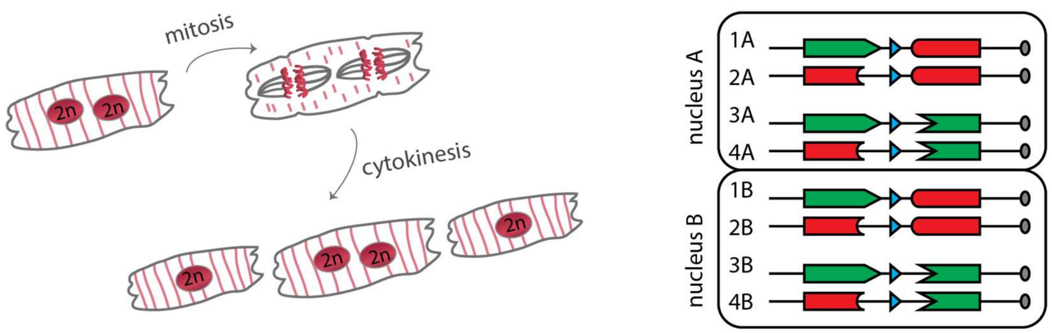

A) Binucleated cardiomyocyte division

B) Binucleated cardiomyocyte in G2, post-recombination

C) Possible outcomes of binucleated cardiomyocyte division

	nucleus A	nucleus B
options	I: x-seg $\begin{smallmatrix}1&2\\3&4\end{smallmatrix}$	V: x-seg $\begin{smallmatrix}1&2\\3&4\end{smallmatrix}$
	II: x-seg $\begin{smallmatrix}2&1\\4&3\end{smallmatrix}$	VI: x-seg $\begin{smallmatrix}2&1\\4&3\end{smallmatrix}$
	III: z-seg $\begin{smallmatrix}1&2\\4&3\end{smallmatrix}$	VII: z-seg $\begin{smallmatrix}1&2\\4&3\end{smallmatrix}$
	IV: z-seg $\begin{smallmatrix}2&1\\3&4\end{smallmatrix}$	VIII: z-seg $\begin{smallmatrix}2&1\\3&4\end{smallmatrix}$

nucleus A	nucleus B	cell 1	cell 2	cell 3
I	V	$\begin{smallmatrix}1\\3\end{smallmatrix}$ G	$\begin{smallmatrix}2&1\\4&3\end{smallmatrix}$ Y	$\begin{smallmatrix}2\\4\end{smallmatrix}$ R
I	VI	$\begin{smallmatrix}1\\3\end{smallmatrix}$ G	$\begin{smallmatrix}2&2\\4&4\end{smallmatrix}$ R	$\begin{smallmatrix}1\\3\end{smallmatrix}$ G
I	VII	$\begin{smallmatrix}1\\3\end{smallmatrix}$ G	$\begin{smallmatrix}2&1\\4&4\end{smallmatrix}$ R	$\begin{smallmatrix}2\\3\end{smallmatrix}$ Y
I	VIII	$\begin{smallmatrix}1\\3\end{smallmatrix}$ G	$\begin{smallmatrix}2&2\\4&3\end{smallmatrix}$ Y	$\begin{smallmatrix}1\\4\end{smallmatrix}$ C
II	V	$\begin{smallmatrix}2\\4\end{smallmatrix}$ R	$\begin{smallmatrix}1&1\\3&3\end{smallmatrix}$ Y	$\begin{smallmatrix}2\\4\end{smallmatrix}$ R
II	VI	$\begin{smallmatrix}2\\4\end{smallmatrix}$ R	$\begin{smallmatrix}1&2\\3&4\end{smallmatrix}$ G	$\begin{smallmatrix}1\\3\end{smallmatrix}$ G
II	VII	$\begin{smallmatrix}2\\4\end{smallmatrix}$ R	$\begin{smallmatrix}1&1\\3&4\end{smallmatrix}$ G	$\begin{smallmatrix}2\\3\end{smallmatrix}$ Y
II	VIII	$\begin{smallmatrix}2\\4\end{smallmatrix}$ R	$\begin{smallmatrix}1&2\\3&3\end{smallmatrix}$ Y	$\begin{smallmatrix}1\\4\end{smallmatrix}$ C
III	V	$\begin{smallmatrix}1\\4\end{smallmatrix}$ C	$\begin{smallmatrix}2&1\\3&3\end{smallmatrix}$ Y	$\begin{smallmatrix}2\\4\end{smallmatrix}$ R
III	VI	$\begin{smallmatrix}1\\4\end{smallmatrix}$ C	$\begin{smallmatrix}2&2\\3&4\end{smallmatrix}$ Y	$\begin{smallmatrix}1\\3\end{smallmatrix}$ G
III	VII	$\begin{smallmatrix}1\\4\end{smallmatrix}$ C	$\begin{smallmatrix}2&1\\3&4\end{smallmatrix}$ Y	$\begin{smallmatrix}2\\3\end{smallmatrix}$ Y
III	VIII	$\begin{smallmatrix}1\\4\end{smallmatrix}$ C	$\begin{smallmatrix}2&2\\3&3\end{smallmatrix}$ Y	$\begin{smallmatrix}1\\4\end{smallmatrix}$ C
IV	V	$\begin{smallmatrix}2\\3\end{smallmatrix}$ Y	$\begin{smallmatrix}1&1\\4&3\end{smallmatrix}$ G	$\begin{smallmatrix}2\\4\end{smallmatrix}$ R
IV	VI	$\begin{smallmatrix}2\\3\end{smallmatrix}$ Y	$\begin{smallmatrix}1&2\\4&4\end{smallmatrix}$ R	$\begin{smallmatrix}1\\3\end{smallmatrix}$ G
IV	VII	$\begin{smallmatrix}2\\3\end{smallmatrix}$ Y	$\begin{smallmatrix}1&1\\4&4\end{smallmatrix}$ C	$\begin{smallmatrix}2\\3\end{smallmatrix}$ Y
IV	VIII	$\begin{smallmatrix}2\\3\end{smallmatrix}$ Y	$\begin{smallmatrix}1&2\\4&3\end{smallmatrix}$ Y	$\begin{smallmatrix}1\\4\end{smallmatrix}$ C

D) Probabilities of outcomes of binucleated cell division

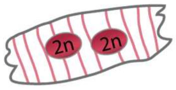

p(green) = 3/16
p(red) = 3/16
p(yellow) = 9/16
p(colorless) = 1/16

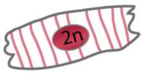

p(green) = 8/32
p(red) = 8/32
p(yellow) = 8/32
p(colorless) = 8/32

Conclusions and Future Directions

In conclusion, results from Mohamed et al. question the paradigm that binucleated cardiac myocytes do not divide. While it cannot be confirmed how exactly binucleated cells divide or under which conditions specifically, these results and our further analysis warrant future research into these questions. Binucleated cardiac myocytes were first purported to lack regenerative capacity in the 1970s and 1980s[25,137]. These original studies showed that the timeframe of binucleation correlated with the timeframe of the loss of proliferative capacity in mice and rats[4]. These studies are widely cited in primary literature and reviews, but until lately, studies have not shown any causative or direct effect of cardiac myocyte binucleation on proliferative capacity.

If binucleated cardiac myocytes have the capacity to divide, we need to know the proportion of binucleated cells *in vivo*. The extent to which cardiac myocytes in mice are binucleated has been largely answered in a recent study, which measured binucleation frequency in 120+ mouse lines[34]. The found that 90-95% of cardiac myocytes are binucleated. This data is supported by several other rodent studies[25,137]. However, the proportion of binucleated cardiac myocytes in humans is still debated. Some studies support the model that 25% of human cardiac myocytes are binucleated at birth and remain at that proportion consistently[19], while other studies report up to 60-100%[138] and that the percentage of binucleated cardiac myocytes increases over a human lifespan[120]. Many other studies report that binucleated cardiac myocytes do not increase over time and that DNA synthesis after birth results in polyploidization[26,129]. However, the field is in agreement that binucleated cardiac myocytes are present in the human heart.

Our calculations question the dogma that binucleated cells lack the capacity to divide. Aurora B localization has shown that 10% of mitotic cardiac myocytes were mononuclear and 90% were binucleated in P15 mouse hearts[139]. While this seems counterintuitive, note that the vast majority of cardiac myocytes in mice are binucleated. Indeed, a total of 34.2% and 30.8% of mononuclear and binucleated cardiac myocytes were undergoing mitosis in isolated p15 control cardiac myocytes[139]. Similarly, isolated control fetal sheep cardiac myocytes had populations of mononuclear cells undergoing mitosis (with or without cytokinesis) as well as binucleated cells undergoing division, but that the majority of Ki-67+ nuclei were in mononucleated cells[140]. Taken together, these results strongly support the hypothesis that mononuclear cardiac myocytes have a higher proliferative capacity than binucleated cardiac myocytes.

If binucleated cells indeed divide, there are multiple mechanisms for how it would occur. Some studies have reported binucleated murine, chick, or sheep cardiac myocytes dividing, producing two cleavage furrows and resulting in two mononucleated cells and one binucleated cell[139,140]. A recent study also reported binucleated cardiac myocytes dividing to produce only two mononucleated cells[120]. These studies were largely in isolated cardiac myocyte cultures. Thus, Mohamed et al. 2018, alongside our calculations, could be among the first evidence that binucleated cardiac myocytes can divide *in vivo*[82].

Several questions remain, including 1) what is the makeup of a human heart/percentage of binucleated or polyploid CMs? 2) is there basal turnover in the human heart, and if so, is it of mononucleated cells dividing, mononucleated cells becoming binucleated, binucleated cells dividing, or a combination of the three? 3) how do binucleated cells divide and what are the resulting cells?

Supplemental Figures

Figure 4-S1: Possible Outcomes of Mitosis, Cell Fusion, or Reversible Recombination

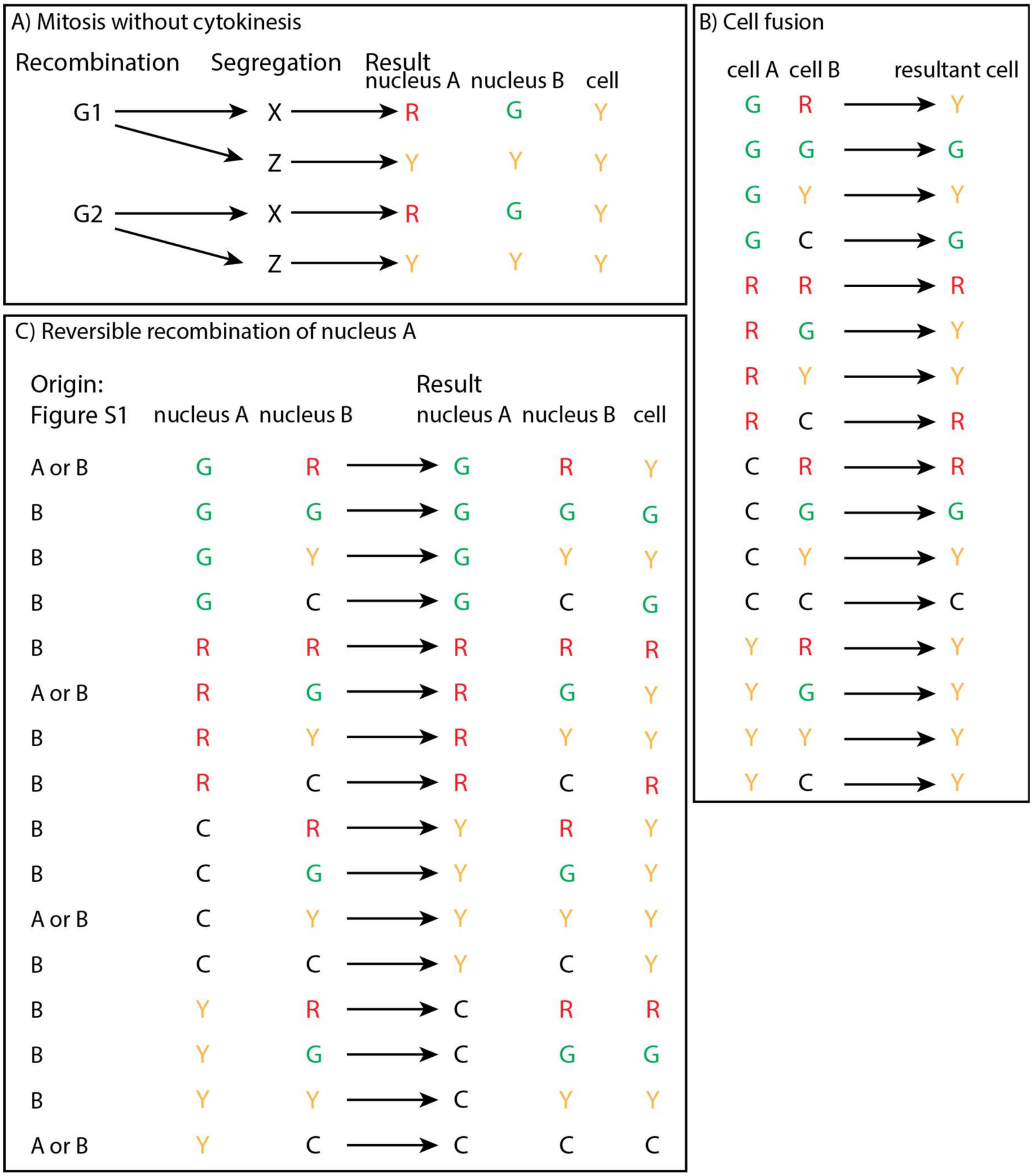

A) Mitosis without cytokinesis

Recombination	Segregation	Result nucleus A	nucleus B	cell
G1	X	R	G	Y
	Z	Y	Y	Y
G2	X	R	G	Y
	Z	Y	Y	Y

B) Cell fusion

cell A	cell B	resultant cell
G	R	Y
G	G	G
G	Y	Y
G	C	G
R	R	R
R	G	Y
R	Y	Y
R	C	R
C	R	R
C	G	G
C	Y	Y
C	C	C
Y	R	Y
Y	G	Y
Y	Y	Y
Y	C	Y

C) Reversible recombination of nucleus A

Origin: Figure S1	nucleus A	nucleus B	Result nucleus A	nucleus B	cell
A or B	G	R	G	R	Y
B	G	G	G	G	G
B	G	Y	G	Y	Y
B	G	C	G	C	G
B	R	R	R	R	R
A or B	R	G	R	G	Y
B	R	Y	R	Y	Y
B	R	C	R	C	R
B	C	R	Y	R	Y
B	C	G	Y	G	Y
A or B	C	Y	Y	Y	Y
B	C	C	Y	C	Y
B	Y	R	C	R	R
B	Y	G	C	G	G
B	Y	Y	C	Y	Y
A or B	Y	C	C	C	C

Figure 4-S2: Possible Outcomes of One Round of Division with No Binucleated Division

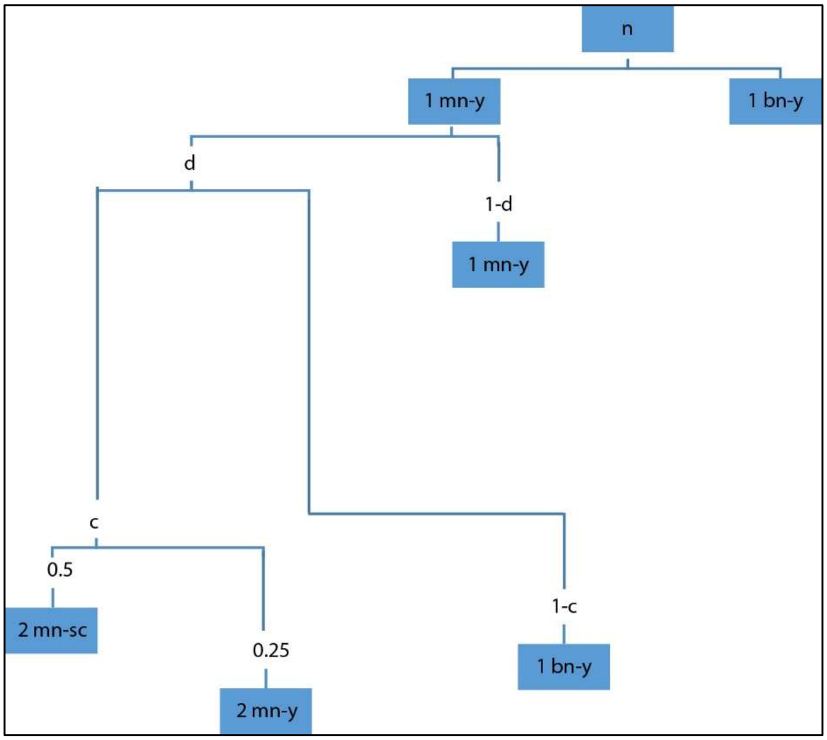

Figure 4-S3: Possible Outcomes of Two Rounds of Division with No Binucleated Division

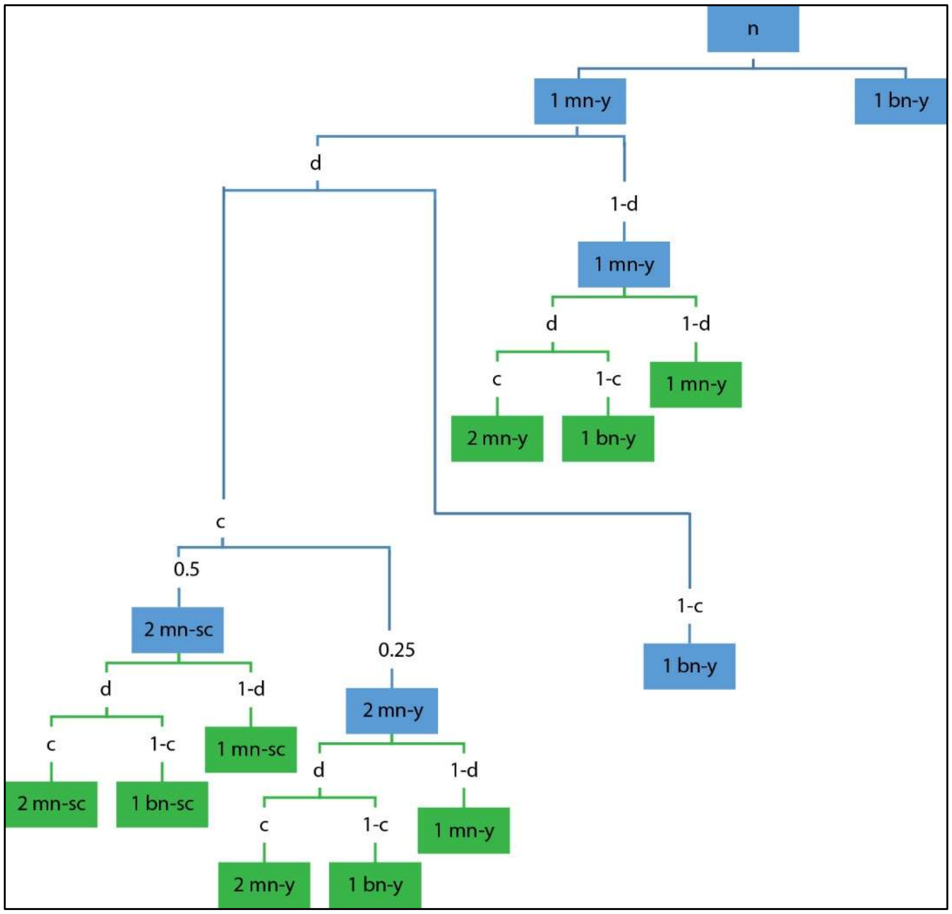

Figure 4-S4: Possible Outcomes of Two Rounds of Division with Binucleated Division

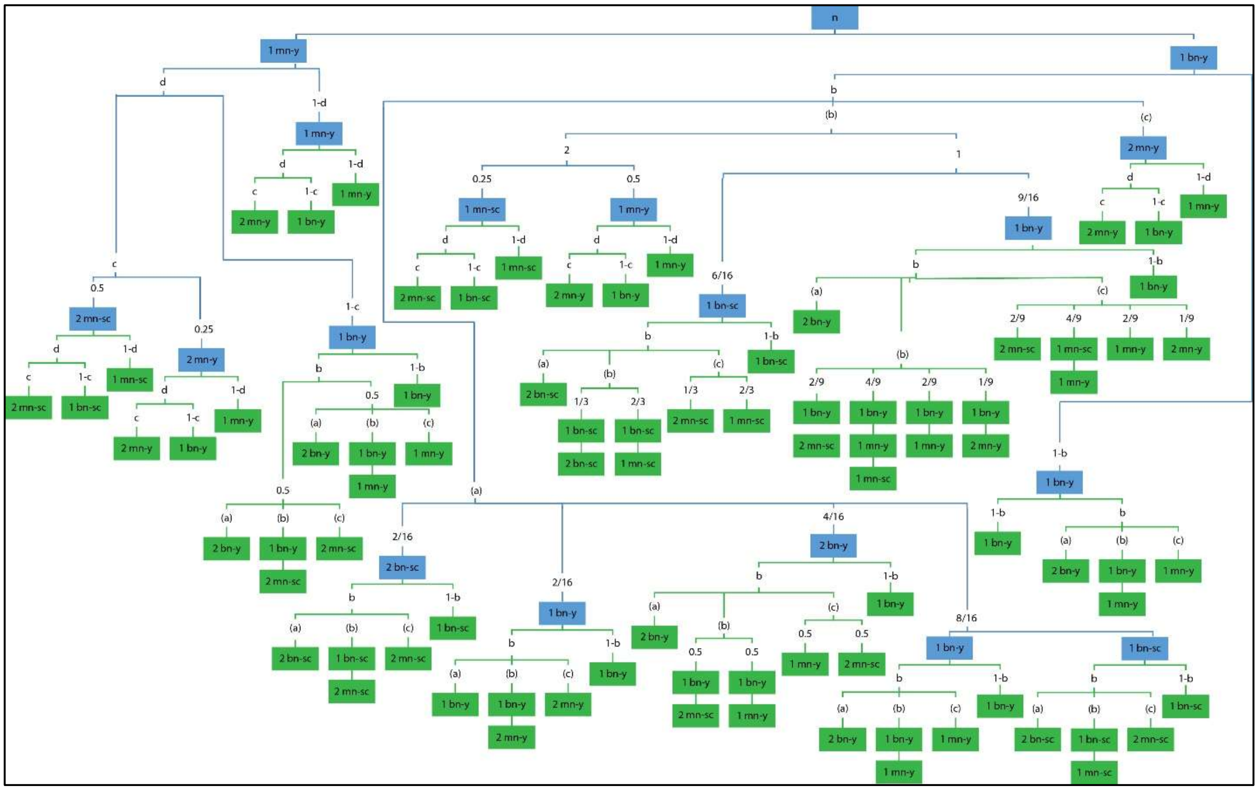

Figure 4-S5: Software GUI

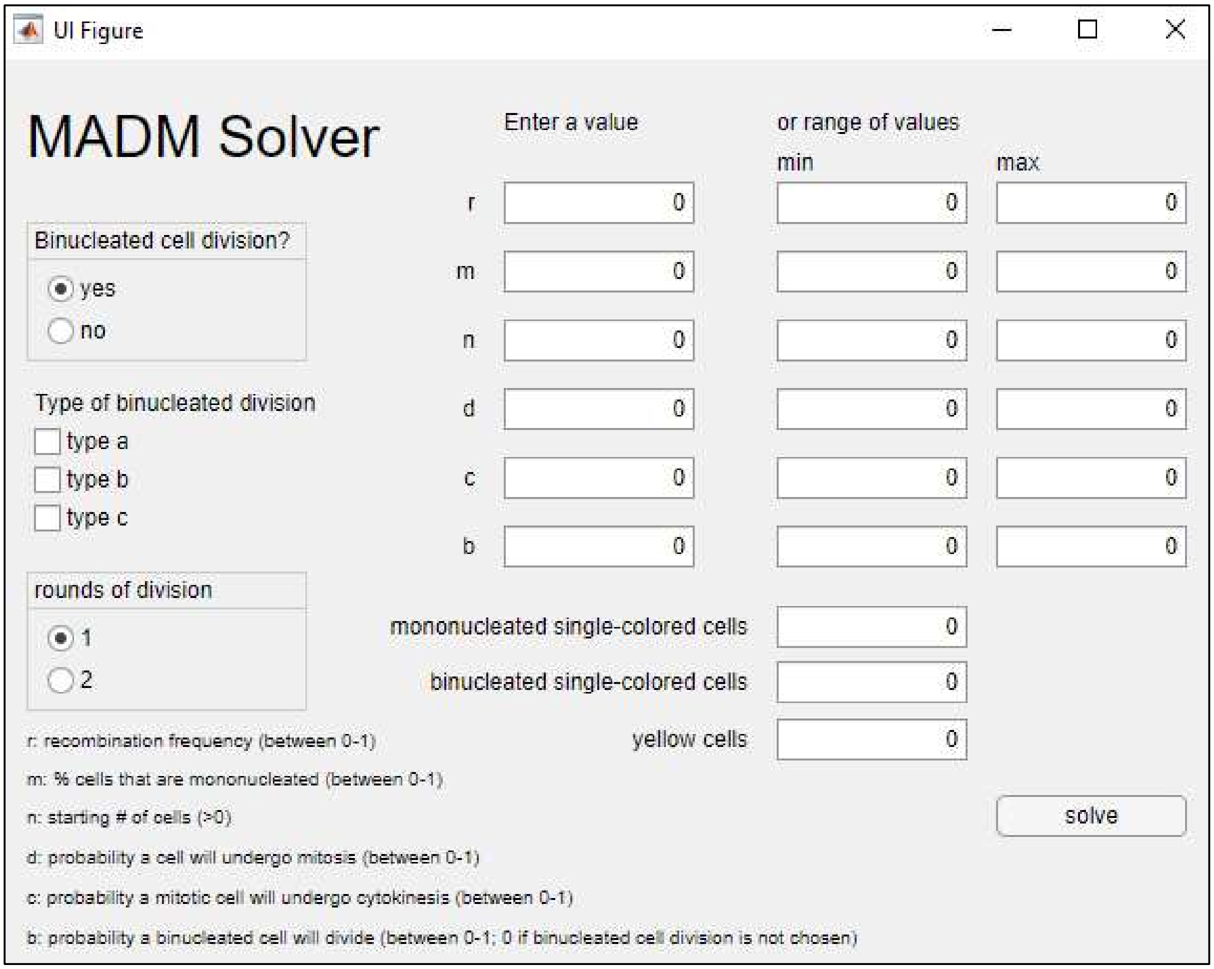

UI Figure

MADM Solver

Binucleated cell division?
● yes
○ no

Type of binucleated division
☐ type a
☐ type b
☐ type c

rounds of division
● 1
○ 2

	Enter a value	or range of values	
		min	max
r	0	0	0
m	0	0	0
n	0	0	0
d	0	0	0
c	0	0	0
b	0	0	0

mononucleated single-colored cells: 0
binucleated single-colored cells: 0
yellow cells: 0

r: recombination frequency (between 0-1)
m: % cells that are mononucleated (between 0-1)
n: starting # of cells (>0)
d: probability a cell will undergo mitosis (between 0-1)
c: probability a mitotic cell will undergo cytokinesis (between 0-1)
b: probability a binucleated cell will divide (between 0-1; 0 if binucleated cell division is not chosen)

Supplemental Equations

```
eq1 = n*m*d*r*c*d*c*2;

eq2 = n*m*d*r*c*d*(1-c);

eq3 = n*m*d*r*c*(1-d);

eq4 = n*m*d*r*c*0.5*d*c*2;

eq5 = n*m*d*r*c*0.5*d*(1-c);

eq6 = n*m*d*r*c*0.5*(1-d);

eq7 = n*m*d*r*(1-c)*b*0.5*bc*2;

eq8 = n*m*d*r*(1-c)*b*0.5*bb;

eq9 = n*m*d*r*(1-c)*b*0.5*bb*2;

eq10 = n*m*d*r*(1-c)*b*0.5*ba*2;

eq11 = n*m*d*r*(1-c)*b*0.5*bc;

eq12 = n*m*d*r*(1-c)*b*0.5*bb;

eq13 = n*m*d*r*(1-c)*b*0.5*bb;

eq14 = n*m*d*r*(1-c)*b*0.5*ba*2;

eq15_a = n*m*d*r*(1-c);

eq15_b = n*m*d*r*(1-c)*(1-b);

eq16 = n*m*(1-d)*r*d*c*2;

eq17 = n*m*(1-d)*r*(1-d);

eq18 = n*m*(1-d)*r*(1-d);

eq19 = n*(1-m)*b*r*bc*2*d*c*2;

eq20 = n*(1-m)*b*r*bc*2*d*(1-c);

eq21 = n*(1-m)*b*r*bc*2*(1-d);

eq22 = n*(1-m)*b*r*bb*2*0.5*d*c*2;

eq23 = n*(1-m)*b*r*bb*2*0.5*d*(1-c);

eq24 = n*(1-m)*b*r*bb*2*0.5*(1-d);

eq25 = n*(1-m)*b*r*bb*2*0.25*d*c*2;

eq26 = n*(1-m)*b*r*bb*2*0.25*d*(1-c);

eq27 = n*(1-m)*b*r*bb*2*0.25*(1-d);

eq28 = n*(1-m)*b*r*bb*(6/16)*b*bc*(2/3);
```

```
eq29 = n*(1-m)*b*r*bb*(6/16)*b*bc*(1/3)*2;
eq30 = n*(1-m)*b*r*bb*(6/16)*b*bb*(2/3);
eq31 = n*(1-m)*b*r*bb*(6/16)*b*bb*(2/3);
eq32 = n*(1-m)*b*r*bb*(6/16)*b*bb*(1/3);
eq33 = n*(1-m)*b*r*bb*(6/16)*b*bb*(1/3)*2;
eq34 = n*(1-m)*b*r*bb*(6/16)*b*ba*2;
eq35 = n*(1-m)*b*r*bb*(6/16)*(1-b);
eq36 = n*(1-m)*b*r*bb*(9/16)*b*bc*(1/9)*2;
eq37 = n*(1-m)*b*r*bb*(9/16)*b*bc*(2/9);
eq38 = n*(1-m)*b*r*bb*(9/16)*b*bc*(4/9);
eq39 = n*(1-m)*b*r*bb*(9/16)*b*bc*(4/9);
eq40 = n*(1-m)*b*r*bb*(9/16)*b*bc*(2/9)*2;
eq41 = n*(1-m)*b*r*bb*(9/16)*b*bb*(1/9);
eq42 = n*(1-m)*b*r*bb*(9/16)*b*bb*(1/9)*2;
eq43 = n*(1-m)*b*r*bb*(9/16)*b*bb*(2/9);
eq44 = n*(1-m)*b*r*bb*(9/16)*b*bb*(2/9);
eq45 = n*(1-m)*b*r*bb*(9/16)*b*bb*(4/9);
eq46 = n*(1-m)*b*r*bb*(9/16)*b*bb*(4/9);
eq47 = n*(1-m)*b*r*bb*(9/16)*b*bb*(4/9);
eq48 = n*(1-m)*b*r*bb*(9/16)*b*bb*(2/9);
eq49 = n*(1-m)*b*r*bb*(9/16)*b*bb*(2/9)*2;
eq50 = n*(1-m)*b*r*bb*(9/16)*b*ba*2;
eq51 = n*(1-m)*b*r*bb*(9/16)*(1-b);
eq52 = n*(1-m)*b*r*ba*(8/16)*b*bc;
eq53 = n*(1-m)*b*r*ba*(8/16)*b*bb;
eq54 = n*(1-m)*b*r*ba*(8/16)*b*bb;
eq55 = n*(1-m)*b*r*ba*(8/16)*b*ba*2;
eq56 = n*(1-m)*b*r*ba*(8/16)*(1-b);
eq57 = n*(1-m)*b*r*ba*(8/16)*b*bc*2;
eq58 = n*(1-m)*b*r*ba*(8/16)*b*bb;
```

```
eq59 = n*(1-m)*b*r*ba*(8/16)*b*bb*2;
eq60 = n*(1-m)*b*r*ba*(8/16)*b*ba*2;
eq61 = n*(1-m)*b*r*ba*(8/16)*(1-b);
eq62 = n*(1-m)*b*r*ba*(4/16)*2*b*bc*0.5;
eq63 = n*(1-m)*b*r*ba*(4/16)*2*b*bc*0.5*2;
eq64 = n*(1-m)*b*r*ba*(4/16)*2*b*bb*0.5;
eq65 = n*(1-m)*b*r*ba*(4/16)*2*b*bb*0.5;
eq66 = n*(1-m)*b*r*ba*(4/16)*2*b*bb*0.5;
eq67 = n*(1-m)*b*r*ba*(4/16)*2*b*bb*0.5*2;
eq68 = n*(1-m)*b*r*ba*(4/16)*2*b*ba*2;
eq69 = n*(1-m)*b*r*ba*(4/16)*2*(1-b);
eq70 = n*(1-m)*b*r*ba*(2/16)*b*bc*2;
eq71 = n*(1-m)*b*r*ba*(2/16)*b*bb;
eq72 = n*(1-m)*b*r*ba*(2/16)*b*bb*2;
eq73 = n*(1-m)*b*r*ba*(2/16)*b*ba;
eq74 = n*(1-m)*b*r*ba*(2/16)*(1-b);
eq75 = n*(1-m)*b*r*ba*(2/16)*2*b*bc*2;
eq76 = n*(1-m)*b*r*ba*(2/16)*2*b*bb;
eq77 = n*(1-m)*b*r*ba*(2/16)*2*b*bb*2;
eq78 = n*(1-m)*b*r*ba*(2/16)*2*b*ba*2;
eq79 = n*(1-m)*b*r*ba*(2/16)*2*(1-b);
eq80 = n*(1-m)*r;
eq81 = n*(1-m)*(1-b)*r*(1-b);
eq82 = n*(1-m)*(1-b)*r*b*ba*2;
eq83 = n*(1-m)*(1-b)*r*b*bb;
eq84 = n*(1-m)*(1-b)*r*b*bb;
eq85 = n*(1-m)*(1-b)*r*b*bc;

mn_sc_2_0 = eq1 + eq3;
mn_y_2_0 = eq4 + eq6 + eq16 + eq18;
```

```
bn_sc_2_0 = eq2;
 bn_y_2_0 = eq5 + eq15_a + eq17 + eq80;

 mn_sc_2_a = eq1 + eq3;
 mn_y_2_a = eq4 + eq6 + eq16 + eq18;
 bn_sc_2_a = eq2 + eq60 + eq61 + eq78 + eq79;
 bn_y_2_a = eq5 + eq10 + eq14 + eq15_b + eq17 + eq55 + eq56 + eq68 + eq69 + ...
     eq73 + eq74 + eq81 + eq82;

 mn_sc_2_b = eq1 + eq3 + eq9 + eq22 + eq24 + eq31 + eq33 + eq47 + eq49;
 mn_y_2_b = eq4 + eq6 + eq12 + eq16 + eq18 + eq25 + eq27 + eq42 + eq44 + ...
     eq46 + eq84;
 bn_sc_2_b = eq2 + eq30 + eq32 + eq35;
 bn_y_2_b = eq5 + eq8 + eq10 + eq13 + eq15_b + eq17 + eq26 + eq41 + eq43 + ...
     eq45 + eq48 + eq51 + eq81 + eq83;

 mn_sc_2_c = eq1 + eq3 + eq7;
 mn_y_2_c = eq4 + eq6 + eq11 + eq16 + eq18 + eq19 + eq21 + eq85;
 bn_sc_2_c = eq2;
 bn_y_2_c = eq5 + eq15_b + eq17 + eq20 + eq81;

 mn_sc_2_ab = eq1 + eq3 + eq9 + eq22 + eq24 + eq31 + eq33 + eq47 + eq49 + ...
     eq59 + eq67 + eq77;
 mn_y_2_ab = eq4 + eq6 + eq11 + eq12 + eq16 + eq18 + eq25 + eq27 + eq42 + ...
     eq44 + eq46 + eq54 + eq65 + eq70 + eq72 + eq84;
 bn_sc_2_ab = eq2 + eq23 + eq30 + eq32 + eq34 + eq35 + eq58 + eq60 + eq61 + ...
     eq76 + eq78 + eq79;
 bn_y_2_ab = eq5 + eq8 + eq10 + eq13 + eq14 + eq15_b + eq17 + eq26 + eq41 + ...
     eq43 + eq45 + eq48 + eq50 + eq51 + eq53 + eq55 + eq56 + eq64 + eq66 + ...
     eq68 + eq69 + eq71 + eq73 + eq74 + eq81 + eq82 + eq83;
```

```
mn_sc_2_ac = eq1 +eq3 + eq7 + eq57 + eq63 + eq75;
 mn_y_2_ac = eq4 + eq6 + eq11 + eq16 + eq18 + eq19 + eq21 + eq52 + eq62 + ...
    eq70 + eq85;
 bn_sc_2_ac = eq2 + eq60 + eq61 + eq78 + eq79;
 bn_y_2_ac = eq5 + eq10 + eq14 + eq15_b + eq17 + eq20 + eq55 + eq56 + ...
    eq68 + eq69 + eq73 + eq74 + eq81 + eq82;

 mn_sc_2_bc = eq1 + eq3 + eq7 + eq9 + eq22 + eq24 + eq28 + eq29 + eq31 + ...
    eq33 + eq38 + eq40 + eq47 + eq49;
 mn_y_2_bc = eq4 + eq6 + eq11 + eq12 + eq16 + eq18 + eq19 + eq21 + eq25 + ...
    eq27 + eq36 + eq37 + eq39 + eq42 + eq44 + eq46 + eq84 + eq85;
 bn_sc_2_bc = eq2 + eq23 + eq30 + eq32 + eq35;
 bn_y_2_bc = eq5 + eq8 + eq13 + eq15_b + eq17 + eq20 + eq26 + eq41 + eq43 + ...
    eq45 + eq48 + eq51 + eq81 + eq83;

 mn_sc_2_abc = eq1 + eq3 + eq7 + eq9 + eq22 + eq24 + eq28 + eq29 + eq31 + ...
    eq33 + eq38 + eq40 + eq47 + eq49 + eq57 + eq59 + eq63 + eq67 + ...
    eq75 + eq77;
 mn_y_2_abc = eq4 + eq6 + eq11 + eq12 + eq16 + eq18 + eq19 + eq21 + eq25 + ...
    eq27 + eq36 + eq37 + eq39 + eq42 + eq44 + eq46 + eq52 + eq54 + eq62 + ...
    eq65 + eq70 + eq72 + eq84 + eq85;
 bn_sc_2_abc = eq2 + eq23 + eq30 + eq32 + eq34 + eq35 + eq58 + eq60 + eq61 + ...
    eq76 + eq78 + eq79;
 bn_y_2_abc = eq5 + eq8 + eq10 + eq13 + eq14 + eq15_b + eq17 + eq20 + eq26 + ...
    eq41 + eq43 + eq45 + eq48 + eq50 + eq51 + eq53 + eq55 + eq56 + eq64 + ...
    eq66 + eq68 + eq69 + eq71 + eq73 + eq74 + eq81 + eq82 + eq83;

 eq86 = n*m*d*r*c;
 eq87 = n*m*d*r*c*0.5;
```

```
eq88 = n*m*d*r*(1-c);

eq89 = n*m*(1-d)*r;

eq90 = n*(1-m)*b*r*bc*2;

eq91 = n*(1-m)*b*r*bb*2*0.5;

eq92 = n*(1-m)*b*r*bb*2*0.25;

eq93 = n*(1-m)*b*r*bb*(6/16);

eq94 = n*(1-m)*b*r*bb*(9/16);

eq95 = n*(1-m)*b*r*ba*(8/16);

eq96 = n*(1-m)*b*r*ba*(8/16);

eq97 = n*(1-m)*b*r*ba*(4/16)*2;

eq98 = n*(1-m)*b*r*ba*(2/16);

eq99 = n*(1-m)*b*r*ba*(2/16)*2;

eq100_a = n*(1-m);

eq100_b = n*(1-m)*(1-b)*r;


mn_sc_1_0 = eq86;

mn_y_1_0 = eq87 + eq89;

bn_sc_1_0 = 0;

bn_y_1_0 = eq88 + eq100_a;


mn_sc_1_a = eq86;

mn_y_1_a = eq87 + eq89;

bn_sc_1_a = eq96 + eq99;

bn_y_1_a = eq88 + eq100_b + eq95 + eq97 + eq98;


mn_sc_1_b = eq86 + eq91;

mn_y_1_b = eq87 + eq89 + eq92;

bn_sc_1_b = eq93;

bn_y_1_b = eq88 + eq100_b + eq94;
```

```
mn_sc_1_c = eq86;
mn_y_1_c = eq87 + eq89 + eq90;
bn_sc_1_c = 0;
bn_y_1_c = eq88 + eq100_b;

mn_sc_1_ab = eq86 + eq91;
mn_y_1_ab = eq87 + eq89 + eq92;
bn_sc_1_ab = eq93 + eq96 + eq99;
bn_y_1_ab = eq88 + eq100_b + eq94 + eq95 + eq97 + eq98;

mn_sc_1_ac = eq86;
mn_y_1_ac = eq87 + eq89 + eq90;
bn_sc_1_ac = eq96 + eq99;
bn_y_1_ac = eq88 + eq100_b + eq95 + eq97 + eq98;

mn_sc_1_bc = eq86 + eq91;
mn_y_1_bc = eq87 + eq89 + eq90 + eq92;
bn_sc_1_bc = eq93;
bn_y_1_bc = eq88 + eq100_b + eq94;

mn_sc_1_abc = eq86 + eq91;
mn_y_1_abc = eq87 + eq89 + eq90 + eq92;
bn_sc_1_abc = eq93 + eq96 + eq99;
bn_y_1_abc = eq88 + eq100_b + eq94 + eq95 + eq97 + eq98;
```

CHAPTER 5

COUPLING TO SUBSTRATE ADHESIONS DRIVES THE MATURATION OF MUSCLE STRESS FIBERS INTO MYOFIBRILS WITHIN CARDIAC MYOCYTES

Neininger, AC.*, Taneja, N.*, & Burnette, DT. Molecular Biology of the Cell, 2020.
*These authors contributed equally to the work and are considered interchangeable co-first authors

Introduction

The heart generates contractile force through the shortening of sarcomeres, which consist of myosin "thick" filaments forming sliding interactions with actin "thin" filaments. Actin filaments of adjacent sarcomeres are cross-linked by α-actinin-2 at Z-discs, which are important sites for intracellular signaling and mechanical stability of cardiac myocytes[59,141]. The basic functional unit of contraction within a cardiac myocyte is the myofibril, comprised of a series of sarcomeres. In healthy cardiac myocytes, contractile forces generated by myofibrils are balanced by adhesive forces, specifically at cell-extracellular matrix (ECM) contacts (referred to as costameres), which transfer these forces to the ECM, and at cell-cell contacts (referred to as intercalated discs)[49,142]. Loss of this force balance can lead to detrimental phenotypes and disease states[49,143]. Previous work has shown that cell-ECM contacts comprise the majority of sites of force generation during early cardiac myocyte spreading, during the time window of myofibril assembly[144]. These sites of force generation are subsequently transferred to cell-cell contacts as cells start to form intercalated discs.

Early studies of cultured primary chick cardiac myocytes localized adhesion proteins, such as vinculin, to the ends of myofibrils, and proposed that "adhesion plaques" serve as sites of myofibril assembly[51]. This idea was supported by multiple genetic studies performed in the skeletal muscle of worms and fruit flies[74,145,146]. Knockout of proteins involved in cell-ECM adhesion, such as integrin or perlecan, resulted in fewer myofibrils compared to the knockout of myofibril components themselves. Thus, the genetic evidence suggests that cell-ECM adhesion is upstream of myofibril assembly[76]. It has additionally been shown that inhibiting contraction of cultured rat primary cardiac myocytes results in a loss of adhesions[147,148]. Conversely, modulating the size of adhesions by varying substrate stiffness can modulate the contractile properties of cardiac myocytes[149,150]. This indicates that there is feedback between cardiac myocyte adhesion and contractile function. Despite this evidence, the mechanistic relationship between cell-ECM adhesion and myofibril assembly has remained unclear. This has been in part due to multiple conflicting models of myofibril assembly itself[72].

Of the multiple competing models of myofibril assembly that have been proposed, the Template (a.k.a., Pre-myofibril) model has the most experimental support. First proposed by Howard Holtzer in 1984, the Template model postulated that "Non-Muscle Stress Fiber-Like Structures (NMSFLS)" are the precursors of myofibrils[64]. We have recently shortened Holtzer's initialism to MSFs (Muscle Stress Fibers) for brevity[80]. While there was substantial evidence from fixed cultured myocytes and tissue to support the Template/Pre-myofibril model, there was little dynamic data directly demonstrating the transition of MSFs to myofibrils[64,70]. We have recently utilized human iPSC-derived cardiac myocytes (hiCMs) to capture this transition[80]. hiCMs are transcriptionally similar to embryonic and neonatal cardiac myocytes, a time at which sarcomere assembly is occurring *in vivo*. We reported that freshly plated hiCMs did not have sarcomeres and subsequently assembled them over 4-16 hours after plating[80]. Live-cell imaging of either actin or α-actinin-2 revealed that MSFs move away from the edge and obtain sarcomeres over time.

Studies in primary skeletal myocytes from β1 integrin-deficient mice proposed that cell-ECM adhesion could regulate the transition of MSFs to myofibrils, rather than the formation of MSFs themselves[151]. In fixed cells, the authors observed that inactivation of β1 integrin led to a lack of myofibrils, but not MSFs[151]. A more recent study, however, claimed a new model of sarcomere assembly, where cell-ECM adhesion sites serve as the site for centripetal nucleation of sarcomeres[78]. In this model, a sarcomere-containing myofibril directly grows out of an adhesion, without the need for a template (i.e. MSFs). The authors imaged α-actinin-2, which marks both focal adhesions and the Z-lines of myofibrils. Indeed, a cursory glance at the movies presented gives the impression that the Z-lines are streaming out of adhesions. However, closer frame-by-frame inspection of the data revealed that these events were pre-formed myofibrils coming from the dorsal surface of the cell to the ventral (in focus) surface. We have now experimentally demonstrated this phenomenon[80]. It is important to note that we were only able to capture these events after 24 hours post-plating, which is the time window in which Chopra et al. imaged their hiCMs.

Here, we sought to investigate the role of cell-ECM adhesion in myofibril assembly within the context of the Template/Pre-myofibril model. By combining high resolution three-dimensional imaging and multiple perturbations to focal adhesion assembly, we show that (1)- Dorsal stress fiber-like actin-based structures couple myofibrils to focal adhesions, (2)- Focal adhesions do not serve as the direct site for nucleation of myofibrils or MSFs, and (3)- Stronger coupling to the ECM correlates with the ability of MSFs to mature into myofibrils.

Results

The Spatiotemporal Relationship Between Cell-ECM Adhesion and Myofibril Maturation

We first wanted to explore how adhesions, which are present on the ventral surface of the cell, are connected to myofibrils on the dorsal surface of the cell. We noticed that the relative organization of the focal adhesions and contractile structures (i.e., MSFs and myofibrils) bore a striking resemblance to that of mesenchymal crawling non-muscle cells (Figure 5-1A). Indeed, we have previously noted that MSFs were similar in their organization to stress fibers found on the dorsal surface of mesenchymal cells called actin arcs[80]. In mesenchymal cells, actin arcs are connected to focal adhesions through specialized actin filament-based structures called dorsal stress fibers (DSFs)[53]. To test if DSF-like structures exist in hiCMs, we examined the actin filament channel throughout the axial (Z) dimension (Figure 5-1B-C, Figure 5-S1A). We found that diffraction limited imaging was not able to resolve the relative axial positions of different actin filament structures, especially those close to the edges of hiCMs (Figure 5-S2). For this reason, we imaged actin filaments with structured illumination microscopy (SIM), which provides a ~2X increase in axial resolution. SIM revealed that strands of actin filaments extended from the ventral surface of the cell up to the dorsal surface (Figure 5-1B). These strands ended in the MSFs and myofibrils on the dorsal surface (Figure 5-1C, Figure 5-S1B).

We next wanted to experimentally test if DSFs were mechanically coupled to MSFs and myofibrils. We hypothesized that the contractile MSFs and myofibrils could be pulling on DSFs. Therefore, we predicted that cutting DSFs would result in MSFs/myofibrils moving away from the edge of the cell. To test this possibility, we cut a DSF that appeared connected to either an MSF (Figure 5-1D) or a myofibril (Figure 5-1E) using a high intensity focused laser. We found that cutting of the DSF resulted in translocation of the MSF or myofibril away from the edge (Figure 5-1D-E). To further test mechanical coupling, we also cut a myofibril that was attached to two DSFs; one on either end. Upon cutting, the two halves of the myofibril retracted away from each other along with the DSF each half was attached to. Taken together, the localization and laser dissection experiments suggest that DSFs mechanically connect MSFs and myofibrils to adhesions.

Given the physical connection between focal adhesions and myofibrils, we next investigated if there was a temporal relationship between the relative assembly of the two structures. We imaged actin filaments and paxillin in live hiCMs during the transition of MSFs into the first myofibrils. We use the term “myofibril maturation” to describe this transition. This should not be confused with “cardiac myocyte maturation”, which involves transcriptional and metabolic changes over developmental time scales[152]. As previously demonstrated, MSFs translocate away from the edge and obtain sarcomeres over time[80]. The purple arrowheads in Figure 5-2A denote this phenomenon. The paxillin channel revealed that focal adhesions also elongate during this same time period (Figure 5-2A, green arrowhead). Consistent with how dorsal stress fibers form in mesenchymal cells[53], we observed the appearance of dorsal stress fiber-like connections between the elongating adhesions and maturing myofibrils (Figure 5-2A, yellow arrowheads). We next wanted to quantify the potential relationship between adhesion growth and myofibril maturation over time.

Figure 5-1: 3D Organization of Myofibrils and Dorsal Stress Fibers

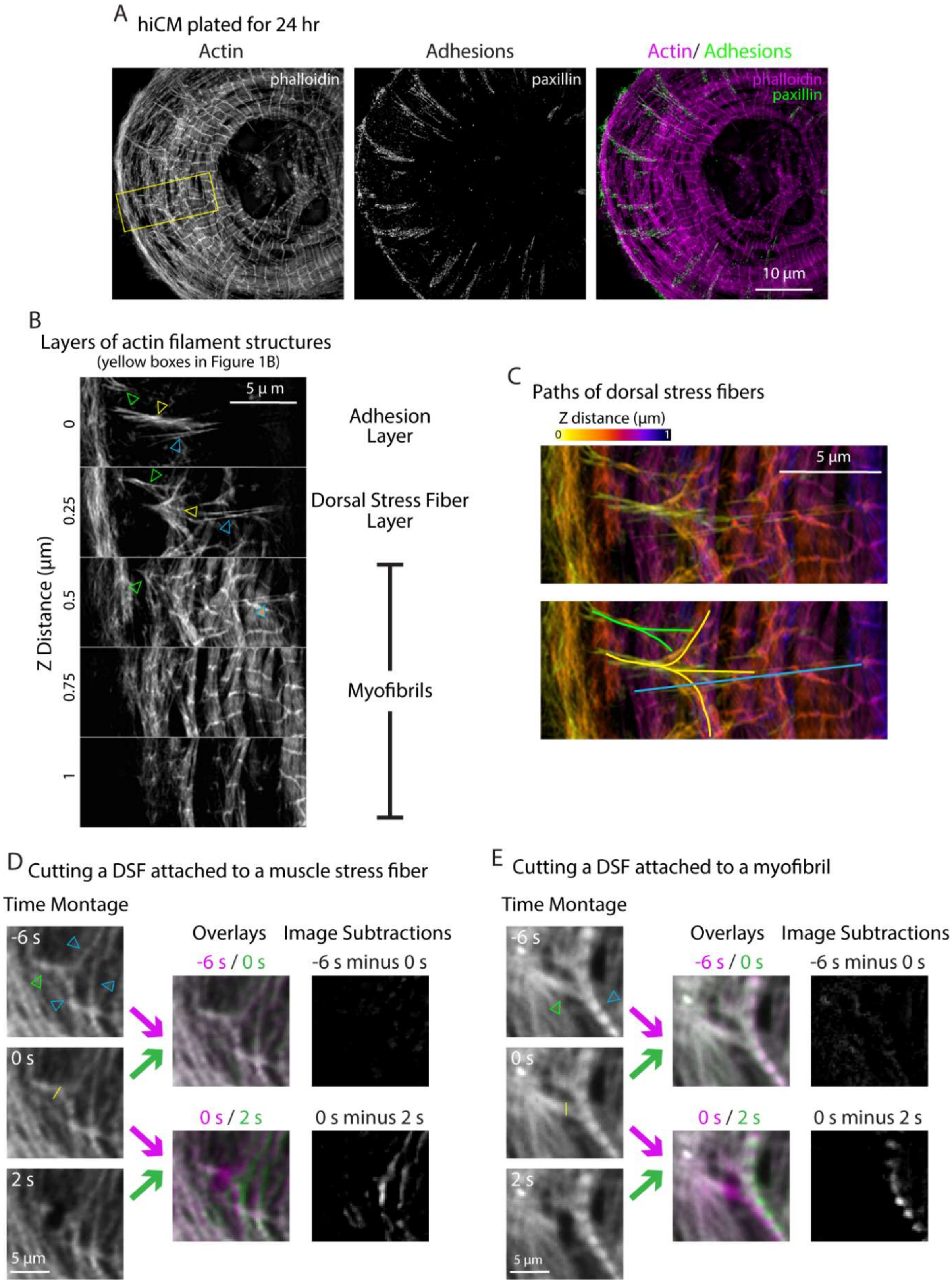

Figure 5-1:

A) SIM of actin filaments (magenta) and paxillin (green) in hiCM plated for 24 hours. B) SIM showing the layers of actin filaments in the axial (Z) dimension from the box in (A). Arrowheads denote different dorsal stress fibers. C) 3D color projection of the data in (B). Lines denote the different dorsal stress fibers denoted in (B). D-E) Focused laser mediated cutting of DSF attached to an MSF (D) or a myofibril (E) in hiCM expressing Lifeact-mApple at 16 hours post plating. Green arrowheads denote dorsal stress fibers and blue arrowheads denote MSF or myofibril. Yellow line denotes cut site. Temporal color-coded overlays and image subtractions show the change in positioning of the MSF or myofibril following cutting of the dorsal stress fiber. See Figure 5-S1C for uncropped views of cells.

As focal adhesions mature, their area increases[56]. Similarly, when myofibrils mature, the length of their Z-lines increase[71]. Therefore, we used total area of focal adhesions as a proxy for adhesion maturity and Z-line length as a proxy for myofibril maturity. To identify focal adhesions, we localized the adhesion protein, paxillin (Figure 5-2B). To identify Z-lines, we localized α-actinin-2 (Figure 5-2B). We then used a computer-assisted analysis method we developed to measure Z-line length and adhesion area in hundreds of cells during hiCM spreading (Figure 5-S3, supplemental software). We analyzed cells that were allowed to spread for 6 hours, 24 hours, and 1 week post-plating (Figure 5-2B). We chose these time points based on our previous observations on the timing of myofibril maturation. At 6 hours post-plating, most hiCMs were characterized by immature myofibrils with punctate Z-lines (i.e., Z-bodies). By 24 hours, hiCMs contained myofibrils with elongated Z-lines. As suggested by our live data, we observed a strong positive correlation between the extent of adhesion and myofibril maturity at 6 hours, 24 hours, and up to 1 week post-plating (Figure 5-2C). We next wanted to further establish the relationship between cell-ECM adhesion and myofibril maturation by altering components of the adhesion machinery and measuring the effects on myofibril maturation.

Figure 5-2: Dynamics of Adhesions and Myofibril Maturation

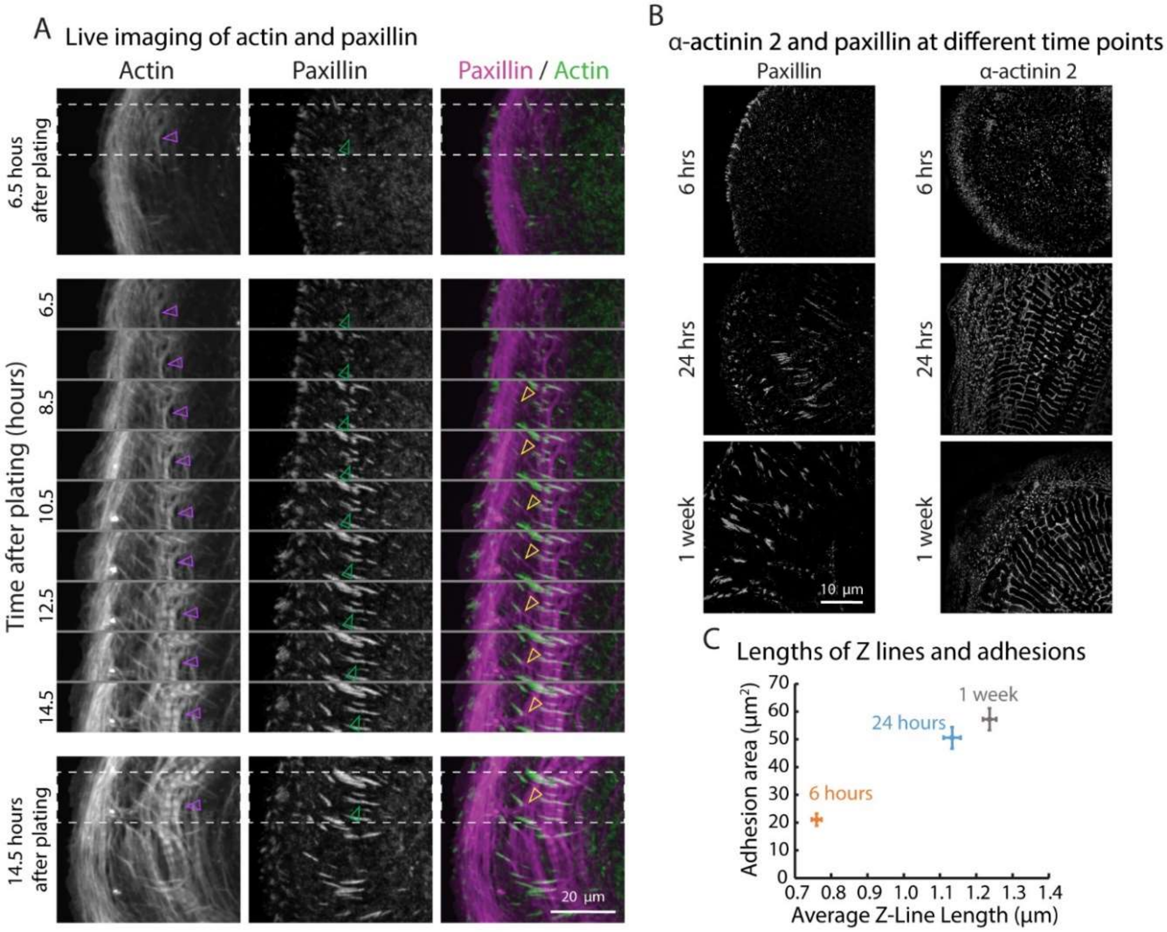

Figure 5-2:

A) Time montage of actin labeled with Lifeact-mEmerald and paxillin-mCherry during myofibril assembly. The first frame (top) and last frame (bottom) are separated by a time montage of the regions shown in the boxes (dotted lines). The purple arrowhead denotes an MSF becoming a myofibril. The green arrowhead denotes a growing adhesion. The yellow arrowhead denotes an extending dorsal stress fiber. B) Representative SIM images of endogenous paxillin and α-actinin-2 in hiCMs plated from 6 hours, 24 hours, or 1 week. C) Quantification of Z-line lengths and adhesion area in hiCMs plated for 6 hours, 24 hours, and 1 week. Z-line measurements: 6H: n= 58 cells, N= 4 independent experiments; 24H: n= 75 cells, N= 4 independent experiments; 1 Week: n=81 cells, 3 independent experiments. Adhesion measurements: 6H; n= 38 cells, N= 5 independent experiments; 24H: n= 48 cells, N= 5 independent experiments; 1 Week: n= 28 cells, N= 3 independent experiments

Decreasing Cell-ECM Adhesion Results in Attenuation of Myofibril Maturation

We chose to start with vinculin, a component of focal adhesions that links the adhesion to the actin cytoskeleton[62]. It was predicted two decades ago by Howard Holtzer and colleagues that vinculin would play a role during myofibril assembly[51]. Furthermore, knockout of vinculin in hiCMs has been shown to alter the organization of Z-lines[78]. We depleted vinculin using a pooled siRNA approach and found a significant reduction in paxillin-positive area (Figure 5-3A-C). To test if reduction in vinculin altered myofibril maturation, we measured the length of Z-lines after 24 hours of spreading, since this is the time point at which most control cells contained myofibrils[80]. Knockdown of vinculin resulted in a significant reduction in Z-line length (Figure 5-3D-E). This reduction in Z-line length was in agreement with previously published data[78].

Figure 5-3: Knockdown of Vinculin Results in Attenuation of Myofibril Maturation

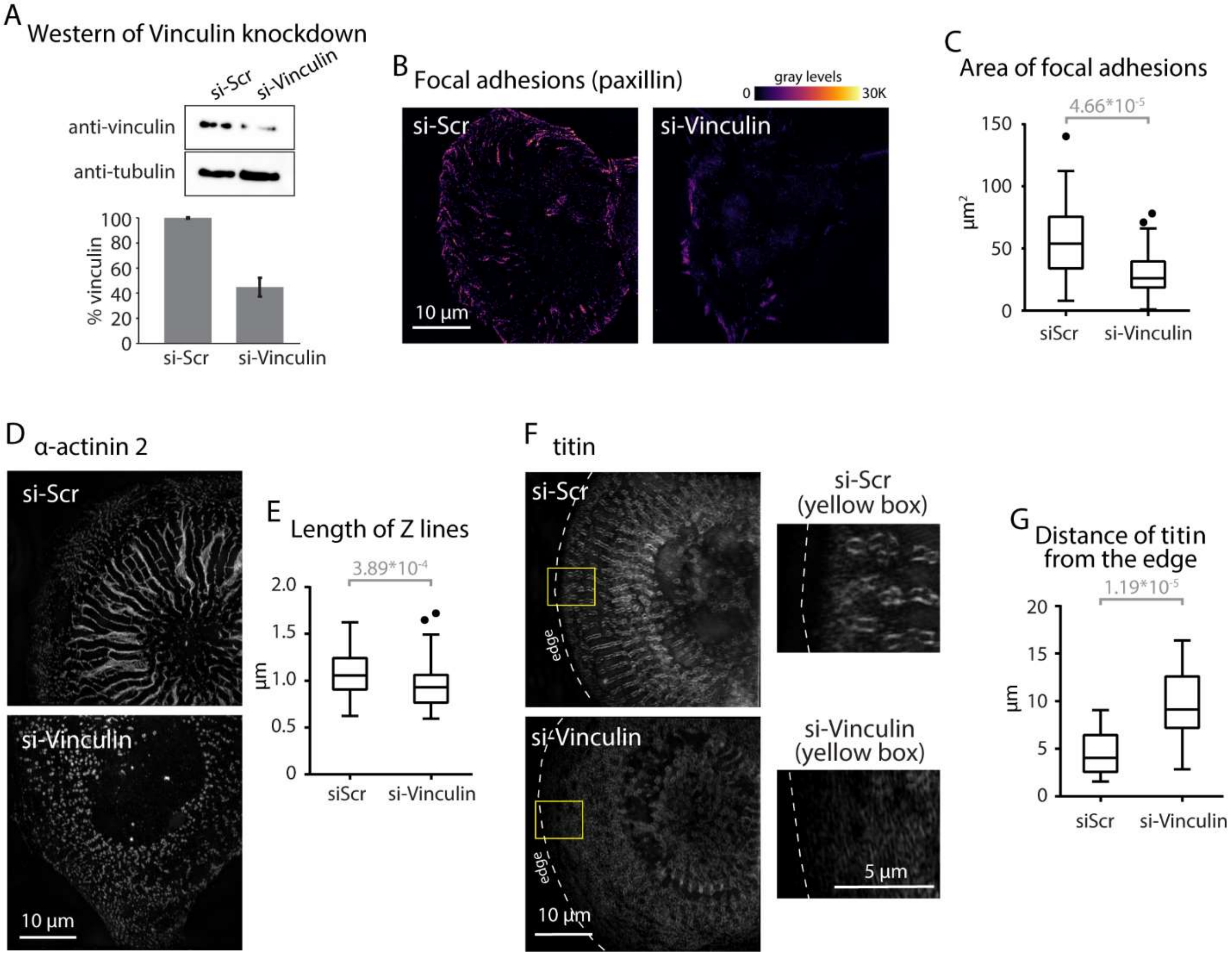

Figure 5-3:

A) Representative western blot for vinculin knockdown using siRNA. Tubulin was used as a loading control. Knockdown efficiency was calculated from 4 independent experiments. B) Paxillin localization (single optical section) in hiCMs treated with either scrambled or vinculin siRNA. C) Quantification of adhesion area. si-Scr: n= 54 cells, N= 6 independent experiments; si-Vinculin: n= 30 cells, N= 4 independent experiments. D) α-actinin-2 localization (maximum Z-projection) in hiCMs treated with either scrambled or vinculin siRNA. E) Quantification of average length of Z-lines. si-Scr: n= 131 cells, N= 6 independent experiments; si-Vinculin: n= 69 cells, N= 5 independent experiments. F) Localization of titin in hiCMs treated with either scrambled or vinculin siRNA. G) Quantification of distance of titin localization from the cell edge. si-Scr: n= 19 cells, N= 3 independent experiments; si-Vinculin: n= 21 cells, N= 3 independent experiments. Exact p-values stated in graphs.

We next wanted an additional measure of myofibril maturation. The incorporation of the large Z-disc protein titin is considered a marker for maturation of myofibrils[72]. We localized the N-terminal region of titin, which should localize on either side of Z-lines (Figure 5-3F)[153]. In control cells plated for 24 hours, we found distinct organization of titin at a mean distance of 4.1 +/- 2.3 μm from the edge (Figure 5-3G). Knockdown of vinculin resulted in severe disruption of overall titin organization, with the first titin structures localizing 9.5 +/- 3.8 μm from the edge (Figure 5-3G). The effects of vinculin knockdown on adhesion area, Z-line length and titin organization were recapitulated using a single siRNA mediated knockdown approach (Figure 5-S4A-D).

In non-muscle cells, vinculin is thought to act as a clutch that mechanically couples focal adhesions to actin stress fibers (e.g., actin arcs) to impede their rearward translocation[154]. As a result, we asked if vinculin could also be slowing the translocation of MSFs. We previously reported that MSFs translocate away from the edge and then slow down as they transition into myofibrils, which undergo little translocation[80]. Therefore, we quantified the rate of rearward movement of MSFs in control versus vinculin depleted cells. We used kymography to measure the rates of MSF translocation (Figure 5-4A-B). In control cells, we found MSFs underwent rearward translocation at comparable rates as our previous report (Figure 5-4A-B, E). Vinculin knockdown resulted in a significant increase in MSF translocation rates (Figure 5-4C-E). This is consistent with a potential role for cell-ECM adhesion in slowing the translocation of MSFs. We next wanted to test if reduction of adhesion size through altering other adhesion components could also attenuate myofibril maturation.

Figure 5-4: Knockdown of Vinculin Results in Faster Translocation of Muscle Stress Fibers

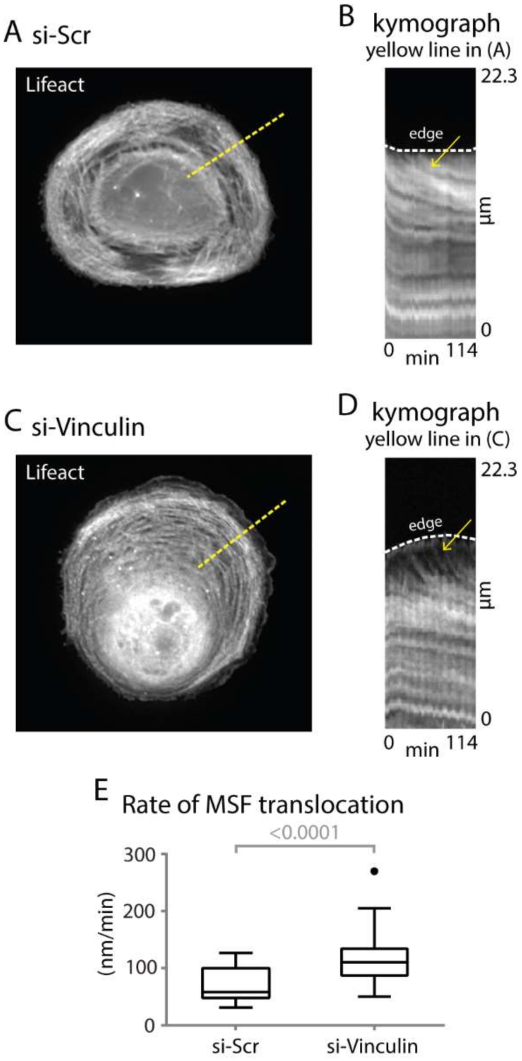

Figure 5-4:

A) Control (scrambled siRNA-treated) cell expressing Lifeact-mApple 16 hours post-plating. B) Kymograph generated using yellow line in (A). Yellow arrow denotes MSFs translocating away from the edge (dotted white line). E) Vinculin depleted cell expressing Lifeact-mApple 16 hours post-plating. D) Kymograph generated using yellow line in (C). Yellow arrow denotes MSFs translocating away from the edge (dotted white line). E) Quantification of MSF translocation rates in control versus vinculin-depleted cells. si-Scr: n= 30 MSFs from 19 cells; si-Vinculin: n= 22 MSFs from 14 cells; N= 3 independent experiments. Exact p-values stated in graphs.

Talin is a focal adhesion protein that directly binds β integrins through its N-terminal “head” domain and to vinculin through its C-terminal “tail” domain[155]. As a result, talin binding to vinculin leads to focal adhesion strengthening by linking vinculin to integrins[60]. It has been previously reported that overexpression of the head domain of talin acts in a dominant negative manner, resulting in attenuation of focal adhesion signaling[156]. We hypothesized that expression of talin head domain should result in reduction in focal adhesion area, similar to vinculin knockdown. Therefore, we measured paxillin-positive area in hiCMs expressing talin head-mEGFP (Figure 5-5A-C). We found a marked decrease in focal adhesion area in hiCMs expressing talin head-mEGFP versus control cells (Figure 5-5B-C, Figure 5-S5). We also found that this decrease in adhesion area correlated with a decrease in Z-line length, as well as an increase in the distance from the edge at which titin localizes (Figure 5-5D-G). The rate of MSF translocation also increased in hiCMs expressing talin head-mEGFP (Figure 5-5H).

Figure 5-5: Expression of Talin Head Domain Results in Attenuation of Myofibril Maturation

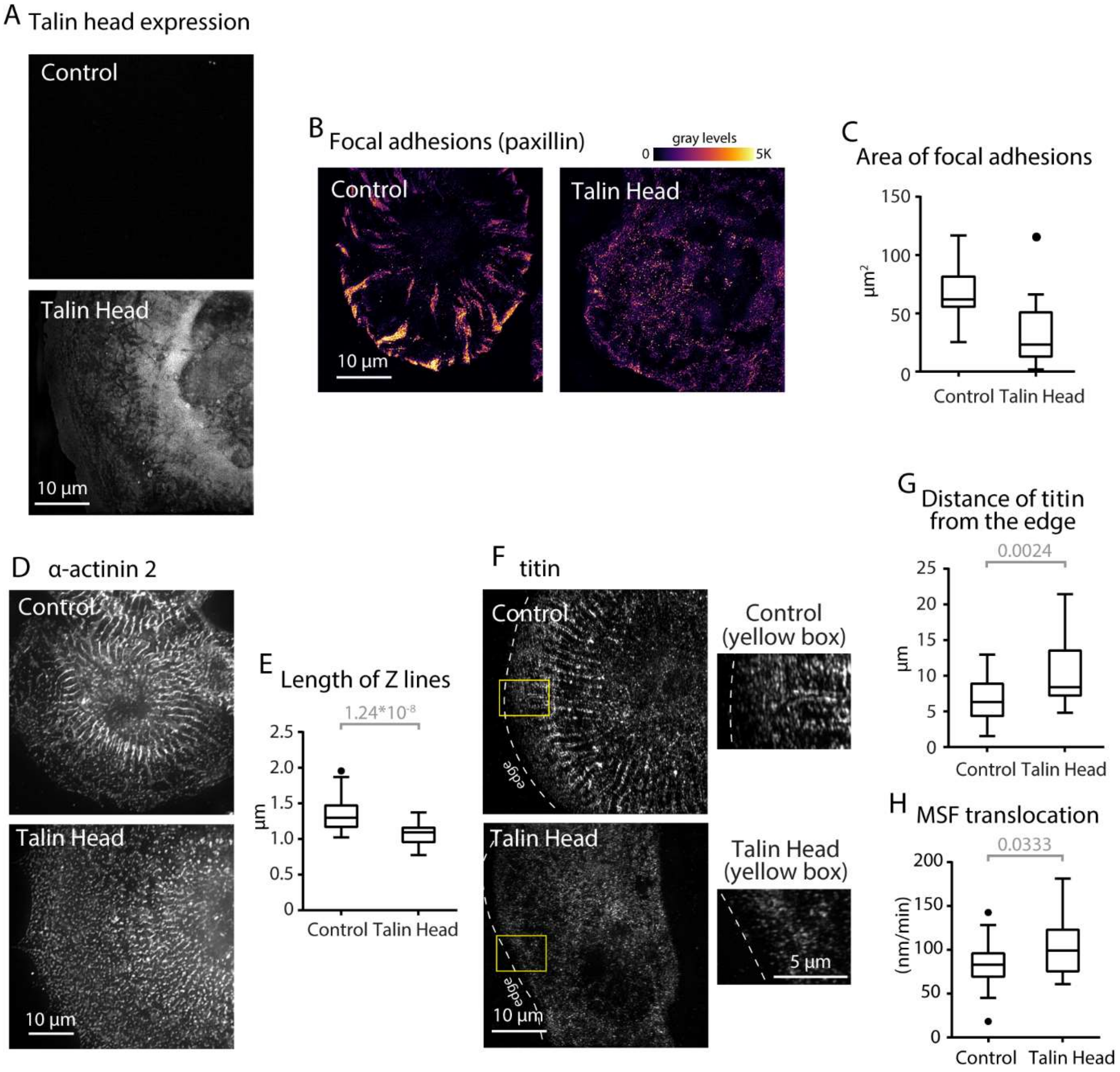

Figure 5-5:

A) Representative hiCM expressing talin head-mEGFP versus non-expressing hiCM. B) Paxillin localization (single optical section) in hiCM overexpressing talin head-mEGFP versus a non-expressing hiCM. C) Quantification of adhesion area. Non-expressing: n= 21 cells; talin head-mEGFP: n= 22 cells, N= 3 independent experiments each. D) α-actinin-2 localization (maximum Z-projection) in hiCM overexpressing talin head-mEGFP versus a non-expressing hiCM. E) Quantification of average Z-lines length . Non-expressing: n= 43 cells; talin head-mEGFP: n= 36 cells; N= 3 independent experiments each. F) Localization of titin in hiCM overexpressing talin head-mEGFP versus a non-expressing hiCM. G) Quantification of distance of titin localization from the cell edge. Non-expressing: n= 19 cells; Talin head: n= 21 cells, N= 3 independent experiments each. H) Quantification of MSF translocation rates in control hiCMs versus hiCMs overexpressing talin head=mEGFP. Control: n= 25 MSFs from 16 cells; talin head-mEGFP: n= 26 MSFs from 17 cells; N= 3 independent experiments. Exact p-values stated in graphs.

We next investigated the role of focal adhesion kinase (FAK), which is a key scaffolding and signaling protein at focal adhesions necessary for regulating focal adhesion growth[157]. A previous study has suggested that knocking down FAK in skeletal muscle precursors (i.e., myoblasts) reduced focal adhesions as well as attenuated myofibril formation[77]. We asked whether this role for FAK is conserved in cardiac myocytes. To that end, we depleted hiCMs of FAK using a pooled siRNA approach (Figure 5-6A) and first measured focal adhesion area. Consistent with previous reports[77], we found a significant reduction in focal adhesion area upon knockdown of FAK (Figure 5-6B-C). In correlation with this reduction in adhesion, we found a decrease in Z-line length as well as an increase in the distance from the edge at which titin localized (Figure 5-6D-G). We verified these phenotypes using single siRNA mediated knockdown of FAK (Figure 5-S4E-H). Furthermore, depletion of FAK resulted in increased rates of MSF translocation (Figure 5-6H). Taken together, we used four different methods to reduce focal adhesions in hiCMs. Our data suggest that reducing focal adhesion area correlates with attenuation of myofibril maturation and an increase in rate of MSF translocation. We next wanted to increase adhesion area to test if it would result in increased or accelerated myofibril maturation.

Figure 5-6: Knockdown of FAK Results in Attenuation of Myofibril Maturation

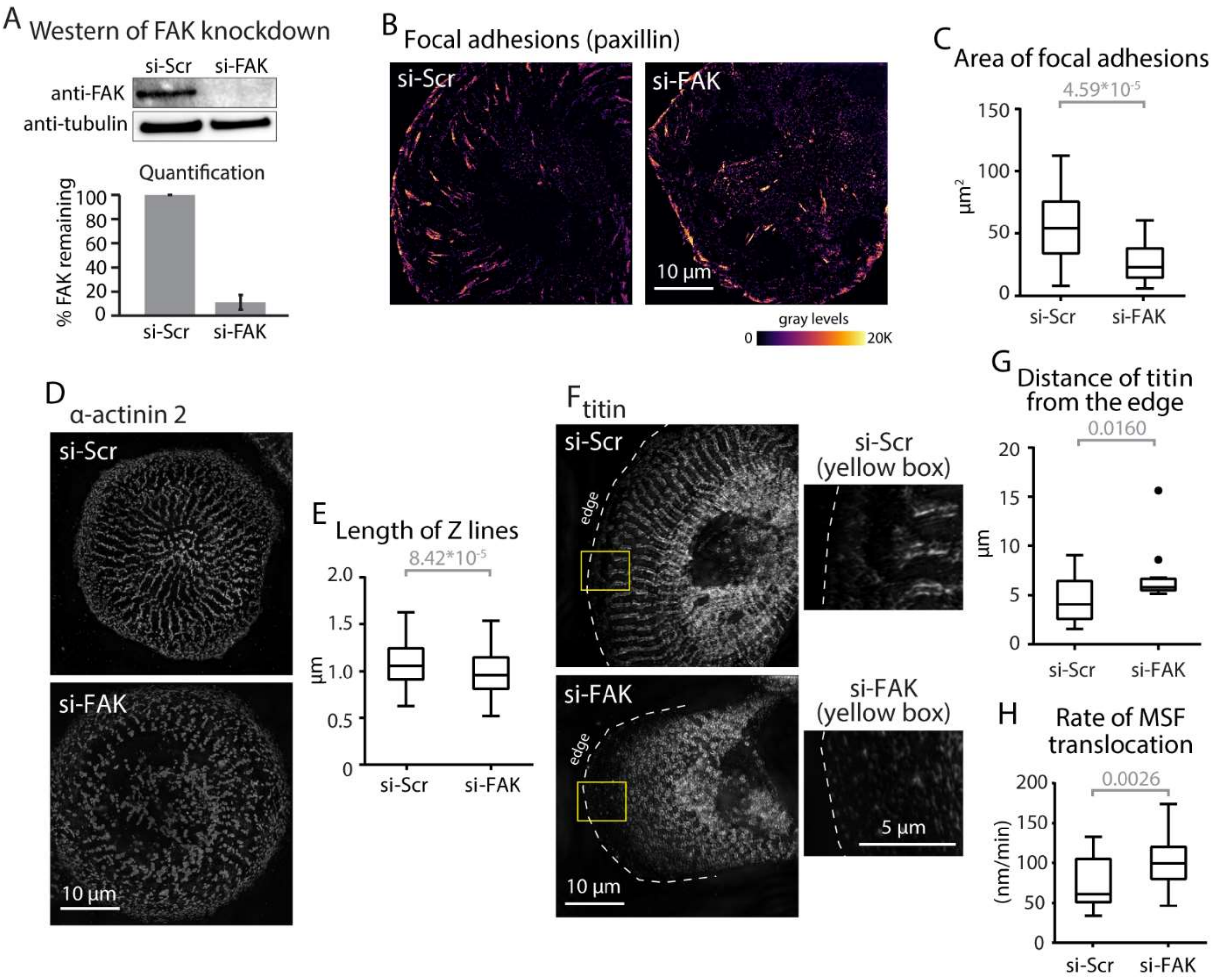

Figure 5-6:

A) Representative western blot for FAK knockdown using siRNA. Tubulin was used as a loading control. Knockdown efficiency was calculated from 3 independent experiments. B) Paxillin localization (single optical section) in hiCMs treated with either scrambled or FAK siRNA. C) Quantification of adhesion area in FAK depleted cells. si-FAK: n= 36 cells, N= 4 independent experiments. The si-Scr dataset is the same as in Fig. 3C. D) α-actinin-2 localization (maximum Z-projection) in hiCMs treated with either scrambled or FAK siRNA. E) Quantification of average length of Z-lines in FAK-depleted cells. si-FAK: n= 106 cells, N= 4 independent experiments. The si-Scr dataset is the same as in Fig. 3E. F) Localization of titin in hiCMs treated with either scrambled or FAK siRNA. G) Quantification of distance of titin localization from the cell edge. si-FAK: n= 12 cells, N= 3 independent experiments. The si-Scr dataset is the same as in Fig. 3F. H) Quantification of MSF translocation rates in FAK-depleted cells versus scrambled siRNA-treated hiCMs. si-FAK: n= 25 MSFs from 16 cells; N= 3 independent experiments. The si-Scr dataset is the same as in Fig. 4E. Exact p-values stated in graphs.

Increasing ECM Adhesion Results in Precocious Myofibril Maturation

It has been shown in non-muscle cells that pharmacologically disrupting the kinase activity of FAK leads to inhibition of adhesion turnover without affecting adhesion assembly, resulting in increase in adhesion area[158,159]. Therefore, we used a specific small-molecule inhibitor, PF-228, to disrupt the kinase activity of FAK in hiCMs. The autophosphorylation of FAK at Y397 is classically used as a readout for FAK kinase activity[158,160,161]. We found that treatment of hiCMs with PF-228 led to a nearly complete loss of localization of pFAK from adhesions (Figure 5-7A). Treatment of hiCMs with PF-228 led to a small increase in focal adhesion area at 24 hours post-plating, but this was not significant (Figure 5-S6). Furthermore, there was a significant, but small change in Z-line length (Figure 5-S6). We wondered whether any potential effects of FAK inhibition could be observed at earlier time points in plating when the first myofibrils are assembling. We previously showed that the first myofibrils arise 4-16 hours after plating[80]. Therefore, we chose to investigate the relationship between focal adhesions and myofibrils at 6 hours post plating. Indeed, we found that at 6 hours post-plating, hiCMs treated with PF-228 had a significantly higher adhesion area (Figure 5-7B-C). Strikingly, we found that hiCMs treated with PF-228 also had significantly longer Z-lines, as well as closer titin localization to the edge (Figure 5-7D-G). Furthermore, we found that PF-228-treated hiCMs had slower rates of MSF translocation compared to control hiCMs (Figure 5-7H). We next wanted to test if the correlation between an increase in adhesion area and precocious myofibril assembly was specific to FAK inhibition. Therefore, we wanted to increase focal adhesion size without any genetic or pharmacological perturbations.

Figure 5-7: Inhibition of FAK Kinase Activity Results in Precocious Myofibril Maturation

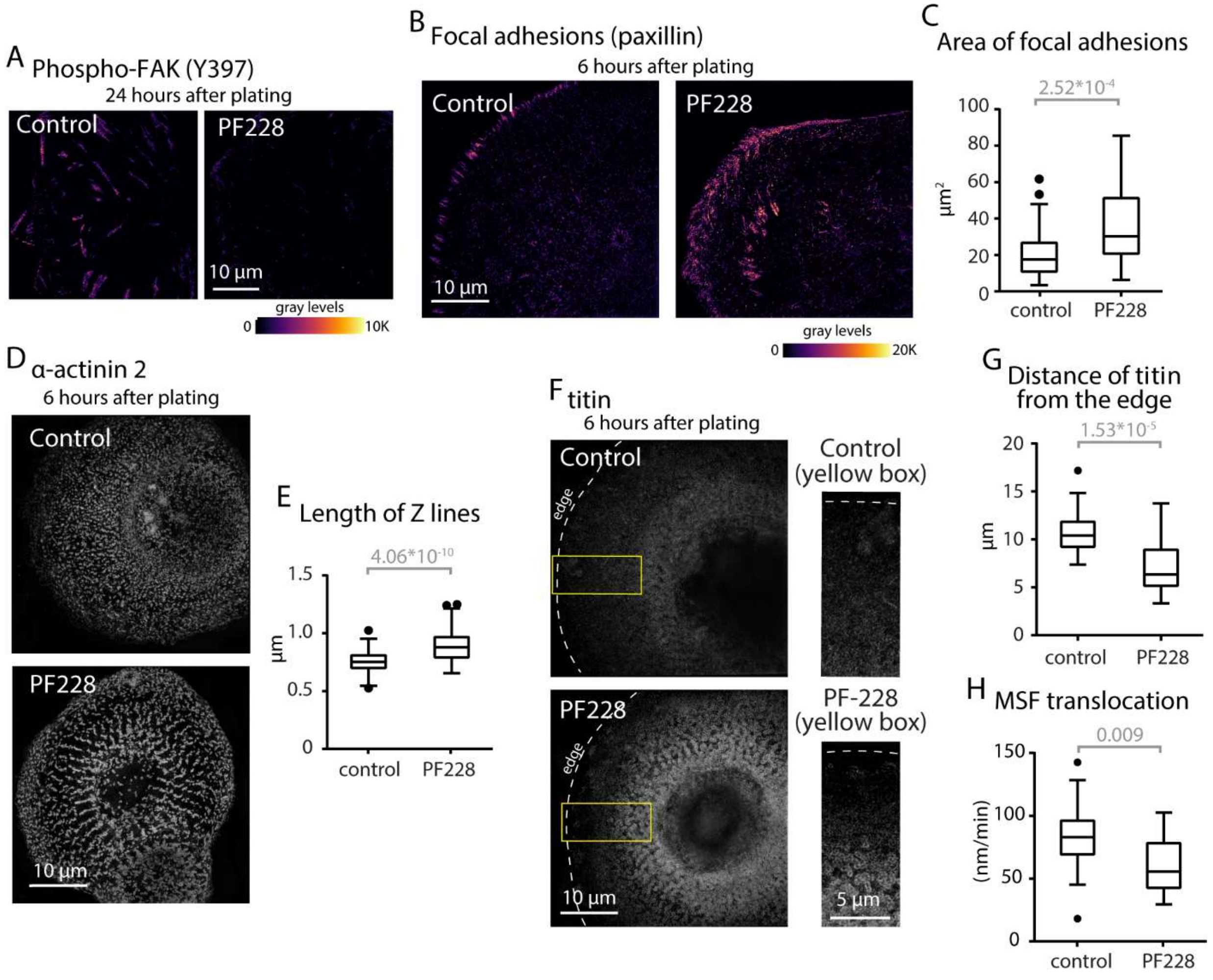

Figure 5-7:

A) Localization of pFAK Y397 in control or 3 µM PF-228-treated hiCMs 24 hours post-plating. B) Paxillin localization (single optical section) in control versus PF-228-treated hiCMs 6 hours post-plating. C) Quantification of adhesion area in PF-228-treated cells. Control: n= 38 cells, N= 5 independent experiments. PF-228: n= 44 cells, N= 4 independent experiments. D) α-actinin-2 localization (maximum Z-projection) in control versus PF-228-treated hiCMs 6 hours post-plating. E) Quantification of average length of Z-lines in PF-228-treated hiCMs. Control: n= 58 cells, N= 4 independent experiments; PF-228: n= 107 cells, N=4 independent experiments. F) Localization of titin in control versus PF-228 treated hiCMs after 6 hours of spreading. G) Quantification of distance of titin localization from the cell edge. Control: n= 23 cells; PF-228: n= 23 cells; N= 3 independent experiments each. H) Quantification of MSF translocation rates in PF-228 treated cells versus control. PF-228: n= 24 MSFs from 17 cells; N= 3 independent experiments. The control data set is the same is in Fig. 5H. Exact p-values stated in graphs.

It has been shown in non-muscle cells that increasing the concentration of the extracellular matrix protein, fibronectin, leads to larger focal adhesions[159,162]. As our standard procedure, we plate hiCMs on glass coverslips coated with 10 µg/mL fibronectin. As such, all the previous experiments presented here were performed with this coating concentration. To test if increasing fibronectin would increase focal adhesion area in hiCMs, we plated them on glass coverslips coated with 50 µg/mL fibronectin, as we have done previously using non-muscle cells[159]. At 6 hours post-plating we found that hiCMs plated on 50 µg/mL fibronectin had a higher paxillin-positive adhesion area compared to control hiCMs plated on 10 µg/mL fibronectin (Figure 5-8A-B). This increase in adhesion area correlated with an increase in Z-line length as well as closer titin localization to the edge (Figure 5-8C-F). The rate of MSF translocation was also significantly slower compared to control hiCMs plated on 10 µg/mL fibronectin (Figure 5-8G). Of note, focal adhesion area and Z-line length were not significantly different for hiCMs plated on 10 or 50 µg/mL fibronectin at 24 hours post-plating, similar to what we observed with FAK inhibition (Figure 5-S6). Taken together, our data suggest that increasing focal adhesion area correlated with precocious myofibril maturation.

Figure 5-8: Increasing Fibronectin Concentration Results in Precocious Myofibril Maturation

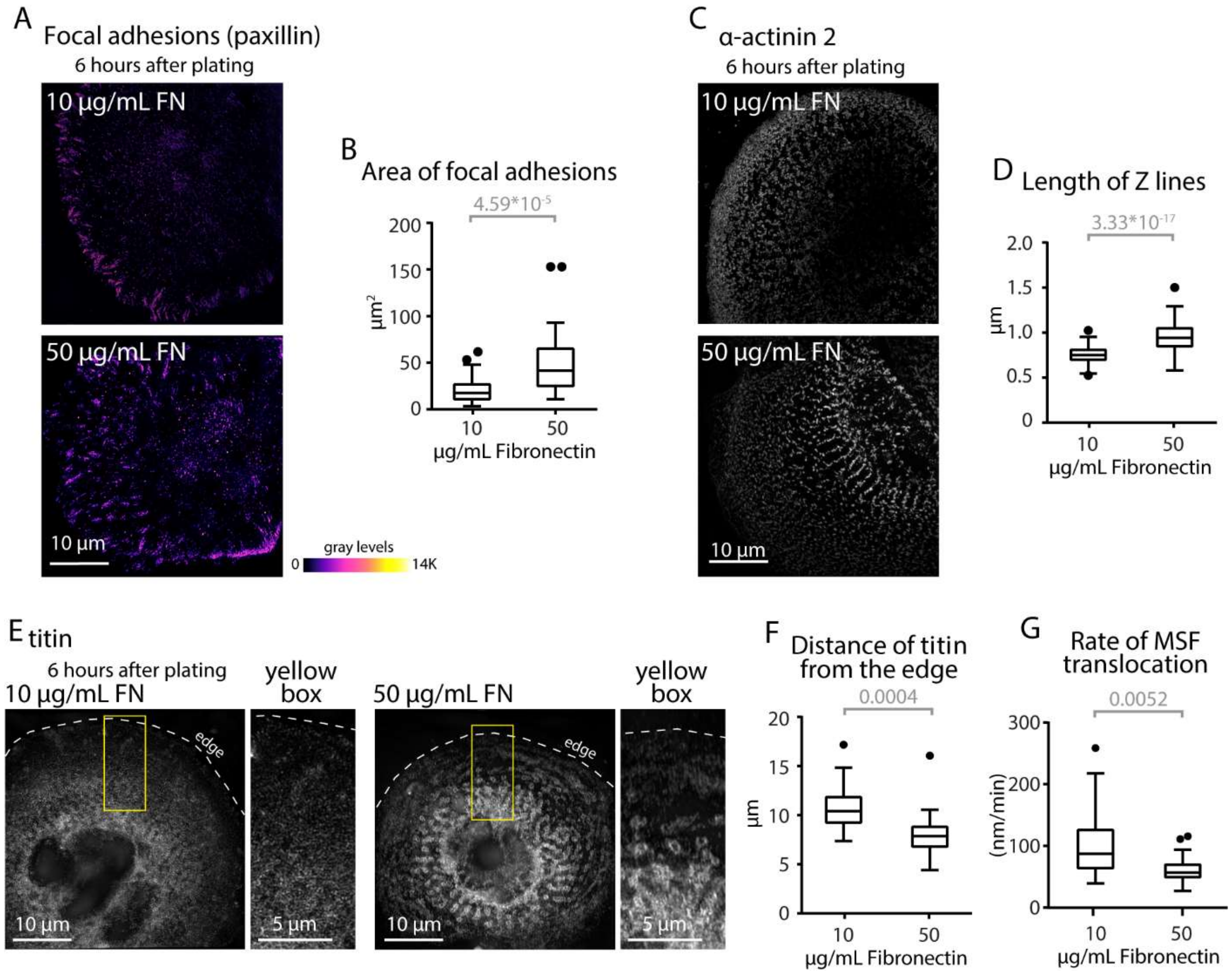

Figure 5-8:

A) Paxillin localization (single optical section) in hiCMs plated on either 10 μg/mL or 50 μg/mL fibronectin. B) Quantification of adhesion area in hiCMs plated on either 10 μg/mL or 50 μg/mL fibronectin. 50 μg/mL: n= 47 cells, N= 5 independent experiments. The 10 μg/mL dataset is the same as Fig. 8C. C) α-actinin-2 localization (maximum Z-projection) in hiCMs plated on either 10 μg/mL or 50 μg/mL fibronectin. D) Quantification of average length of Z-lines in hiCMs plated on either 10 μg/mL or 50 μg/mL fibronectin. 50 μg/mL: n= 201 cells, N= 6 independent experiments. The 10 μg/mL dataset is the same as Fig. 8E. E) Localization of titin in hiCMs plated on either 10 μg/mL or 50 μg/mL fibronectin. F) Quantification of distance of titin localization from the cell edge. 50 μg/mL: n= 23 cells, N= 3 independent experiments. The 10 μg/mL dataset is the same as Fig. 8F. G) Quantification of MSF translocation rates in hiCMs plated on either 10 μg/mL or 50 μg/mL fibronectin. 50 μg/mL: n= 20 MSFs from 12 cells; N= 3 independent experiments. The 10 μg/mL dataset is the same as in Fig. 5H. Exact p-values stated in graphs.

DIAPH1 is Required for the Maturation of Myofibrils

We next wanted to further investigate the mechanism controlling substrate coupling during myofibril maturation. As dorsal stress fibers form the connection between adhesions and myofibrils, we hypothesized that reducing this connection could lead to less mature myofibrils. In non-muscle cells, the actin filament nucleator DIAPH1 is known to be critical for focal adhesion growth and its depletion results in fewer and smaller focal adhesions[163,164]. We previously showed that DIAPH1 is expressed in hiCMs using RNAseq[80]. In that study, we also showed that another formin, FHOD3, is critical for the assembly of myofibrils[80]. However, FHOD3 only localized to MSFs and myofibrils but not to dorsal stress fibers[80]. To examine whether DIAPH1 localized to dorsal stress fibers, we expressed DIAPH1-mEGFP. In contrast to FHOD3, we found that DIAPH1 localized to the actin filaments of dorsal stress fibers (Figure 5-9A). Furthermore, depletion of DIAPH1 using siRNA resulted in a reduction of dorsal stress fibers but not MSFs (Figure 5-9B-C).

Figure 5-9: Knockdown of DIAPH1 Results in Attenuation of Myofibril Maturation

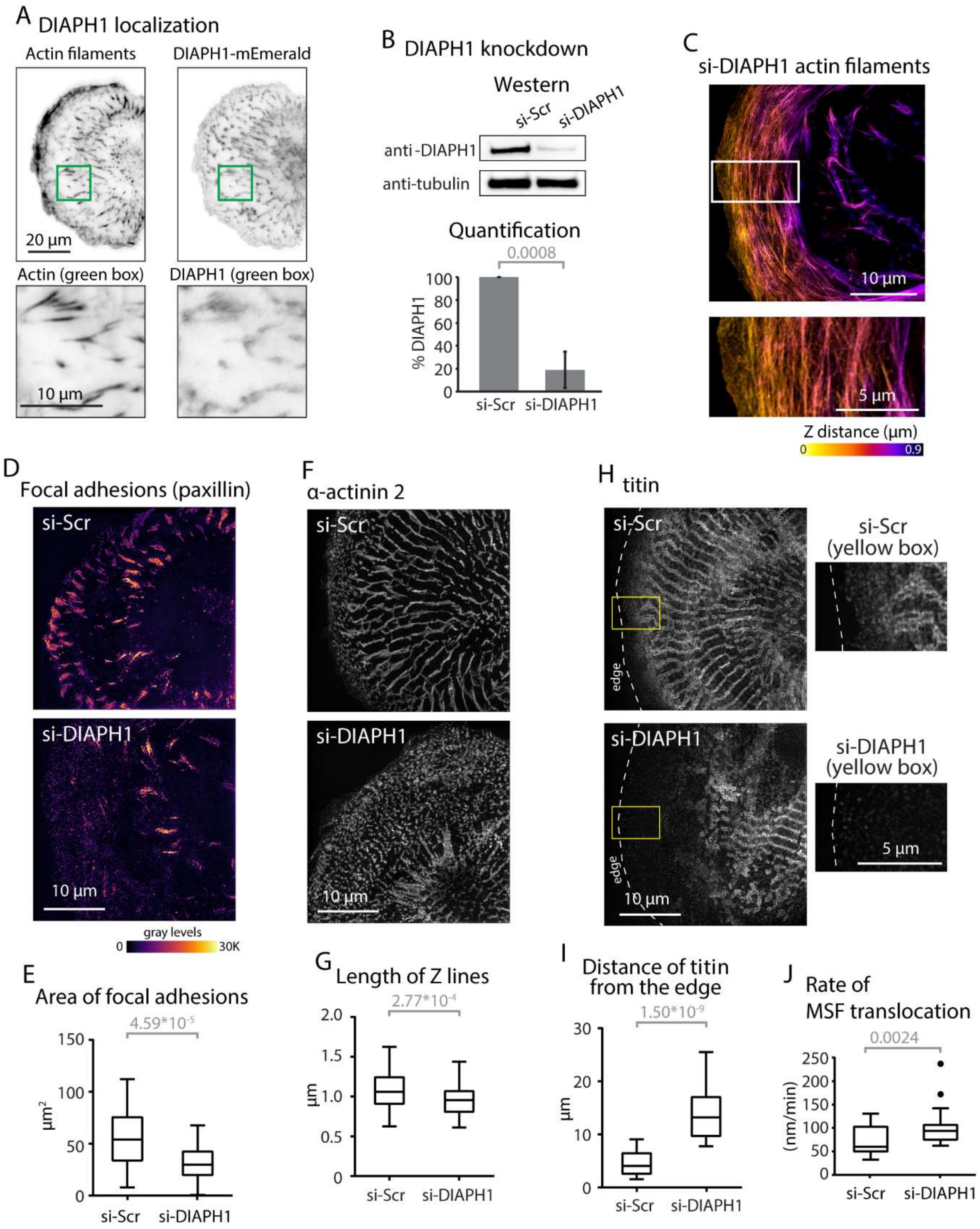

Figure 5-9:

A) Total internal reflection microscopy (TIRF) image showing the ventral section of an hiCM spread for 24 hours. Actin filaments (phalloidin) and DIAPH1-mEmerald are shown in inverted gray. Note the co-localization of DIAPH1 with actin filaments associated with focal adhesions. B) Representative western blot for DIAPH1 knockdown using siRNA. Tubulin was used as a loading control. Knockdown efficiency was calculated from 3 independent experiments. C) 3D SIM of actin filaments in a si-DIAPH1 KD hiCM at 24 hours post plating. Note the lack of prominent dorsal stress fibers. D) Paxillin localization (single optical section) in hiCMs treated with either scrambled or DIAPH1 siRNA. E) Quantification of adhesion area in DIAPH1- depleted cells. si-DIAPH1: n= 33 cells, N= 4 independent experiments. The si-Scr dataset is the same as Fig. 3C. F) α-actinin-2 localization (maximum Z-projection) in hiCMs treated with either scrambled or DIAPH1 siRNA. G) Quantification of average length of Z-lines in DIAPH1-depleted cells. si-DIAPH1: n= 58 cells, N= 3 independent experiments. The si-Scr dataset is the same as Fig. 3E. H) Localization of titin in hiCMs treated with either scrambled or DIAPH1 siRNA. I) Quantification of distance of titin localization from the cell edge. si-DIAPH1: n= 23 cells, N= 3 independent experiments. The si-Scr dataset is the same as Fig. 3F. J) Quantification of MSF translocation rates in DIAPH1 depleted cells versus scrambled siRNA-treated hiCMs. si-DIAPH1: n= 25 MSFs from 16 cells; N= 3 independent experiments. The si-Scr dataset is the same as in Fig. 4E. Exact p-values stated in graphs.

We next examined if DIAPH1 knockdown reduced focal adhesions and myofibril maturation. Indeed, we found that hiCMs did have a significant reduction in focal adhesion area after DIAPH1 depletion using pooled siRNA (Figure 5-9D-E). Further establishing the correlation between focal adhesion area and myofibril maturation, we found a significant decrease in Z-line length (Figure 5-9F-G). There was also an increase in the distance from the edge at which titin localized in DIAPH1-depleted cells (Figure 5-9H-I). The phenotypes observed for focal adhesion area, Z-line length and titin organization were recapitulated using a single siRNA mediated knockdown of DIAPH1. Further supporting the hypothesis that DIAPH1 is required for substrate coupling in hiCMs, we found a significant increase in the rate of MSF translocation (Figure 5-9J).

Discussion

Here we present a new model of how cell-ECM adhesions regulate the maturation of sarcomere-containing myofibrils (Figure 5-10). We started by examining the architecture of focal adhesions relative to the contractile machinery in hiCMs during *de novo* assembly of myofibrils. Sarcomeres formed on the top (dorsal) surface of the cell[80], while adhesions matured on the bottom (ventral) surface of the cell. In striking resemblance to the architecture of actin stress fibers in non-muscle cells, we found thin, actin-based connections spanning the axial distance between focal adhesions and myofibrils. We showed using laser-mediated cutting that dorsal stress fibers mechanically link both MSFs and myofibrils to focal adhesions. Live imaging of adhesions and actin filaments during myofibrillogenesis revealed that these structures arise and elongate out of focal adhesions as MSFs translocate away from the edge and mature into myofibrils. This results in the long axis of focal adhesions being parallel to the long axis of Z-lines.

In our attempt to modulate adhesion area, our results have implicated a canonical adhesion pathway that is well-characterized in non-muscle cells. We started with the hypothesis that this canonical signaling axis would be conserved in cardiac myocytes. Previous super-resolution studies have elaborated the nanoscale architecture of focal adhesions, revealing layers of focal adhesion components[165]. Here we modulate each of these layers and reveal multiple positive correlations between the extent of adhesion and myofibril maturation. We modulated the integrin layer by increasing the concentration of fibronectin, the signaling layer by modulating talin and FAK, the force transduction layer by modulating vinculin and the actin regulatory layer by modulating DIAPH1. Interestingly, these data revealed that the perturbations that led to reduced adhesion area and decreased MSF maturation correlated with an increase in the rate of MSF translocation, while the perturbations that led to increased adhesion resulted in a decrease in the rate of MSF translocation.

Figure 5-10: Working Model for the Role of Substrate Adhesion in Myofibril Maturation

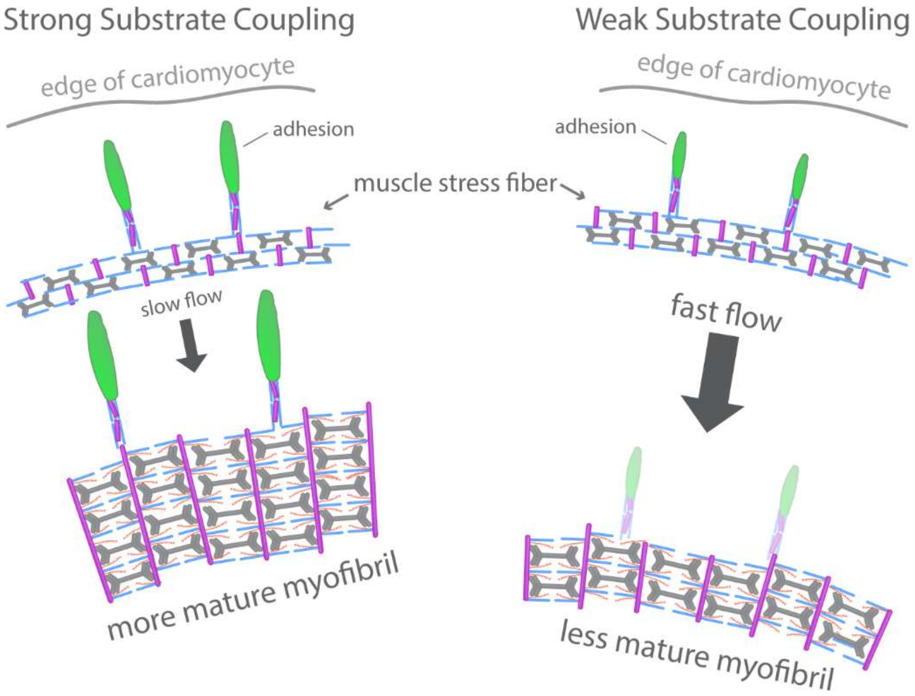

Figure 5-10:

Increasing cell-ECM adhesion results in greater mechanical coupling of muscle stress fibers to the ECM through dorsal stress fibers. This is accompanied by slowing down of muscle stress fibers as they translocate away from the edge. Greater substrate coupling leads to the transition of the muscle stress fiber to a myofibril, possibly by increased mechanical forces. Decreasing cell-ECM adhesion leads to reduced mechanical coupling, accompanied by faster translocation of muscle stress fibers and an inability to mature into force-generating myofibrils.

The inverse relationship between the rate of MSF translocation and the extent of adhesion parallels observations made in migrating cells. In migrating cells, adhesions slow the movement of actin arcs[52,166], which are the orthologs of MSFs[80]. Actin arcs are physically linked to focal adhesions through dorsal stress fibers[53,167]. DIAPH1 has been shown to be required for dorsal stress fiber assembly in non-muscle cells[53]. Therefore, it was not surprising that knockdown of DIAPH1 led to an increase in the rate of MSF translocation. Dorsal stress fibers are linked to adhesions through vinculin, which has been proposed to act as a "clutch" in non-muscle cells[154]. Indeed, MSF translocation was also accelerated upon vinculin depletion. Talin mechanically links vinculin to integrins. In non-muscle cells, overexpression of the head domain of talin disrupts the ability of endogenous talin to bind integrins, thus effectively losing this mechanical coupling[156]. In line with the vinculin depletion phenotype, overexpression of the head domain of talin also accelerated MSF translocation.

These multiple correlations between cell-ECM adhesion and MSF translocation, as well as direct mechanical coupling through DSFs, strongly suggest a role for mechanical forces in the maturation of myofibrils. Focal adhesions are ideally suited for allowing an increase in tension since they can both sense and adapt to the magnitude and direction of mechanical forces[55,168]. Components such as integrins, talin and vinculin are mechano-sensitive[58,61,169]; that is, they change their structural conformation upon application of mechanical forces. Furthermore, it was reported that only a small proportion of talin molecules at cell-ECM attachment sites in the *Drosophila* flight muscle experience significant forces, suggesting a large pool of talin is primed for adapting to changes in load[170]. Therefore, our data support a model where adhesions could serve as load bearing sites and allow an increase in mechanical tension in MSFs, which wozuld allow their maturation into myofibrils (Figure 5-10). Indeed, in the flight muscles of *Drosophila*, the establishment of cell-ECM sites with tendons precedes the maturation of stress fibers to myofibrils[171].

A bidirectional interplay between myofibrils and cell-ECM adhesion has also been implicated using computational modeling, where it was proposed that myofibrils and stress fibers form along the maximal principal stress direction[172]. Interestingly, cell-ECM adhesion was dominant over the contribution of cell shape to determine the direction of stress; “immature” iPSC derived cardiac myocytes with uniformly arranged smaller adhesions formed radially arranged myofibrils on square micropatterns, while more mature neonatal cardiac myocytes with larger adhesions formed linear substrate attached myofibrils[172]. Our data is in agreement with these theoretical predictions, since trypsinized hiCMs form radially arranged focal adhesions at early time points (6 hours, Figure 5-2B), and thus form radially arranged myofibrils. At later time points (beyond 24 hours), as adhesions grow larger, a symmetry breaking process occurs where these myofibrils linearize and become substrate attached.

A recent study claimed to have delved into the fundamental mechanics of sarcomere assembly, where they propose that myofibrils stream out of “protocostameres” (i.e., focal adhesions) through a “centripetal” assembly mechanism[78]. It is important to note again that the authors made these claims about “*de novo”* sarcomere assembly during a time window when sarcomeres are already assembled. The apparent appearance of myofibrils perpendicular to focal adhesions was interesting, and different than the parallel arrangement we find during sarcomere assembly. This is an effect of imaging the ventral plane of the cell and capturing the pre-formed myofibrils falling down from the dorsal surface; a phenomenon observed routinely in non-muscle cells[53,173]. In non-muscle cells, actin arcs on the dorsal surface fuse with at least two dorsal stress fibers as they move to the ventral surface and convert to a ventral stress fiber with an adhesion at both ends[53,173]. The data from Chopra et al. appears to support such a mechanism of creating ventrally attached myofibrils, and may be a manifestation of the symmetry breaking that occurs at later stages of hiCM spreading[78]. We speculate DSFs are key structures that may relay the direction of principal stress from adhesions to MSFs or myofibrils.

Furthermore, Chopra et al. reported that knockout of β-myosin II led to a decrease in sarcomere content[78]. This led the authors to propose that a force balance between β-myosin II, but not other myosin II paralogs, and focal adhesions directs the centripetal assembly of sarcomeres. Interestingly, subsequent studies have called into question the relative roles of the myosin II paralogs during sarcomere formation[80,174]. Another lab has also generated β-myosin II knockout hiCMs, and sarcomere formation in these cells still occurs[174]. This calls into question the requirement for β-myosin II in sarcomere formation. Furthermore, we have recently shown that knockdown of "non-muscle" myosin IIs does lead to attenuation of sarcomere formation[80]. These requirements are also mirrored in Drosophila flight muscles, where non-muscle myosin II-mediated tension, but not muscle myosin II, was required for the increased ordering in actin filaments[79].

It is important to note that our data suggests that centripetal assembly does, in part, contribute to myofibril formation. Centripetal assembly is likely to be the mechanism of nucleating the connections between myofibrils and focal adhesions (i.e., dorsal stress fibers). The concept of centripetal assembly was first proposed in 1984 in non-muscle cells, where stress fibers arise at the edge and elongate in a "centripetal" manner towards the middle of the cell[175]. Subsequent studies established this mode of assembly to be driving dorsal stress fiber formation, but not the assembly of actin arcs[53]. This concept of centripetal assembly was applied to myofibril formation as early as 1990, where vinculin "plaques" at the edge were proposed to give rise to the precursors of myofibrils [51]. Our data argues while myofibrils do not directly arise from adhesions through centripetal assembly, dorsal stress fibers that link myofibrils to adhesions are likely to arise due to centripetal assembly. In support of this idea, disruption of β1 integrin in skeletal muscle *in vitro* led to the absence of mature myofibrils, but not MSF-like structures[151].

Cell-cell adhesion is another source of balancing forces generated by myofibrils[142]. However, cell-cell adhesion is still unknown to play a significant role in *de novo* myofibril assembly. It has been demonstrated previously that cell-ECM adhesion sites are responsible for the majority of traction force generation during early cardiac myocyte spreading; as the cell continues to spread and makes cell-cell contacts, load-bearing sites are transferred to cell-cell contact sites [144]. As such, it is interesting to note that focal adhesion proteins such as FAK and vinculin also localize to intercalated discs once they form[176,177]. Indeed, a recent study found that vinculin localizes to cell-cell-adhesion sites under increased load in zebrafish hearts *in vivo,* driving the thickening of myofibrils[178]. Determining the mechanisms driving the localization of such proteins to sites of increased load should be the focus of future studies.

Finally, we show a similar actin architecture in spreading hiCMs, namely a force generating contractile stress fiber (i.e., muscle stress fibers and myofibrils) connected to a load bearing structure (i.e., focal adhesion) via a non-contractile stress fiber (i.e. dorsal stress fiber), that is commonly observed in mesenchymal cells. It is interesting to note while this architecture is conserved, there are minor differences in the regulatory mechanisms between the formation of muscle stress fibers and actin arcs[80]. We speculate that this may allow a mesodermal progenitor cell to modify the same mechanical system to perform two distinct functions, cell migration in the case of mesenchymal lineages, and sarcomere assembly in the case of cardiac lineages.

Supplemental Figures

Figure 5-S1: 3D Organization of Actin Structures Using SIM

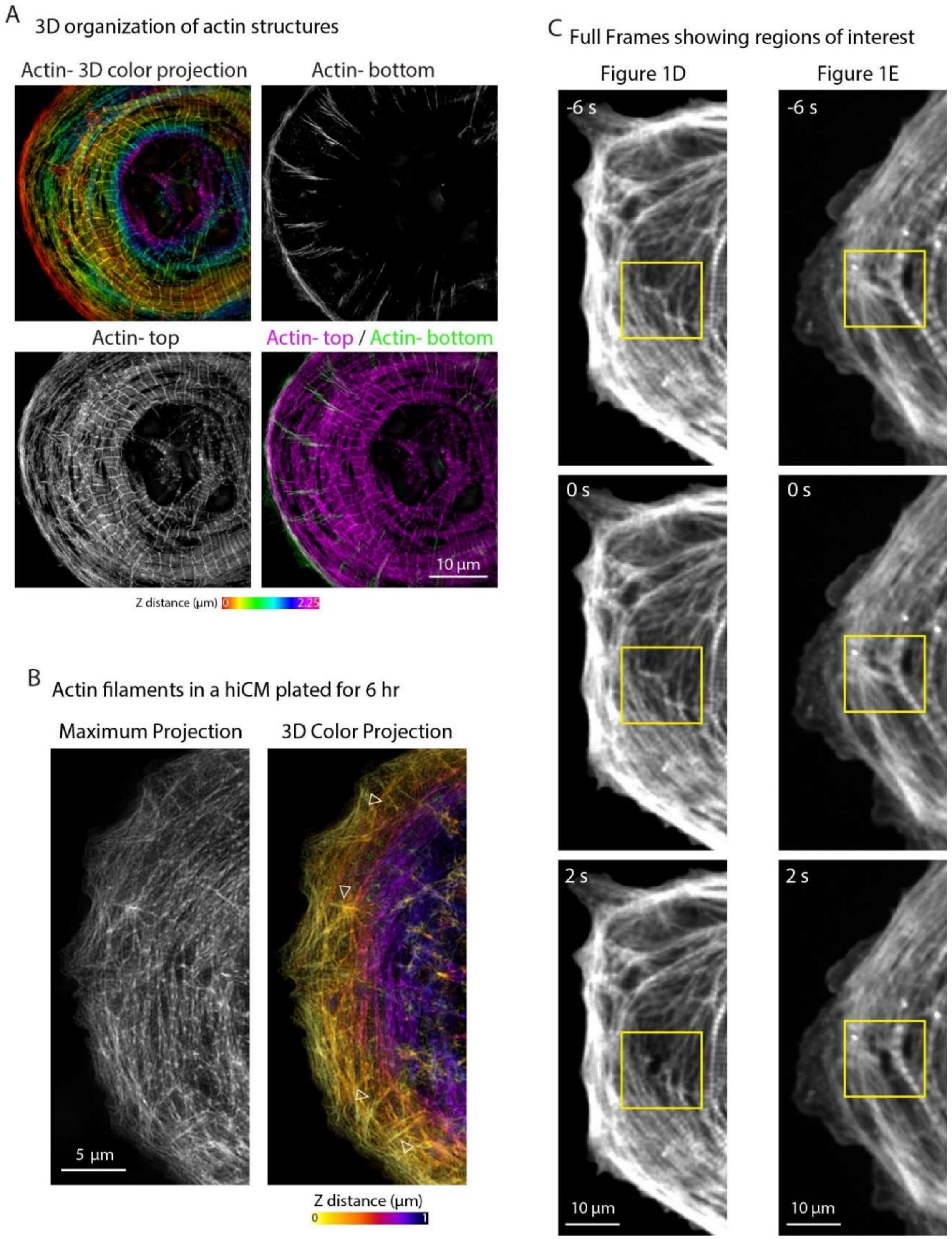

Figure 5-S1:

A) Different views of the SIM micrograph in Figure 5-1. Top left: Color-coded Z-projection of actin filaments as performed for Fig. 1C in Fenix et al, 2018. Total Z-depth used was 2.25 μm. Top right: “bottom” optical section showing the actin filaments associated with adhesions. Bottom left: Maximum project of Z sections excluding the bottom section. This “top” view is comprised of mostly dorsal actin filament structures. Bottom right: Overlay of “top” section (magenta) with “bottom” section (green) showing actin filament populations in myofibrils and adhesions, respectively. B) SIM of actin filaments in hiCM plated for 6 hours. Layers of actin filaments in the axial dimension are displayed using a color-coded Z-projection. Arrowheads show different dorsal stress fibers. B) Uncropped view showing region of interest used in Figure 5-1D and 1E.

Figure 5-S2: Deconvolution Widefield Microscopy of Actin Filaments in hiCMs

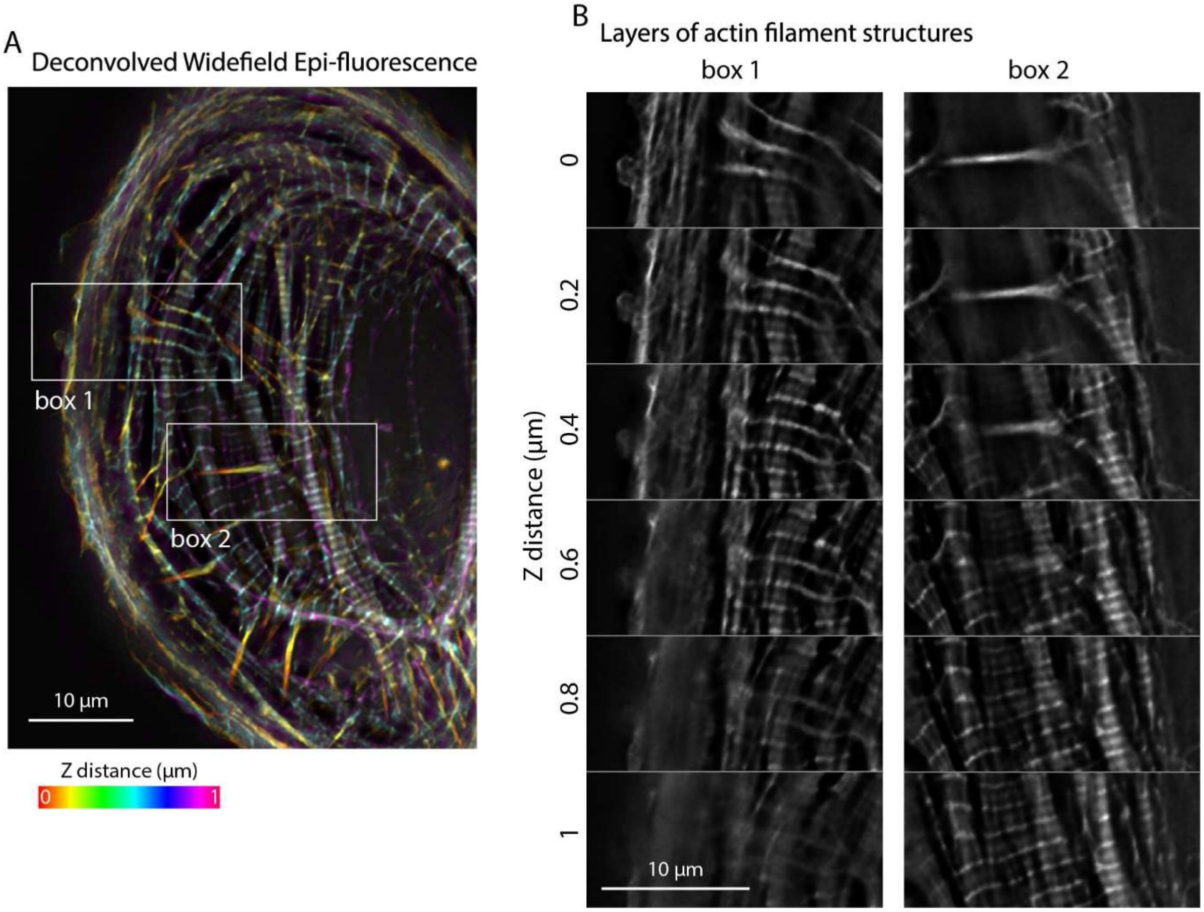

Figure 5-S2:

A) Color-coded Z-projection of actin filaments in hiCM spread for 24 hours, acquired using a widefield microscope at 150X magnification and using 0.2 μm Z-steps. The image was deconvolved using Nikon Elements software. B) Montages of ROIs depicted by box1 and box2 in (A). Each montage shows individual Z-sections depicting similar layering of actin filaments as shown by SIM in Figure 5-1

Figure 5-S3: Computer-Assisted Image Analysis Pipeline

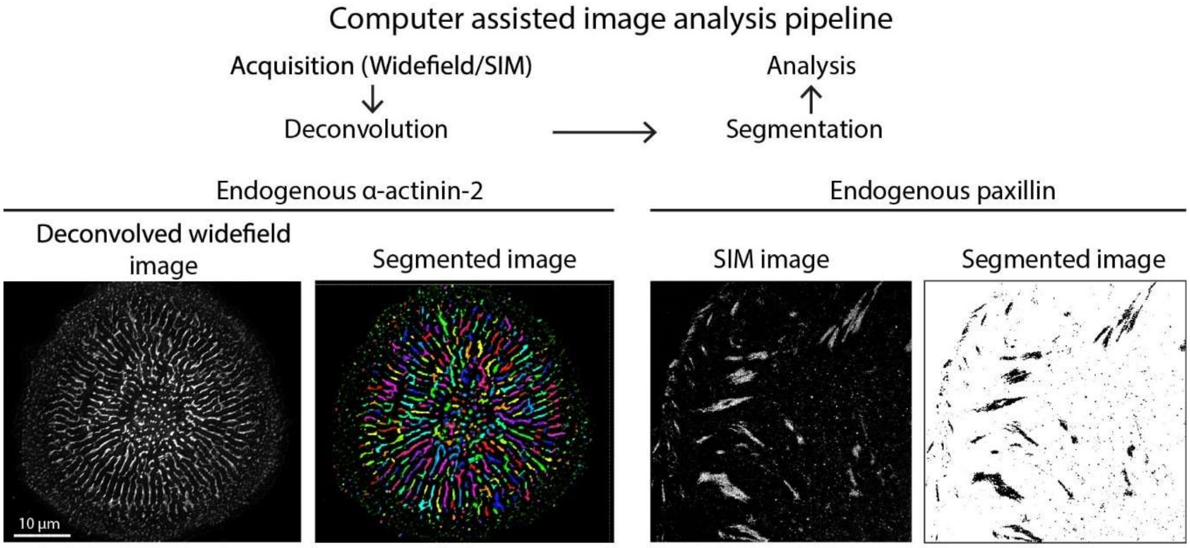

Figure 5-S3:

For measurement of α-actinin-2 Z-line lengths, widefield fluorescence image stacks (gray) were deconvolved and segmented using Nikon Elements Software (colorized binary file). The long axis lengths of Z-bodies/lines were exported to MATLAB and data was filtered and processed to generate a mean Z-line measurement for each cell. For paxillin quantification, SIM micrographs were used for thresholding in FIJI. Filtering and further analysis was performed in MATLAB.

Figure 5-S4: Effects of Knockdown Using Single siRNAs

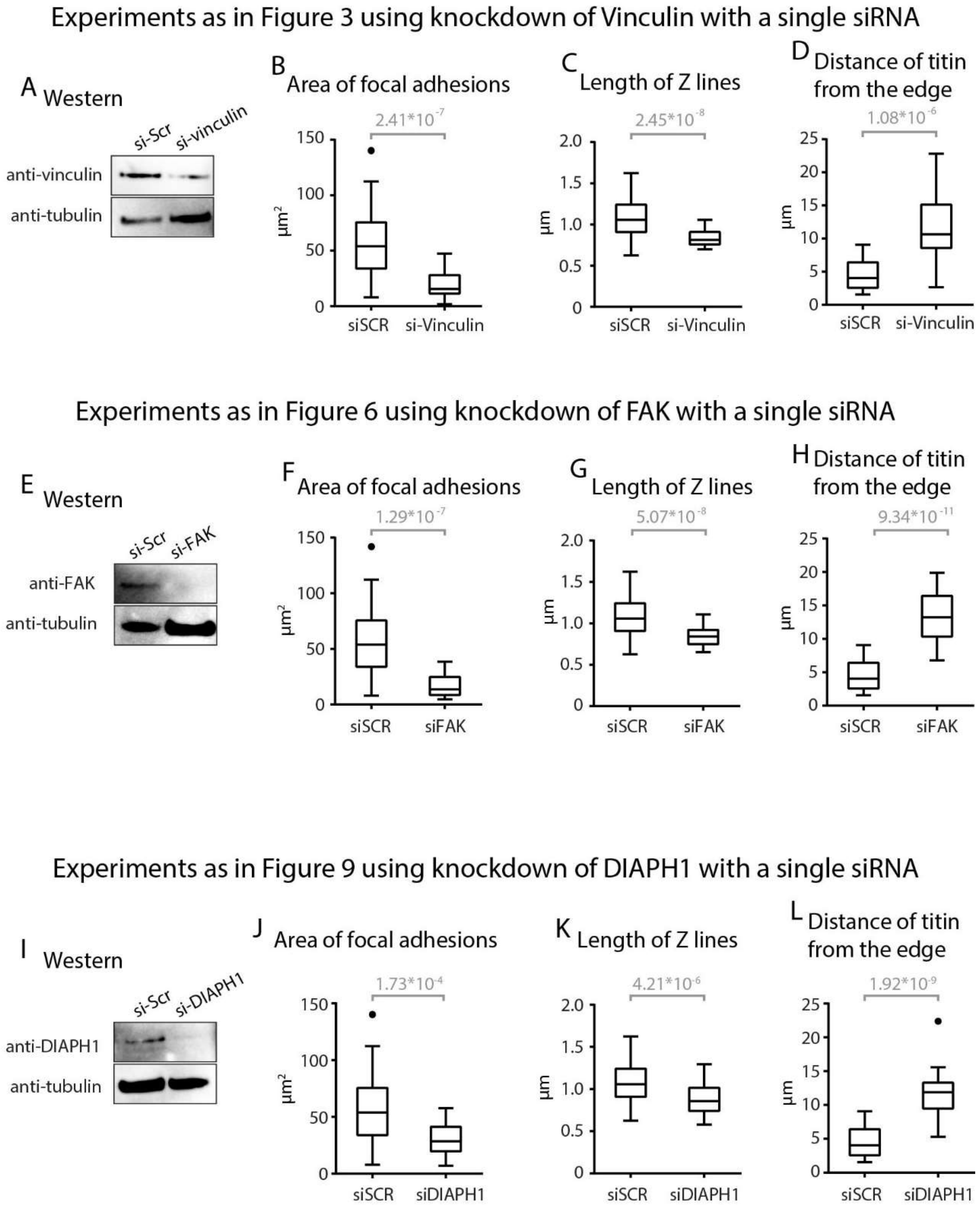

Figure 5-S4:

A) Western blot for Vinculin knockdown using a single siRNA. Tubulin was used as a loading control. B) Quantification of adhesion area in Vinculin-depleted cells. si-Vinculin: n= 20 cells, N= 3 independent experiments. The si-Scr dataset is the same as Fig. 3D. C) Quantification of average length of Z-lines in Vinculin-depleted cells. si-Vinculin: n= 30 cells, N= 3 independent experiments. The si-Scr dataset is the same as Fig. 3E. D) Quantification of distance of titin localization from the cell edge. si-Vinculin: n= 21 cells, N= 3 independent experiments. The siScr dataset is the same as Fig. 3F. E) Western blot for FAK knockdown using a single siRNA. Tubulin was used as a loading control. F) Quantification of adhesion area in FAK-depleted cells. si-FAK: n= 20 cells, N= 3 independent experiments. The si-Scr dataset is the same as Fig. 3D. G) Quantification of average length of Z-lines in FAK-depleted cells. si-FAK: n=31 cells, N= 3 independent experiments. The si-Scr dataset is the same as Fig. 3E. H) Quantification of distance of titin localization from the cell edge. si-FAK: n= 21 cells, N= 3 independent experiments. The si-Scr dataset is the same as Fig. 3F. I) Western blot for DIAPH1 knockdown using a single siRNA. Tubulin was used as a loading control. J) Quantification of adhesion area in DIAPH1-depleted cells. si-DIAPH1: n= 20 cells, N= 3 independent experiments. The si-Scr dataset is the same as Fig. 3D. K) Quantification of average length of Z-lines in DIAPH1- depleted cells. si-DIAPH1: n= 30 cells, N= 3 independent experiments. The si-Scr dataset is the same as Fig. 3E. L) Quantification of distance of titin localization from the cell edge. si-DIAPH1: n= 21 cells, N= 3 independent experiments. The si-Scr dataset is the same as Fig. 3F.

Figure 5-S5: Full length talin-mEGFP expression in hiCMs

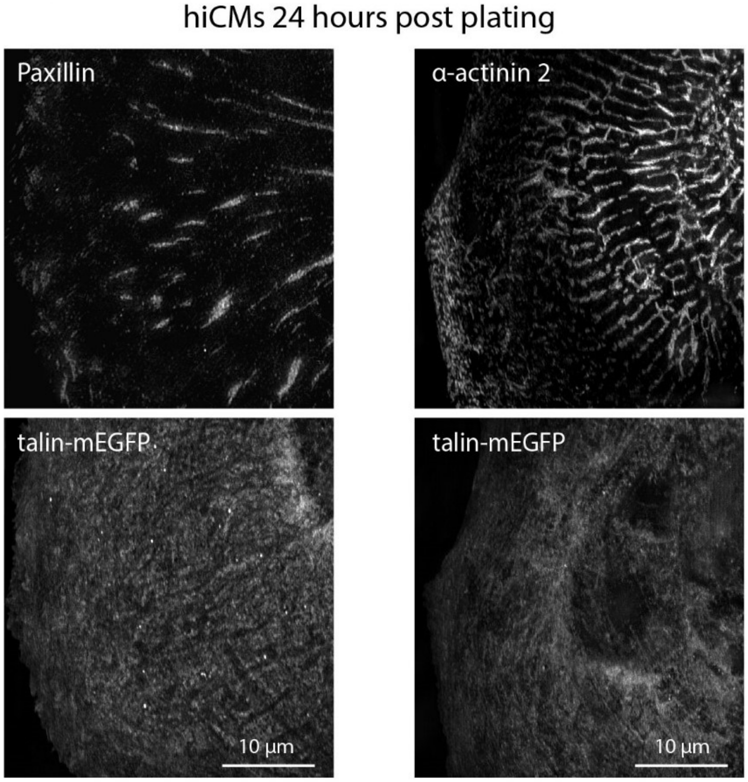

Figure 5-S5:

Paxllin (top left panel) and α-actinin 2 (top right panel) in hiCMs that are expressing talin-mEGFP (bottom panels).

Figure 5-S6: Effects of FAK Inhibition and Increased Fibronectin Concentration on Z-Lines and Adhesions.

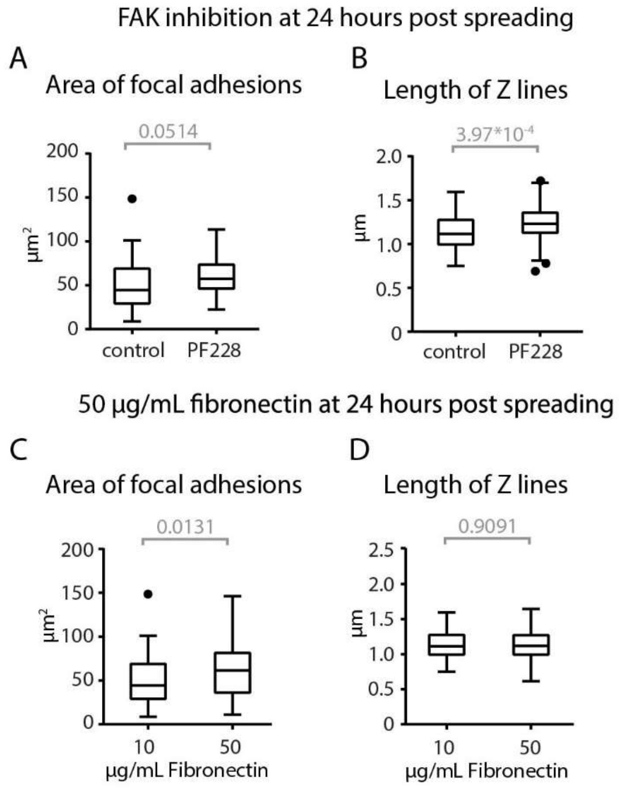

Figure 5-S6:

Tukey plots of Z-line lengths and adhesion area upon FAK inhibition (A-B) and increasing fibronectin concentration (C-D) in hiCMs spread for 24 hours. Z-lines: Control: n= 75 cells, N= 3 independent experiments; PF-228: n= 128 cells, N= 4 independent experiments; 50 µg/mL fibronectin: n= 204 cells, N= 6 independent experiments. Adhesions: Control: n= 48 cells, N= 5 independent experiments; PF-228: n= 39 cells, N= 4 independent experiments; 50 µg/mL fibronectin: n= 59 cells, N= 6 independent experiments. Exact p-values stated over graphs.

Materials and Methods

Cell Culture

Human iPSC-derived cardiac myocytes (CMM-100-012-000.5, Cellular Dynamics, Madison, WI) were cultured as per manufacturer's instructions in proprietary manufacturer provided cardiac myocyte maintenance medium in polystyrene 96-well cell culture plates.

Cells were maintained at 37°C and 5% CO_2. For re-plating hiCMs onto glass substrates, cells were washed 2 times with 100 µL 1x PBS with no Ca^{2+}/Mg^{2+} (PBS*, 70011044, Gibco, Grand Island, NY). PBS* was completely removed from hiCMs and 40 µL 0.1% Trypsin-EDTA with no phenol red (15400054, Gibco, Grand Island, NY) was added to hiCMs and incubated at 37°C for 2 minutes. Following incubation, the cells were washed 3 times with trypsin, the plate rotated 180 degrees, and washed another 3 times. Trypsinization was then quenched by adding 160 µL of culture media and total cell mixture was pipetted into a 1.5 mL Eppendorf tube. Cells were centrifuged at 200xg for 5 minutes, and the supernatant was aspirated. The cell pellet was re-suspended in 200 µL of culture media and plated on 35 mm dishes with a 10 mm glass bottom (D35-10-1.5-N; CellVis, Sunnydale, CA) pre-coated with 10 µg/mL fibronectin (354008, Corning) for 1 hr at 37°C.

Chemicals

FAK inhibitor PF-228 (PZ0117) was purchased from Sigma. Alexa Fluor 488-phalloidin (A12379), Alexa Fluor 568-phalloidin (A12380), Alexa Fluor 488-goat anti-mouse (A11029), Alexa Fluor 488-goat anti-rabbit (A11034), Alexa Fluor 568-goat-anti-rabbit (A11011), and Alexa Fluor 568-goat anti-mouse (A11004) antibodies were purchased from Life Technologies (Grand Island, NY).

Mouse anti-Paxillin (1:200, 610051) and mouse anti-FAK (1:500, 610088) antibodies were purchased from BD Biosciences. Rabbit anti-FAK pY357 (1:200, ab81298) was purchased from

Abcam. Mouse anti-α-actinin 2 (1:200, A7811) was purchased from Sigma Aldrich. Titin (9D10) antibody was purchased from the Developmental Studies Hybridoma Bank (University of Iowa). Primary antibody conjugation was performed using Mix-n-Stain kits (92233) purchased from Biotium (Fremont, CA) according to the instructions provided by the manufacturer. Paraformaldehyde (15710) was purchased from Electron Microscopy Sciences (Hatfield, PA). Triton X-100 (BP151100) was purchased from Fischer Scientific (Suwanee, GA).

Fixation and immunostaining

Cells were fixed with 4% paraformaldehyde (PFA) in PBS at room temperature for 20 min and then permeabilized for 5 min with 1% Triton X-100/4% PFA in PBS. For actin visualization, phalloidin 488 or 568 in 1× PBS (15 µl of stock phalloidin per 200 µl of PBS) was used for 2 hours at room temperature. For immunofluorescence experiments, cells were blocked in 10% bovine serum albumin (BSA) in PBS for 20 min, followed by antibody incubations.

For visualizing titin, a live cell extraction was performed to remove cytoplasmic background as described previously[167]. Briefly, a cytoskeleton-stabilizing live-cell extraction buffer was made fresh containing 2 ml of stock solution (500 mM 1,4-piperazinediethanesulfonic acid, 25 mM ethylene glycol tetra acetic acid, 25 mM $MgCl_2$), 4 ml of 10% polyoxyethylene glycol (PEG; 35,000 molecular weight), 4 ml H2O, and 100 µl of Triton X-100, 10 µM paclitaxel, and 10 µM phalloidin. Cells were treated with this extraction buffer for 1 min, followed by a 1-min wash with wash buffer (extraction buffer without PEG or Triton X-100). Cells were then fixed with 4% PFA for 20 min, followed by antibody labeling. VectaShield with DAPI (H-1200, Vector Laboratories Inc., Burlingame, CA) was used for mounting.

Protein Expression

For protein expression in hiCMs, 200 ng plasmid and 0.4 µl ViaFect (E4981, Promega, Madison WI) were added to a total of 10 µl of Opti-MEM (ThermoFisher, Waltham, MA) and added to a single well of hiCMs in a 96 well plate. The transfection was incubated overnight (~16 hrs) prior to plating for imaging.

Plasmids

All plasmids used in this study are available from Addgene (Cambridge, MA). mCherry-Alpha-Actinin2-N-18 was a gift from Michael Davidson (Addgene plasmid # 54974). mApple-Lifeact-7 was a gift from Michael Davidson (Addgene plasmid # 54747). mEmerald-Lifeact-7 was a gift from Michael Davidson (Addgene plasmid # 54148). mCherry-Paxillin-22 was a gift from Michael Davidson (Addgene plasmid # 55114) [179]. EGFP-Talin-H-18 was a gift from Michael Davidson (Addgene plasmid # 56448). EGFP-Talin-CW-18 was a gift from Michael Davidson (Addgene plasmid # 56446).

Knockdown Experiments

Knockdowns for FAK (PTK2), DIAPH1 and VCL were performed using Accell SmartPool siRNA (PTK2: E-003164-00-0005; DIAPH1: E-010347-00-0005; VCL: E-009288-00-0005; scrambled control: D-001910-10-05) purchased from GE Dharmacon. Experiments were performed in 96-well culture plates, using the TransIT-TKO transfection reagent using instructions provided by the manufacturer (MIR2154, Mirus Bio). Single siRNA-mediated knockdown experiments were performed using PTK2: A-003164-21-0005; DIAPH1: A-010347-14-0005; VCL: A-009288-13-0005; and scrambled control: D-001910-10-05 purchased from GE Dharmacon. Three consecutive rounds of knockdown were performed to deplete protein levels. Following knockdown, cells were re-plated onto glass substrates for 24 hours and fixed for immunofluorescence or lysed for western blotting.

Western Blotting

Gel samples were prepared by mixing cell lysates with LDS sample buffer (Life Technologies, NP0007) and Sample Reducing Buffer (Life Technologies, NP0009) and boiled at 95°C for 5 minutes. Samples were resolved on Bolt 4-12% gradient Bis-Tris gels (Life Technologies, NW04120BOX). Protein bands were blotted onto a nylon membrane (Millipore). Blots were blocked using 5% nonfat dry milk (Research Products International Corp, Mt. Prospect, IL, M17200) in TBST. Antibody incubations were also performed in 5% NFDM in TBST. Blots were developed using the Immobilon Chemiluminescence Kit (Millipore, WBKLS0500).

Structured Illumination Microscopy

SIM imaging and processing was performed using a GE Healthcare DeltaVision OMX equipped with a 60×1.42 NA Oil objective and sCMOS camera or using a Nikon N-SIM equipped with a 100X 1.49 NA Oil objective and EMCCD camera.

Fluorescence, Live-Cell Microscopy, and Focused Laser-Mediated Cutting

High-resolution wide-field fluorescence images (for Z-line measurement) and live imaging of actin filaments (to measure MSF translocation rates) were acquired on a Nikon Eclipse Ti equipped with a Nikon 100× Plan Apo 1.45 numerical aperture (NA) oil objective and a Nikon DS-Qi2 CMOS camera. Live imaging for Figure 5-2 and focused laser mediated cutting for Figure 5-1 was performed on a Nikon Spinning Disk confocal microscope equipped with a 60X 1.4 NA objective and an Andor iXON Ultra EMCCD camera, provided by the Nikon Center of Excellence, Vanderbilt University. Cutting of dorsal stress fibers was performed using a 100 mW UV laser (Coherent technologies) at 75% power, using a dwell time of 500 μs for a total period of 1 second. TIRF imaging was performed using a Nikon TiE inverted light microscope equipped with a 100x/1.49 NA TIRF objective, and an Andor Neo sCMOS camera. was Cells were maintained at 37°C with 5% CO2 using a Tokai Hit stage incubator.

Quantification and Statistical Analysis

To measure Z-line length in hiCMs, Z-sections were acquired at 200 nm intervals using widefield imaging at 100X with 1.5 Zoom. Images were deconvolved with the Automatic deconvolution using Nikon Elements software. All α-actinin 2 structures were 3D thresholded manually in Nikon Elements using the clean algorithm 3 times. The lengths of the major axis of each body were exported from Elements for the calculation of Z-line length. Using a length minimum exclusion criterion of 0.2 μm, Z-line lengths were calculated using MATLAB (supplementary software).

To measure sum adhesion area of hiCMs, one single Z-slice of a reconstructed SIM image where the focal adhesions were in focus was selected. Focal adhesions were thresholded and the sum area was measured in Fiji, using a size minimum exclusion criterion of 0.1 μm^2.

For measurement of the distance of titin to the edge (Figure 5-3F-G), we measured the length of a line from the edge to the first titin ring in Fiji. The researcher analyzing the data was blinded to treatment groups.

For measurement of MSF translocation rates, hiCMs were transfected with Lifeact-mApple and allow to spread for 16 hours post plating. Two Z-sections were acquired, one at the ventral plane and one 0.5 μm above the ventral plane, at 2-minute intervals for a total time of 2 hours. Maximum Z-projections were performed on the time montages, followed by alignment of the image stacks using the StackReg plugin in Fiji. A 3-pixel thick line was drawn parallel to the direction of MSF translocation to create a kymograph, following which the rates were measured for MSFs. 1-3 trajectories were counted for each cell.

Statistical significance was determined using unpaired two-tailed Student’s t-tests performed in MATLAB or Excel. Each experiment was performed a minimum of 3 times and each cell was counted as a data point and was pooled over the biological replicates. All data was displayed as Tukey plots, which were represented with boxes (with Q1, median, Q3 percentiles), whiskers (minimum and maximum values within 1.5 times interquartile range) and outliers (solid circles). No outliers were removed from the analysis. For western blot graphs, error bars represent standard error of the means.

CHAPTER 6

SARCOMERE FORMATION IN CARDIAC MYOCYTES IS ONLY PARTIALLY DEPENDENT ON MYOSIN II-BASED TENSION

Introduction

The sarcomere is the essential unit of contraction, making up the force behind a heartbeat[1]. Sarcomeres are structures contained within cardiac muscle cells, or cardiac myocytes. When heart cells grow larger, that is, when they undergo hypertrophy, new sarcomeres are added laterally. However, it is unknown how sarcomeres form initially and how new sarcomere precursors add to pre-formed sarcomeres. Several decades of studies have separated the field into differing models of sarcomere formation, however, these studies were almost entirely done with manual quantification[80]. Here, I present a preliminary study using both qualitative and quantitative techniques to probe the role of contractility in sarcomere formation using an unbiased automated quantification tool.

Contractility has been shown previously to be required for sarcomere formation. Cellular contractility is defined by a cells ability to apply contractile forces to its environment and within the cell, while also sensing forces done to the cell. Frequently, and in this case, cellular contractility refers to the forces myosin motors apply to actin filaments. A recent study has proposed that nonmuscle myosins are *not* required for sarcomere formation, by treating cardiac myocytes with Blebbistatin, a potent myosin-II inhibitor, and by using CRISPR to knock out NMIIA and/or NMIIB. They treated cardiac myocytes with pre-formed sarcomeres with Blebbistain and showed that the cells lose traction force and, eventually, their sarcomeres[78]. However, Blebbistatin also inhibits muscle myosin isoforms, and NMII's role in sarcomere formation cannot be assessed when pre-formed sarcomeres are being studied[80]. Next, the authors utilized lentiviral CRISPR KO to knock out NMIIA, NMIIB, or both. This is a creative way to knock out proteins in cardiac myocytes, as they do not divide and more classical CRISPR techniques cannot be used[78]. They determined that cells lacking NMII isoforms formed regular sarcomeres, while their images disagree. Using 5-8 cells per treatment, the authors quantified “sarcomere content” as an output for myofibril formation, calculated by a software utilizing Fourier transformation of images to frequency space, taking the summation in the Y direction of the Fourier transformation, and fitting the summation to a curve with both periodic and aperiodic components, representing the organized and non-organized structures, respectively[180]. However, Fourier transforms are sensitive to rotation, that is, the outcome of the transform changes depending on how the cell is oriented. For example, text is oriented in the horizontal direction (Figure 6-1A, top), producing a bright white line vertically in its Fourier Transform. The lines found in a Fourier Transform image represent the orientation of the original image, whereas the spacing and patterns of the bright lines represent the periodicity, patterning, and spacing of the image. If the text is rotated 45 degrees clockwise, the Fourier Transform fundamentally changes (Figure 6-A, bottom) [181]. These input images are the same image, but the outputs are vastly different. I tested the software used in Chopra et al and found the same phenomenon: the sarcomere content output of the same cell ROI changes when it is rotated. In this way, this software is generally not of use unless every cardiac myocyte is plated on a patterned substrate and each image is oriented the same exact way. This is time consuming, and the output of the software itself does not have units and does not refer to an actual, real space calculation that researchers can see reflected in the image[78].

By eye, it appears that cells depleted of NMIIA and/or NMIIB in Chopra et al. do not have proper sarcomeres by visualizing actinin2, however, their calculations determine that the sarcomere content is not significantly affected[78]. However, this manuscript showed an essential gap in the field of cardiac biology: an automated image analysis technique that measures sarcomere formation in real space.

Figure 6-1: Fourier Transforms are Susceptible to Rotation

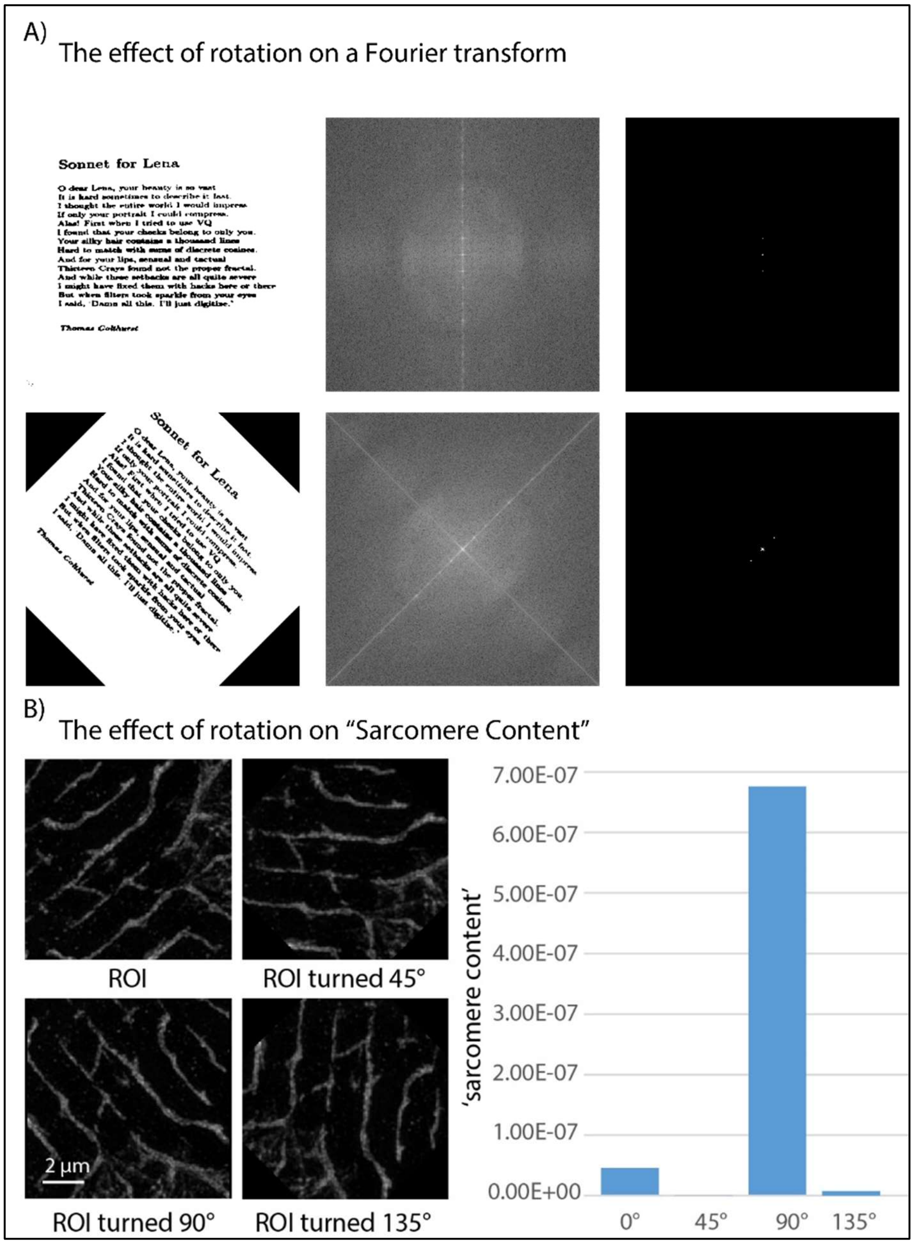

Sonnet for Lena

O dear Lena, your beauty is so vast
It is hard sometimes to describe it fast.
I thought the entire world I would impress
If only your portrait I could compress.
Alas! First when I tried to use VQ
I found that your cheeks belong to only you.
Your silky hair contains a thousand lines
Hard to match with sums of discrete cosines.
And for your lips, sensual and tactual
Thirteen Crays found not the proper fractal.
And while these setbacks are all quite severe
I might have fixed them with hacks here or there
But when filters took sparkle from your eyes
I said, 'Damn all this. I'll just digitize.'

Thomas Colthurst

Figure 6-1:

A) The effect of rotation on a Fourier transform[181]. Left: an example image of text oriented in the horizontal direction, either transformed clockwise 0 or 45 degrees. Middle: logarithm of the magnitude of the Fourier transform of left images. Right: Thresholded magnitude of the Fourier images. B) The effect of rotation on sarcomere content as calculated in Chopra et al[78]. ROI is of an actinin2-labeled cardiac myocyte, rotated 0, 45, 90, or 135 degrees clockwise.

I have developed a software that measure sarcomere formation in real space rather than frequency space, and calculates over 36 measurements with units that can be seen in the image, such as “Z-lines per cell”, “Myofibril length”, and “Z-line spacing” (Table 6-1). These calculations have always been done by-hand, which limits the number of experiments a single researcher or team can do. This software is called “sarcApp” and thresholds a-actinin-2, a marker for the Z-line, and uses geometry and trigonometry to calculate sarcomere maturity and organization. I then utilize this software to automatically quantify hundreds of cells at once to probe the role of both muscle and nonmuscle myosin II contractility in sarcomere formation. I determined thus far that while general myosin II contractility results in the reduction of sarcomere formation via actinin2 staining, titin and myomesin (widely considered more mature sarcomere components) still form sarcomeric structures. Further, muscle myosin II knockdowns show that muscle myosin II is not required for sarcomere formation. These findings support a preliminary hypothesis that nonmuscle myosin II contractility is required for local actin organization during the formation and coalescence of Z-bodies, but not in localization and organization of titin and myomesin.

Results

sarcApp Development and Functionality

sarcApp was developed initially as a tool to quantify a-actinin-2 in cardiac myocytes to measure sarcomere structure in an unbiased and automatic way. In order to do so, first I use machine learning techniques to threshold deconvolved spinning disk images of immunolocalized a-actinin-2. Briefly, the software first calculates statistics and morphology information about each actinin2-positive structure in the cell. Each structure is initially classified as either a potential Z-body or Z-line based on size. Then, each Z-line is paired to other Z-lines in the cell based on shape, orientation, and location in order to partition Z-lines that belong to the same myofibril. Finally, statistics are calculated on each Z-line, myofibril, and Z-body in the cell (Figure 6-2C).

Figure 6-2: sarcApp Appearance and Functionality

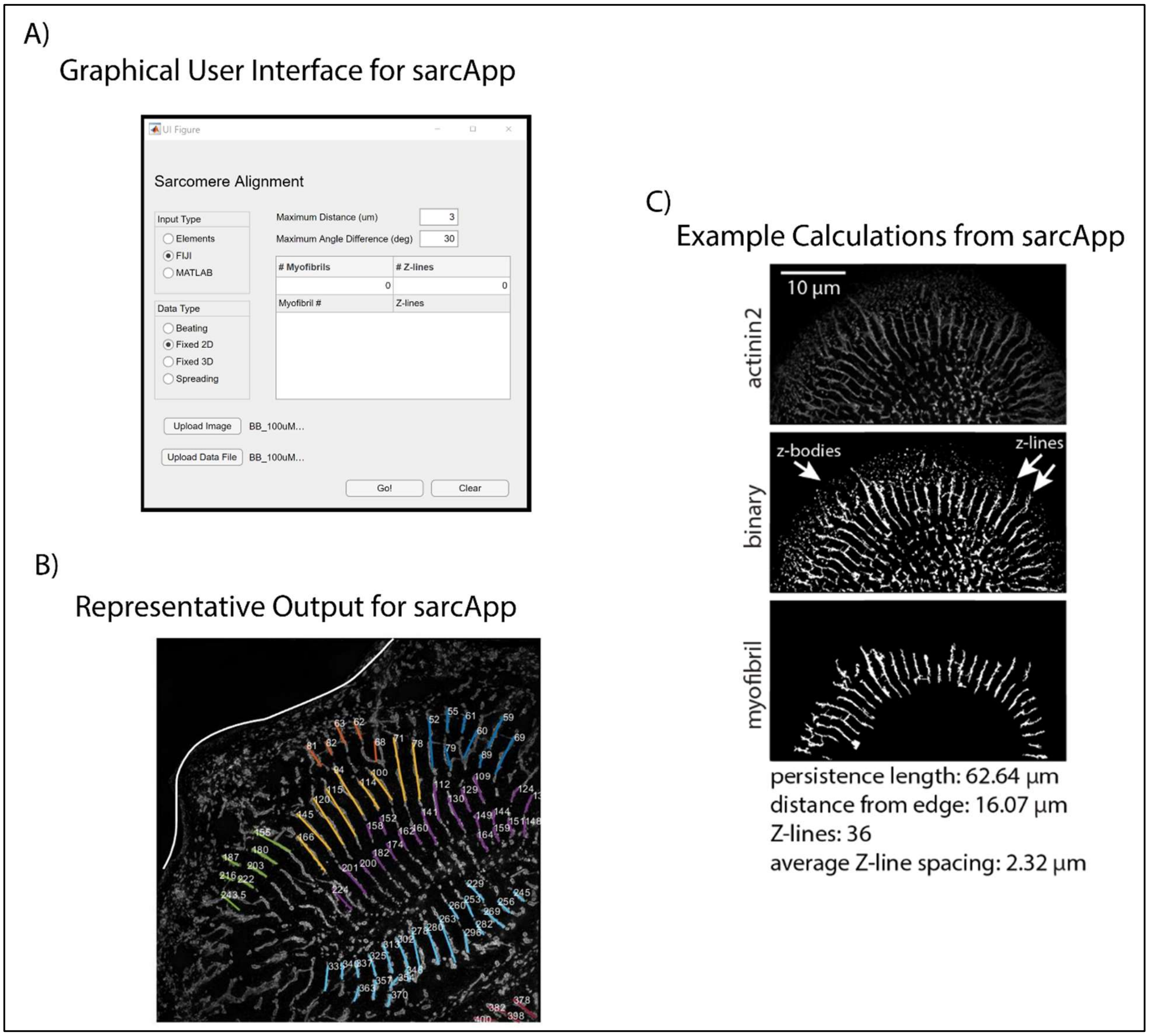

A) Graphical User Interface for sarcApp

UI Figure

Sarcomere Alignment

Input Type

○ Elements
● FIJI
○ MATLAB

Data Type

○ Beating
● Fixed 2D
○ Fixed 3D
○ Spreading

Maximum Distance (um): 3

Maximum Angle Difference (deg): 30

# Myofibrils	# Z-lines
0	0

Myofibril #	Z-lines

Upload Image: BB_100uM...

Upload Data File: BB_100uM...

B) Representative Output for sarcApp

C) Example Calculations from sarcApp

persistence length: 62.64 μm
distance from edge: 16.07 μm
Z-lines: 36
average Z-line spacing: 2.32 μm

Figure 6-2:

A) Graphical user interface for sarcApp, written in MATLAB programming language. Inputs include an actinin2 image and an optional file with threshold information. Information can be imported from Nikon Elements and FIJI, or can be calculated within the software. Images can be fixed 2D images, fixed 3D images, live beating movies, or long-term spreading movies. B) Representative example for sarcApp output. White line denotes the cell edge, whereas different colored lines represent Z-lines. Each color denotes a different myofibril, and each number represents the Z-line number, listed in the output spreadsheet so individual Z-lines can be tracked. C) An example actinin2 image, its binary, and one defined myofibril in the region of interest, calculated using sarcApp. Below are four examples of measurements produced by sarcApp: persistence length (overall myofibril length), distance of the myofibril from the edge, number of Z-lines, and average spacing between neighboring Z-lines.

There are several outputs to sarcApp, listed in Table 6-1. sarcApp was initially developed as a graphical user interface (Figure 6-2B) which can accommodate either pre-thresholded images from other platforms, and can also accept raw fluorescent images to produce a threshold and quantify particle properties automatically. sarcApp outputs an image of the cell with color-coded myofibrils and numbered Z-lines, along with an excel spreadsheet of each calculation performed and the raw data used, numbered the same way so users can analyze individual Z-lines of interest afterwards (Figure 6-2B).

Myosin II-Based Contractility is Required for Thin Filament organization

To test sarcApp's functionality and accuracy, I quantified a previously published dataset from our lab of NMIIA or NMIIB knockdown hiCMs. These data were quantified manually, which is a time-consuming process which can be prone to bias unless researchers are blinded. When quantified using sarcApp, the same conclusions were found: NMIIA and NMIIB are each required for sarcomere assembly (Figure 6-S1). However, these images were only stained for actinin2 and actin, which are only part of the overall sarcomere structure. Further, cardiac myocytes contain alpha and beta cardiac myosin II, which are also found in cofilaments with NMIIA and NMIIB near the sarcomere-forming region of the cell, further from the leading edge. In order to further investigate the role of myosin II-based contractility in all aspects of sarcomere formation, I plated cardiac myocytes on a dish and treated with Blebbistatin 1 hour post-plating and fixed them after 6, 12, or 24 hours (Figure 6-3A). Blebbistatin inhibits nonmuscle and muscle myosin II isoforms. When cardiac myocytes are trypsinized and re-plated, they lose and re-form their sarcomeres over 24 hours, producing an ideal model system for sarcomere formation. As mentioned previously, waiting until 24 hours post-plating to perform perturbations measures sarcomere maintenance and stability rather than formation.

Table 6-1: Outputs of sarcApp

Outputs per Cell	**Outputs per Myofibil**	**Outputs per MSF**	**Outputs for remaining unorganized structures**
Total number of myofibrils	Total number of Z-lines	Total number of Z-bodies	Number of unorganized structures
Total number of Z-lines	Average length of Z-lines	Average length of Z-bodies	Average length of unorganized structures
Average myofibril persistence length	Average spacing between Z-lines	Average spacing between Z-bodies	Average spacing between unorganized structures
Average Z-line length	Distance from the cell edge	Distance from the cell edge	Distance from the cell edge
Total number of Z-bodies	Angle of myofibril long axis	Angle of MSF long axis	
Average MSF persistence length	Persistence length	Persistence Length	
Average size of all actinin2 puncta within the cell			

Figure 6-3: Sarcomere Formation is Inhibited Upon Myosin II-Inhibition

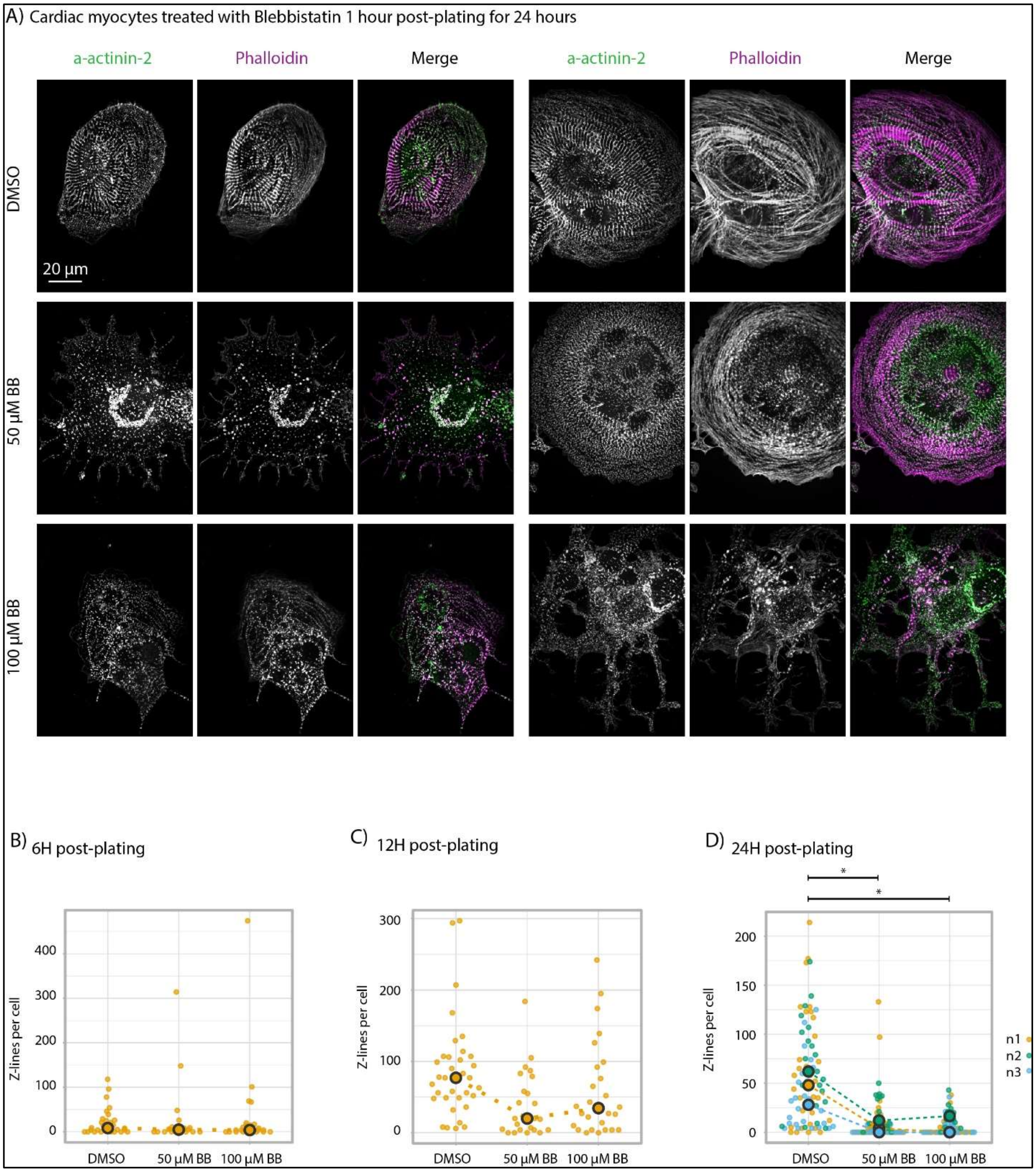

Figure 6-3:

A) Representative (Left) and most organized (Right) images of cardiac myocytes treated with DMSO or 50-100 µm Blebbistatin 1 hour post-plating and fixed 24 hours-post plating. B) Quantification of Z-lines per cell using sarcApp for cells treated with DMSO or 50-100 µm Blebbistatin 1 hour post-plating and fixed 6 hours post-plating. C) Quantification of Z-lines per cell using sarcApp for cells treated with DMSO or 50-100 µm Blebbistatin 1 hour post-plating and fixed 12 hours post-plating. D) Quantification of Z-lines per cell using sarcApp for cells treated with DMSO or 50-100 µm Blebbistatin 1 hour post-plating and fixed 24 hours post-plating.

Figure 6-3A (left) shows a 24 hour cell in each treatment group that represents the mean calculated number of Z-lines per cell (quantified Figure 6-3D). DMSO-treated hiCMs reliably formed sarcomeres over 24 hours. The number of Z-lines per cell was significantly reduced in cells treated with either 50 or 100 µm Blebbistatin. Figure 6-3A (right) shows the cell in each treatment group that had the most Z-lines per cell over all three datasets, to show that even the most organized Blebbistatin-treated cells did not have the same structures as DMSO-treated cells. Preliminary calculations suggest no difference between DMSO-treated and Blebbistatin-treated cells 6 hours post-plating, before most sarcomeres have begun forming (Figure 6-3B). The differences in DMSO- and Blebbistatin-treated cells appears to arise around 12 hours post-plating (Figure 6-3C), however, these data are preliminary and must be repeated to confirm. Further, sarcApp outputs several more measurements than Z-lines per cell, some of which may show differences in sarcomere organization, structure, and spacing that are not detectable by eye in these first experiments. As actinin2 is only one portion of a sarcomere, I also stained these cells with phalloidin to localize F-actin, the cytoskeletal component of the thin filament of the sarcomere. Indeed, organized F-actin thin filament structures are less detectable by eye in Blebbistatin-treated cells. Taken together, these data provide preliminary insight into the role of muscle myosin II contractility in formation of the thin filament structure and sarcomere borders (Z-lines).

Myosin II-Based Contractility is Not Required for Titin and Myomesin Organization

Titin is a springlike, massive protein that spans from the Z-line to the M-line of a sarcomere. Myomesin is an M-line protein required for muscle myosin crosslinking in the sarcomere. Titin and myomesin, along others, are widely considered markers of mature sarcomeres and are proposed in most sarcomere assembly models to not load onto the sarcomere until the thin filament is produced and organized. I wished to test the localization of titin and myomesin in myosin II-inhibited cardiac myocytes to investigate which components of the sarcomere are affected by cellular contractility. As before, phalloidin staining of F-actin filaments showed a disorganized cytoskeleton in Blebbistatin-treated cells, while control cells has organized myofibrils (Figure 6-4). Control cells show a canonical pattern of titin and myomesin localization, with the titin antibody recognizing the I/Z interface region of titin and localizing directly to either side of the Z-line and myomesin localizing directly between Z-lines at the M-line. Interestingly, in 100uM Blebbistatin-treated cells, the overall ultrastructure of the sarcomere appeared changed, but striated arrays of titin and myomesin still existed in the same pattern toward the middle of the cell (Figure 6-4, insets). While sarcApp can only currently measure actinin2, a goal of this software is to eventually measure titin and myomesin as well, which will likely provide insight into these small striated structures. My current hypothesis is that myosin II-based tension is not required for assembly of some sarcomere components, but is required for overall total sarcomere formation.

Figure 6-4: Myosin II-Based Contractility is only Partially Required for Titin and Myomesin Striation

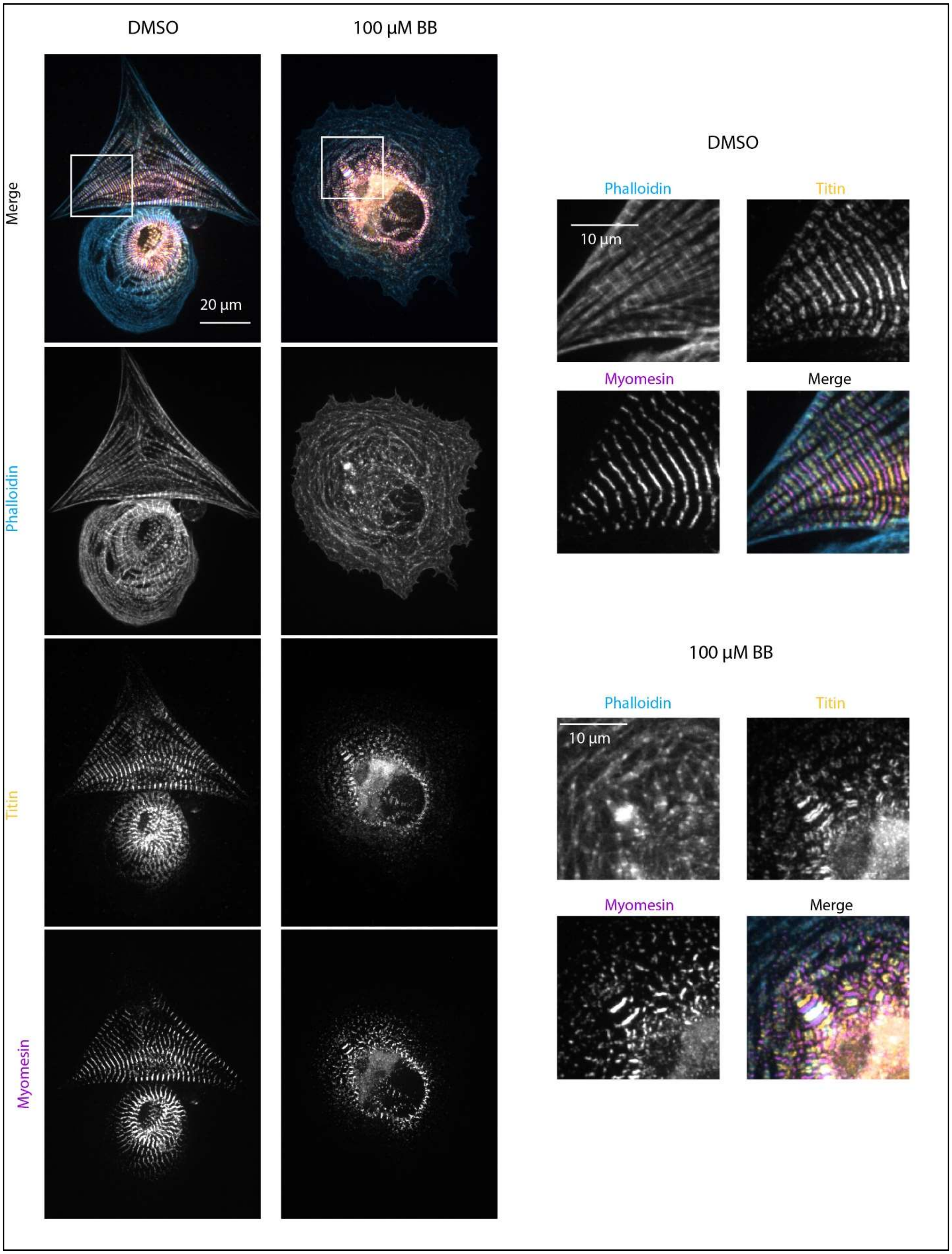

Figure 6-4:

Cardiac myocytes treated with either DMSO or 100 uM Blebbistatin 1 hour post-plating, then fixed and stained 24 hours post-plating and imaged on a Nikon Spinning Disk. Insets show regions of striation.

Cardiac Myosin II Isoforms are Not Required for Sarcomere Assembly

Because Blebbistatin inhibits both nonmuscle myosin II and cardiac myosin II, I next wished to test if the lack of sarcomeres in blebbistatin-treated cells was due to loss of nonmuscle myosin contractility, muscle myosin contractility, or both. Cardiac myocytes express both alpha cardiac myosin (gene name MYH6) and beta cardiac myosin (gene name MYH7), in different ratios depending on the developmental maturity of the cell. While Chopra et al. demonstrated that MYH7 was required for sarcomere formation in cardiac myocytes (but MYH6 was not), other studies suggest that neither myosin is required, at least in skeletal muscle. To study this, I turned to siRNA-mediated knockdown of either a scrambled sequence, MYH6, or MYH7, then plated the cells for 24 hours to examine sarcomere structure (Figure 6-5A). Preliminary experiments with 70-90% knockdown show sarcomeres that appear similar to control sarcomeres, with no significant difference in Z-lines per cell (Figure 6-5B-C). There appears to be a slight increase in Z-lines per cell in siMYH7 cardiac myocytes, which contrasts with the findings from Chopra et al. that MYH7 KO cells have less sarcomere content while MYH6 KO cells have more sarcomere content. It will be important to follow up on these experiments and examine all outputs of sarcApp to identify any sarcomere components that are altered upon muscle myosin knockdown.

Figure 6-5: Sarcomere Formation is not Affected by Knockdown of Muscle Myosin Isoforms

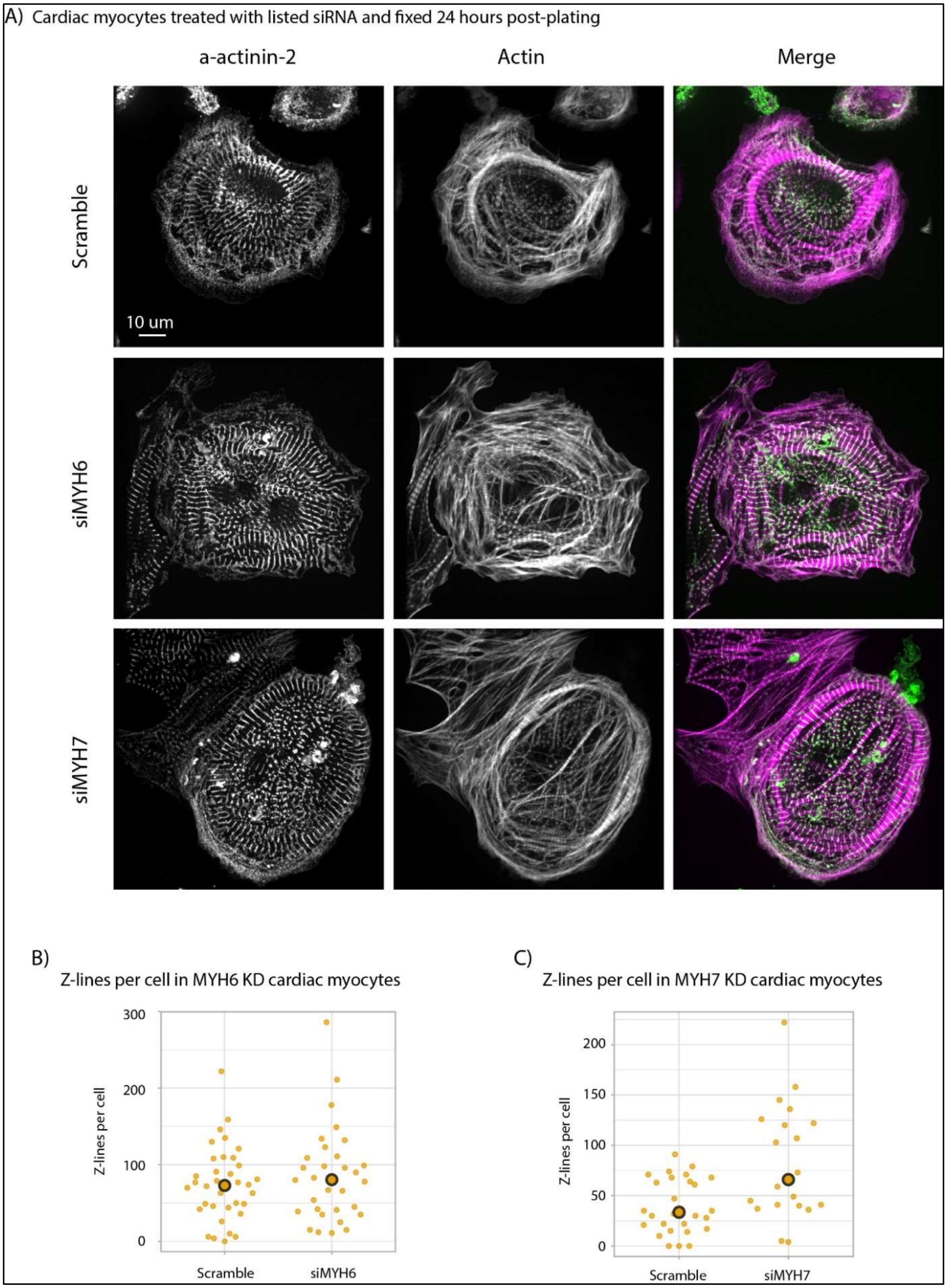

A) Cardiac myocytes treated with listed siRNA and fixed 24 hours post-plating

B) Z-lines per cell in MYH6 KD cardiac myocytes

C) Z-lines per cell in MYH7 KD cardiac myocytes

Figure 6-5:

A) Cardiac myocytes treated with siRNA to a scrambled sequence, MYH6 (alpha cardiac myocyte), or MYH7 (beta cardiac myosin), then fixed and stained 24 hours post-plating. B) Quantification of Z-line per cell using sarcApp of cardiac myocytes given siRNA to either a scrambled sequence of MYH6. C) Quantification of Z-lines per cell using sarcApp of cardiac myocytes given siRNA to either a scrambled sequence of MYH7.

Conclusions and Future Directions

This descriptive, but quantitative, study provides a framework for automatically quantifying several aspects of sarcomere formation and structure in an unbiased way. There are several possible next steps, including mining the sarcApp output data to determine which specific components of the sarcomere blebbistatin treatment and/or muscle myosin knockdown. Introducing titin, myomesin, phalloidin, and adhesion quantification into sarcApp will provide even more markers to quantify. Sarcomeres are frequently quantified using one or two proteins, when sarcomeres are indeed dense structures with several independent components. One must quantify and observe as many of these components as possible in order to make the most accurate hypotheses about sarcomere formation and maintenance.

These data implicate nonmuscle myosin II-based contractility in thin filament and Z-line formation, while muscle myosin does not appear to be required. However, cells with inhibited nonmuscle myosin II contractility can still form striated titin and myomesin patterns, suggesting the formation of A-bands. Whether muscle myosin localizes in stacks typical of the A-band in Blebbistatin has not been determined and is a relevant follow up study, and I hypothesize they do. However, it is important to consider what these findings mean in the grand scheme of sarcomere formation. Studies have previously proposed a model of local thin filament organization requiring tropomodulins and nonmuscle myosins[182,183]. Almenar-Queralt et al. propose that tropomodulin regulates actin filament length during sarcomere formation in skeletal muscle cells, by rearranging unorganized thin filaments into striated myofibrils, moving laterally until Z-line and M-line components arrange laterally[182]. McKenna et al. proposed a similar mechanism in 1986, hypothesizing that newly formed premyofibrils with Z-bodies or short Z-lines on actin thin filaments shift side to side until the myofibrils are aligned in a trial and error process[183]. This hypothesis of Z-bodies shifting through actin capping and rearrangement fits with a model I am hypothesizing, that nonmuscle myosins in muscle stress fibers crosslink actin filaments and provide the contractility required for such a rearrangement, along with tropomodulin to cap the actin pointed end at the desired length, and some actin severing protein (I propose Cofilin, based on localization and its distinct relationship with vinculin)[173,184]. Cofilin also has been shown to sever filaments in noncontractile stress fibers, regulating their formation and only allowing properly-formed contractile stress fibers to develop further[173] . Of course, this hypothesis requires stringent testing and experiments, which are on the horizon.

Materials and Methods

Cell Culture

Human iPSC-derived cardiac myocytes (CMM-100-012-000.5, Cellular Dynamics, Madison, WI) were cultured as per manufacturer's instructions in proprietary manufacturer provided cardiac myocyte maintenance medium in polystyrene 96-well cell culture plates.

Cells were maintained at 37°C and 5% CO_2. For re-plating hiCMs onto glass substrates, cells were washed 2 times with 100 µL 1x PBS with no Ca^{2+}/Mg^{2+} (PBS*, 70011044, Gibco, Grand Island, NY). PBS* was completely removed from hiCMs and 40 µL 0.1% Trypsin-EDTA with no phenol red (15400054, Gibco, Grand Island, NY) was added to hiCMs and incubated at 37°C for 2 minutes. Following incubation, the cells were washed 3 times with trypsin, the plate rotated 180 degrees, and washed another 3 times. Trypsinization was then quenched by adding 160 µL of culture media and total cell mixture was pipetted into a 1.5 mL Eppendorf tube. Cells were centrifuged at 200xg for 5 minutes, and the supernatant was aspirated. The cell pellet was re-suspended in 200 µL of culture media and plated on 35 mm dishes with a 10 mm glass bottom (D35-10-1.5-N; CellVis, Sunnydale, CA) pre-coated with 10 µg/mL fibronectin (354008, Corning) for 1 hr at 37°C.

Chemicals

Alexa Fluor 488-phalloidin (A12379), Alexa Fluor 568-phalloidin (A12380), Alexa Fluor 488-goat anti-mouse (A11029), Alexa Fluor 488-goat anti-rabbit (A11034), Alexa Fluor 568-goat-anti-rabbit (A11011), and Alexa Fluor 568-goat anti-mouse (A11004) antibodies were purchased from Life Technologies (Grand Island, NY).

Titin (9D10) antibody and Myomesin (MYOM) was purchased from the Developmental Studies Hybridoma Bank (University of Iowa). Mouse anti-α-actinin 2 (1:200, A7811) was purchased from Sigma Aldrich.

Blebbistatin was purchased from Sigma (B0560) and reconstituted to 10 mM in DMSO.

Fixation and immunostaining

Cells were fixed with 4% paraformaldehyde (PFA) in PBS at room temperature for 20 min and then permeabilized for 5 min with 1% Triton X-100/4% PFA in PBS as previously described (Burnette et al., 2014). For actin visualization, phalloidin 488 or 568 in 1× PBS (15 μl of stock phalloidin per 200 μl of PBS) was used for 2 hours at room temperature. For immunofluorescence experiments, cells were blocked in 5% bovine serum albumin (BSA) in PBS for 20 min, followed by antibody incubations.

For visualizing titin and myomesin, a live cell extraction was performed to remove cytoplasmic background as described previously [167]. Briefly, a cytoskeleton-stabilizing live-cell extraction buffer was made fresh containing 2 ml of stock solution (500 mM 1,4-piperazinediethanesulfonic acid, 25 mM ethylene glycol tetra acetic acid, 25 mM $MgCl_2$), 4 ml of 10% polyoxyethylene glycol (PEG; 35,000 molecular weight), 4 ml H2O, and 100 μl of Triton X-100, 10 μM paclitaxel, and 10 μM phalloidin. Cells were treated with this extraction buffer for 1 min, followed by a 1-min wash with wash buffer (extraction buffer without PEG or Triton X-100). Cells were then fixed with 4% PFA for 20 min, followed by antibody labeling. VectaShield with DAPI (H-1200, Vector Laboratories Inc., Burlingame, CA) was used for mounting.

Knockdown Experiments

Knockdowns for MYH6 and MYH7 were performed using SmartPool siRNA (MYH6: A-012645, MYH7: A-11086) purchased from GE Dharmacon. Experiments were performed in 96-well culture plates, using the Lipofectamine RNAiMAX reagent and instructions provided by the manufacturer (ThermoFisher, LMRNA015). Following knockdown, cells were re-plated onto glass substrates for 24 hours and fixed for immunofluorescence or lysed for western blotting.

Fluorescence Microscopy

Imaging was performed on a Nikon Spinning Disk confocal microscope equipped with Apo TIRF Oil 100X 1.49 NA objective and a Photometrics Prime 95B cMOS monochrome camera, provided by the Nikon Center of Excellence, Vanderbilt University. Images were deconvolved post-acquisition using the FIJI Microvolution software plugin (Microvolution, Cupertino, CA).

CHAPTER 7

CHAPTER SUMMARIES AND FUTURE DIRECTIONS

Chapter 2 Summary

In Chapter 2, we present a strategy for identifying small molecules that induce cardiac myocyte proliferation. This screening platform was designed with the purpose of being cost-effective, straight-forward, and attainable for laboratories interested in new fields of study. As such, we chose to use purchased human iPSC-derived cardiac myocytes (hiCMs), which minimizes experiment time and cost. As a proof of concept, we screened a library of 429 kinase inhibitors and identified three small molecules which significantly increase cardiac myocyte proliferation over time.

Chapter 3 Summary

In chapter 3, we investigated the role of the Hippo pathway in density-dependent cardiac myocyte proliferation. In chapter 2, we demonstrated that cardiac myocytes have a higher proliferative capacity when plated sparsely than when plated in a dense monolayer. I then wished to determine the mechanism of this contact inhibition-related phenotype, and performed a literature search to determine any potential pathways. Serendipitously, I went to a developmental biology journal club the next week on the role of the Hippo pathway in the growing heart, and I noticed that this pathway had all of the requirements I was looking for in a potential regulatory pathway for cardiac myocyte density-dependent cell division. I first wished to perform an acute experiment to see if the Hippo pathway was altered upon loss of contact inhibition, and performed a scratch assay and stained for the downstream Hippo pathway protein YAP. Interestingly, the cardiac myocytes near the scratch had a higher nuclear YAP to cytosolic YAP ratio, which represents YAP activity and generalizes to a higher proliferative capacity. Throughout the rest of the manuscript, we showed that the Hippo pathway regulates density-dependent proliferation in a scratch assay and in population-wide studies where cells were sparsely-plated or densely-plated. Further, we showed that the proliferative capacity induced upon sparse plating of cardiac myocytes can be increased by combinatorial pharmacological perturbation of the Hippo pathway.

Chapter 4 Summary

In chapter 4, I investigated the proliferative capacity of binucleated cardiac myocytes by re-analyzing data from a lineage tracing experiment published previously. The initial study used Mosaic Analysis with Double Markers (MADM) to trace dividing cells in a mouse heart. In this technique, cells that have not undergone mitosis are either yellow (by expressing both green and red fluorescent proteins) or colorless, whereas cells that have undergone mitosis are either yellow, colorless, red, or green. Thus, one can conclude that the only pathway for red and green cells (or, single-colored cells) to arise is through cell division. Interestingly, however, these authors measured that 7% of identified binucleated cells were single-colored. Based on the genetics of the MADM model, I hypothesized that the only ways for single-colored binucleated cells to arise were either through a single-colored mononucleated cell becoming binucleated or through a binucleated cell dividing. To test this hypothesis, I identified each way a cell could proceed through two consecutive rounds of division and calculated the probabilities of each path. Given my calculations, I determined that the most likely scenario is that binucleated cells are able to divide at low rates. However, as this was a quantitative thought experiment, I do not have evidence of this happening in a cardiac myocyte. A potential follow-up study would be to search through rodent cardiac tissue stained for DNA to find mitotic figures. In other cell types, binucleated cell division is marked by a tripolar spindle structure resembling a Mercedes symbol. Identification of tripolar spindles in a rodent cardiac myocytes would provide further evidence that binucleated cardiac myocytes can divide. In order to find these symbols, I would likely look at postnatal day 7-9 rodent hearts, as 90% of these cardiac myocytes are binucleated and there is a likelihood that there is still some regenerative capacity in the heart as it is still relatively immature at this stage. Finally, if binucleated cells do indeed divide, it would be interesting to follow up and determine if the daughter cells are functional and to identify factors which regulate binucleated cell division.

Chapter 5 Summary

In chapter 5, we present a model for how cell-ECM adhesions regulate myofibril formation. We use high resolution imaging and focal adhesion perturbations to show that substrate coupling (coupling the cell's contractile forces to the ECM) is a requirement for proper myofibril formation, and that myofibrils do not form directly from focal adhesions, but are connected to focal adhesions through dorsal stress fiber-like structures. Briefly, decreased adhesion stability through either FAK knockdown, vinculin knockdown, diaphanous-1 knockdown, or expression of a dominant negative talin mutant delays myofibril formation. Further, increased adhesion stability through FAK inhibition or plating cardiac myocytes on higher concentrations of substrate led to precocious sarcomere formation up to 6 hours post-plating. These findings produced a model for a role of cell-ECM adhesions in myofibril formation: increased adhesion area correlated with an increased rate of muscle stress fiber translocation, which led to decreased rates of myofibril formation (and vice-versa). We do find evidence, however, for some centripetal sarcomere assembly, in which asymmetric cell rotation in one direction can form stress fibers along the cell edge which rotate radially inward as they elongate. However, this does not occur in every myocyte, and appears to mostly occur in myocytes with a round shape.

Chapter 6 Summary

In chapter 6, we investigated the role of myosin-generated tension in sarcomere formation and provided evidence that myosin II-based contractile force is only partially required for sarcomere formation. However, these preliminary experiments have several required future directions and follow up experiments. A future experiment is to knock out MYH6 and/or MYH7 in iPSCs using CRISPR, before they differentiate into myocytes and lose their proliferative capacity. Incomplete knockdown of either myosin could explain how sarcomeres still form, especially if only a small amount of muscle myosin force or abundance is required to organize the A-band. A full knockdown could test this possibility. Further, proteins can compensate for the knockdown of a protein of similar sequences or function[185]. In this case, it will be important to quantify the protein and RNA expression of each muscle myosin isoform when the other is knocked down or knocked out. A potential mechanism for sarcomere formation in the absence of one muscle myosin isoform could be due to upregulation of the other.

Conclusion and Future Directions

Taken together, this dissertation combines several techniques to probe the cardiac myocyte cell cycle and sarcomere formation. Several of these techniques were relatively cheap and low magnification, while several others were superresolution and novel techniques. However, each technique used was best suited for the question at hand, and shows that novel findings can still be published using affordable and simple quantification techniques.

Interestingly, upon manual observation of cardiac myocytes treated with various kinase inhibitors, I noticed that several of the wells had similar phenotypes which could be classified into categories, including cell shape changes, membrane tension loss, and cytoskeleton rearrangement. The screening platform we produced in this study could be used to test a discovery library of thousands of compounds, and upon integration with sarcApp, could assist our laboratory in our goal of studying cell biology on a systems level. Several anti-cancer therapeutics can cause heart damage, and a future potential study could combine this screening platform with automatic sarcomere alignment calculations to identify which anti-cancer therapeutics can be damaging before being advanced to further study. Another possible follow-up study could be in obtaining a natural products library and screening cardiac myocytes to identify natural products which affect sarcomere structure or functionality. Finally, this protocol can be combined with 96-well plates with multi-electrode arrays in each well to take cardiac myocyte functionality measurements throughout the screening time.

Several future directions and follow up studies could interrogate the mechanism behind Hippo pathway regulation of density-dependent proliferation. For example, it would be interesting to further study the role of combinatorial drug addition as a therapeutic for heart disease. Several studies have shown that single compound therapies have not yet been able to be proven as an effective therapy for cardiac myocyte proliferation and regeneration following a myocardial infarction. As such, the new direction in the field is to attempt combinatorial therapies in hope that some compounds will synergize and produce the large proliferative burst required for regenerative healing of the infarct zone.

However, it must also be discussed whether inducing cardiac myocyte proliferation is sufficient to completely regenerate heart muscle tissue and restore full function. In mouse models, several individual components have been shown to decrease scar size post-infarction, but none of these have yet passed clinical trials. Other considerations include the timing of such a compound: the average patient will not have immediate access to a compound when a heart attack starts and will not have treatment for several hours post-loss of oxygen. Future studies should test compounds pre-infarct, peri-infarct, and post-infarct as well as test various modes of entry. After a myocardial infarct, fibroblasts enter the infarct zone and form a non-force-producing fibrotic scar within the muscular heart wall. It may be important to prevent this pathological remodeling while inducing cardiac myocyte proliferation and to also consider the other cell types and tissue layers that make up the heart that are also required for proper functioning. A multi-pronged approach may be warranted, with a cocktail of drugs and methods angled at inducing cardiac myocyte proliferation, reducing scar size, and repairing other damaged structures while keeping the patient alive and increasing the speed of their care.

Further directions for our project involving substrate coupling in sarcomere formation would include determining the turnover of sarcomere and focal adhesion proteins given these adhesion perturbations to determine the role of protein turnover in sarcomere formation. Along these lines, it would also be advantageous to determine the mechanism of protein recruitment to the sites of myofibril formation, and which adhesion proteins are involved. Vinculin is poised to be the mechanosensitive master recruiter, as a recent study showed that vinculin localizes to adhesion sites upon increased load.

My preliminary project outlined in Chapter 6 has several future directions that are partially described above. Here, I begin to test the hypothesis that thin and thick filaments form simultaneously during sarcomere formation. It appears from my preliminary data and other previous publications that proper thin filament formation is not required for thick filament formation, and that myosin II-generated forces are only required for thin filaments. This seems counterintuitive, as thick filaments include myosin IIs. This opens several lines of inquiry, including how muscle myosin II stacks are formed when myosin II contractility is inhibited. We have shown previously that muscle myosin II stacks are largely formed through concatenation rather than filament expansion. Does concatenation and/or expansion require myosin motor activity? Is there a master regulator of thick filament formation, or one which interdigitates thin and thick filaments? And how are extremely dense pre-formed filaments aligned and connected in a spreading cardiac myocyte? To answer these questions, I am utilizing live-cell imaging of cardiac myocytes developing sarcomeres with various markers and quantifying 4D dynamics of each sarcomere component to start to generate an atlas of sarcomeric proteins, where each component localizes during sarcomere formation, and if it is required for proper sarcomere formation.

While the cell cycle and sarcomere formation do not at first seem to be linked, these are the two major mechanisms of heart growth through hyperplasia and hypertrophy. Further, these studies contribute to our laboratory's long-term goal of studying cell biology on a systems level, while also contributing to my long-term goal of developing quantitative measurements of microscopy images and cell biological data.

CHAPTER 8

REFERENCES

1 Au, Y. The muscle ultrastructure: a structural perspective of the sarcomere. *Cell Mol Life Sci* **61**, 3016-3033, doi:10.1007/s00018-004-4282-x (2004).

2 Organization, W. H. *The top 10 causes of death*, <https://www.who.int/news-room/fact-sheets/detail/the-top-10-causes-of-death> (2020).

3 Harvey, P. A. & Leinwand, L. A. The cell biology of disease: cellular mechanisms of cardiomyopathy. *J Cell Biol* **194**, 355-365, doi:10.1083/jcb.201101100 (2011).

4 Soonpaa, M. H., Kim, K. K., Pajak, L., Franklin, M. & Field, L. J. Cardiomyocyte DNA synthesis and binucleation during murine development. *Am J Physiol* **271**, H2183-2189, doi:10.1152/ajpheart.1996.271.5.H2183 (1996).

5 Eschenhagen, T. *et al.* Cardiomyocyte Regeneration: A Consensus Statement. *Circulation* **136**, 680-686, doi:10.1161/CIRCULATIONAHA.117.029343 (2017).

6 Gunthel, M., Barnett, P. & Christoffels, V. M. Development, Proliferation, and Growth of the Mammalian Heart. *Mol Ther* **26**, 1599-1609, doi:10.1016/j.ymthe.2018.05.022 (2018).

7 Buijtendijk, M. F. J., Barnett, P. & van den Hoff, M. J. B. Development of the human heart. *Am J Med Genet C Semin Med Genet* **184**, 7-22, doi:10.1002/ajmg.c.31778 (2020).

8 Pinto, A. R. *et al.* Revisiting Cardiac Cellular Composition. *Circ Res* **118**, 400-409, doi:10.1161/CIRCRESAHA.115.307778 (2016).

9 Cao, J. & Poss, K. D. The epicardium as a hub for heart regeneration. *Nat Rev Cardiol* **15**, 631-647, doi:10.1038/s41569-018-0046-4 (2018).

10 Hoit, B. D. Anatomy and Physiology of the Pericardium. *Cardiol Clin* **35**, 481-490, doi:10.1016/j.ccl.2017.07.002 (2017).

11 Hou, P. *et al.* Pluripotent stem cells induced from mouse somatic cells by small-molecule compounds. *Science* **341**, 651-654, doi:10.1126/science.1239278 (2013).

12 Pfeffer, M. A. & Braunwald, E. Ventricular remodeling after myocardial infarction. Experimental observations and clinical implications. *Circulation* **81**, 1161-1172, doi:10.1161/01.cir.81.4.1161 (1990).

13 Cirino, A. L. & Ho, C. in *GeneReviews((R))* (eds M. P. Adam *et al.*) (1993).

14 Laflamme, M. A. & Murry, C. E. Regenerating the heart. *Nat Biotechnol* **23**, 845-856, doi:10.1038/nbt1117 (2005).

15 Soonpaa, M. H., Rubart, M. & Field, L. J. Challenges measuring cardiomyocyte renewal. *Biochim Biophys Acta* **1833**, 799-803, doi:10.1016/j.bbamcr.2012.10.029 (2013).

16 De Vries, H. Atomic bomb effect: variation of radiocarbon in plants, shells, and snails in the past 4 years. *Science* **128**, 250-251, doi:10.1126/science.128.3318.250 (1958).

17 Bhardwaj, R. D. *et al.* Neocortical neurogenesis in humans is restricted to development. *Proc Natl Acad Sci U S A* **103**, 12564-12568, doi:10.1073/pnas.0605177103 (2006).

18 Spalding, K. L. *et al.* Dynamics of fat cell turnover in humans. *Nature* **453**, 783-787, doi:10.1038/nature06902 (2008).

19 Bergmann, O. *et al.* Evidence for cardiomyocyte renewal in humans. *Science* **324**, 98-102, doi:10.1126/science.1164680 (2009).

20 Mollova, M. *et al.* Cardiomyocyte proliferation contributes to heart growth in young humans. *Proc Natl Acad Sci U S A* **110**, 1446-1451, doi:10.1073/pnas.1214608110 (2013).

21 Ahuja, P., Sdek, P. & MacLellan, W. R. Cardiac myocyte cell cycle control in development, disease, and regeneration. *Physiol Rev* **87**, 521-544, doi:10.1152/physrev.00032.2006 (2007).

22 Olivetti, G. *et al.* Aging, cardiac hypertrophy and ischemic cardiomyopathy do not affect the proportion of mononucleated and multinucleated myocytes in the human heart. *J Mol Cell Cardiol* **28**, 1463-1477, doi:10.1006/jmcc.1996.0137 (1996).

23 Schmid, G. & Pfitzer, P. Mitoses and binucleated cells in perinatal human hearts. *Virchows Arch B Cell Pathol Incl Mol Pathol* **48**, 59-67, doi:10.1007/BF02890115 (1985).

24 Gan, P., Patterson, M. & Sucov, H. M. Cardiomyocyte Polyploidy and Implications for Heart Regeneration. *Annu Rev Physiol* **82**, 45-61, doi:10.1146/annurev-physiol-021119-034618 (2020).

25 Paradis, A. N., Gay, M. S. & Zhang, L. Binucleation of cardiomyocytes: the transition from a proliferative to a terminally differentiated state. *Drug Discov Today* **19**, 602-609, doi:10.1016/j.drudis.2013.10.019 (2014).

26 Gonzalez-Rosa, J. M. *et al.* Myocardial Polyploidization Creates a Barrier to Heart Regeneration in Zebrafish. *Dev Cell* **44**, 433-446 e437, doi:10.1016/j.devcel.2018.01.021 (2018).

27 Engel, F. B., Schebesta, M. & Keating, M. T. Anillin localization defect in cardiomyocyte binucleation. *J Mol Cell Cardiol* **41**, 601-612, doi:10.1016/j.yjmcc.2006.06.012 (2006).

28 Miller, A. L. The contractile ring. *Curr Biol* **21**, R976-978, doi:10.1016/j.cub.2011.10.044 (2011).

29 Ahuja, P., Perriard, E., Perriard, J. C. & Ehler, E. Sequential myofibrillar breakdown accompanies mitotic division of mammalian cardiomyocytes. *J Cell Sci* **117**, 3295-3306, doi:10.1242/jcs.01159 (2004).

30 Li, F., Wang, X. & Gerdes, A. M. Formation of binucleated cardiac myocytes in rat heart: II. Cytoskeletal organisation. *J Mol Cell Cardiol* **29**, 1553-1565, doi:10.1006/jmcc.1997.0403 (1997).

31 Li, F., Wang, X., Bunger, P. C. & Gerdes, A. M. Formation of binucleated cardiac myocytes in rat heart: I. Role of actin-myosin contractile ring. *J Mol Cell Cardiol* **29**, 1541-1551, doi:10.1006/jmcc.1997.0381 (1997).

32 Leone, M., Musa, G. & Engel, F. B. Cardiomyocyte binucleation is associated with aberrant mitotic microtubule distribution, mislocalization of RhoA and IQGAP3, as well as defective actomyosin ring anchorage and cleavage furrow ingression. *Cardiovasc Res* **114**, 1115-1131, doi:10.1093/cvr/cvy056 (2018).

33 Leone, M. & Engel, F. B. Pseudo-bipolar spindle formation and cell division in postnatal binucleated cardiomyocytes. *J Mol Cell Cardiol* **134**, 69-73, doi:10.1016/j.yjmcc.2019.07.005 (2019).

34 Patterson, M. *et al.* Frequency of mononuclear diploid cardiomyocytes underlies natural variation in heart regeneration. *Nat Genet* **49**, 1346-1353, doi:10.1038/ng.3929 (2017).

35 D'Amico, A. *et al.* Fatal hypertrophic cardiomyopathy and nemaline myopathy associated with ACTA1 K336E mutation. *Neuromuscul Disord* **16**, 548-552, doi:10.1016/j.nmd.2006.07.005 (2006).

36 Hughes, S. E. The pathology of hypertrophic cardiomyopathy. *Histopathology* **44**, 412-427, doi:10.1111/j.1365-2559.2004.01835.x (2004).

37 Thierfelder, L. *et al.* Alpha-tropomyosin and cardiac troponin T mutations cause familial hypertrophic cardiomyopathy: a disease of the sarcomere. *Cell* **77**, 701-712, doi:10.1016/0092-8674(94)90054-x (1994).

38 Martinez, H. R., Beasley, G. S., Miller, N., Goldberg, J. F. & Jefferies, J. L. Clinical Insights Into Heritable Cardiomyopathies. *Frontiers in Genetics* **12**, doi:10.3389/fgene.2021.663450 (2021).

39 Teekakirikul, P., Padera, R. F., Seidman, J. G. & Seidman, C. E. Hypertrophic cardiomyopathy: translating cellular cross talk into therapeutics. *J Cell Biol* **199**, 417-421, doi:10.1083/jcb.201207033 (2012).

40 Murphy, A. C. & Young, P. W. The actinin family of actin cross-linking proteins - a genetic perspective. *Cell Biosci* **5**, 49, doi:10.1186/s13578-015-0029-7 (2015).

41 Ribeiro Ede, A., Jr. *et al.* The structure and regulation of human muscle alpha-actinin. *Cell* **159**, 1447-1460, doi:10.1016/j.cell.2014.10.056 (2014).

42 Herzog, W. The multiple roles of titin in muscle contraction and force production. *Biophys Rev* **10**, 1187-1199, doi:10.1007/s12551-017-0395-y (2018).

43 Anderson, B. R. & Granzier, H. L. Titin-based tension in the cardiac sarcomere: molecular origin and physiological adaptations. *Prog Biophys Mol Biol* **110**, 204-217, doi:10.1016/j.pbiomolbio.2012.08.003 (2012).

44 Azad, A., Poloni, G., Sontayananon, N., Jiang, H. & Gehmlich, K. The giant titin: how to evaluate its role in cardiomyopathies. *J Muscle Res Cell Motil* **40**, 159-167, doi:10.1007/s10974-019-09518-w (2019).

45 Myhre, J. L., Hills, J. A., Prill, K., Wohlgemuth, S. L. & Pilgrim, D. B. The titin A-band rod domain is dispensable for initial thick filament assembly in zebrafish. *Dev Biol* **387**, 93-108, doi:10.1016/j.ydbio.2013.12.020 (2014).

46 Lyons, G. E., Schiaffino, S., Sassoon, D., Barton, P. & Buckingham, M. Developmental regulation of myosin gene expression in mouse cardiac muscle. *J Cell Biol* **111**, 2427-2436, doi:10.1083/jcb.111.6.2427 (1990).

47 Ng, W. A., Grupp, I. L., Subramaniam, A. & Robbins, J. Cardiac myosin heavy chain mRNA expression and myocardial function in the mouse heart. *Circ Res* **68**, 1742-1750, doi:10.1161/01.res.68.6.1742 (1991).

48 Wang, Z. *et al.* The molecular basis for sarcomere organization in vertebrate skeletal muscle. *Cell* **184**, 2135-2150 e2113, doi:10.1016/j.cell.2021.02.047 (2021).

49 Samarel, A. M. Costameres, focal adhesions, and cardiomyocyte mechanotransduction. *Am J Physiol Heart Circ Physiol* **289**, H2291-2301, doi:10.1152/ajpheart.00749.2005 (2005).

50 Kresh, J. Y. & Chopra, A. Intercellular and extracellular mechanotransduction in cardiac myocytes. *Pflugers Arch* **462**, 75-87, doi:10.1007/s00424-011-0954-1 (2011).

51 Lu, M. H. *et al.* The vinculin/sarcomeric-alpha-actinin/alpha-actin nexus in cultured cardiac myocytes. *J Cell Biol* **117**, 1007-1022, doi:10.1083/jcb.117.5.1007 (1992).

52 Alexandrova, A. Y. *et al.* Comparative dynamics of retrograde actin flow and focal adhesions: formation of nascent adhesions triggers transition from fast to slow flow. *PLoS One* **3**, e3234, doi:10.1371/journal.pone.0003234 (2008).

53 Hotulainen, P. & Lappalainen, P. Stress fibers are generated by two distinct actin assembly mechanisms in motile cells. *J Cell Biol* **173**, 383-394, doi:10.1083/jcb.200511093 (2006).

54 Tojkander, S., Gateva, G. & Lappalainen, P. Actin stress fibers--assembly, dynamics and biological roles. *J Cell Sci* **125**, 1855-1864, doi:10.1242/jcs.098087 (2012).

55 Janostiak, R., Pataki, A. C., Brabek, J. & Rosel, D. Mechanosensors in integrin signaling: the emerging role of p130Cas. *Eur J Cell Biol* **93**, 445-454, doi:10.1016/j.ejcb.2014.07.002 (2014).

56 Geiger, B., Spatz, J. P. & Bershadsky, A. D. Environmental sensing through focal adhesions. *Nat Rev Mol Cell Biol* **10**, 21-33, doi:10.1038/nrm2593 (2009).

57 Webb, D. J. *et al.* FAK-Src signalling through paxillin, ERK and MLCK regulates adhesion disassembly. *Nat Cell Biol* **6**, 154-161, doi:10.1038/ncb1094 (2004).

58 Pasapera, A. M., Schneider, I. C., Rericha, E., Schlaepfer, D. D. & Waterman, C. M. Myosin II activity regulates vinculin recruitment to focal adhesions through FAK-mediated paxillin phosphorylation. *J Cell Biol* **188**, 877-890, doi:10.1083/jcb.200906012 (2010).

59 Kovacic-Milivojevic, B. *et al.* Focal adhesion kinase and p130Cas mediate both sarcomeric organization and activation of genes associated with cardiac myocyte hypertrophy. *Mol Biol Cell* **12**, 2290-2307, doi:10.1091/mbc.12.8.2290 (2001).

60 Case, L. B. *et al.* Molecular mechanism of vinculin activation and nanoscale spatial organization in focal adhesions. *Nat Cell Biol* **17**, 880-892, doi:10.1038/ncb3180 (2015).

61 del Rio, A. *et al.* Stretching single talin rod molecules activates vinculin binding. *Science* **323**, 638-641, doi:10.1126/science.1162912 (2009).

62 Carisey, A. & Ballestrem, C. Vinculin, an adapter protein in control of cell adhesion signalling. *Eur J Cell Biol* **90**, 157-163, doi:10.1016/j.ejcb.2010.06.007 (2011).

63 Sanger, J. W., Mittal, B. & Sanger, J. M. Formation of myofibrils in spreading chick cardiac myocytes. *Cell Motil* **4**, 405-416, doi:10.1002/cm.970040602 (1984).

64 Dlugosz, A. A., Antin, P. B., Nachmias, V. T. & Holtzer, H. The relationship between stress fiber-like structures and nascent myofibrils in cultured cardiac myocytes. *J Cell Biol* **99**, 2268-2278, doi:10.1083/jcb.99.6.2268 (1984).

65 Schultheiss, T. *et al.* Differential distribution of subsets of myofibrillar proteins in cardiac nonstriated and striated myofibrils. *J Cell Biol* **110**, 1159-1172, doi:10.1083/jcb.110.4.1159 (1990).

66 Holtzer, H. *et al.* Independent assembly of 1.6 microns long bipolar MHC filaments and I-Z-I bodies. *Cell Struct Funct* **22**, 83-93, doi:10.1247/csf.22.83 (1997).

67 Hill, C. S., Duran, S., Lin, Z. X., Weber, K. & Holtzer, H. Titin and myosin, but not desmin, are linked during myofibrillogenesis in postmitotic mononucleated myoblasts. *J Cell Biol* **103**, 2185-2196, doi:10.1083/jcb.103.6.2185 (1986).

68 Du, A., Sanger, J. M. & Sanger, J. W. Cardiac myofibrillogenesis inside intact embryonic hearts. *Dev Biol* **318**, 236-246, doi:10.1016/j.ydbio.2008.03.011 (2008).

69 Peter, A. K., Bjerke, M. A. & Leinwand, L. A. Biology of the cardiac myocyte in heart disease. *Mol Biol Cell* **27**, 2149-2160, doi:10.1091/mbc.E16-01-0038 (2016).

70 Rhee, D., Sanger, J. M. & Sanger, J. W. The premyofibril: evidence for its role in myofibrillogenesis. *Cell Motil Cytoskeleton* **28**, 1-24, doi:10.1002/cm.970280102 (1994).

71 Dabiri, G. A., Turnacioglu, K. K., Sanger, J. M. & Sanger, J. W. Myofibrillogenesis visualized in living embryonic cardiomyocytes. *Proc Natl Acad Sci U S A* **94**, 9493-9498, doi:10.1073/pnas.94.17.9493 (1997).

72 Sanger, J. W. *et al.* How to build a myofibril. *J Muscle Res Cell Motil* **26**, 343-354, doi:10.1007/s10974-005-9016-7 (2005).

73 Sanger, J. W., Wang, J., Holloway, B., Du, A. & Sanger, J. M. Myofibrillogenesis in skeletal muscle cells in zebrafish. *Cell Motil Cytoskeleton* **66**, 556-566, doi:10.1002/cm.20365 (2009).

74 Hresko, M. C., Williams, B. D. & Waterston, R. H. Assembly of body wall muscle and muscle cell attachment structures in Caenorhabditis elegans. *J Cell Biol* **124**, 491-506, doi:10.1083/jcb.124.4.491 (1994).

75 Ehler, E., Rothen, B. M., Hammerle, S. P., Komiyama, M. & Perriard, J. C. Myofibrillogenesis in the developing chicken heart: assembly of Z-disk, M-line and the thick filaments. *J Cell Sci* **112 (Pt 10)**, 1529-1539 (1999).

76 Sparrow, J. C. & Schock, F. The initial steps of myofibril assembly: integrins pave the way. *Nat Rev Mol Cell Biol* **10**, 293-298, doi:10.1038/nrm2634 (2009).

77 Quach, N. L. & Rando, T. A. Focal adhesion kinase is essential for costamerogenesis in cultured skeletal muscle cells. *Dev Biol* **293**, 38-52, doi:10.1016/j.ydbio.2005.12.040 (2006).

78 Chopra, A. *et al.* Force Generation via beta-Cardiac Myosin, Titin, and alpha-Actinin Drives Cardiac Sarcomere Assembly from Cell-Matrix Adhesions. *Dev Cell* **44**, 87-96 e85, doi:10.1016/j.devcel.2017.12.012 (2018).

79 Loison, O. *et al.* Polarization-resolved microscopy reveals a muscle myosin motor-independent mechanism of molecular actin ordering during sarcomere maturation. *PLoS Biol* **16**, e2004718, doi:10.1371/journal.pbio.2004718 (2018).
80 Fenix, A. M. *et al.* Muscle-specific stress fibers give rise to sarcomeres in cardiomyocytes. *Elife* **7**, doi:10.7554/eLife.42144 (2018).
81 Li, F., Wang, X., Capasso, J. M. & Gerdes, A. M. Rapid transition of cardiac myocytes from hyperplasia to hypertrophy during postnatal development. *J Mol Cell Cardiol* **28**, 1737-1746, doi:10.1006/jmcc.1996.0163 (1996).
82 Mohamed, T. M. A. *et al.* Regulation of Cell Cycle to Stimulate Adult Cardiomyocyte Proliferation and Cardiac Regeneration. *Cell* **173**, 104-116 e112, doi:10.1016/j.cell.2018.02.014 (2018).
83 Hartman, M. E., Dai, D. F. & Laflamme, M. A. Human pluripotent stem cells: Prospects and challenges as a source of cardiomyocytes for in vitro modeling and cell-based cardiac repair. *Adv Drug Deliv Rev* **96**, 3-17, doi:10.1016/j.addr.2015.05.004 (2016).
84 Bassat, E. *et al.* The extracellular matrix protein agrin promotes heart regeneration in mice. *Nature* **547**, 179-184, doi:10.1038/nature22978 (2017).
85 Sharma, A. *et al.* Stage-specific Effects of Bioactive Lipids on Human iPSC Cardiac Differentiation and Cardiomyocyte Proliferation. *Sci Rep* **8**, 6618, doi:10.1038/s41598-018-24954-3 (2018).
86 McClatchey, A. I. & Yap, A. S. Contact inhibition (of proliferation) redux. *Curr Opin Cell Biol* **24**, 685-694, doi:10.1016/j.ceb.2012.06.009 (2012).
87 Park, S. *et al.* Yes-associated protein mediates human embryonic stem cell-derived cardiomyocyte proliferation: Involvement of epidermal growth factor receptor signaling. *J Cell Physiol* **233**, 7016-7025, doi:10.1002/jcp.26625 (2018).
88 Uosaki, H. *et al.* Identification of chemicals inducing cardiomyocyte proliferation in developmental stage-specific manner with pluripotent stem cells. *Circ Cardiovasc Genet* **6**, 624-633, doi:10.1161/CIRCGENETICS.113.000330 (2013).
89 Kim, Y. S. *et al.* Natural product derivative BIO promotes recovery after myocardial infarction via unique modulation of the cardiac microenvironment. *Sci Rep* **6**, 30726, doi:10.1038/srep30726 (2016).
90 Engel, F. B. *et al.* p38 MAP kinase inhibition enables proliferation of adult mammalian cardiomyocytes. *Genes Dev* **19**, 1175-1187, doi:10.1101/gad.1306705 (2005).
91 Engel, F. B., Hsieh, P. C., Lee, R. T. & Keating, M. T. FGF1/p38 MAP kinase inhibitor therapy induces cardiomyocyte mitosis, reduces scarring, and rescues function after myocardial infarction. *Proc Natl Acad Sci U S A* **103**, 15546-15551, doi:10.1073/pnas.0607382103 (2006).
92 Chan, A. Y., Soltys, C. L., Young, M. E., Proud, C. G. & Dyck, J. R. Activation of AMP-activated protein kinase inhibits protein synthesis associated with hypertrophy in the cardiac myocyte. *J Biol Chem* **279**, 32771-32779, doi:10.1074/jbc.M403528200 (2004).
93 Singh, A. P. *et al.* Inhibition of GSK-3 to induce cardiomyocyte proliferation: a recipe for in situ cardiac regeneration. *Cardiovasc Res* **115**, 20-30, doi:10.1093/cvr/cvy255 (2019).
94 Mills, R. J. *et al.* Drug Screening in Human PSC-Cardiac Organoids Identifies Pro-proliferative Compounds Acting via the Mevalonate Pathway. *Cell Stem Cell* **24**, 895-907 e896, doi:10.1016/j.stem.2019.03.009 (2019).
95 Uosaki, H. *et al.* Transcriptional Landscape of Cardiomyocyte Maturation. *Cell Rep* **13**, 1705-1716, doi:10.1016/j.celrep.2015.10.032 (2015).
96 Hesse, M. *et al.* Midbody Positioning and Distance Between Daughter Nuclei Enable Unequivocal Identification of Cardiomyocyte Cell Division in Mice. *Circ Res* **123**, 1039-1052, doi:10.1161/CIRCRESAHA.118.312792 (2018).

97 Ponnusamy, M., Li, P. F. & Wang, K. Understanding cardiomyocyte proliferation: an insight into cell cycle activity. *Cell Mol Life Sci* **74**, 1019-1034, doi:10.1007/s00018-016-2375-y (2017).

98 Porrello, E. R. *et al.* Transient regenerative potential of the neonatal mouse heart. *Science* **331**, 1078-1080, doi:10.1126/science.1200708 (2011).

99 Laflamme, M. A. & Murry, C. E. Heart regeneration. *Nature* **473**, 326-335, doi:10.1038/nature10147 (2011).

100 Walsh, S., Ponten, A., Fleischmann, B. K. & Jovinge, S. Cardiomyocyte cell cycle control and growth estimation in vivo--an analysis based on cardiomyocyte nuclei. *Cardiovasc Res* **86**, 365-373, doi:10.1093/cvr/cvq005 (2010).

101 Heallen, T. *et al.* Hippo pathway inhibits Wnt signaling to restrain cardiomyocyte proliferation and heart size. *Science* **332**, 458-461, doi:10.1126/science.1199010 (2011).

102 Xin, M. *et al.* Hippo pathway effector Yap promotes cardiac regeneration. *Proc Natl Acad Sci U S A* **110**, 13839-13844, doi:10.1073/pnas.1313192110 (2013).

103 Dong, J. *et al.* Elucidation of a universal size-control mechanism in Drosophila and mammals. *Cell* **130**, 1120-1133, doi:10.1016/j.cell.2007.07.019 (2007).

104 He, C. *et al.* The Hippo/YAP pathway interacts with EGFR signaling and HPV oncoproteins to regulate cervical cancer progression. *EMBO Mol Med* **7**, 1426-1449, doi:10.15252/emmm.201404976 (2015).

105 Zhao, B., Li, L., Tumaneng, K., Wang, C. Y. & Guan, K. L. A coordinated phosphorylation by Lats and CK1 regulates YAP stability through SCF(beta-TRCP). *Genes Dev* **24**, 72-85, doi:10.1101/gad.1843810 (2010).

106 Gumbiner, B. M. & Kim, N. G. The Hippo-YAP signaling pathway and contact inhibition of growth. *J Cell Sci* **127**, 709-717, doi:10.1242/jcs.140103 (2014).

107 Kim, N. G., Koh, E., Chen, X. & Gumbiner, B. M. E-cadherin mediates contact inhibition of proliferation through Hippo signaling-pathway components. *Proc Natl Acad Sci U S A* **108**, 11930-11935, doi:10.1073/pnas.1103345108 (2011).

108 Totaro, A. *et al.* YAP/TAZ link cell mechanics to Notch signalling to control epidermal stem cell fate. *Nat Commun* **8**, 15206, doi:10.1038/ncomms15206 (2017).

109 Zhao, B. *et al.* Inactivation of YAP oncoprotein by the Hippo pathway is involved in cell contact inhibition and tissue growth control. *Genes Dev* **21**, 2747-2761, doi:10.1101/gad.1602907 (2007).

110 Schlegelmilch, K. *et al.* Yap1 acts downstream of alpha-catenin to control epidermal proliferation. *Cell* **144**, 782-795, doi:10.1016/j.cell.2011.02.031 (2011).

111 Varelas, X. The Hippo pathway effectors TAZ and YAP in development, homeostasis and disease. *Development* **141**, 1614-1626, doi:10.1242/dev.102376 (2014).

112 Kim, J. H., Kushiro, K., Graham, N. A. & Asthagiri, A. R. Tunable interplay between epidermal growth factor and cell-cell contact governs the spatial dynamics of epithelial growth. *Proc Natl Acad Sci U S A* **106**, 11149-11153, doi:10.1073/pnas.0812651106 (2009).

113 von Gise, A. *et al.* YAP1, the nuclear target of Hippo signaling, stimulates heart growth through cardiomyocyte proliferation but not hypertrophy. *Proc Natl Acad Sci U S A* **109**, 2394-2399, doi:10.1073/pnas.1116136109 (2012).

114 Wang, J., Liu, S., Heallen, T. & Martin, J. F. The Hippo pathway in the heart: pivotal roles in development, disease, and regeneration. *Nat Rev Cardiol* **15**, 672-684, doi:10.1038/s41569-018-0063-3 (2018).

115 Neininger, A. C., Long, J. H., Baillargeon, S. M. & Burnette, D. T. A simple and flexible high-throughput method for the study of cardiomyocyte proliferation. *Sci Rep* **9**, 15917, doi:10.1038/s41598-019-52467-0 (2019).

116 Cory, G. Scratch-wound assay. *Methods Mol Biol* **769**, 25-30, doi:10.1007/978-1-61779-207-6_2 (2011).

117 Hansen, C. G., Ng, Y. L., Lam, W. L., Plouffe, S. W. & Guan, K. L. The Hippo pathway effectors YAP and TAZ promote cell growth by modulating amino acid signaling to mTORC1. *Cell Res* **25**, 1299-1313, doi:10.1038/cr.2015.140 (2015).
118 Gerdes, J. *et al.* Cell cycle analysis of a cell proliferation-associated human nuclear antigen defined by the monoclonal antibody Ki-67. *J Immunol* **133**, 1710-1715 (1984).
119 Miller, I. *et al.* Ki67 is a Graded Rather than a Binary Marker of Proliferation versus Quiescence. *Cell Rep* **24**, 1105-1112 e1105, doi:10.1016/j.celrep.2018.06.110 (2018).
120 D'Uva, G. *et al.* ERBB2 triggers mammalian heart regeneration by promoting cardiomyocyte dedifferentiation and proliferation. *Nat Cell Biol* **17**, 627-638, doi:10.1038/ncb3149 (2015).
121 Wang, W. E. *et al.* Dedifferentiation, Proliferation, and Redifferentiation of Adult Mammalian Cardiomyocytes After Ischemic Injury. *Circulation* **136**, 834-848, doi:10.1161/CIRCULATIONAHA.116.024307 (2017).
122 Venkataramani, V. *et al.* CD31 Expression Determines Redox Status and Chemoresistance in Human Angiosarcomas. *Clin Cancer Res* **24**, 460-473, doi:10.1158/1078-0432.CCR-17-1778 (2018).
123 Kim, M. K., Jang, J. W. & Bae, S. C. DNA binding partners of YAP/TAZ. *BMB Rep* **51**, 126-133, doi:10.5483/bmbrep.2018.51.3.015 (2018).
124 Lee, D. H. *et al.* LATS-YAP/TAZ controls lineage specification by regulating TGFbeta signaling and Hnf4alpha expression during liver development. *Nat Commun* **7**, 11961, doi:10.1038/ncomms11961 (2016).
125 Fan, F. *et al.* Pharmacological targeting of kinases MST1 and MST2 augments tissue repair and regeneration. *Sci Transl Med* **8**, 352ra108, doi:10.1126/scitranslmed.aaf2304 (2016).
126 Miller, E. *et al.* Identification of serum-derived sphingosine-1-phosphate as a small molecule regulator of YAP. *Chem Biol* **19**, 955-962, doi:10.1016/j.chembiol.2012.07.005 (2012).
127 Liu-Chittenden, Y. *et al.* Genetic and pharmacological disruption of the TEAD-YAP complex suppresses the oncogenic activity of YAP. *Genes Dev* **26**, 1300-1305, doi:10.1101/gad.192856.112 (2012).
128 Triastuti, E. *et al.* Pharmacological inhibition of Hippo pathway, with the novel kinase inhibitor XMU-MP-1, protects the heart against adverse effects during pressure overload. *Br J Pharmacol* **176**, 3956-3971, doi:10.1111/bph.14795 (2019).
129 Aharonov, A. *et al.* ERBB2 drives YAP activation and EMT-like processes during cardiac regeneration. *Nat Cell Biol* **22**, 1346-1356, doi:10.1038/s41556-020-00588-4 (2020).
130 Ramjee, V. *et al.* Epicardial YAP/TAZ orchestrate an immunosuppressive response following myocardial infarction. *J Clin Invest* **127**, 899-911, doi:10.1172/JCI88759 (2017).
131 Meckert, P. C. *et al.* Endomitosis and polyploidization of myocardial cells in the periphery of human acute myocardial infarction. *Cardiovasc Res* **67**, 116-123, doi:10.1016/j.cardiores.2005.02.017 (2005).
132 Morikawa, Y., Heallen, T., Leach, J., Xiao, Y. & Martin, J. F. Dystrophin-glycoprotein complex sequesters Yap to inhibit cardiomyocyte proliferation. *Nature* **547**, 227-231, doi:10.1038/nature22979 (2017).
133 Zong, H., Espinosa, J. S., Su, H. H., Muzumdar, M. D. & Luo, L. Mosaic analysis with double markers in mice. *Cell* **121**, 479-492, doi:10.1016/j.cell.2005.02.012 (2005).
134 Sawamiphak, S., Kontarakis, Z., Filosa, A., Reischauer, S. & Stainier, D. Y. R. Transient cardiomyocyte fusion regulates cardiac development in zebrafish. *Nat Commun* **8**, 1525, doi:10.1038/s41467-017-01555-8 (2017).
135 van Berlo, J. H. *et al.* c-kit+ cells minimally contribute cardiomyocytes to the heart. *Nature* **509**, 337-341, doi:10.1038/nature13309 (2014).

136 Tasic, B. *et al.* Extensions of MADM (mosaic analysis with double markers) in mice. *PLoS One* **7**, e33332, doi:10.1371/journal.pone.0033332 (2012).

137 Claycomb, W. C. & Bradshaw, H. D., Jr. Acquisition of multiple nuclei and the activity of DNA polymerase alpha and reinitiation of DNA replication in terminally differentiated adult cardiac muscle cells in culture. *Dev Biol* **99**, 331-337, doi:10.1016/0012-1606(83)90283-x (1983).

138 Botting, K. J. *et al.* Early origins of heart disease: low birth weight and determinants of cardiomyocyte endowment. *Clin Exp Pharmacol Physiol* **39**, 814-823, doi:10.1111/j.1440-1681.2011.05649.x (2012).

139 Naqvi, N. *et al.* A proliferative burst during preadolescence establishes the final cardiomyocyte number. *Cell* **157**, 795-807, doi:10.1016/j.cell.2014.03.035 (2014).

140 Jonker, S. S. *et al.* Myocyte enlargement, differentiation, and proliferation kinetics in the fetal sheep heart. *J Appl Physiol (1985)* **102**, 1130-1142, doi:10.1152/japplphysiol.00937.2006 (2007).

141 Knoll, R., Buyandelger, B. & Lab, M. The sarcomeric Z-disc and Z-discopathies. *J Biomed Biotechnol* **2011**, 569628, doi:10.1155/2011/569628 (2011).

142 Liu, H. *et al.* Disassembly of myofibrils and potential imbalanced forces on Z-discs in cultured adult cardiomyocytes. *Cytoskeleton (Hoboken)* **73**, 246-257, doi:10.1002/cm.21298 (2016).

143 Dabiri, B. E., Lee, H. & Parker, K. K. A potential role for integrin signaling in mechanoelectrical feedback. *Prog Biophys Mol Biol* **110**, 196-203, doi:10.1016/j.pbiomolbio.2012.07.002 (2012).

144 McCain, M. L., Lee, H., Aratyn-Schaus, Y., Kleber, A. G. & Parker, K. K. Cooperative coupling of cell-matrix and cell-cell adhesions in cardiac muscle. *Proc Natl Acad Sci U S A* **109**, 9881-9886, doi:10.1073/pnas.1203007109 (2012).

145 Bloor, J. W. & Brown, N. H. Genetic analysis of the Drosophila alphaPS2 integrin subunit reveals discrete adhesive, morphogenetic and sarcomeric functions. *Genetics* **148**, 1127-1142 (1998).

146 Volk, T., Fessler, L. I. & Fessler, J. H. A role for integrin in the formation of sarcomeric cytoarchitecture. *Cell* **63**, 525-536, doi:10.1016/0092-8674(90)90449-o (1990).

147 Sharp, W. W., Simpson, D. G., Borg, T. K., Samarel, A. M. & Terracio, L. Mechanical forces regulate focal adhesion and costamere assembly in cardiac myocytes. *Am J Physiol* **273**, H546-556, doi:10.1152/ajpheart.1997.273.2.H546 (1997).

148 Simpson, D. G., Decker, M. L., Clark, W. A. & Decker, R. S. Contractile activity and cell-cell contact regulate myofibrillar organization in cultured cardiac myocytes. *J Cell Biol* **123**, 323-336, doi:10.1083/jcb.123.2.323 (1993).

149 Hersch, N. *et al.* The constant beat: cardiomyocytes adapt their forces by equal contraction upon environmental stiffening. *Biol Open* **2**, 351-361, doi:10.1242/bio.20133830 (2013).

150 Jacot, J. G., McCulloch, A. D. & Omens, J. H. Substrate stiffness affects the functional maturation of neonatal rat ventricular myocytes. *Biophys J* **95**, 3479-3487, doi:10.1529/biophysj.107.124545 (2008).

151 Schwander, M. *et al.* Beta1 integrins regulate myoblast fusion and sarcomere assembly. *Dev Cell* **4**, 673-685, doi:10.1016/s1534-5807(03)00118-7 (2003).

152 Jiang, Y., Park, P., Hong, S. M. & Ban, K. Maturation of Cardiomyocytes Derived from Human Pluripotent Stem Cells: Current Strategies and Limitations. *Mol Cells* **41**, 613-621, doi:10.14348/molcells.2018.0143 (2018).

153 Wang, S. M. & Greaser, M. L. Immunocytochemical studies using a monoclonal antibody to bovine cardiac titin on intact and extracted myofibrils. *J Muscle Res Cell Motil* **6**, 293-312, doi:10.1007/BF00713171 (1985).

154 Thievessen, I. *et al.* Vinculin-actin interaction couples actin retrograde flow to focal adhesions, but is dispensable for focal adhesion growth. *The Journal of cell biology* **202**, 163-177, doi:10.1083/jcb.201303129 (2013).
155 Dumbauld, D. W. *et al.* How vinculin regulates force transmission. *Proc Natl Acad Sci U S A* **110**, 9788-9793, doi:10.1073/pnas.1216209110 (2013).
156 Tan, C. L. *et al.* Full length talin stimulates integrin activation and axon regeneration. *Mol Cell Neurosci* **68**, 1-8, doi:10.1016/j.mcn.2015.03.011 (2015).
157 Parsons, J. T., Martin, K. H., Slack, J. K., Taylor, J. M. & Weed, S. A. Focal adhesion kinase: a regulator of focal adhesion dynamics and cell movement. *Oncogene* **19**, 5606-5613, doi:10.1038/sj.onc.1203877 (2000).
158 Slack-Davis, J. K. *et al.* Cellular characterization of a novel focal adhesion kinase inhibitor. *J Biol Chem* **282**, 14845-14852, doi:10.1074/jbc.M606695200 (2007).
159 Taneja, N. *et al.* Focal adhesions control cleavage furrow shape and spindle tilt during mitosis. *Sci Rep* **6**, 29846, doi:10.1038/srep29846 (2016).
160 Schaller, M. D. *et al.* Autophosphorylation of the focal adhesion kinase, pp125FAK, directs SH2-dependent binding of pp60src. *Mol Cell Biol* **14**, 1680-1688, doi:10.1128/mcb.14.3.1680 (1994).
161 O'Brien, S. *et al.* FAK inhibition with small molecule inhibitor Y15 decreases viability, clonogenicity, and cell attachment in thyroid cancer cell lines and synergizes with targeted therapeutics. *Oncotarget* **5**, 7945-7959, doi:10.18632/oncotarget.2381 (2014).
162 Gupton, S. L. & Waterman-Storer, C. M. Spatiotemporal feedback between actomyosin and focal-adhesion systems optimizes rapid cell migration. *Cell* **125**, 1361-1374, doi:10.1016/j.cell.2006.05.029 (2006).
163 Fessenden, T. B. *et al.* Dia1-dependent adhesions are required by epithelial tissues to initiate invasion. *The Journal of cell biology* **217**, 1485-1502, doi:10.1083/jcb.201703145 (2018).
164 Riveline, D. *et al.* Focal contacts as mechanosensors: externally applied local mechanical force induces growth of focal contacts by an mDia1-dependent and ROCK-independent mechanism. *The Journal of cell biology* **153**, 1175-1186, doi:10.1083/jcb.153.6.1175 (2001).
165 Kanchanawong, P. *et al.* Nanoscale architecture of integrin-based cell adhesions. *Nature* **468**, 580-584, doi:10.1038/nature09621 (2010).
166 Burnette, D. T. *et al.* A role for actin arcs in the leading-edge advance of migrating cells. *Nat Cell Biol* **13**, 371-381, doi:10.1038/ncb2205 (2011).
167 Burnette, D. T. *et al.* A contractile and counterbalancing adhesion system controls the 3D shape of crawling cells. *J Cell Biol* **205**, 83-96, doi:10.1083/jcb.201311104 (2014).
168 Swaminathan, V. *et al.* Actin retrograde flow actively aligns and orients ligand-engaged integrins in focal adhesions. *Proceedings of the National Academy of Sciences of the United States of America* **114**, 10648-10653, doi:10.1073/pnas.1701136114 (2017).
169 Katsumi, A., Naoe, T., Matsushita, T., Kaibuchi, K. & Schwartz, M. A. Integrin activation and matrix binding mediate cellular responses to mechanical stretch. *J Biol Chem* **280**, 16546-16549, doi:10.1074/jbc.C400455200 (2005).
170 Lemke, S. B., Weidemann, T., Cost, A. L., Grashoff, C. & Schnorrer, F. A small proportion of Talin molecules transmit forces at developing muscle attachments in vivo. *PLoS Biol* **17**, e3000057, doi:10.1371/journal.pbio.3000057 (2019).
171 Lemke, S. B. & Schnorrer, F. Mechanical forces during muscle development. *Mech Dev* **144**, 92-101, doi:10.1016/j.mod.2016.11.003 (2017).
172 Yuan, H., Marzban, B. & Kit Parker, K. Myofibrils in Cardiomyocytes Tend to Assemble Along the Maximal Principle Stress Directions. *J Biomech Eng* **139**, doi:10.1115/1.4037795 (2017).

173 Tojkander, S., Gateva, G., Husain, A., Krishnan, R. & Lappalainen, P. Generation of contractile actomyosin bundles depends on mechanosensitive actin filament assembly and disassembly. *Elife* **4**, e06126, doi:10.7554/eLife.06126 (2015).

174 Yang, K. C. *et al.* Novel Adult-Onset Systolic Cardiomyopathy Due to MYH7 E848G Mutation in Patient-Derived Induced Pluripotent Stem Cells. *JACC Basic Transl Sci* **3**, 728-740, doi:10.1016/j.jacbts.2018.08.008 (2018).

175 Wang, Y. L. Reorganization of actin filament bundles in living fibroblasts. *The Journal of cell biology* **99**, 1478-1485, doi:10.1083/jcb.99.4.1478 (1984).

176 Koteliansky, V. E. & Gneushev, G. N. Vinculin localization in cardiac muscle. *FEBS Lett* **159**, 158-160, doi:10.1016/0014-5793(83)80437-2 (1983).

177 Yi, X. P., Wang, X., Gerdes, A. M. & Li, F. Subcellular redistribution of focal adhesion kinase and its related nonkinase in hypertrophic myocardium. *Hypertension* **41**, 1317-1323, doi:10.1161/01.HYP.0000072772.74183.5F (2003).

178 Fukuda, R. *et al.* Mechanical Forces Regulate Cardiomyocyte Myofilament Maturation via the VCL-SSH1-CFL Axis. *Dev Cell* **51**, 62-77 e65, doi:10.1016/j.devcel.2019.08.006 (2019).

179 Paszek, M. J. *et al.* Scanning angle interference microscopy reveals cell dynamics at the nanoscale. *Nat Methods* **9**, 825-827, doi:10.1038/nmeth.2077 (2012).

180 Hinson, J. T. *et al.* HEART DISEASE. Titin mutations in iPS cells define sarcomere insufficiency as a cause of dilated cardiomyopathy. *Science* **349**, 982-986, doi:10.1126/science.aaa5458 (2015).

181 Fisher, R., Perkins, S., Walker A., & Wolfart, E. *Fourier Transform*, <https://homepages.inf.ed.ac.uk/rbf/HIPR2/fourier.htm> (2003).

182 Almenar-Queralt, A., Gregorio, C. C. & Fowler, V. M. Tropomodulin assembles early in myofibrillogenesis in chick skeletal muscle: evidence that thin filaments rearrange to form striated myofibrils. *J Cell Sci* **112 (Pt 8)**, 1111-1123 (1999).

183 McKenna, N. M., Johnson, C. S. & Wang, Y. L. Formation and alignment of Z lines in living chick myotubes microinjected with rhodamine-labeled alpha-actinin. *J Cell Biol* **103**, 2163-2171, doi:10.1083/jcb.103.6.2163 (1986).

184 Bryce, N. S. *et al.* Specification of actin filament function and molecular composition by tropomyosin isoforms. *Mol Biol Cell* **14**, 1002-1016, doi:10.1091/mbc.e02-04-0244 (2003).

185 El-Brolosy, M. A. *et al.* Genetic compensation triggered by mutant mRNA degradation. *Nature* **568**, 193-197, doi:10.1038/s41586-019-1064-z (2019).